

Project No. 15-9231

# Multimodal Nondestructive Dry Cask Basket Structure and Spent Fuel Evaluation

---

## Integrated Research Project

**Joseph Gladden**

University of Mississippi

### Collaborators

Oregon State University

University of Florida

University of South Carolina

Suibel Schuppner, Federal POC

TJ Ulrich, Technical POC



# **Multimodal Nondestructive Dry Cask Basket Structure and Spent Fuel Evaluation**

Final Technical Report

DE\_NE0008400

U.S. Department of Energy – Nuclear Energy University Programs

University of Mississippi

Dr. Joseph R Gladden – Principal Investigator

Teaming Members:

University of Florida  
University of South Carolina  
Oregon State University  
AREVA  
EPRI

## Acknowledgement

This material is based upon work supported by the U. S. Department of Energy  
under Award No. DE\_NE0008400.

## Disclaimer

Any opinions, findings, and conclusions or recommendations expressed in this  
publication are those of the author(s) and do not necessarily reflect the views of the  
U. S. Department of Energy.

## **Table of Contents**

Executive Summary .....	3
University of Florida.....	6
University of Mississippi .....	24
University of South Carolina .....	47
Oregon State University.....	69
AREVA.....	100
EPRI.....	101
Scale-Up Proposal for a Field Deployable Systems .....	120

## **Executive Summary**

This NEUP-IRP assembled a team from diverse institutions and a diverse set of expertise to examine the problem of assessing the structural health of dry nuclear fuel storage casks, specifically the TN-32 design. With no physical access designed into these storage casks and the high cost and risk associated with opening casks for direct inspection, the technical difficulty of structural assessment of the basket structure and fuel assemblies is high. In response to this challenge, this IRP brought together experts in both traditional and novel NDE methodologies: active acoustics (University of Mississippi), emissions tomography (University of Florida), muon tomography (Oregon State University), and passive-active ultrasonics (University of South Carolina). Further, our industry partners in the Electric Power Research Institute (EPRI) and AREVA provided invaluable insight into technical design details for the cask, practical knowledge of operating parameters at a storage facility, and key relationships that enabled activities unforeseen at the time of the proposed work but were critical in guiding the path of the research. The team decided early in the project that we had a collective goal of laying the technical ground work for practical solutions that could be implemented in the field with reasonable cost, time, and reliability.

A fortunate opportunity arose early in this IRP project to obtain access to a new TN-32 cask at Columbiana High Tech. Both acoustics teams were given access for testing concepts in the first year of the project. This ended up providing critical guidance in the design of subsequent laboratory experiments. Specifically, it became clear that the only reliable acoustic pathways to the interior were through the trunnions, base plate, and top ring of the cask. Based on these field tests and discussions about what would be of practical interest, the team as a whole decided a realistic goal was to detect catastrophic failure of a single fuel assembly, or one that was missing. It is clear from this work that the active acoustics / resonance and muon tomography methodologies would be capable of detecting interior structural integrity problems at this level. The other two areas of investigation (emissions tomography and passive/active ultrasonics) would need more testing to determine a successful implementation, but each may also have other applications such as long term monitoring and monitoring during transportation. This IRP project resulted in technical advances with applications that extend beyond the problem at hand, supported the training of 10 graduate students + 1 post doc, 21 publications, and 13 conference presentations. The remainder of this summary highlights significant activities and achievements in each of the methodologies and a brief discussion on how they can be combined to leverage strengths.

### **Active Acoustics**

The active acoustics team at UM used both linear and non-linear structural resonance methods to infer information about the internal structure of a cask. Significant activities were a set of four field test measurements on a full scale TN-32 cask at the Columbiana Hi Tech facility in Greensboro, NC and the design and fabrication of a 1/6<sup>th</sup> scale model TN-32 cask for laboratory measurements. A significant set of acoustic data has been acquired on both the full scale and laboratory scale casks. It was determined early in the project that mechanical resonance techniques were not going to be sensitive to small scale (centimeter) cracks and structural defects in the basket structure or fuel assemblies. We were able to ascertain that both the energy and complexity of the resonance spectra were sensitive to “bulk state” of the fuel assemblies – an intact assembly versus a severely degraded assembly. By developing a novel combination of metrics, we are able to



measure a statistically significant shift due to one out of the 32 fuel assemblies being either missing or degraded to a point of complete loss of structural coherence (i.e. “rubble”). We believe this combination of resonance metrics is new to the field and will have applications beyond the fuel storage problem.

### **Emissions Tomography**

The Emissions Tomography team at the University of Florida explored the concept of using scattering of radiation emissions from the stored fuel as method of evaluating the internal structural health of the cask. Due to the need for emissive fuel assemblies and the difficulties of gaining access to storage facilities, this team primarily relied on simulations to inform feasibility. A key question was the flux estimates of neutrons with a small enough number of scattering events to retain spatial information. Some key conclusions from the transmission component of this work are that the number of scattering events falls rapidly with energy – setting a 11MeV threshold, the average number of scattering events is  $8 \pm 4$ . Rough estimates of scanning times using an ideal detector array would be 1 week. The team also explored the case of significant structural failure resulting in a shift of the source material (fuel). The result is that a  $\pm 2\%$  mass shift results in a detectable (5.13%) shift in the correlated 2 neutron emission counts and thus may be a candidate as an initial survey. Finally, simulations for predicting the azimuthal dependence of the flux based on specific loading patterns were conducted. Due to self-shielding effects of the assemblies, a periodic pattern results and could potentially be used to identify missing or severely degraded assemblies. This work forms a basis for proper detector placement with the goal of optimizing sensitivity.

### **Muon Tomography**

Muon tomography (MT) is a relatively novel method of interrogating interior structure on a large scale. One of the advantages of this technique is that the exciting energy source (cosmic muons) is ubiquitous and relatively stable in time. Challenging aspects are relatively low flux rates and appropriate detector technologies. The efforts of the muon group at Oregon State University focused on two areas: (1) simulation of various combinations of muon scattering events and detection schemes to assess sensitivities and time scales for image construction and (2) building a prototype muon detection system applicable to the dry storage cask problem as well as many other similar systems. Significant accomplishments in this area are: (1) demonstration that MT is a viable method for detecting missing or severely degraded rod assemblies, (2) a scintillation based detector with 4 panels and 32 channels of position data each were constructed, tested, and calibrated. Testing of the panels using natural muon background and no scattering objects yielded largely expected results – a straight line path for the muon through the four panels. However some anomalies (paths deviating from a line) were also detected. A redesign of the board improved the signal which greatly improved the muon tracking through the panels. Testing with lead bricks as scattering bodies showed a reduction in the coincidence rate with increasing bricks indicating increased scattering events. A refinement of the scintillator detector design resulted in a spatial image resolution of around 2 cm based on lead brick spacing tests lasting 24 hours.

### **Passive/Active Ultrasonics**

This team at the University of South Carolina investigated the feasibility of combining passive ultrasonics, in which an elastic pulse is generated by a degradation process (such as a crack

extending), and active ultrasonics, in which a known excitation is introduced into the structure and detected by an array of transducers. Significant accomplishments in this area include the development of elastic wave propagation simulation in relevant materials, development of diagnostic algorithms, and laboratory testing and validation using laser doppler vibrometry. This group demonstrated the applicability of various non-contact vibration detection methodologies such as air-coupled ultrasonic transducers and scanning laser doppler vibrometry. While passive acoustic emissions monitoring will likely have a role during the transportation of a fuel storage cask, the level of detailed information about the defect generating the event which can be ascertained from the detections in a complex structure remains for future work.

### **Thermography**

The EPRI team contributed early in the project a series of thermography measurements in which various levels of water pooled in a mock-up canister were analyzed using commercially available infrared imaging technologies. While large levels of water (100 L, ~10cm deep) were observable in the thermograms, more realistic levels of pooled water (1 L) were not detectable whether localized or distributed.

# University of Florida

## Emissions Tomography

Dr. James Tulenko - PI

### Introduction and Scope

Our original project scope called for prototype or test measurements, preferably at a suitable loaded spent fuel cask. Unlike some of the other measurement approach methodologies, the nuclear measurements (neutron & gamma-ray) is fully reliant on measuring a cask loaded with actual fuel rather than an empty cask, a cask loaded with fuel dummies, or a dimension-scaled model cask. This has presented a larger measurement obstacle than foreseen due to the length of time needed to plan and execute site-access and measurements. The Nuclear measurement and analysis scope thus stops short of prototype measurements on actual loaded spent fuel casks, but as is detailed in the work a number of computer simulation investigations, Theoretical analysis methods, test measurements on radiation samples other than spent fuel, and measurement feasibility approach studies were completed.

### 1.1 Background

Dry storage casks for spent nuclear fuels were first employed in 1986 to the Surry Nuclear plant as a temporary solution for high level nuclear waste storage until a permanent solution was found. None of the permanent solution has been proved valid for many of the world's nuclear power plants over years, and then dry storage casks have become more of a semi-permanent solution rather than a temporary one. The number of loaded dry storage casks was rising dramatically, until 2013 around 2300 dry storage casks were loaded, and it was estimated that 4500 dry storage casks will be loaded until 2025[1]. Because of the increased service life and rapid growth of loaded dry storage casks, the safety concern about the integrity of the internal structures is rising. There are no internal sensors was placed in the casks and these casks are not easy to open for the high radiation waste inside.

Emission source tomography is based on radiation signal emitted from the object itself. Then the research about radiative signatures and radiation shielding analysis are the fundamental work of our objective, meanwhile the shielding analysis about the cask can verify the radiation safety of current used dry storage cask models. Among all the cask models exist, Transnuclear TN-32 was chosen as the investigating target, which is one of the non-canistered SNF (spent nuclear fuel) storage casks used in U.S. The spent fuel dry casks radiation shielding analysis involve difficult problems of deep penetration and radiation transport from volumetric source. It has been studied by several researchers in past few years. Among all these work, the deterministic (discrete ordinates) and stochastic (Monte Carlo) methods are the most often used methods. Monte Carlo method is considered as the most accurate method but require more computational cost.

Automated variance reduction technique, which is applying the deterministic adjoint function in Monte Carlo code can improve the computation efficiency [2]. Recently, the new SCALE6.2.1 code system was released [3], and the radiation computation sequence MAVRIC (The Monaco with Automated Variance Reduction using Importance Calculations) was updated as well [4]. MAVRIC can perform radiation deep penetration problem with automatic variance reduction

using an adjoint biased source and importance map to improve the Monte Carlo computation speed. Compared with its predecessor, the SAS4 sequence [5], MAVRIC computation results are closer to the measured dose rates because of its three-dimensional variance reduction technique than the one-dimensional biasing scheme in SAS4 [6]. Chen et al (2011) compared the surface dose rate calculations of a spent fuel storage cask with MAVRIC [7], SAS4 and MCNP, and he concluded that MAVRIC is the most efficient code with a satisfactory uncertainty. In this study, we used the new MAVRIC sequence of SCALE 6.2.1 with the latest ENDF/B-VII.1 cross-section library, according all those advantages listed above.

The accuracy of a complete shielding analysis for a spent fuel cask not only depend on the Monte Carlo transport code itself but also depend on the cask geometry modeling and radiation source term. In this work, we model the fuel cask geometry and radiation source term as detail as possible to predict a realistic dose rate distribution over the cask surface and surrounding. The high accuracy of this simulation work will be great fundamental for our emission source imaging work in the future. And we verified and validated the shielding design and radiation analysis of TN-32 cask through this work.

## **1.2 Radiation Transmission and Imaging Background**

High energy neutron transmission analysis of dry cask was studied with MCNP, which covered a couple fundamental parts of some of the project milestone. We chose MCNP as our computation sequence in this study, because MCNP was regarded as the most accurate Mont-Carlo transport code, and the flux mesh tally can record all the information including interaction events, and also running MCNP simulation parallel can be more efficiency. This work focuses on an external D-T neutron generator creating a source beam that is transmitted through the cask to a detector array tallies placed on the opposite side. If the source and detectors are rotated completely around the cask, the planar radiation projection is generated, more commonly called the Radon transform. This projection can be processed with filtered back projection or other more advanced reconstructive imaging algorithms to recreate the interior structures. The mathematics of image reconstruction and the Radon transform date back to 1917 when first introduced by Johann Radon. Modern computed tomography was invented in 1972 by Godfrey Hounsfield, who took the theoretical calculations of Allan Cormack and created the first CT scanner. CT scanning saw widespread adoption by the medical field in just a matter of years.

Due to the difficulties inherit to conventional methods of dealing with down-scatter to cope with this application, a new simpler method is preferred. Scattering at its core is a method of neutrons as a function of number of scatters is practical given a uniform medium of known dimensions. A single hydrogen scatter in the resin shield can cause the neutron to lose all of its energy, less than 1% of its energy. Due to this disparity, the distribution of particle energy by number of scatters in the cask is most easily determined stochastically. Once the distribution is known, a threshold value could be determined such that neutrons above the energy threshold are likely to have undergone a lower number of relatively small angle scatters. If the number and angle of the scatters are low the events may retain enough position information to reconstruct an image.

### **Spent Fuel Dry Cask**

We reviewed the shielding evaluation work in Chapter 5 of FSAR for TN-32 cask [8]. Dose rate distribution around the TN-32 were determined by choosing Westinghouse 17×17 Standard fuel assembly and using it within a three-dimensional SAS4 model. The SAS4 model was divided

into half from the mid plane, the minor geometry features such like fuel cladding, aluminum basket is homogenized into active fuel region, the computation was separated into radial and axial directions, and the four source areas are utilized into one homogeneous source. With the improvement of MAVRIC computation sequence and computer computation ability in the past decade, we can model the geometry and radiation source into detail as much as possible in order to improve the calculation accuracy. In this work, we prepared two geometry models: a homogenous fuel assembly model and a detail fuel assembly model (see Fig. 1). The difference between these two geometry models is that we build the fuel assembly detail into fuel rod level. We build the most geometry feature detail of the real cask, except some minor structure features those don't affect the radiation shielding such as lid protective cover and trunnions. The fuel assembly consists of four regions on axial direction, top end fitting zone, plenum, fuel zone and bottom end fitting zone, except the fuel zone the rest were treated as homogenous in this work. In the detail fuel assembly model, we build the fuel assemblies rod by rod, the dimension of fuel rod and control rod coming from the Westinghouse 17×17 standard fuel assembly [9], the model detail is shown in Fig. 2. We present only the shielding result from the detail fuel assembly model.

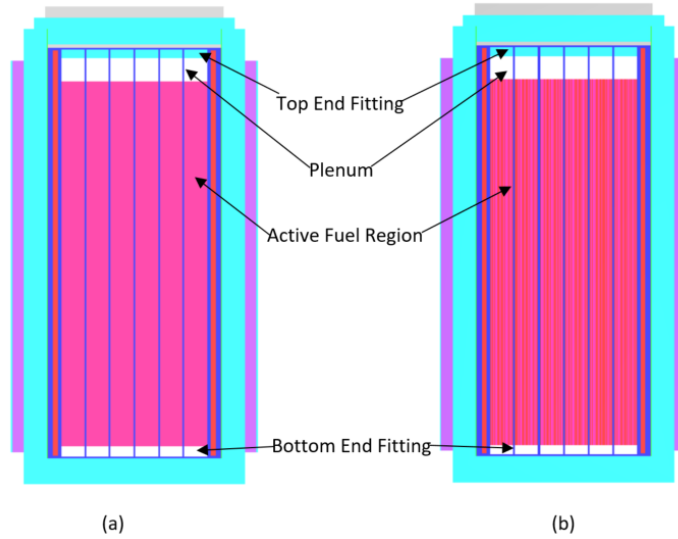


Fig. 1. Cross sectional views of TN-32 cask: (a) homogenous fuel assembly model, (b) detail fuel assembly model

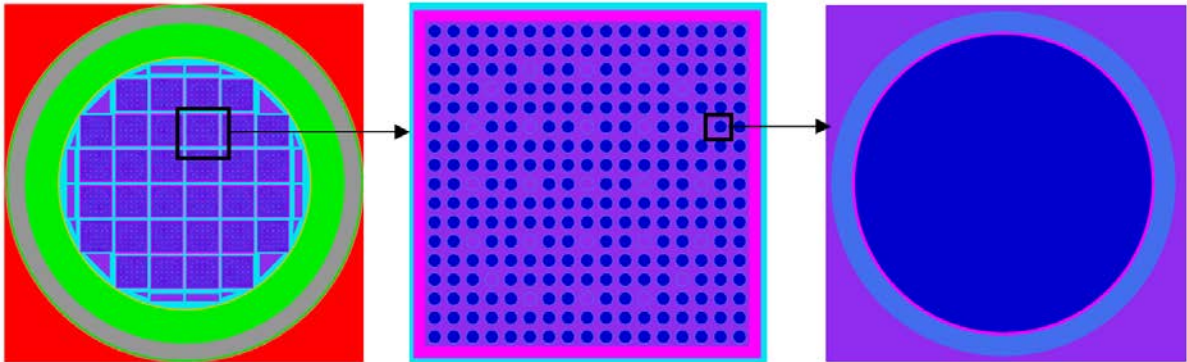


Fig. 2. Cross section view of detail fuel assembly model for TN-32 cask: (a) cross-section view (b) detail of one fuel assembly, includes: fuel rod (blue circles), control rod and instrument tube (purple circles) (c) fuel rod cross section.

## 2.1 Shielding evaluation radiation source term

To calculate the surface dose rates of spent fuel dry cask, source term evaluation was carried out. There are five principal radiation sources associated with dry cask storage that are of concern for radiation shielding, and listed below:

1. Primary gamma rays emitted from fission products and actinides
2. Gamma rays emitted from decay of Co-60 in fuel assembly structure material
3. Secondary gamma rays generated from attenuation of neutrons by cask shielding materials,  $(n,\gamma)$  reaction
4. Neutrons generated from spontaneous fission
5. Neutrons emitted from  $(\alpha, n)$  reaction of fissile material

The TN-32 dry cask is designed to store several fuel types, such as Westinghouse 17×17 standard, 17×17 optimized, B&W 17×17 Mark BW. Among all these fuel types, Westinghouse 17×17 standard fuel assembly was chosen as the spent fuel source in this work. The control module ORIGEN-ARP code of SCALE 6.1 was used to simulate the primary gamma ray and neutron source [10]. The SCALE 6.1 200 gamma ray energy group and 47 neutron energy group was selected. The fuel assembly has an initial enrichment of 3.6%, and the fuel is operated at a constant power of 20 MW/fuel assembly with a 35,000 MWd/MTU burnup, and the cooling time was set up as 11 years. These spent fuel data were calculated by average the spent fuel assemblies stored in TN-32 cask. The primary gamma ray and neutron source spectra are shown in fig.4. The axial burnup profile was provided by FSAR of TN-32, gamma profile and neutron peaking factor are shown in Fig. 3.

In addition, Co-59 is contained in fuel assembly structure material, such as grid, plenum and cladding. The neutron generated from fuel can activate Co-59 to Co-60, and Co-60 emits strong gamma rays of 1.173 MeV and 1.332 MeV and should be considered as radiation source term. The gamma ray flux can be calculated by multiplying the Co-59 impurities in each region with the neutron flux scaling factor and with activities from 1g of Co-60 after 11 years' decay. The cobalt impurities in Inconel, Zircaloy and stainless steel are 0.47%, 0.001% and 0.08% respectively [11]. The neutron factors are 0.1 in top end fitting and cladding region, 0.2 in plenum and bottom end fitting zone [12]. The activates for 1g of Co-60 after 11 years' decay was calculated by ORIGEN-ARP code of SCALE 6.1.

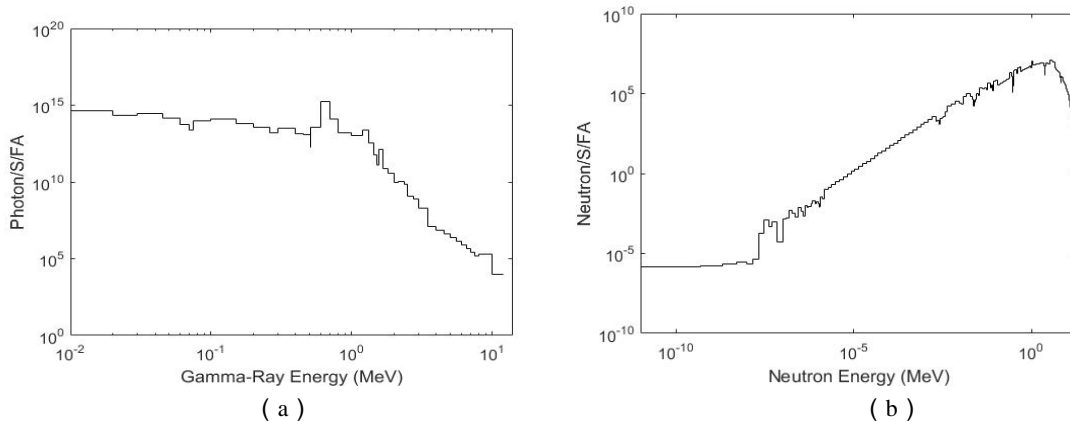


Fig. 3. Source terms of Westinghouse 17×17 standard fuel assembly: (a) primary gamma ray energy spectra, (b) neutron energy spectra.

### 3 Results and Discussion

The dose rate distributions at side, top, and azimuthal surface of two cask geometry model was calculated using MAVRIC sequence with continuous-energy nuclear cross-section libraries in SCALE 6.2. The average dose rate at multiple distance from cask side surface was calculated with a MATLAB script [13]. Three kinds of dose rate distribution were shown in our results, namely, the primary gamma ray, neutron, and secondary gamma. All the MAVRIC calculated results were compared. The results obtained with detail fuel assembly model and continuous-energy nuclear cross-sections were treated as the reference values for this study, because it reproduced the structure feature into fuel rod and uses the CE nuclear cross sections that reduced the uncertainties due to self-shielding correction in MG libraries.

#### 3.1 Dose rate profile of TN-32 cask

We presented our simulation models for TN-32 cask loaded 32 spent fuel assemblies in section 2.1 and our methodology and simulation results of shielding evaluation radiation source term in section 2.2. Based on detail fuel assembly model, the dose rate distributions at the side and top surfaces of the cask using MAVRIC sequence. To measure the secondary gamma-ray induced by neutron attenuation, two separate runs for neutron and gamma-ray sources, respectively, were performed in each simulation case. All the results were summarized in total gamma-ray and neutron dose rates for future measurements. The computing time for each neutron source simulation case took  $\sim 3$  days, for each gamma-ray source simulation case took  $\sim 1$  day. Fig. 4 shows the predicted gamma-ray, neutron, neutron-induced gamma-ray and total dose rate distribution on side surface of the TN-32 cask. From Fig. 4(a), we can tell the maximum gamma-ray dose rate at the side surface occurs near the cask top surface, because of the high dose generated by decay of Co-60 in plenum and top end fitting region. Fig. 4(b) presents the neutron dose rate distribution, the maximum neutron dose rate locates at the bottom of the cask, because of the neutron peaking factor profile and less neutron shielding material at bottom. Fig. 4(c) shows the neutron-induced gamma-ray distribution profile, the general shape is quite different with the previous two, the maximum dose rate locates at the middle of cask and minimum locate at the bottom of cask, because the radial neutron shielding material at side surface can attenuate more neutron and produce more neutron-induced gamma-ray. Fig. 4(d) is the total dose rate distribution profile and is the sum of Fig. 4 (a), Fig. 4(b) and Fig. 4(c). Since gamma-ray produced by gamma-ray source is the major component of total dose rate distribution, the general shape of total dose rate distribution is very close to that of gamma-ray sources. The total dose rate along the side surface are flat, from 5 mrem/h to 7 mrem/h, while at the bottom and top of the cask are one order higher. The TN-32 cask will be placed vertically on ground, so the hot bottom dose rate will be absorbed by ground, and the hot top dose rate locate at  $\sim 4$ m from ground and much higher than normal men height.

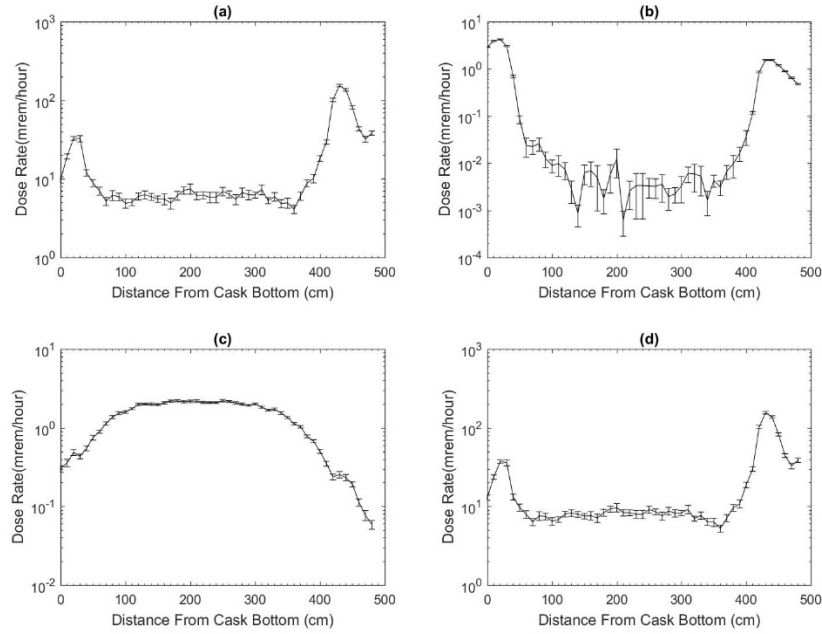


Fig. 4. Dose rate distribution at cask side surface from different particle: (a) primary gamma-ray dose rate profile, (b) neutron dose rate profile, (c) secondary gamma-ray dose rate profile, (d) total dose rate profile.

Fig. 5. shows the dose rate dependence on azimuthal angle at side surface of cask from different particles. Fig. 5(a) presents the primary gamma-ray dose rate dependence on azimuthal angle, we can see that the shape is very similar to a sine function with a period around 180 degrees. The ‘pond’ spent fuel assemblies pattern in the cask made the primary gamma-ray shapes like this. The maximum primary gamma-ray dose rate happens at the four corner of spent fuel assembly basket, where gather more spent fuel assemblies. Fig. 5(b) shows the neutron dose rate dependence on azimuthal angle, and it didn’t shape the same trend with that of primary gamma-ray. Because the neutron flux was affect by the spatial self-shielding effect a lot. Fig. 5(c) shows the trend of secondary gamma-ray dose rate on azimuthal angle, it is quite flat except two spike point at 180 and 270 degrees. The total dose rate dependence on azimuthal degree is shown in Fig. 5(d), since the primary gamma-ray is one order larger than the rest particle, the trend is quite similar with Fig. 5(a).



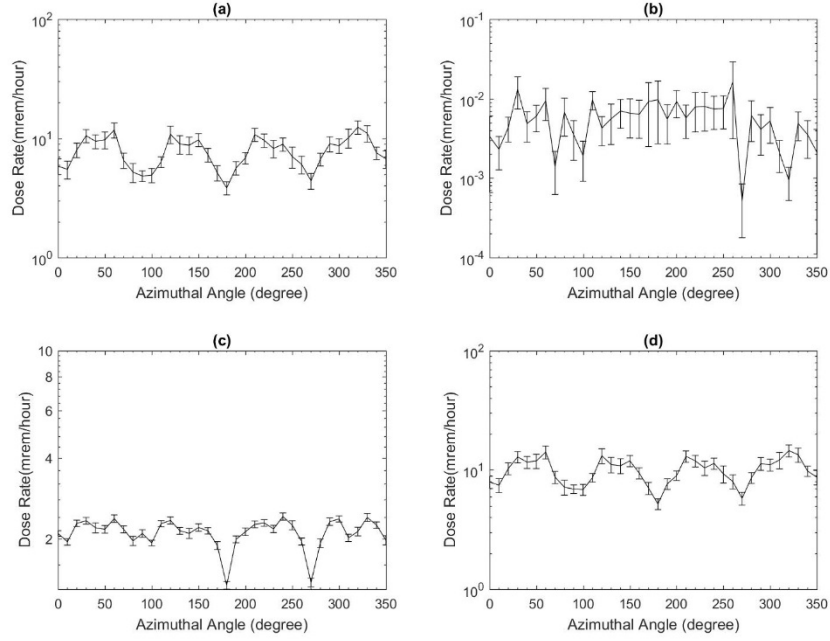


Fig. 5. Azimuthal angle dependence on side surface of cask from different particle, (a)primary gamma-ray dose rate, (b) neutron dose rate, (c) secondary gamma-ray dose rates, (d) total dose rate.

The average dose rate at side surface from all type particles along cask from 0m to 10m is shown in Fig.6, and a second order exponential curve fit is added into this result. The curve fit equation is shown in equation (1), the R-square is 0.99 which means the curve fit to the raw data very well, and we can use this equation to conclude the total dose rate at control area, 250m from cask. The total dose rate at 250m is  $7.29 \times 10^{-21}$ mrem/year, is much smaller than the radiation requirement, and proved the cask radiation shielding design.

$$y = 1.4685e^{-0.0138x} + 7.8093e^{-0.0023x} \quad (1)$$

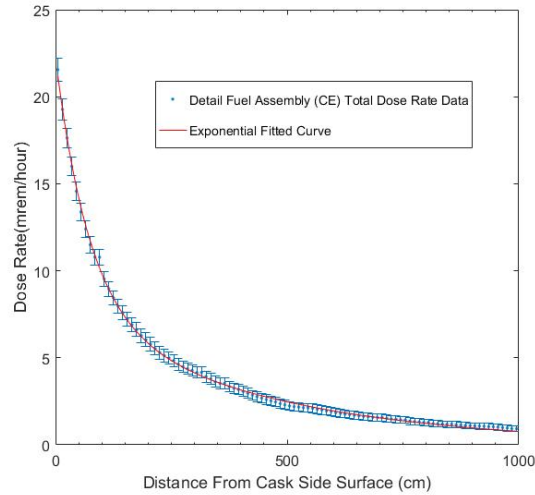


Fig. 6. The curve fit of total dose rate distribution calculated by detail fuel assembly (Continuous energy).

### 3.2 High Energy Transmission Analysis Results

An initial flux estimation using a super imposed mesh tally (fmesh) was used to identify how well neutrons transmitted through the cask. The fmesh was discretized over energy into two bins: low energy ( $<10$  MeV) and high energy ( $>10$  MeV). Fig. 7(left) shows the cask flux of the two different energy bins for a starting angle of  $0^\circ$ . Fig. 7(right) shows the result of the fmesh tally for the two energy bins with an initial angle of  $45^\circ$ . The low energy bin or down scattered images of Fig. 7(top) show the extent to which the cask broadens the cone beam and creates noise across the detector region, which would need to be filtered. Fig. 7(bottom left) shows the potential for streaming terms, where the primary beam would not interact with any fuel which creates higher counts than observed when no streaming term exists like Fig. 7(bottom right). Combining the MCNP output and the four fmesh plots, information about the neutron transmission can be deduced. Neutrons scatter off the iron and helium and then are absorbed by boron, but an appreciable number of neutrons do transmit through the cask. This along with the streaming term introduces the possibility of image reconstruction. If nothing else the streaming term may be used with simple counting to demonstrate large positional shifts or reorganization of the fuel.

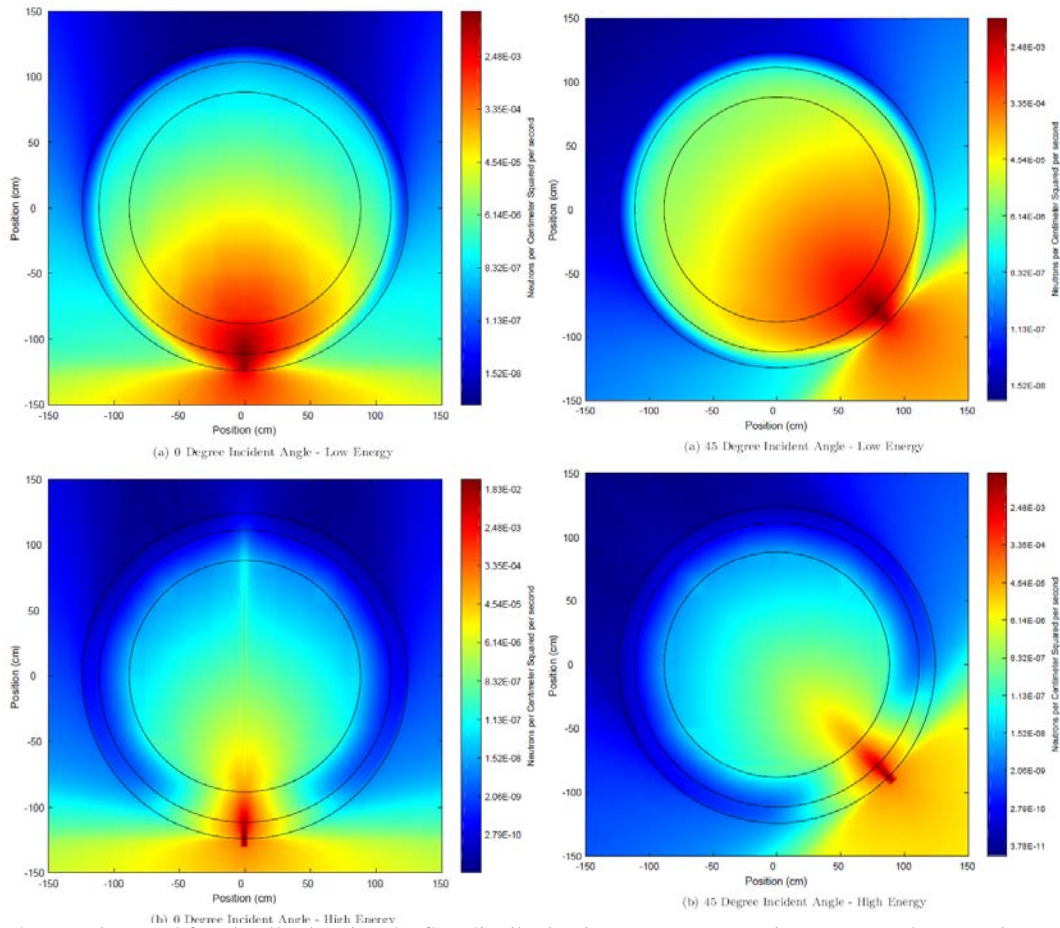


Fig. 7. The superimposed fmesh tally showing the flux distribution in neutrons per centimeter squared per starting particle for neutron energies in excess of 10 MeV (top left: Low energy neutrons, Bottom left: High energy neutrons). Same flux distribution for a 45 degree incident angle per starting particle is shown on right (top right: Low-energy neutrons, bottom right high-energy neutrons).

Fig. 7 show a strong back scatter component, despite the declining probability of back scatter at high energies. The expected depth of penetration is very small; therefore, the back scatter methodology may have trouble imaging the interior fuel structures. Future work may attempt to quantify the penetration depth. The average particle exits the cask at 0.31 MeV after undergoing an average of 122 collisions. The number of events drops off rapidly with energy. Of the events inside the bounding box shown in Fig. 8, the energy distribution is similar to the total but slightly shifted towards higher energy. The population statistics for the two distributions are within the uncertainty of each other.

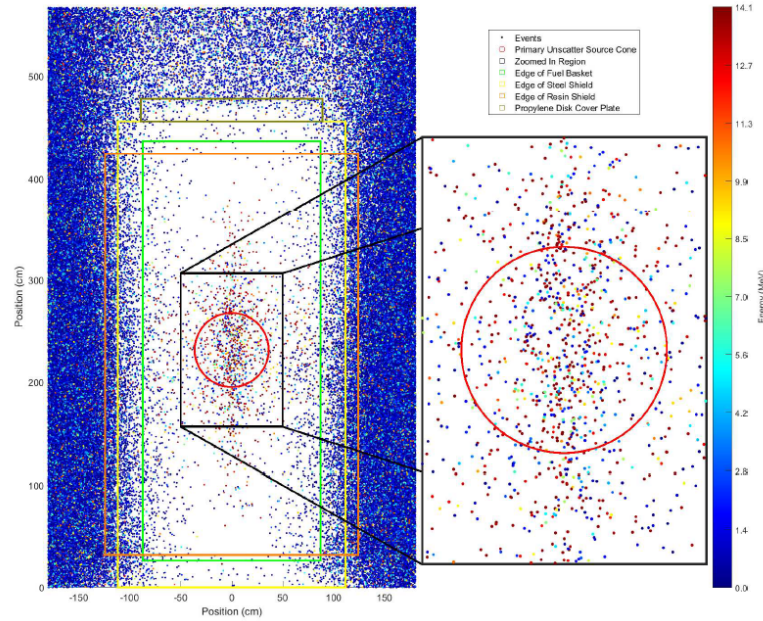


Fig. 8. The plotted events with fewer than 10 scatters colored by energy. The energy distribution binned by number of scatters is shown in Fig. 9.

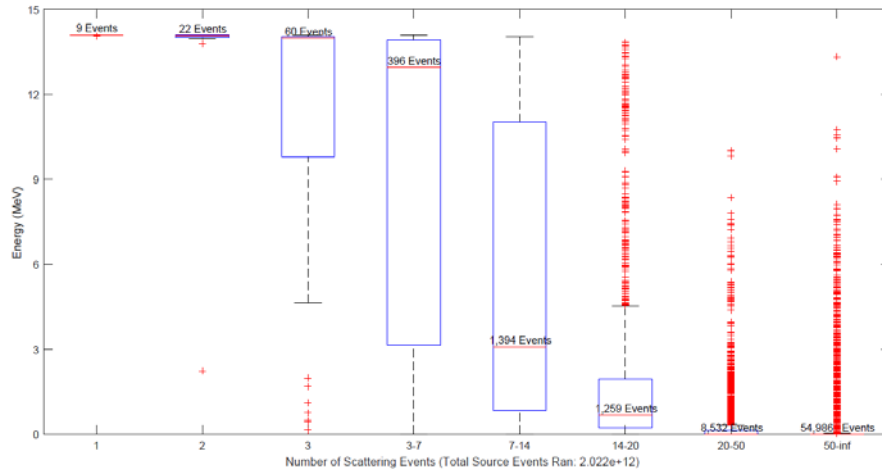


Fig. 9. The energy distributions as a function of number of scatters. Each box plot shows the distribution of energy of events that scatter exactly the number stated or the inclusive range shown.

The first thing of note is the extremely small number of counts with fewer than 2 scatters, which represents the ideal number for image reconstruction since the particles retain the most spatial resolution information. There were no events that passed completely through the cask without interacting once, and only 9 counts that interacted only a single time before exiting the cask. As

expected the energy distributions shift lower in energy as the number of scatters increase. The average energies of events with fewer than 7 scatters remain relatively high which suggests that the neutrons undergo several small angle scatters which would allow for the possibility to utilize multiple scattering theory and reconstruct an image with an additional noise term compared to traditional image reconstruction. A one-way analysis of variance (ANOVA) statistical test was performed on the various distributions. The p-value was zero to the working precision of MATLAB; This means we can reject the possibility that the distributions were simple random samplings from a common distribution. This low p-value was 9 the result of the high number of samples in each distribution excluding the single scatter distribution. While the ANOVA p-value gives clear indication that the separation of means of the distributions are statistically significant, it does little to quantify if the overlapping distributions can be properly resolved and separated when only the total energy distribution is given. To quantify the ability to separate the distributions, Fig. 10 was created which shows the sum of the events with fewer than the number of collisions stated and in the energy range given up to the maximum energy range divided by the sum of all events in the energy range given up to the maximum energy.

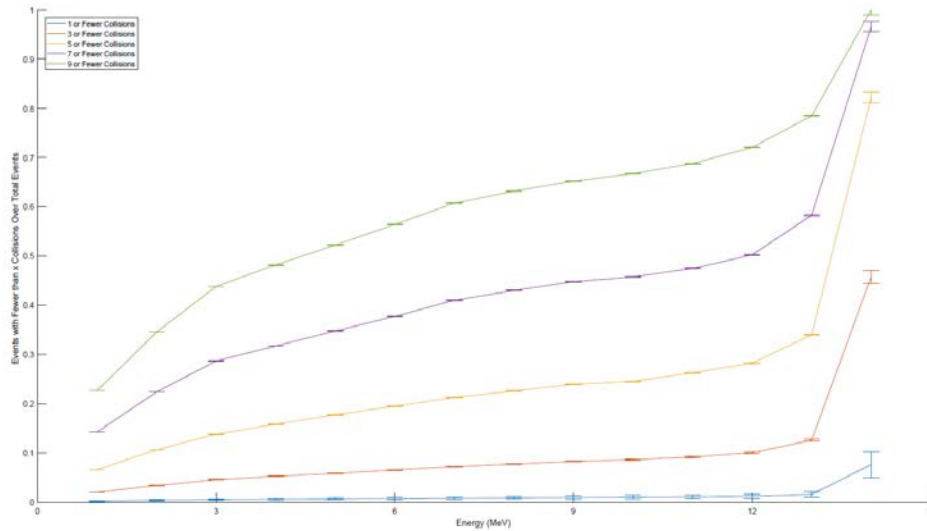


Fig. 10. The fraction of events with fewer than the stated number of collisions over the total number of events for the range of the given energy to the maximum energy.

Roughly 80% of the signal above a few MeV comes from events that scatter fewer than 10 times despite the average particle scattering 122 times. The graph shows the expected trend of increasing fraction with energy. At number of average scatters is inversely proportional to the minimum energy. With no energy threshold the average event scatters  $122 \pm 80$  but with a threshold of 11 MeV the average event scatters only  $8 \pm 4$  times. Therefore, it may be possible to implement an energy discriminator so that the recorded events are more likely to retain positional information. In order to address the potential regulatory issues, a MCNP simulation was performed to quantify the fission reaction rate. Results showed that roughly for every 60 source neutrons only one resulted in a fission. When the reaction rate is combined with the beam intensity of the best-case neutron generator and the average energy per fission the result is the heat generation rate. The product comes to an additional volumetric heat generation rate on the order of microwatts per assembly. A number are well within the margin of error for the designed dissipation rate of 1.02 kilowatt per assembly. Increased dose is another regulatory concern. Results show that roughly 80% of the neutron beam is absorbed by the cask. The source intensity

of the beam is roughly equivalent to the emissions from a single cask but with a higher average energy therefore the neutron radiation weighting factor would be lower. The combination of the lower radiation weighting factor and absorption by the cask results in a lower dose than that from a single cask. An ISFSI typically has several casks present, therefore the additional dose of the scanning should be negligible. With a perfect detector array 100 centimeters wide by 150 centimeters tall roughly  $1 \times 10^{-7}$  events per starting particle are detected with remaining energies above 11 MeV. Assuming a neutron generator that generate  $10^8$  neutrons a second, in order to ensure measurements of a few thousand counts in each pixel with a detector consisting of a few hundred pixels with a minimum number of slices a scanning time on the order of a week or more would be required. Newer neutron generators are in development that over substantially higher flux which will reduce the projected required time.

### 3.3 Multi-Layer Neutron Analysis of a Filled Dry Storage Cask

Monte Carlo simulations of dry storage casks tend to be resource-intensive due to the complex nature of the fuel inside and the large amounts of shielding surrounding the fuel. For monitoring applications of these casks, detection efficiency becomes another important variable. To account for the variations in both the cask and the detectors, a mathematical model is introduced that uses neutron source multiplicity information and a master equation to determine the probability to obtain detectable neutrons on a per source event basis.

Equations from the mathematical model in [14, 15] were used to predict the number of detectable neutrons that would escape each layer of the dry storage cask. These calculations begin with finding and comparing the probabilities of a first collision of a neutron to result in a fission or be absorbed,  $p'$ , or to only result in a fission,  $p$ . This comparison can be done through the formula:

$$\tilde{p}_i(n) = \frac{p'-p}{p'} \delta_{n,0} + \frac{p}{p'} p_i(n). \quad (2)$$

In this equation,  $p_i(n)$  is the probability to produce  $n$  number of neutrons from an induced fission caused by a single, initial neutron and  $\tilde{p}_i(n)$  is the properly weighted probability to produce  $n$  number of neutrons from fission accounting for capture. Additionally, since  $p' - p$  is equivalent to the absorption probability, the number of neutrons generated by absorptions,  $\delta_{n,0}$ , is zero. Values for inputs  $p$ ,  $p'$ , and  $p_i(n)$  were extracted from MCNPX-PoliMi, which allows for tracking of every fission event and neutrons per fission while determining the type of each collision event before calculating the particle energy loss associated with the collision. These inputs from MCNPX-PoliMi ensure that proper data tables are input into the analytical solution rather than through a Monte Carlo approach. Using this approach, the  $\tilde{p}_i$  values for different layer combinations are found and compared.

Once the probabilities for neutron production are found, the overall probabilities for neutrons to reach a detector at the end of a layer combination can be found. This process begins with the generating functions for  $n$  number of neutrons being created from induced fissions or spontaneous fissions,  $\tilde{q}_i$  and  $q_s$ , respectively.

$$\tilde{q}_i(z) = \sum_n \tilde{p}_i(n) z^n \quad \text{and} \quad q_s(z) = \sum_n p_s(n) z^n \quad (3)$$

In these equations,  $z$  is the probability generating function (PGF) variable used to generate true probabilities. Furthermore, the PGF for the number of neutrons to be both produced and detected from a single neutron event (spontaneous fission), can be explained by

$$H_d(z) = q_s[h_d(z)] \quad (4)$$

where  $h_d(z)$  is the PGF for the number of neutrons to be both produced and detected from one initial neutron

$$h_d(z) = h(\varepsilon(z)) = (1 - p')\varepsilon(z) + p'\tilde{q}_i[h(\varepsilon(z))]. \quad (5)$$

Additionally,  $\varepsilon(z)$  is the absolute detector efficiency, the number of neutrons detected per neutron emitted. Finally, the probability for  $n$  neutrons to be detected outside the cask layers from a single source neutron  $p_d$  or a single neutron event (spontaneous fission)  $P_d$  can be described by

$$p_d(n) = \frac{1}{n!} \frac{d^n h_d(z)}{dz^n} \Big|_{z=0} \quad \text{and} \quad P_d(n) = \frac{1}{n!} \frac{d^n H_d(z)}{dz^n} \Big|_{z=0}, \quad (7)$$

In this analytical model, three major parameters can be modified to reduce the number of Monte Carlo runs required to account for minor differences in dry storage casks. The first parameter that can be modified is the probability to induce fission,  $p$ , which relies on the percent burn-up and cooling time of the fuel along with the number of assemblies and their geometrical placement inside the storage cask. Secondly, the absorption probability,  $p' - p$ , can be modified to observe the effects of different amounts of fuel and/or layers of shielding. Finally, the detector efficiency,  $\varepsilon$ , can be modified to account for different detector types, as well as different geometric setups around the cask.

Additionally, the effects of  $(n, xn)$  reactions can be observed by modifying  $p'$  to become the probability of a first collision of a neutron inducing fission, absorption, or creating an  $(n, xn)$  reaction. In this case,  $\tilde{p}_i(n)$  becomes the probability to create  $n$  number of neutrons from fission and  $(n, xn)$  reactions, weighted with neutron capture.

The initial MCNP6 simulations were based off a SolidWorks model of a TN-32 dry storage cask provided by Areva for the project. The fuel inside was based off NGSF Spent Fuel Library #2 asymmetric fuel assembly with 1 radial region and additional fission products produced from Monteburns linkage code between MCNPX and CINDER90 [16,17]. This fuel was 3.0% initial  $^{235}\text{U}$  weight enrichment, 30 GWd/MTU average burnup, and had a material composition matching a cooling time of 40 years. The fuel was then homogenized with the basket to create a homogenous layer for simplified layer analysis and reduced calculation times (120 minutes versus approximately 2.5 days for a non-homogenized basket with 1 million source fission events).

When  $(n, xn)$  reactions are added to the induced fission neutron production distribution, the probability for two particles to be produced from a first collision increases as seen in Fig. 11. This accounts for 3.85% of the overall induced neutron production, increasing interactions from  $341266 \pm 584$  to  $354406 \pm 699$ . This is significant as it is 18.8 times larger than the uncertainty of these interactions occurring for the case of 1 million source fissions. Additionally, as a result of normalization, the probability for three particles to be produced is lowered.



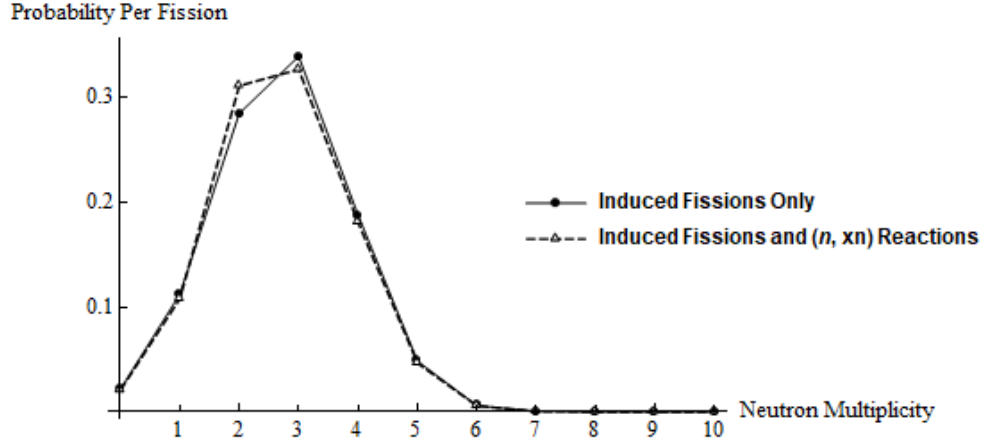


Fig. 11. Induced Fission and (n,xn) Reaction Neutron Production Distribution for Full Cask

The largest effect on the distribution occurs when the probability of neutron capture is also included to the previous distributions. This results in nearly 90% of all first collisions resulting in 0 neutrons being produced. This effect can be seen in Fig. 12.

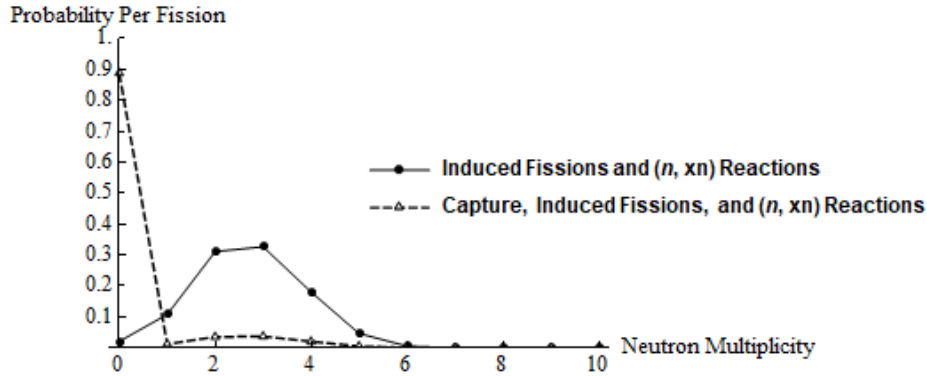


Fig. 12: Neutron First Collision Probabilities with and without Capture Normalization

For the case of using detectors to image a dry storage cask, the probabilities for detecting more than one particle from an initial neutron event are priority. When multiple particles from the same neutron event hit detectors around the dry storage cask, the particle's origin can be then traced back to its origin and provide location information of the source event. From an MCNP6 simulation of a fully loaded dry storage cask featuring the fuel observed in this study, it was found that there are approximately 1 billion neutrons that are produced per second inside the fuel and basket layer through fissions and (n,xn) reactions. The results in Table I show the probabilities of neutrons to be detected per source event when considering induced fissions, neutron capture, and (n,xn) reactions. From the table it is found that there are approximately 2600 neutron pairs that can be traced back to their origin per day of scanning with a detector efficiency of 10%.

Table I. Probabilities for Neutrons to be Detected per Source Event with (n,xn)

Probabilities for Detection	1 Particle	2 Particles	3 Particles	4 Particles	5 Particles
Basket Only	0.000739409	$3.45319 \times 10^{-7}$	$1.7247 \times 10^{-10}$	$1.03328 \times 10^{-13}$	$6.94556 \times 10^{-17}$
Basket and Steel	0.000337556	$7.19618 \times 10^{-8}$	$1.64111 \times 10^{-11}$	$4.48956 \times 10^{-15}$	$1.37801 \times 10^{-18}$
Full Cask	$6.90135 \times 10^{-6}$	$3.00751 \times 10^{-11}$	$1.40222 \times 10^{-16}$	$7.84277 \times 10^{-22}$	$4.92154 \times 10^{-27}$
Full Cask and Air	$6.7991 \times 10^{-6}$	$2.91908 \times 10^{-11}$	$1.34086 \times 10^{-16}$	$7.3886 \times 10^{-22}$	$4.56795 \times 10^{-27}$

Ultimately we looked at the ability of the methodology to detect fuel cask structural failure events, a collapse of basket separation walls, or mechanical shifting, results in a reconfiguration of the nuclear material in the fuel, a simplified case was studied (Fig. 13.) where the shift of material resulted in an increase in spent fuel density on one side and a corresponding decrease in density on the other side (for conservation of spent fuel contents).

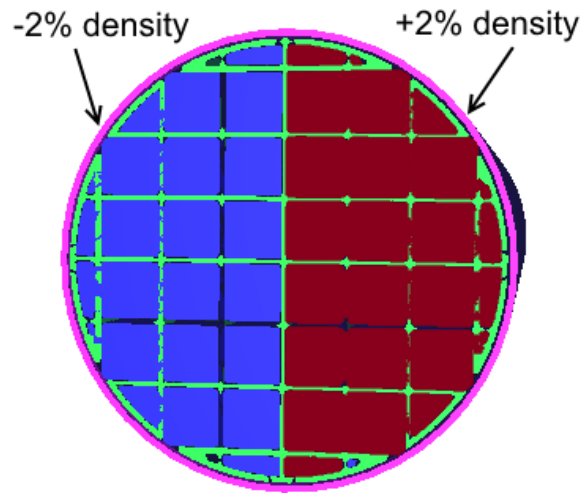


Fig. 13. Schematic of shifted fuel content from a hypothetical catastrophic fuel basket structural failure.

Table II Resulting neutron detection statistics from a density shift.

Fuel Distribution	1 Neutron	2 Neutrons	3 Neutrons
Uniform Fuel	$7.74 \times 10^{-6}$	$4.29 \times 10^{-11}$	$2.89 \times 10^{-16}$
Fuel Shifted	$7.54 \times 10^{-6}$	$4.07 \times 10^{-11}$	$2.68 \times 10^{-16}$
Percent Difference	-2.58%	-5.13%	-7.27%

The results in Table II shows that the correlated counts shift (“2 neutrons”) shift significantly more and could be a candidate to identify internal fuel movement in a cask as an initial survey method.

### 3.4 Predicting External Neutron Count Rates Using Operator Declared Information

Lastly a method for predicting the flux at specific locations outside the cask using parameters specific to the cask and assembly loading patterns was also investigated. This provides a solution to a significant shortcoming of before-and-after fingerprinting measurement techniques, the requirement of having a before fingerprint for successful comparison. Flux measurements from a



100-detector simulated array around a cask-system follow a periodic function as you move around the cask due to self-shielding from the assemblies and cask attenuation effects. The attenuation effect from the dry cask system is the flux measured by each detector using the cask loaded with identical assemblies. The attenuation effect has a periodic behavior as shown in Fig. 14.

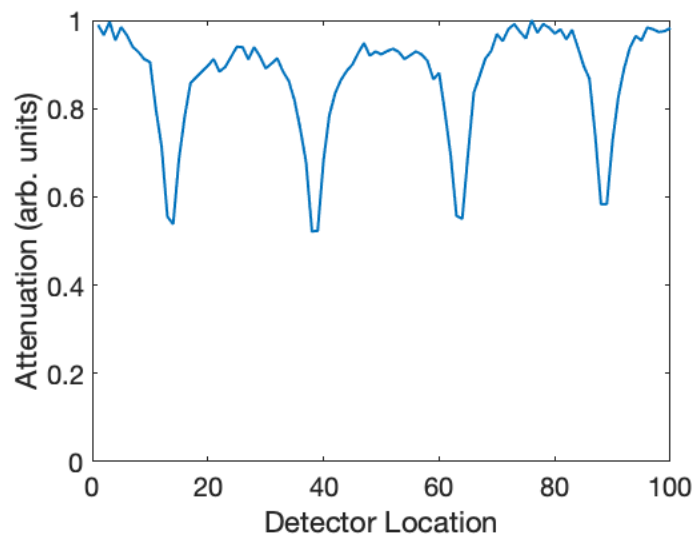


Fig. 14. Attenuation from the cask system and assemblies at specific detector locations.

Fig. 15 shows the matrix multiplication needed to calculate the external neutron flux around the cask at 100 specific detector locations. Fig. 16 shows the actual (MCNP) flux versus predicted (mathematical) measurements at detectors around a single quadrant of the cask. The predicted fluxes overestimated the flux from MCNP for most detector locations, however the relative magnitudes and overall trends are correct. Since the values are normalized, the diagonal locations were underestimated. The greatest change in the flux from one detector to the next occurs at the diagonal locations. Practical application of this technique would require crucial placement of detectors to ensure they are not placed between two measurement points.

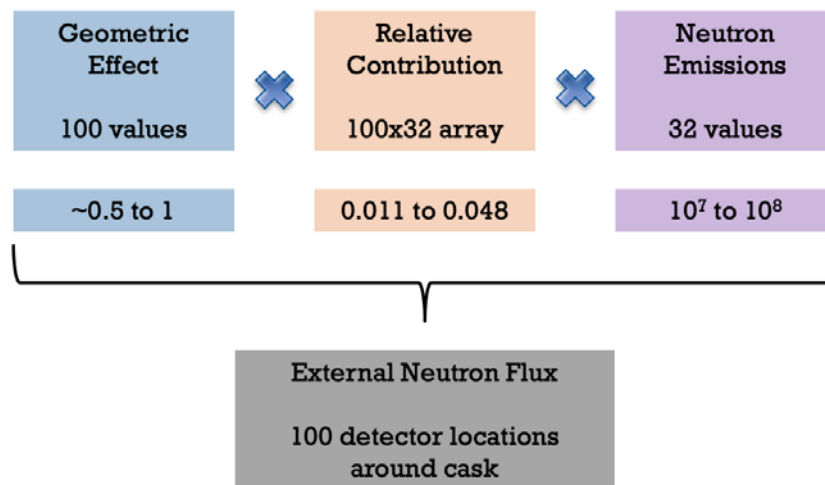


Fig. 15. Matrix multiplication needed to calculate the external neutron flux at 100 detector locations around the cask.

This work provides one possible solution to the lack of a prior fingerprint existing for casks. While these results are specific to the HI-STORM 100S cask system, the techniques are applicable to any spent fuel storage cask. MCNP models exist for other dry cask systems, such as the TN-32 cask [18]. If additional sensitivity is desired, another dimension could be added to the parameters, such as neutron energy or variations in flux along the z-axis of the cask. Additional dimensions may require more measurements and would involve more data analysis.

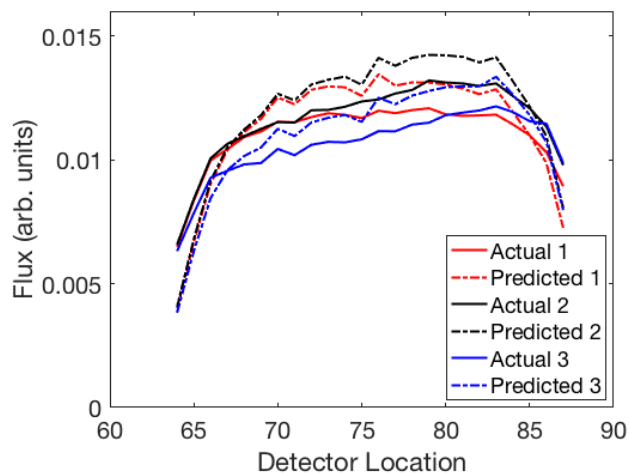


Fig. 16. Actual (MCNP) versus predicted (mathematical) neutron flux for detectors 64 to 87. This study created a way to mathematically model the fingerprint of a spent fuel cask using parameters specific to the cask and operator declared information about the fuel. Computational methods were developed to calculate these parameters using the HI-STORM 100S dry cask system and the Next Generation Safeguards Initiative Spent Fuel Libraries. The neutron flux can be predicted with three parameters: (1) geometric effect from the dry cask system and self-shielding from the assemblies; (2) relative contributions from each assembly for the specific azimuthal detector location; and (3) loading pattern with average neutron source strength per assembly.

## References

- [1] U.S. Department of Energy, Fuel Cycle Research & Development, Nuclear Fuels Storage & Transportation (FCRD-NFST), (2013) Commercial Spent Nuclear Fuel and High-Level Radioactive Waste Inventory Report, FCRD-NFST-2013-263, Rev. 4
- [2] J.C. Wagner and A. Haghighat, "Automated Variance Reduction of Monte Carlo Shielding Calculations Using the Discrete Ordinates Adjoint Function," Nucl. Sci. Eng., 128,186 (1998)
- [3] J.F. Briesmeister, "MCNP-A General Monte Carlo N-Particle Transport Code, Version 4C, LA-13709-M," Los Alamos National Laboratory, U.S. (2000)
- [4] B.T. Rearden and M.A. Jessee, Eds., "SCALE Code System, ORNL/TM-2005/39, Version 6.2.1," Oak Ridge National Laboratory, Oak Ridge, Tennessee (2016).
- [5] D. E. Peplow, "Monte Carlo Shielding Analysis Capabilities with MAVRIC," Nucl. Technol. 174(2), 289-313, May 2011.

- [6] B. L. Broadhead, J. S. Tang, and C. V. Parks, "SAS1 and SAS4, Two New Shielding Analysis Sequences for Spent Fuel Casks," pp. 210-221 in *Proc. Seminar on SCALE-4 and Related Modular Systems for the Evaluation of Nuclear Facilities and Package Design Featuring Criticality, Shielding and Transfer Capabilities*, Saclay, France, September 17-19, 1991.
- [7] H. Thiele and F.-M. Borst, "Shielding Benchmark Calculations with SCALE/MAVRIC and Comparison with Measurements for the German Cask Castor HAW 20/28 CG," Nucl. Technol., 168,867 (2009)
- [8] P. Rinard, G. Bosler, Safeguarding lwr spent fuel with the fork detector, Tech. rep., LA-11096-MS, Los Alamos (1988).
- [9] Westinghouse Electric Corporation, Water Reactor Division. "The Westinghouse Pressurized Water Reactor Nuclear Power Plant," Westinghouse Electric Divisions, 1984
- [10] S. Bowman and I. Gauld, "OrigenArp Primer: How to Perform Isotopic Depletion and Decay Calculations with SCALE/ORIGEN," Oak Ridge National Laboratory, Oak Ridge, TN, 2010
- [11] A. Croff, M. Bjerke, G. Morrison and L. Petrie, "Revised U-Pu Cycle PWR and BWR Models for the ORIGEN Computer Code," Oak Ridge National Laboratory, Oak Ridge, Tennessee, 1978
- [12] US NRC, "NUREG/CR-6802 Recommendations for Shielding Evaluations for Transport and Storage Packages," 2010.
- [13] MATLAB and Statistics Toolbox Release 2016a, The MathWorks, Inc., Natick, Massachusetts, United States
- [14] A. Enqvist, I. Pázsit, and S. Pozzi, "The number distribution of neutrons and gamma photons generated in a multiplying sample," Nucl. Instr. And Meth. A, 566 (2), pp. 598-608 (2006).
- [15] A. Enqvist, S. Pozzi, and I. Pázsit, "The detection statistics of neutrons and photons emitted from a fissile sample," Nucl. Instr. And Meth. A, 607 (2), pp. 451-457 (2009).
- [16] LANL, "NGSI Spent Fuel Libraries", LA-UR-10-08244 (2012).
- [17] H. R. Trellue, M. L. Fensin, J. R. Richard, J. G. Galloway, and J. L. Conlin, "Description of the Spent Nuclear Fuel Used in Next Generation Safeguards Initiative to Determine Plutonium in Spent Fuel," LA-UR 11-00300 (2011).
- [18] S. E. Smith, X. Sun, C. A. Ford, and A. W. Fentiman, "MCNP simulation of neutron energy spectra for a TN-32 dry shielded container," Ann. Nucl. Energy, vol. 35, no. 7, pp. 1296–1300, 2008.

## List of Publications and Presentations

Journal papers:

*"High energy neutron transmission analysis of dry cask storage"*, C. Greulich, C. Hughes, Y. Gao, A. Enqvist, J. Baciak, Nucl. Instr. Meth. A, 874, (2017), pp. 5-11

*“Radiation dose rate distributions of spent fuel dry casks estimated with MAVRIC based on detailed geometry and continuous-energy models”*, Y. Gao, Yuan, C. R. Hughes, C. R. Greulich, J. E. Tulenko, A. Enqvist, J. E. Baciak, *Annals of Nuclear Energy*, 117, (2018) pp. 84-97

Thesis/Dissertations/Non-Thesis degree work:

*“Safeguards Approaches For Spent Nuclear Fuel In Dry Cask Storage”*, PhD Thesis, Allen Ira Harkness III

*“Radiography Of Dry Cask Storage For Used Nuclear Fuel”*, PhD Thesis, Christopher Greulich

*“Advanced MCNP Modeling of the TN-32 Storage Cask with Advanced Radiation Transport Computations and Additional Cask Characterization”*, MSc non-thesis project, Justin Paluch

*“MCNP Modeling of the TN-32 Storage Cask and Preliminary Radiation Transport Computations”*, MSc non-thesis project, Jonathan Wyers

Conference contributions:

*“Evaluation of Spent Fuel Cask Condition using Emission Source Tomography”*, H.T. Wang, J. Wyers, Y. Gao, C. Greulich, J. Tulenko, J. Baciak, A. Enqvist, *INMM Annual Meeting, Atlanta, Georgia, 24-28 July 2016*

*“Spent Fuel Cask Basket Structure Evaluation with Emission Source Tomography: Radiation Transport Investigation”* H. Wang(G), J. Wyers(G), C. Greulich, Y. Gao, J. Tulenko, J. Baciak, A. Enqvist, *TAPIA2016: ACM Richard Tapia Celebration of Diversity in Computing, Austin TX, sept 14-17 2016*

*“Computed Tomography of Dry Cask Storage for Used Fuel”*, Christopher Greulich, Yuan Gao, Andreas Enqvist, James Tulenko, James Baciak, *ANS Winter meeting Nov. 2016*.

*“Shielding analysis of TN-32 spent fuel dry cask with SCALE”*. Yuan Gao, Haitang Wang, Andreas Enqvist, James. E. Baciak, *ANS Winter meeting Nov. 2016*.

*“Development of Neutron Energy Spectral Signatures for Passive Monitoring of Spent Nuclear Fuels in Dry Cask Storage”*, I. Harkness, T. Zhu, Y. Liang, E. Rauch, A. Enqvist, K. A. Jordan, *Advancements in Nuclear Instrumentation Measurement Methods and their Applications (ANIMMA), Liege, Belgium, 19- 23 June 2017*

*“Surface Dose Rate Distribution of a Spent Fuel Cask with SCALE”*, Y. Gao, C. R. Greulich, J. S. Tulenko, A. Enqvist, J. E. Baciak, *ANS Winter Meeting, Washington DC, Oct 28-Nov 2, 2017*

*“Spent Fuel Dry Cask Dose Rate Distribution Obtained with MAVRIC”*, Yuan Gao, Christopher R. Greulich, James S. Tulenko, Andreas Enqvist, James E. Baciak, *ANS student conference, Gainesville, FL, April 5-8, 2018*

*“Feasibility of Fast Neutron Spectroscopy for Safeguards and Verification of Spent Fuel in Dry Cask Storage”*, I. Harkness, X. Wen, E. Rauch, A. Enqvist, *INMM Annual Meeting, Baltimore, MD, 22-26 July 2018*

# University of Mississippi

## Physical and Structural Acoustics

Dr. Joseph R. Gladden - PI

### Introduction

The Nuclear Regulatory Commission (NRC) has been looking into various Non-Destructive Evaluation (NDE) approaches to assess the long-term integrity of a variety of storage casks including CASTOR V/21<sup>1</sup> and other models<sup>2,3</sup>. These NDE efforts include visual inspection, eddy current, temperature monitoring, gamma ray scanning, and ultrasonic pulse-echo techniques. The limitation of these methods lies in the difficulty of extracting information from the interior of the casks, especially regarding the spent fuel. One concern for the extended storage is that the spent fuel needs to remain below criticality for nuclear reaction under transportation after more than a century of storage. The subcriticality is ensured in dry storage casks by suitable burnup credit, fuel configuration, neutron absorbers, basket spacing and moderator exclusion<sup>4</sup>. This Integrated Research Project under the Nuclear Energy University Program thus aims to provide tools for identifying structural failures in the basket and fuel assembly to avoid criticality.

The active acoustics aspect of this work is in the application of vibrational spectroscopy to assess the state of the contents and internal structural components in the TN-32. The use of acoustics as a viable tool for structural monitoring has been studied extensively for decades<sup>5-11</sup>. In particular, the active acoustic characterization of nuclear fuel storage vessels has also drawn attention in recent years. A primary subject is the steel used for the inner canister for storage casks; it also constitutes most of the containing vessel for the TN-32. Steel cylindrical shells are the most similar structure to nuclear casks that can be reproduced in a lab setting. However, global acoustic resonant NDE studies on the internal structure of an enclosed cylinder are lacking. A few relevant experimental studies are listed in the following. Mode shapes were found to be more sensitive to cracks on a carbon steel cylindrical shell than the change of resonant frequency<sup>12</sup>. A resonant frequency shift curve method can locate the damage caused by an auxiliary mass on a steel cylindrical shell<sup>13</sup>. The resonant frequencies and modal shapes of a geometrically imperfect steel tank filled with and without water show good agreement between large-amplitude theory and experiments<sup>14</sup>. Damage scenarios in steel that are used in nuclear technology have also been investigated. Second harmonic generation was applied to steel samples simulating a reactor pressure vessel with various degrees of neutron damage<sup>15</sup> and with annealing<sup>16</sup>. Stress corrosion cracks on the inner steel canister of a storage cask can be detected using electromagnetic ultrasonic transducers on a delivery robot<sup>17</sup>. Along with the work above<sup>17</sup>, there have been some acoustic studies on commercially available dry storage casks. Ultrasonic tomography is used to examine the welds in a dry storage cask (Patent RU 2500045)<sup>18</sup>. In contrast to earlier work, this study is not concerned with the state of the containing vessel but in assessing the state of the cargo contained therein using only measurements made at the surface. The vibrational properties of fuel rod assemblies (cargo) have been studied since the 1970s. However, most are studied in the context of fluid-structure interaction in the power plant<sup>19,20</sup>, while some others are focused on the interaction with the supporting grid<sup>21,22</sup>. For the interaction between the vessel and the cargo, there has been a lot of attention on the vibrational interaction between the tank and the sloshing fluid inside, instead of solid in our case, in the seismic community<sup>23-27</sup>. To our knowledge there has not been a

reported study on the integrity of the internal cargo of an enclosed cylinder, including the large scale of dry storage casks for high burn-up nuclear fuel.

Linear and nonlinear resonant vibrometry are applied in this project. These techniques are global methods, therefore the information on the inaccessible components of the TN-32, the basket and fuel assemblies, can be acquired from the exterior. For linear vibrometry, modal frequencies and the associated mode shapes are the primary focus. Finite element (FE) simulations of complex structures have emerged as a valuable tool to assist damage identification from mode shape measurements<sup>28</sup>. Through FE modeling, modes with large activity in the internal structure can be identified and exploited for NDE purposes. For the nonlinear vibrometry, harmonic generation<sup>29,30</sup> and modal frequency shift<sup>31</sup> techniques are investigated.

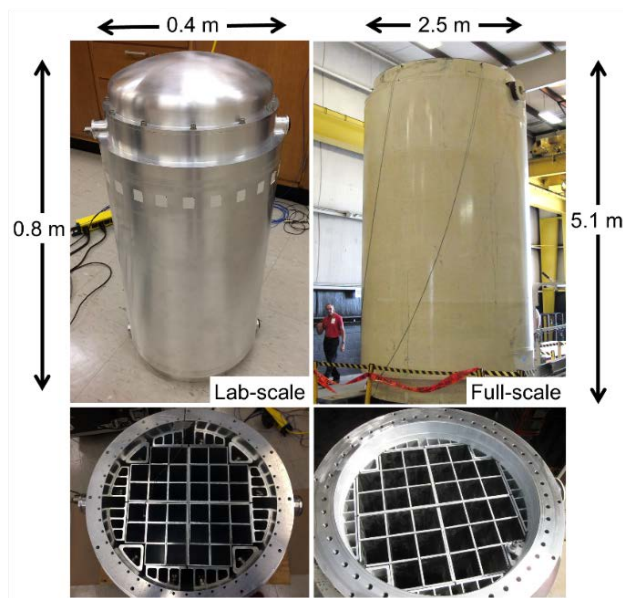


Figure 1. Visual comparison between the full-scale TN-32 (right) and the 6:1 lab-scale model cask (left)

## Major Accomplishments

This section highlights the major accomplishments of the active acoustics methods. For conciseness, the technical details of the results are purposefully omitted and can be found in the next section. During the first 2 years of the 3-year grant period, four field test opportunities emerged, and experiments were performed on the same healthy full-scale TN-32, which was previously located at the Columbiana Hi Tech facility in Greensboro, NC. Also, a 6:1 scale TN-32 cask for laboratory studies was constructed at the National Center for Physical Acoustics [Figure 1]. Various damage scenarios for the fuel assemblies were simulated on the lab-scale cask. The active acoustics setup consists of an electrodynamic shaker, a sensor array, lock-in amplifier(s) and a data collection interface. For both the full-scale and lab-scale casks, the shaker is mounted on one of the trunnions, and accelerometers are attached at trunnions and rims of the casks. For the lab-scale cask, a laser Doppler vibrometer is also used in order to map the surface vibration of the cask. Refer to Figure 2 for the nomenclatures and experimental setup.

To validate the correspondence between our lab-scale model and the TN-32, the measured resonant modes are compared between these two casks and also to FE simulations while both of the casks are intact and unloaded. Figure 3 shows the first three identified modes. There is a clear correspondence between the measurements and the simulations, thus the NDE techniques derived

from the lab-scale cask can be reasonably applied to the full-scale TN-32 with some adjustments. In particular, the (1, 2) global bending mode shows large activity at the bottom of the cask. We expect this mode can efficiently couple energy into the fuel assemblies, so it can potentially achieve higher sensitivity to the internal structure than other two identified modes.

After validating the lab cask, internal damage scenarios were studied with steel rod bundles as surrogate fuel assemblies and steel shot to simulate structural decay (referred to in this report as rubble). Pictures of the materials and setup are shown in the inset of Figure 4. Three types of damage scenarios - intact rod bundles, rubble filled, and empty - are the possible states for each slot. The configurations were examined using both symmetric and asymmetric arrangements (See the x-axis of Figure 4). The frequency range of interest covers the (1, 2) and (2, 1) modes [Figure 3(b) and (c)]. With a single sensor at the top trunnion opposite from the shaker at the bottom trunnion, two amplitude-based metrics were developed to characterize the internal conditions. The total energy metric shows how much energy is measured at the trunnion, while the 2nd moment metric quantifies the complexity of the spectral distribution. These two metrics are very sensitive to the number of intact bundles, but much less sensitive to the locations of bundles or to whether the remaining slots are filled with shot or are empty. Our hypothesis is that the intact structure is able to retain vibrational energy, so the sensor will measure less energy at the trunnion on the outer shell and the spectra will also be more complicated. On the other hand, empty slot or randomly-packed steel shot does not retain vibrational energy, thus less energy is measured from the outside and the modal structure is less complex. The field data on a full-scale TN-32 can be used to calculate 2nd moment and is consistent with the measurements in the lab [labeled in Figure 4(bottom)].

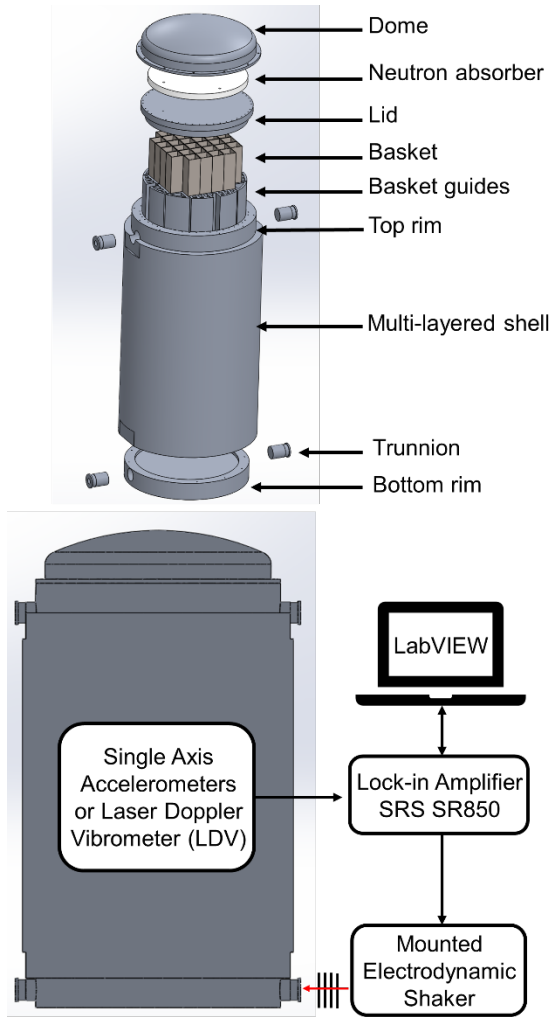


Figure 2. (top) The schematic for the 6:1 scaled TN-32 with the nomenclatures used in this report. (bottom) A simplified experimental setup for both the full-scale and lab-scale TN-32 experiments.

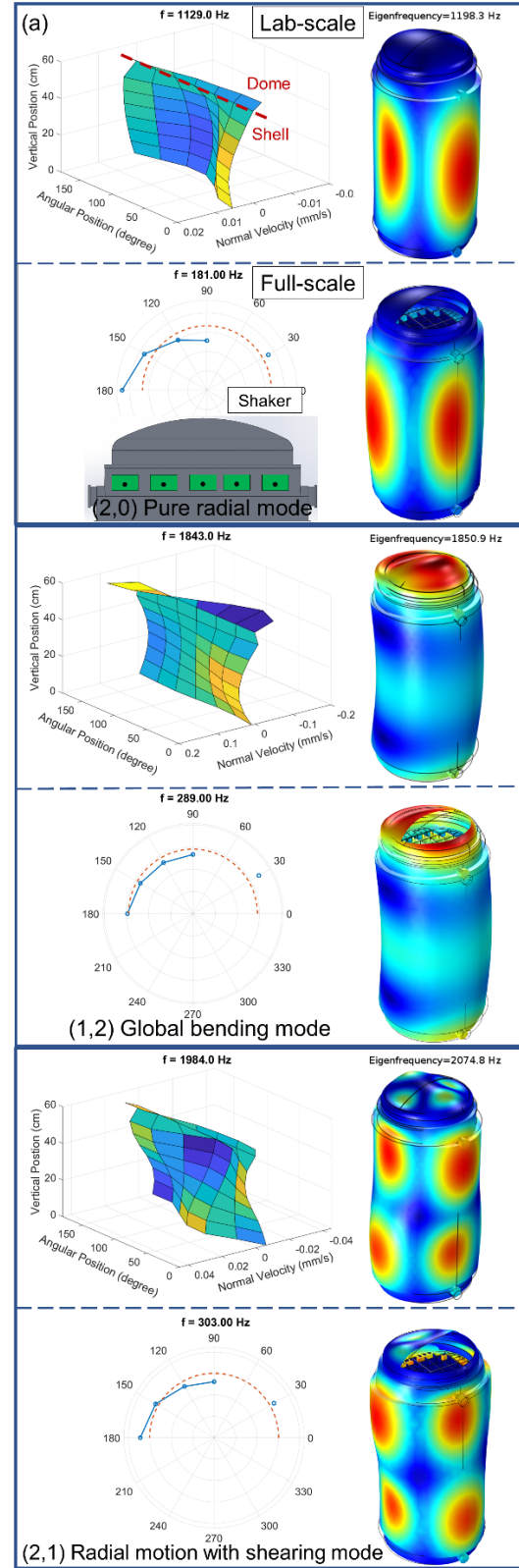


Figure 3. The comparison among (right) FE simulations and (left) measured motion of (top) unwrapped shell of lab-scale and (bottom) top rim of the full-scale TN-32.



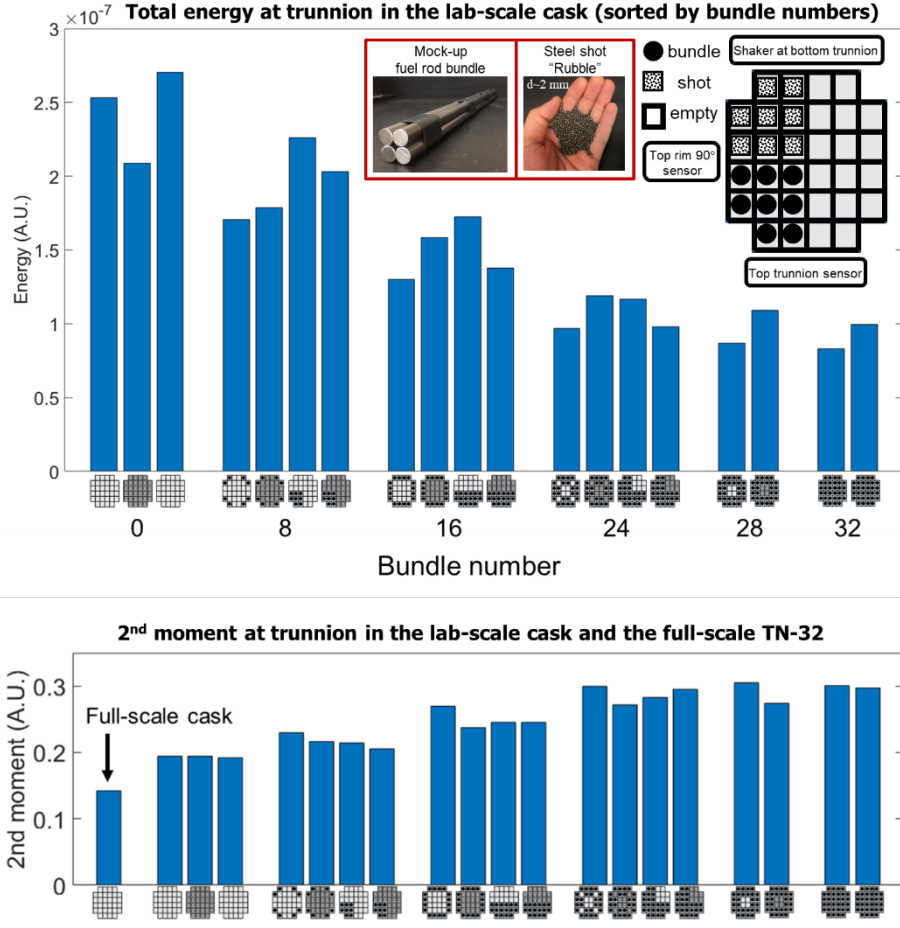


Figure 4. (inset) Simplified experimental setup, pictures and legends of the internal states of the model cask. (top) The total energy metric for various internal configurations. (bottom) The 2nd moment metric with the full-scale TN-32 data.

With an extra sensor at the top rim 90° from the top trunnion sensor, another set of amplitude metrics can be calculated [Figure 5]. Additionally, a set of phase-based metrics were developed by utilizing the relative phases between the two sensors [Figure 6]. Positive and negative relative phases were tracked around the (1, 2) and (2, 1) modes individually. Based on the results in Figure 4, only symmetric and empty configurations were subsequently performed. In addition, the single bundle missing case was explored through a combination of 8 different missing locations in the bottom-left quadrant. Each configuration was repeated five times and normalized with respect to the fully-loaded case in order to establish the sensitivity of the active acoustics techniques. By using principle components analysis on both the amplitude and phase metrics, a combined metric with best representation (i.e. largest eigenvalue) was chosen [Figure 7]. With just one shaker and two sensors, the error bar shows that the sensitivity of the active acoustics method can detect whether a single assembly completely decays into rubble or is missing, and it also has the potential to reach the sub-assembly sensitivity level.

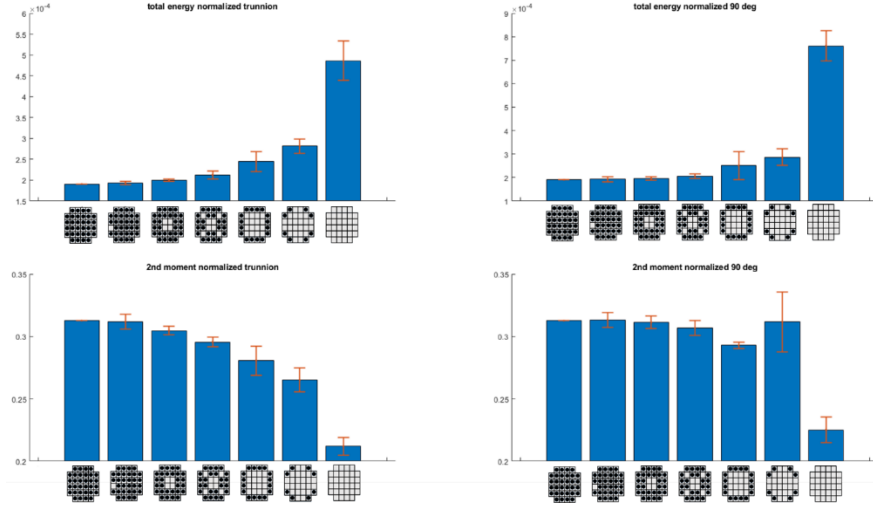


Figure 5. The amplitude metrics of both trunnion and 90° rim sensor. The error bar is the standard deviation. Each configuration was repeated 5 times and normalized to fully-loaded case.

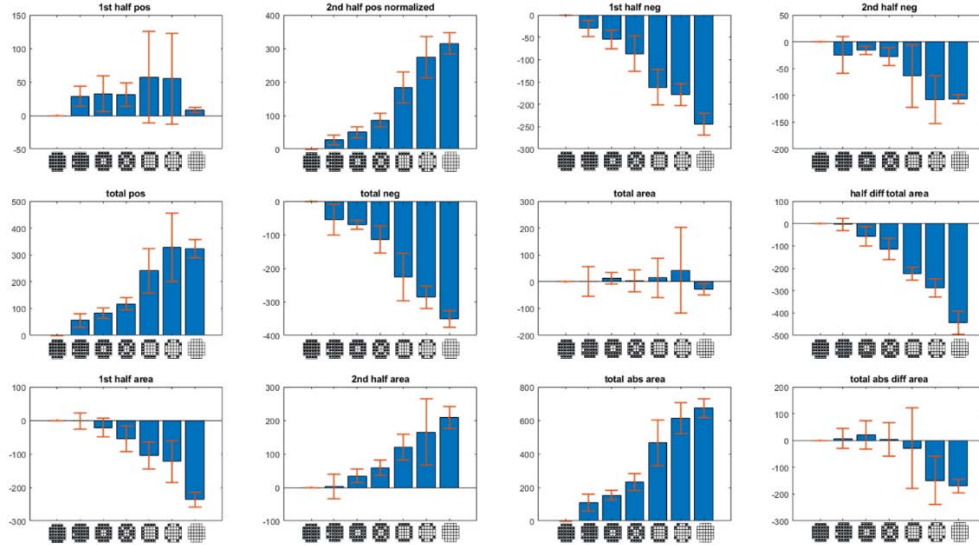


Figure 6. The phase metrics are calculated by tracking the relative phases between the trunnion and top rim 90° sensor around (1, 2) and (2, 1) mode on the spectra.

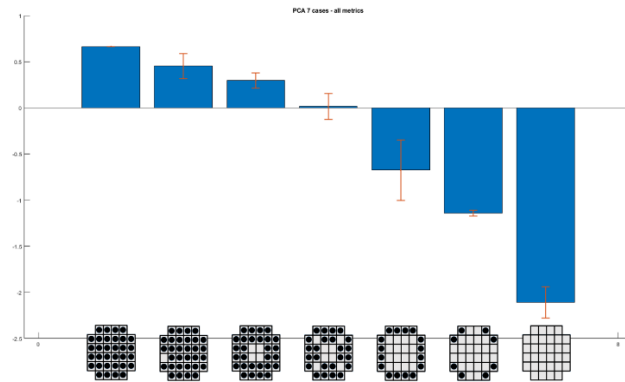


Figure 7. The combined metric calculated by principle component analysis using both the amplitude and phase metrics. The error bar shows that the sensitivity of active acoustics methods can detect a single assembly complete turns into rubble, and it also has the potential to reach sub-assembly level.

We recommend applying the active acoustic method for both storage and transportation scenarios. To achieve the highest possible sensitivity, acoustic fingerprints for each cask need to be acquired before and right after the cask is loaded. This will create lower and upper bounds for each of the amplitude and phase metrics. The developed active acoustics method can be rapidly deployed and applied and does not require a large space. However, at present it is not sensitive to sub-assembly level damage and location. With regular active acoustics tests, casks that deviate from the measured metrics of the fully-loaded configuration should be examined with more accurate but time-consuming techniques, like neutron and gamma ray tomography.

## Description of Tasks and Results

The opportunities to access a full-scale TN-32 at the early stage of this project prompted a reassessment of the tasks from the original proposal. Thus, the tasks from the original proposal have been modified and reordered as appropriate in this final report.

*Task 3.2 Perform finite element analysis for optimizing sensor network*

*Task 3.3 Build measurement system and data acquisition and analysis algorithms*

*Task 3.7 Scale-up methods for full scale field test on a TN-32 cask*

During the course of the project, four opportunities for on-site measurements at Columbiana High Tech (CHT) facility in Greensboro, NC were made available. Each of these opportunities provided a different configuration of the same healthy Transnuclear-32 (TN-32) cask [Table 1]. After the last study in October 2017, this TN-32 was transferred to North Anna Power Station to be loaded with actual spent nuclear fuel assemblies. Due to strict regulations on loaded casks and the inability to access this TN-32 within the timeline of the project, on-site demonstration of the active acoustics system on a TN-32 loaded with spent fuel was impossible. Therefore, Task 3.7 was modified to indicate the field testing performed on the TN-32 in an earlier stage, and the resulting data provided a means of confirming the validity of the lab-scale cask as a relevant surrogate system.

*Table 1. Information on each study on the same TN-32 performed at CHT. In method row, I stands for impulse method and CW stands for swept continuous wave method.*

	Study 1	Study 2	Study 3	Study 4
Date	Sept. 2016	Feb. 2017	Sept. 2017	Oct. 2017
Internal config	With surrogate fuel rod assemblies		Unloaded	
External config	Lid/dome off	Lid/dome on	Dome off	Lid/dome on horizontally placed on a skid
Method(s)	Impulse (I)	I & CW	I & CW	I & CW

## Experimental Setup and Methods

The construction of the cask limits the placing of sensors to the top and bottom regions (i.e., trunnions and top/bottom rims) of the cask where there are solid, direct pathways to the interior. The sides of the cask have a 4.5” layer of plastic underneath the steel outer shell, making the shell unreliable for acoustic

interrogation. The trunnions, however, are directly coupled into the base, cap and inner walls, and were therefore chosen as points of acoustic excitation and sensor placement. They are also rugged as they are used as grab points in the transportation of the cask. The sensor optimization in Task 3.2 is adjusted due to the above restrictions.

The experimental setup is shown in Figure 8. Two excitation methods were used in this work. For the impulse study, a custom metal pendulum and a dead blow hammer were used to provide high and low frequency stimuli, respectively. The excitations were applied at the surfaces of trunnions and the top and bottom rims, which are the direct pathways into the internal structure. For the swept continuous wave (CW) method, an electrodynamic shaker (Crowson T108SM), was mounted on one of the trunnions using a custom magnetic mount. The shaker was driven by a lock-in amplifier (Stanford Research System SR850). For both studies, an array of 7 single-axis PCB accelerometers (10 mV/g) were deployed around the cask to collect signals. The data acquisition system consists of two 4-channel digitizers (NI-9233, 50 kHz sampling rate) and was controlled using a custom Labview interface. See Appendices A-D for field trip details and Appendix E for the custom shaker mount design.

Figure 8 shows examples of the experimental and data analysis techniques. Data from the impulse studies were analyzed using a time-frequency approach (spectrogram). Modal frequencies can be determined by identifying the peaks which persist in time in the spectrogram [Figure 8(a)], and the quality factor (Q), which is an indicator of structural integrity, can be calculated by fitting the decay time of the signal amplitude [Figure 8(b)]. Data from the continuous-wave study were analyzed by performing Fourier transforms of the time-domain response at each frequency step from which the fundamental and harmonic responses were obtained. Linear and non-linear vibrational spectra of the cask were thus acquired. The quality factor is obtained by fitting the linear spectrum with a Lorentzian function. The nonlinear effects of interest are harmonic generation and modal frequency shift. The former method measures the harmonics of the excitation frequency [Figure 8(c)], while the latter method measures the modal frequency shift with increasing excitation amplitude [Figure 8(d)]. The development of a measurement system and analysis algorithm (Task 3.3) was completed.

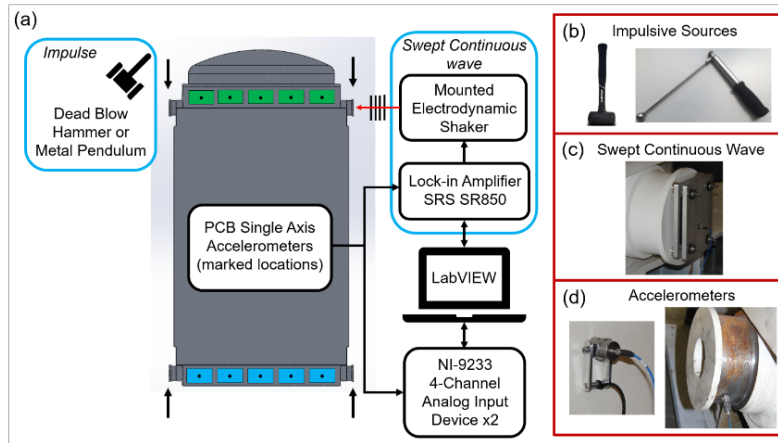


Figure 8. Experimental setup (a) Schematic diagram of the measurement system. (b) Dead blow hammer and metal pendulum used as excitation sources. (c) Shaker mounted on a trunnion for continuous wave studies. (d) Accelerometers with magnetic mounts deployed at various locations.

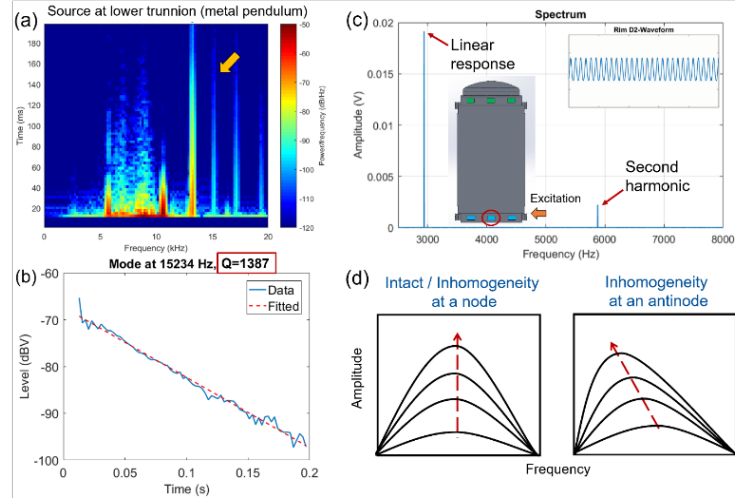


Figure 9. Examples of experimental techniques (a) Spectrogram of representational impulse data from Study 1, and (b) the associated amplitude vs. time for an indicated single mode from which quality factor is determined. (c) Harmonic generation at a single frequency taken from a signal (inset) acquired from Study 2. (d) Modal frequency shift that appears when inhomogeneity is at an anti-node and the driving amplitude is increased.

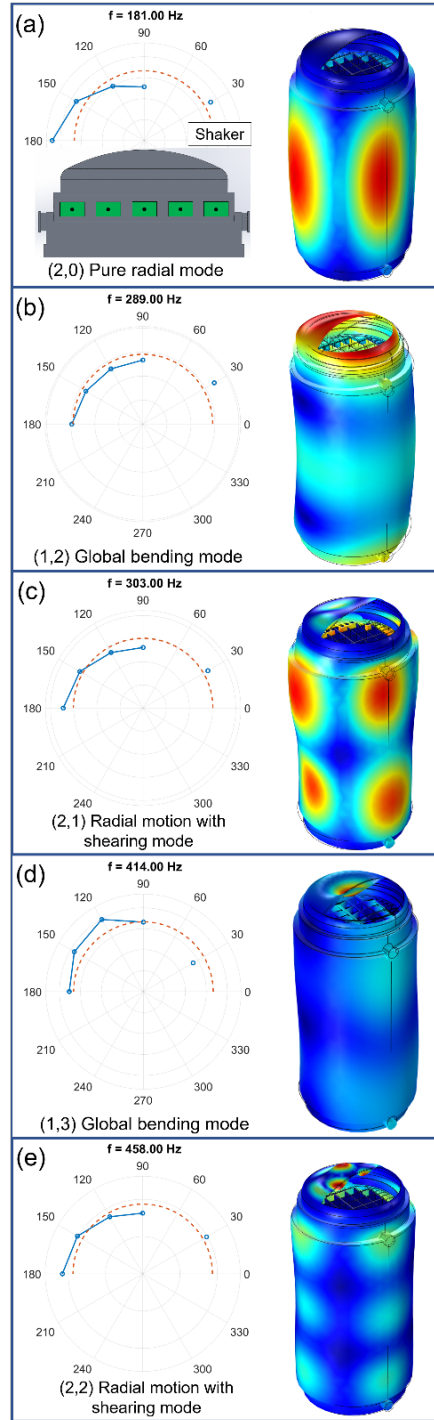


Figure 10. Mode shapes along the top rim identified from the vertical configuration (left) and the corresponding modes from finite element simulations (right). The boxes on the cask show five of the measurement points on the top rim of the TN-32, along with one on the opposite trunnion and one on the excitation source. The dashed line indicates the equilibrium position and the circles indicate the sensors. The second sensor from the right is not phase referenced to the other sensors as it was run through a lock-in amplifier instead of the NI-5532; thus, it is not shown.

## Results

The reported results come from Studies 3 & 4 (Table 1) because our methods had been refined based on the earlier studies.

### 1. Comparison of Swept Continuous-wave and Impulse Method

The swept continuous-wave and impulse data were acquired using the same sensor locations and similar excitation positions as in Study 3. Good signal-to-noise ratios ( $> 40\text{dB}$ ) and well-defined modal structures were observed with both methods. There is a reasonable agreement in the 1st, 3rd, 4th, 5th and 6th measured modal frequencies in both techniques [Table 2]. For the 2nd identified mode from the swept-continuous wave (CW) measurements, the frequency resolution (12 Hz) of the impulse method is insufficient to resolve it. The associated quality factors calculated are higher in the impulse method, but the relative relationships between them are conserved, with the 6th mode as an exception.

Mode shapes are identified by the CW method. In Study 3, seven sensors (including one at the excitation source) were deployed around the top rim. Six modes were identified using the magnitude and phase information from the Fourier transform of the waveforms. The completion of Task 3.2 is summarized in Figure 10, where the first five measured modes are compared with results from the Finite Element (FE) simulations. The cylinder modes are labeled as (m, n) - the circumferential and axial mode numbers, respectively. The average surface displacement ratio between the trunnion and the bottom of the cask was calculated in FE simulations to quantify the ability to couple energy into the interior due to excitation on the trunnion. The (1, 2) and (1, 3) global bending modes, which have the largest displacement ratios and activity in the basket, were identified [Figure 10(b) and (d)], while the other modes showed less activity in those locations [Figure 10(a), (c) and (e)]. In particular, the displacement ratio for the (1, 2) mode is 3 to 10 times larger compared to the other identified modes. The (3, 0) pure radial mode was numerically predicted to appear between the 3rd and 4th mode, but it is not identified experimentally. The FE predicted resonant frequency starts to deviate even more at the 5th mode [Figure 10(e)], and FE failed to predict the observed 6th mode, which is a 4th order circumferential mode. There are no further correspondences between the measurements and FE beyond the 5th mode.

Table 2. Comparison of modal frequencies and associated quality factors ( $Q$ ) from swept continuous-wave and impulse method. The frequency resolution (12 Hz) of the impulse method cannot resolve the 2<sup>nd</sup> mode.

Frequency / $Q$	1 <sup>st</sup> mode	2 <sup>nd</sup> mode	3 <sup>rd</sup> mode	4 <sup>th</sup> mode	5 <sup>th</sup> mode	6 <sup>th</sup> mode
Swept CW	181 Hz / 51	289 Hz / 28	303 Hz / 16	414 Hz / 191	458 Hz / 17	601 Hz / 76
Impulse	183 Hz / 68	-	305 Hz / 32	415 Hz / 200	464 Hz / 31	598 Hz / 67

### 2. Nonlinear Response

The nonlinear measurements, the results of which are shown in Figure 11 and Figure 12, were taken in Study 3. For the harmonic generation method, a baseline measurement of the fundamental, 2<sup>nd</sup>, and 3<sup>rd</sup> harmonics was performed with the shaker driven at a power of 15 W, as shown in Figure 12. The cask exhibited no significant nonlinearity at frequencies below 1 kHz in our measurements. The five modes identified with FE simulations are marked in the fundamental spectrum. The harmonic structures in this region are about two orders of magnitude below the fundamental, and they have good correspondence to the fundamental which is an indication that



the source of these weak harmonics is in the excitation source and not due to the cask itself [Figure 11(b)]. Above 1 kHz, the nonlinear responses are within one order of magnitude relative to the fundamental [Figure 11(a)]. The 2<sup>nd</sup> harmonic predominates the nonlinear spectra from 1 to 1.6 kHz, while the 3<sup>rd</sup> harmonic predominates from 1.6 to 2 kHz. These observations agree with the modal frequency shift results discussed in the next paragraph. As a baseline measurement, these spectra are expected to be used for comparison to identify nonlinear activity associated with internal abnormal conditions.

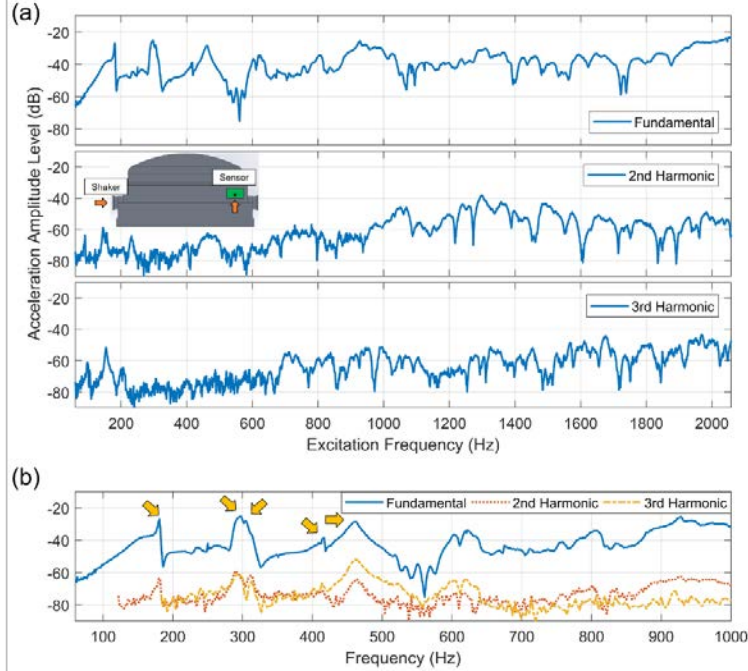


Figure 11. Linear and nonlinear response from the vertical configuration. (a) The fundamental, 2<sup>nd</sup> and 3<sup>rd</sup> harmonic are plotted with respect to the frequencies at which the shaker is being excited. For the nonlinear responses, the harmonic response was more prominent above 1 kHz. (b) The same harmonics are plotted with respect to the measured frequencies. A good resemblance between the three is observed up to 1 kHz. The five modes which are identified with finite element simulations are marked with arrows on the fundamental spectrum.

For the modal frequency shift method, the shaker was driven up to 60 W in 3 equal voltage increments [Figure 12]. For the modes below 1.6 kHz, the frequency shifts are below the resolution of the study (1 Hz). Between 1.6 and 2 kHz, there are two modes that have significant frequency shifts [Figure 12(a)]. The results show that both the regions where the 3<sup>rd</sup> harmonic predominates, and modal frequency shifts occur fall in the 1.6 to 2 kHz band. This is in agreement with the hysteretic type nonlinearity reported in the literature<sup>32,33</sup>. Although the exact cause of the nonlinearity is unknown at present, this result supports the idea that different modes are sensitive to nonlinearity at different locations in the cask.



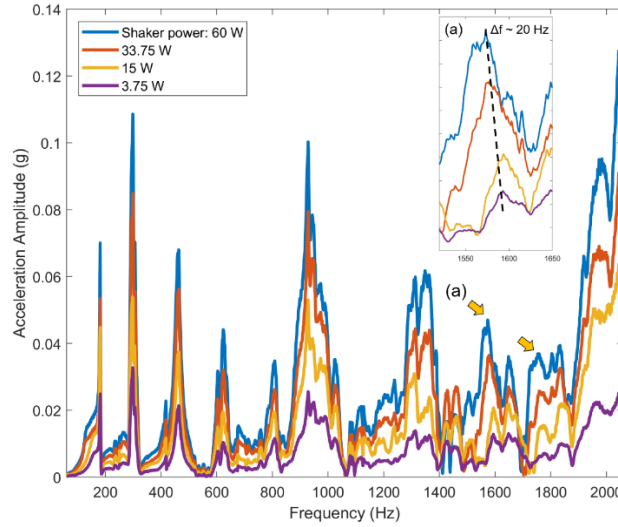


Figure 12. Modal frequency shift with 4 equally spaced driving voltages. Refer to Figure 11 for experimental setup. The arrows indicate modes of interest. The two indicated modes in the higher frequency range have significant shifts with increasing driving amplitude. (a) A mode with a 20 Hz frequency shift.

### 3. Comparison of horizontal and upright configurations

When the TN-32 is to be transported, it will be mounted horizontally on a transportation skid and then loaded on a truck [Figure 13(bottom right)]. The contacts between the cask and the skid happen at the top rim and bottom trunnions. These contacts are buffered with rubber. In this configuration, the acquired spectra showed that the modal frequencies are shifted to lower values in the region below 800 Hz relative to the upright configuration [Figure 13]. This suggests that a mass loading effect due to the skid predominates below 800 Hz, and that the effect of the change in the cask configuration on the shape of the spectrum is more prominent above 800 Hz. This implies the methodology developed for the vertical configuration can be applied to transportation by studying only the modes that are below 800 Hz.

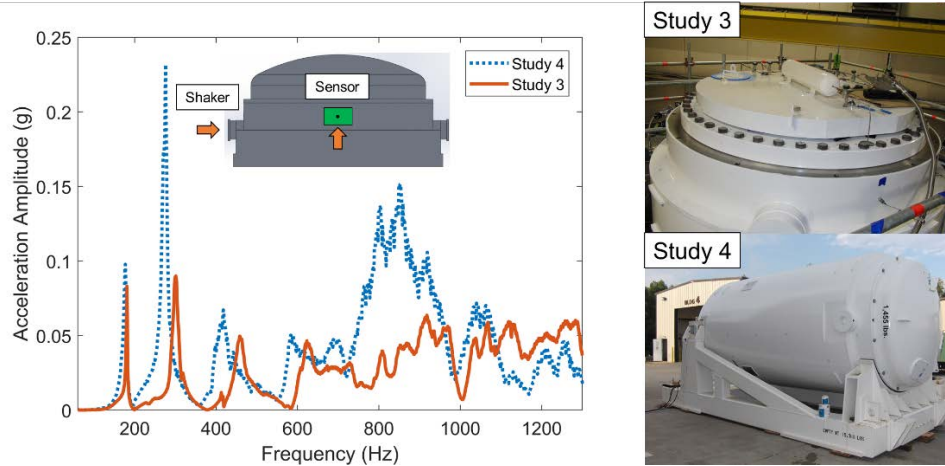


Figure 13. Comparison of the spectra between vertical (storage) and horizontal (transportation) configurations. Modes below 800 Hz are less susceptible to change of the configuration.

#### Task 3.1 Design and construction of a scaled model test cask

The data acquired on a full-scale TN-32 is extremely valuable. However, the internal state of the cask could not be altered so it was not possible to change the internal configuration or introduce any kind of abnormality. Therefore, a 6:1 detailed lab-scale was constructed at the machine shop

at the National Center for Physical Acoustics (See Figure 1). The schematic is based on the original TN-32 and is shown in Figure 2(top). Refer to Appendix F for the drawings. Due to practical reasons like cost, weight and machinability, the material of choice is aluminum instead of steel, and the shell is a single-layer of aluminum rather than a multi-layer structure (no heat conducting and polymer type neutron absorption layers).

#### *Task 3.4 Conduct linear and nonlinear resonance experiments on a healthy model cask*

Measurements on the unloaded healthy lab cask were conducted in a similar fashion as the full-scale cask [Figure 2(bottom)]. A shaker (Dayton Audio DAEX32U-4 exciter speaker, 4ohm, 40W) was glue-mounted on one of the lower trunnions and driven with the output of a lock-in amplifier (Stanford Research System SR850). For the measurement on the single-layered shell and trunnions, a laser Doppler vibrometer (Polytec PDV-100) was mounted on a custom scanning track, which was used to map out the mode shapes on the shell. For the measurements on the basket, a single-axis Kistler accelerometer (3.02 mV/g) was wax mounted. Both sensors were separately connected to the lock-in amplifier which was controlled using a custom LabView interface. The amplitudes and phases of the fundamental and harmonic spectra were obtained from the lock-in amplifier. The first three modes were mapped out and matched the first three modes identified on the full-scale TN-32 [Figure 3]. This agreement validates the lab cask as a good linear acoustics representation to the full-scale TN-32. Furthermore, by mounting an accelerometer at the top basket in the sealed lab cask, data with high signal-to-noise ratios can be acquired from the basket, and similar features can be seen in both of the spectra from the basket and the trunnion [Figure 14]. This further illustrates that energy can be propagated into internal structure, and thus information about the internal configuration can be measured from the outside. (Completion of *Task 3.4* - the nonlinear part - is in the next section for comparison.)

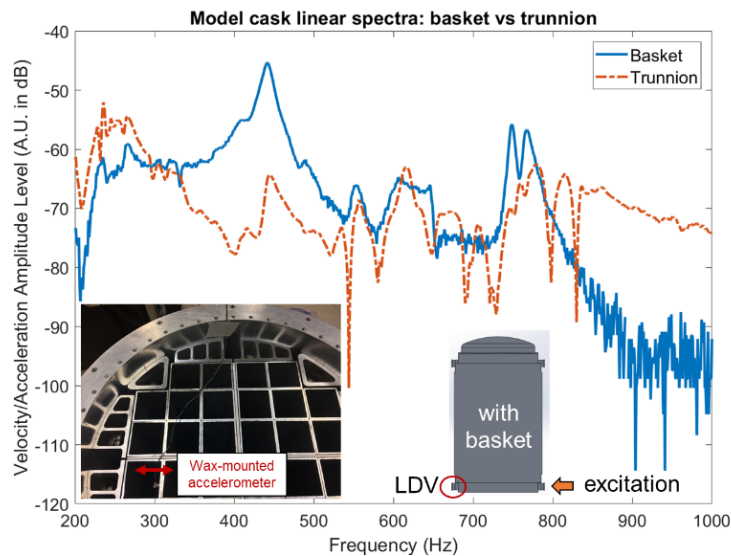


Figure 14. Spectra acquired from both the top of the basket and the bottom trunnion. The relative level of the two spectra is shifted for visibility.

#### *Task 3.5 Conduct linear and nonlinear resonance experiments on a damaged model cask*

#### *Task 3.6 Establishment of criteria for quantifying the degree of degradation*

The purpose of this project is to develop a way to assess the structural integrity of basket and spent fuel assemblies inside a sealed TN-32. To understand and quantify the vibrational effects

due to damaged cargo inside the sealed cask, one of three states is introduced to each slot in the basket: mock-up fuel assembly, steel shot in place (“rubble”) and empty. Our mock-up fuel rod assembly consists of four steel rods, which are bundled together with heat shrink. The catastrophic failure of the assembly, “rubble,” is mimicked with steel shot of approximately 2mm diameter and with the same mass as a mock-up assembly. The empty state is to simulate either a missing fuel assembly or originally unloaded slot [Figure 5(inset)]. The shaker was driven at 3.5 W at the bottom trunnion while a PCB accelerometer (10 mV/g) was glued with thin cyanoacrylate adhesives to the opposite top trunnion. The LDV was not used because of the lack of sensitivity.

For the nonlinear damage studies, the 2<sup>nd</sup> and 3<sup>rd</sup> harmonics and fundamental frequency shift were measured for three cases: all bundles (healthy), all shot (complete failure) and one slot of shot among bundles. The harmonics measurements were taken by reloading of the cargo five times so that the statistical significance could be established [Figure 15]. The 2<sup>nd</sup> harmonic spectra show trends in both changes of peak frequencies and peak amplitude, while the 3<sup>rd</sup> harmonics show only the latter. The total measured harmonic energy is also calculated by integrating over the frequency of interest [Table 3]. The results suggest more harmonic energy will be measured with healthier internal conditions. The fundamental frequency shift measurements were focused on the (1, 2) and (2, 1) modes, where the (1, 2) global bending mode was identified to be more capable to couple energy to the internal structure. With a larger number of intact bundles, the frequency shifts are larger for both modes, indicating structural complexity due to intact bundles [Figure 16]. Interestingly, the resonant frequency for the (1, 2) mode increases with more bundles, while it decreases for the (2, 1) mode. Although the nonlinear techniques show the potential to identify internal failures, the large standard deviations show that they are very sensitive to minute changes. Thus, we turned our focus to the more robust linear techniques (Completion of nonlinear part of *Task 3.4* and 3.5).

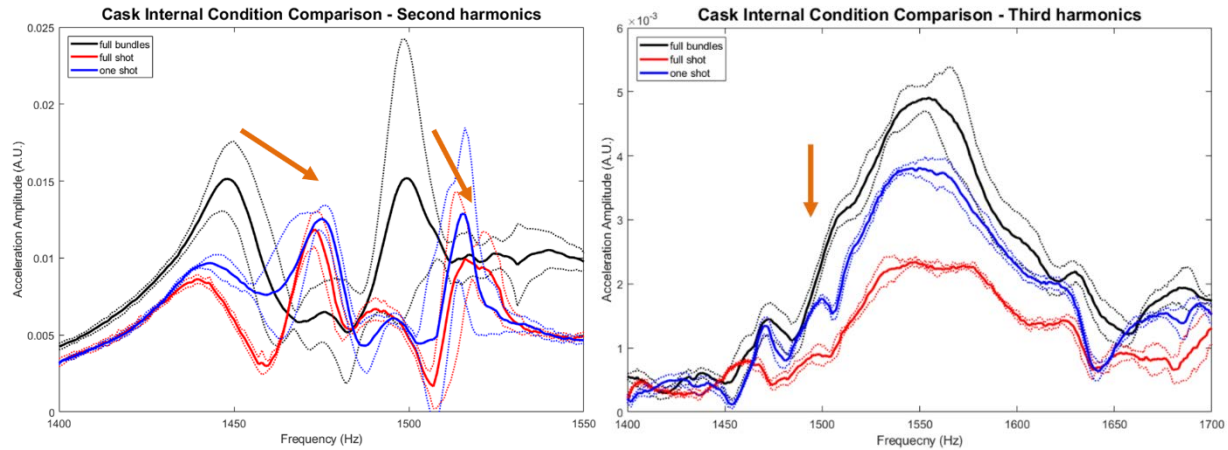


Figure 15. (left) The 2nd harmonic spectra for the three internal conditions: all bundles (healthy), all shot (completely failure) and all bundles but one slot of shot. The frequency axis is the excitation frequency. Two indicated modes show trends in the change of the amplitude and the peak frequency shift. The dotted lines are the error bars of each of the curve. (right) The 3rd harmonic spectra for the three internal conditions. The indicated peak has a clear trend in the change of the amplitude.

Table 3. Total harmonic energy of the three configurations as in Figure 15. The energy is estimated by taking the acceleration spectra and convert them into amplitude spectra, squared and integrating over the frequency range of interest. A reducing energy trend for more slots of shot is observed for both 2<sup>nd</sup> and 3<sup>rd</sup> harmonics.

Config	2 <sup>nd</sup> Harmonic Energy (A.U.)	3 <sup>rd</sup> Harmonic Energy (A.U.)
Full bundles	$3.5 \pm 0.6$	$2.0 \pm 0.3$
One shot	$1.00 \pm 0.06$	$0.78 \pm 0.04$
Full shot	$0.77 \pm 0.05$	$0.51 \pm 0.02$

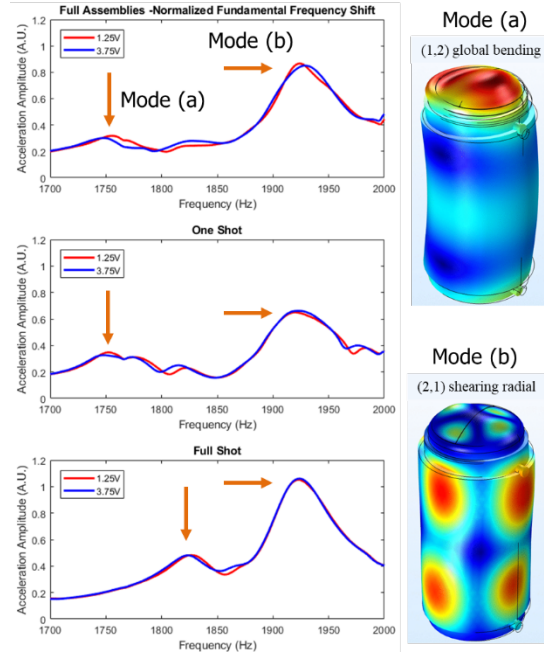


Figure 16. Modal frequency shift due to increase of excitation amplitude for the same three configurations as Figure 15. The modes of interest are (1, 2) and (2, 1) modes. More shifts are observed in the full assembly case than full shot case while one shot case is in between.

For the linear studies, a combination of symmetric and asymmetric patterns of slot states were studied (See the x-axis of Figure 4). The same excitation and sensor locations as the nonlinear damage studies were used for the first part of the study. The frequency range of interest is from 1.6 - 2.1 kHz, where the two modes in Figure 16 reside. To quantify the condition of the internal structure, two amplitude-based metrics were derived from the fundamental spectra. The first amplitude metric is the total energy measured at the sensor, which is calculated by integrating the measured squared amplitude over the frequency of interest. The second amplitude metric is the second moment of amplitude spectrum, which is calculated for the normalized amplitude spectrum with respect to the weighted average frequency [Figure 17(a) & (b)]. The first metric quantifies how much energy can be measured externally, and the second one quantifies the separation in frequency between these two modes and the complexity of the spectra. Both metrics are sensitive to the number of intact bundles but insensitive to whether or not the remaining slots are filled with shot or to their locations [Figure 5]. With more intact bundles, the (1, 2) mode is observed to shift to a lower frequency while the (2, 1) mode exhibits no shift. Our hypothesis is that an intact internal structure is able to retain vibrational energy that is coupled from exterior. Therefore, the sensor

will measure less energy from the external structure (trunnion), and the acquired spectra are also more complicated due to extra internal degrees of freedom. On the other hand, an empty slot or one randomly-packed with steel shot does not vibrate, thus less energy and a simpler modal structure are measured externally. Furthermore, the field data on an unloaded TN-32 can be used to calculate 2<sup>nd</sup> moment and it is consistent with the unloaded lab cask [labeled in Figure 4(bottom)].

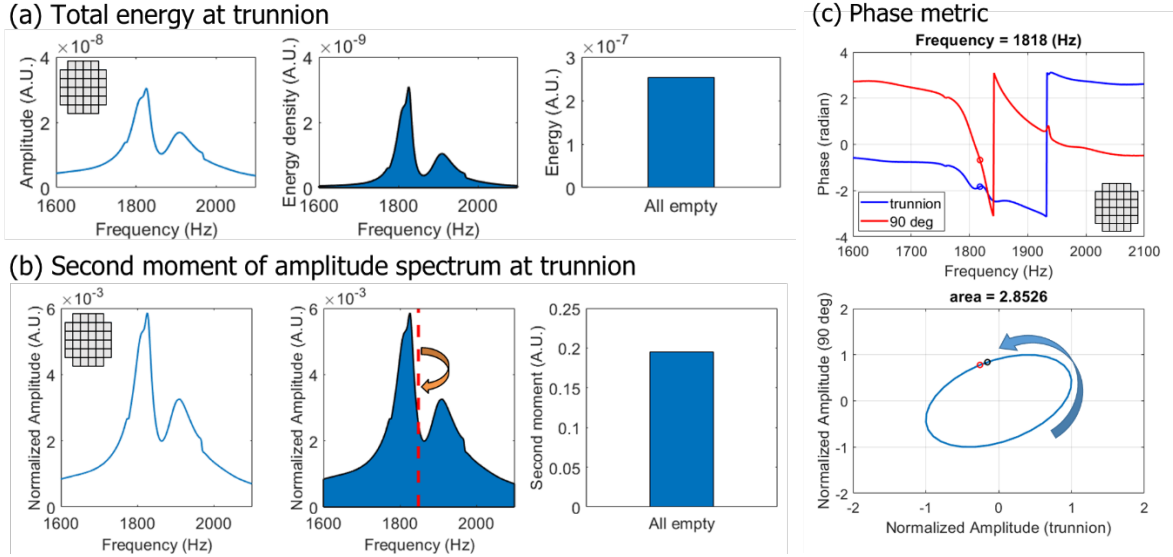


Figure 17. Examples of calculation of metrics with all empty case (a) & (b) Two amplitude-based metrics. The calculation flow goes from left to right (c) Phase spectra for both sensors (top). For each frequency step, the enclosed area of the phase space (bottom) is recorded to calculate the phase metrics. The sign of the area is determined by the flow of the curve (arrow).

The second part of the linear studies focused on further determination of the sensitivity of the active acoustic method. An extra accelerometer was introduced at the top rim 90° from the trunnions. This extra sensor was connected to another lock-in amplifier which was phase-locked to the original one. This allows relative phase between the two sensors to be measured. In the previous part of linear studies [Figure 4], the results showed that the number of intact bundles is the predominating factor of the metrics. Based on that, only the missing and symmetric configurations were subsequently studied. In addition, cases of a single missing bundle in eight different slots were added to test the sensitivity limit (x-axis of Figure 18). To obtain statistically significant results, five measurements of each configuration were acquired.

Large variations of mechanical coupling between the bundles and the bottom of the cask, as seen in the nonlinear studies, result from the repositioning of the bundles. This factor is eliminated by using the experimental procedure and data analysis techniques discussed below. By starting with the full bundle configuration, then gradually pulling out bundles and taking measurements without repositioning the rest, the consistency of the coupling in the five runs can be ensured. To normalize the coupling effects, the amplitude or phase spectra from different configurations in each run are divided or subtracted by the full-bundle spectrum in the beginning of each run. Amplitude and phase metrics for both sensors are calculated using these normalized spectra. With an extra sensor, twelve phase metrics can be calculated from the relative phase between the two sensors. A phase ellipse is constructed from the normalized spectra of each sensor [Figure 17(c)]. For each frequency step, the enclosed positive or negative area in the phase ellipse is recorded individually for the first and the second half of the frequency range of interest. The sign of the area



is determined by the flow of curve in the phase space (clockwise or counter-clockwise), and the first and second half corresponds to the (1, 2) and (2, 1) mode individually. Four basic components, negative and positive area of 1<sup>st</sup> and 2<sup>nd</sup> half, are combined into twelve metrics.

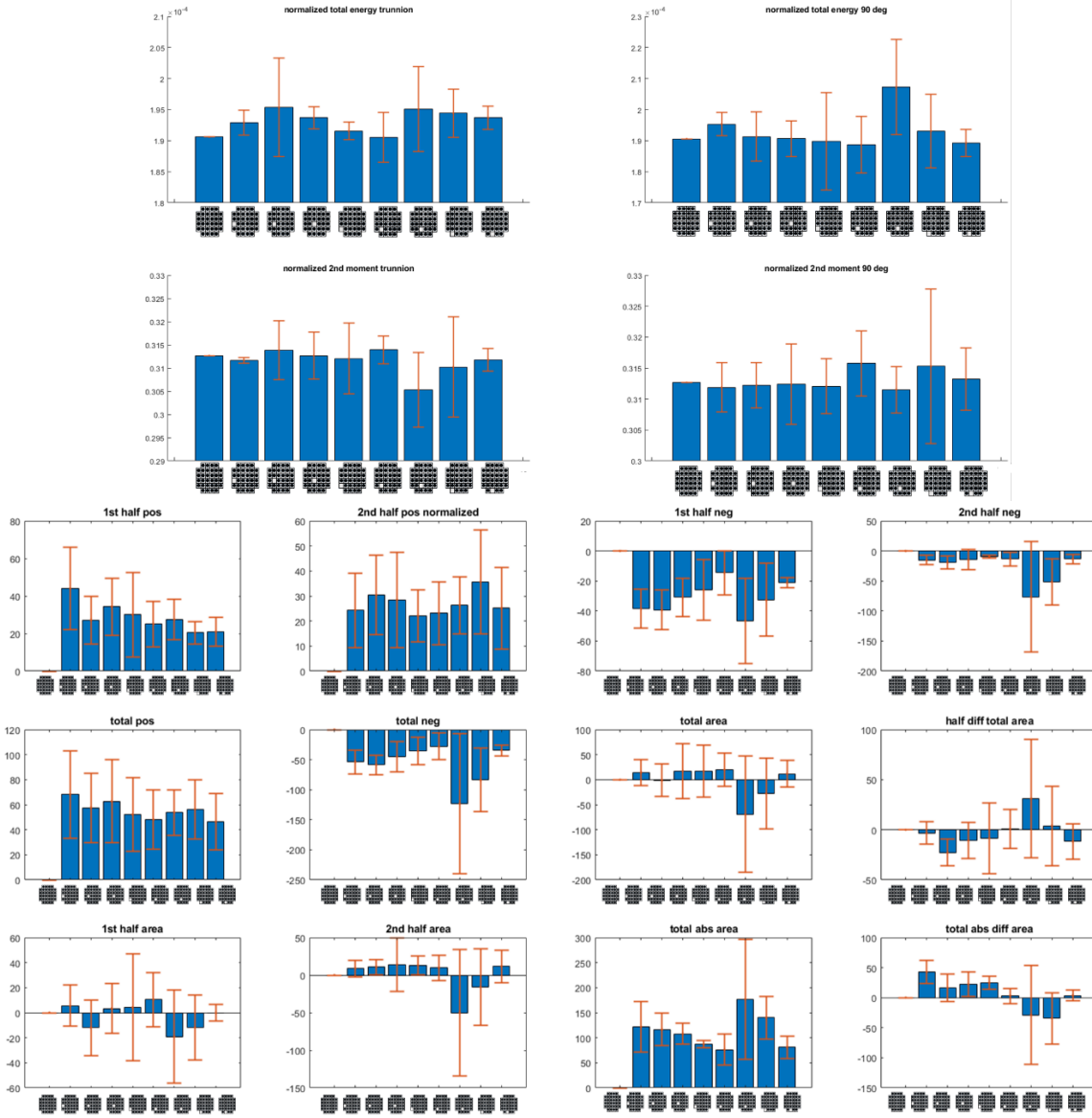


Figure 18. (top) Amplitude and (bottom) phase metrics of single missing bundle cases. The error bar is the standard deviation from 5 measurements. The phase metrics are more sensitive to single bundle missing than the amplitude metrics. No statistically significant difference is observed for different locations.

The resultant metrics for the single missing bundle cases are shown in Figure 18, with the error bars as the standard deviation from five measurements. From these results it can be seen that the phase metrics can detect a single bundle missing while the amplitude metrics cannot. No statistically significant difference is found for different locations of the empty slot. Combining the eight single bundle missing cases into one and comparing with the normalized symmetric cases, the number of intact bundles inside the cask can be identified disregarding their locations [Figure 5 and Figure 6]. By using principle components analysis (PCA) on both the amplitude and phase

metrics, a combined final metric with best representation (i.e. largest eigenvalue) is chosen. The error bar is further reduced in this final metric. With just one shaker and two sensors locations, the result shows the active acoustic methodology can detect a single bundle missing or having complete structural failure, and that the potential exists to reach sub-bundle sensitivity (Completion of *Task 3.6*).

#### *Task 3.8 Technical transfer: Recommendations for a field deployable active acoustic NDE testing system*

To apply the amplitude and phase metrics developed from the lab cask on full-scale TN-32s, a measurement system modified from our field measurement system can be easily constructed. Two PCB single-axis accelerometer (352C04, 10 mV/g) with magnetic mounts (080A179) can be attached to and removed from the top trunnion and top rim 90° locations. These two sensors go into two separate lock-in amplifiers (Stanford Research System SR850) which are mutually phase-locked. The CW output from the lock-in amplifiers will go through an audio amplifier and connect to an electrodynamic shaker (Crowson T108SM), which is mounted magnetically on the bottom trunnion opposite to the sensor trunnion. (Refer to Appendix E for the design of the custom mount.) To reduce undesired contact nonlinearity, put a rubber sheet in between the mount and the back of the shaker. The two lock-in amplifiers are connected to a computer and controlled by a LabVIEW/Matlab interface that can calculate the metrics once each frequency sweep is complete (< 15 mins). All the equipment can easily fit into a cart. Two technicians with access to a manlift are sufficient to perform measurements on multiple casks in the field. The procedure can be as simple as the following: (1) Deploy the sensors and shaker; (2) Start the acquisition program; (3) Read and interpret the results; (4) Remove sensors and shaker; (5) Move on to the next cask. The above process can be done in less than an hour for each cask. To achieve the highest possible sensitivity, acoustic fingerprints for each cask need to be acquired before and after the cask is loaded. This will create lower and upper bounds for each amplitude and phase metric. The active acoustics method is fast and does not require a large amount of space. Further work is needed to establish the process for damage detection and localization at the sub-assembly level.

We recommend applying the active acoustic method in both storage and transportation scenarios, based on the similarities discovered in the field tests. Our active acoustics method is expected to provide the highest sensitivity when the casks are in storage on concrete pads, since the couplings between the fuel assemblies and the bottom of the casks are maximal. Testing should be performed on a regular basis. For the transportation aspect, sweeps can be done before, while and after transportation to monitor the change in internal structures. Casks that significantly deviate from the fully-loaded values should be examined with more sensitive but time-intensive techniques, like neutron and gamma ray tomography.

## **Conclusions**

All the active acoustics tasks have been completed with reasonable modifications reflecting realistic constraints. A summary of the completion for each task is listed in Table 4. The results from the four field studies showed that data can be acquired at high signal-to-noise ratios from the full-scale TN-32, and thus extracting information from the interior is feasible. The six modes identified from impulse and swept continuous-wave methods agree reasonably well with each other, and the first five identified modes also match with finite element analysis. In particular, two global bending modes with large response in the basket and at the bottom of the cask were

identified. For the nonlinear techniques, baseline measurements were acquired using both harmonic generation and modal frequency shift methods. The response of the TN-32 cask is linear below 1 kHz, while nonlinear spectra are more prominent above 1 kHz. Subsequent studies will allow the comparison of these baseline measurements with the spectra from other casks with a focus on the five identified modes in the linear regime. Casks with abnormally high nonlinear responses may require further investigation. Spectra acquired in both transportation and storage configurations also suggest that the five identified modes are rather robust to changes in boundary conditions regarding in their spectral shape, so these five modes can also be useful for monitoring the cask during transportation. These results provide a robust and extensive knowledge base for further lab studies involving abnormalities in the internal configuration.

A detailed 6:1 scaled lab cask was built at National Center for Physical Acoustics based on the schematics of an actual TN-32 but with realistic simplifications. Because of the poor acoustic coupling between the shell and internal structure of the TN-32, the experimental setup and sensor placements are similar to field tests. The first three modes identified in the lab are identical to the first three modes identified in the field. This result validates our lab-scale cask being a good acoustic representation of an actual TN-32. These three modes also reside in the linear regime of the full-scale TN-32, enabling the nonlinear techniques to be applied around these three modes in the lab. In particular, the (1, 2) global bending mode is identified again in the lab cask. This mode has a large response at the bottom and it is expected to efficiently couple energy into the basket and fuel assemblies. Data with high signal-to-noise ratios is acquired with a sensor on the basket in the sealed cask, which further proves the feasibility of the active acoustic technique. Catastrophic damage scenarios on the fuel assemblies were mimicked and studied on the lab cask. Due to time restrictions, the nonlinear techniques, although showing some promise, did not reach a level of refinement to justify their further investigation. For the linear approach, amplitude- and phase-based metrics were developed around the (1, 2) and (2, 1) modes to quantify the damage level of the fuel assemblies. They are most sensitive to the total number of intact fuel assemblies in the basket, but less sensitive to the locations and whether other slots are rubble filled or empty. With just one shaker and two sensors, these metrics can determine if one of the fuel assemblies is missing or completely rubblized. This methodology can be applied to a full-scale TN-32 with minor adjustments based on our field system. The system can be built with mostly off-the-shelf equipment and easily fitted into a mobile cart. We recommend applying the active acoustic method on both storage and transportation scenarios, based on the acoustic similarity discovered in the field tests. Granted the opportunity of a follow-on project, the metrics and the nonlinear techniques will be further studied and combined to increase the sensitivity to reach sub-assembly damage identification and localization.

*Table 4. Summary of the completion for each task.*

<b>Task 3.1</b>	<b>Design and construction of a scaled model test cask</b>
A detailed 6:1 scaled model cask was built at the National Center for Physical Acoustics.	
<b>Task 3.2</b>	<b>Perform finite element analysis for optimizing sensor network</b>
The sensor locations are chosen to be at the trunnions and rims, while the source is at the trunnions.	
<b>Task 3.3</b>	<b>Build measurement system and data acquisition and analysis algorithms</b>



Measurement system and analysis algorithms were built and used for both lab- and full-scale casks.	
<b>Task 3.4</b>	<b>Conduct linear and nonlinear resonance experiments on a healthy model cask</b>
Experiments were performed on both lab- and full-scale casks, and the mode shapes agree with FE.	
<b>Task 3.5</b>	<b>Conduct linear and nonlinear resonance experiments on a damaged model cask</b>
Studies were conducted on damage scenarios of intact bundle, rubble and empty in each slot.	
<b>Task 3.6</b>	<b>Establishment of criteria for quantifying the degree of degradation</b>
Developed amplitude- and phase-based metrics can detect complete failure of a single fuel assembly.	
<b>Task 3.7</b>	<b>Scale-up methods for full scale field test on a TN-32 cask</b>
This was modified to perform initial tests on a healthy full-scale TN-32 in earlier stage of the project.	
<b>Task 3.8</b>	<b>Technical transfer: Recommendations for a field deployable active acoustic testing system</b>
A mobile field system can acquire data and calculate the metrics within an hour for each cask.	

## References

1. Bare, W. C. & Torgerson, L. D. Dry Cask Storage Characterization CASTOR V / 21 Cask Opening and Examination. 1–68 (2001).
2. Lambert, J. D., Bakhtiari, S., Bodnar, I., Kot, C. & Pence, J. NRC Job Code V6060: Extended In-Situ and Real Time Monitoring Task 3: Long-Term Dry Cask Storage of Spent Nuclear Fuel. 1–55 (2012).
3. Meyer, R. M. NDE to Manage Atmospheric SCC in Canisters for Dry Storage of Spent Fuel. *US NRC Rep.* (2013).
4. Hanson, B. Gap Analysis to Support Extended Storage of Used Nuclear Fuel. (2013).
5. Carden, E. P. & Fanning, P. Vibration Based Condition Monitoring: A Review. *Struct. Heal. Monit. An Int. J.* **3**, 355–377 (2004).
6. Salawu, O. S. Detection of structural damage through changes in frequency: a review. *Eng. Struct.* **19**, 718–723 (1997).
7. Jhang, K. Y. Nonlinear ultrasonic techniques for non-destructive assessment of micro damage in material: A Review. *Int. J. Precis. Eng. Manuf.* **10**, 123–135 (2009).
8. Pieczonka, L., Klepka, A., Martowicz, A. & Staszewski, W. J. Nonlinear vibroacoustic wave modulations for structural damage detection: an overview. *Opt. Eng.* **55**, 011005 (2015).
9. Chang, P. C., Flatau, A. & Liu, S. C. Review Paper: Health Monitoring of Civil Infrastructure. *Struct. Heal. Monit. An Int. J.* **2**, 257–267 (2003).
10. Brownjohn, J. M. W. Structural health monitoring of civil infrastructure. *Philos. Trans. R. Soc. A Math. Phys. Eng. Sci.* **365**, 589–622 (2007).
11. Doebling, S. W. S., Farrar, C. R. C., Prime, M. B. M. & Shevitz, D. W. D. Damage identification and health monitoring of structural and mechanical systems from changes in their vibration characteristics: a literature review. *Distribution* 133p (1996). doi:10.2172/249299
12. Srinivasan, M. G. & Kot, C. a. Effect of damage on the modal parameters of a cylindrical shell. (1992).
13. Zhang, Y., Lie, S. T., Xiang, Z. & Lu, Q. A frequency shift curve based damage detection method for cylindrical shell structures. *J. Sound Vib.* **333**, 1671–1683 (2014).

14. Amabili, M. Theory and experiments for large-amplitude vibrations of empty and fluid-filled circular cylindrical shells with imperfections. *J. Sound Vib.* **262**, 921–975 (2003).
15. Matlack, K. H. *et al.* Evaluation of radiation damage using nonlinear ultrasound. *J. Appl. Phys.* **111**, 054911 (2012).
16. Matlack, K. H. *et al.* Sensitivity of ultrasonic nonlinearity to irradiated , annealed , and re-irradiated microstructure changes in RPV steels. **448**, 26–32 (2014).
17. Mayuzumi, M. & Hara, N. Initiation and Propagation of Stress Corrosion Cracking of Stainless Steel Canister for Concrete Cask Storage of Spent Nuclear Fuel. **65**, 187–194 (2009).
18. Salchak, Y. *et al.* Dry Storage Casks Monitoring by Means of Ultrasonic Tomography. *Phys. Procedia* **70**, 484–487 (2015).
19. Chen, S. Vibration of Nuclear Fuel Bundles. *Nucl. Eng. Des.* **35**, 399–422 (1975).
20. Planchard, J. Vibrations of nuclear fuel assemblies: a simplified model. *Nucl. Eng. Des.* **86**, 383–391 (1985).
21. Zeman, V. & Hlaváč, Z. Mathematical modelling of friction-vibration interactions of nuclear fuel rods. **10**, 57–70 (2016).
22. Kang, H. S., Song, K. N., Kim, H. K., Yoon, K. H. & Jung, Y. H. Verification test and model updating for a nuclear fuel rod with its supporting Structure. *J. Korean Nuclear Soc.* **33**, 73–82 (2001).
23. Haroun, M. A. Vibration studies and tests of liquid storage tanks. *Earthq. Eng. Struct. Dyn.* **11**, 179–206 (1983).
24. Kruncheva, M. R. Free Vibrations of Cylindrical Storage Tanks : Finite-Element Analysis and Experiments. *J. Eng. Mech.* **133**, 728–733 (2007).
25. Amiri, M. Thin-Walled Structures Ambient vibration test and finite element modeling of tall liquid storage tanks. *Thin Walled Struct.* **49**, 974–983 (2011).
26. Takahara, H. & Kimura, K. Frequency response of sloshing in an annular cylindrical tank subjected to pitching excitation. *J. Sound Vib.* **331**, 3199–3212 (2012).
27. Gonçalves, P. B. & Ramos, N. R. S. S. Free Vibration Analysis of Cylindrical Tanks Partially Filled With Liquid. *J. Sound Vib.* **195**, 429–444 (1996).
28. Ren, W. Structural damage identification using modal data. II: Test verification. *J. Struct. Eng.* **128**, 96–104 (2002).
29. Dutta, D., Sohn, H., Harries, K. a. & Rizzo, P. A Nonlinear Acoustic Technique for Crack Detection in Metallic Structures. *Struct. Heal. Monit.* **8**, 251–262 (2009).
30. Matlack, K. H., Kim, J. Y., Jacobs, L. J. & Qu, J. Review of Second Harmonic Generation Measurement Techniques for Material State Determination in Metals. *J. Nondestruct. Eval.* **34**, (2015).
31. Bas, J. U. P. L. E. *et al.* Localization of Closed Cracks Using Multi-Mode Nonlinear Resonant. 571–578
32. Van Den Abeele, K. E.-A., Carmeliet, J., Ten Cate, J. A. & Johnson, P. A. Nonlinear Elastic Wave Spectroscopy (NEWS) Techniques to Discern Material Damage, Part II: Single-Mode Nonlinear Resonance Acoustic Spectroscopy. *Res. Nondestruct. Eval.* **12**, 31–42 (2000).
33. Van Den Abeele, K. Multi-mode nonlinear resonance ultrasound spectroscopy for defect imaging: an analytical approach for the one-dimensional case. *J. Acoust. Soc. Am.* **122**, 73–90 (2007).

## List of Publications and Presentations

Two presentations were given for the 171<sup>st</sup> Acoustical Society of America Meeting in December 2017:

- Lin, K. Y., Prather, W. E., Lu, Z., Mobley, J., Priyadarshan, G. & Gladden, J. R. *Vibrometric characterization of a TN-32 dry storage cask for spent nuclear fuel. J. Acoust. Soc. Am.* **142**, 2517 (2017).
- Lin, K. Y., Prather, W. E., Lu, Z., Mobley, J., Priyadarshan, G. & Gladden, J. R. *Vibrometric characterization of a TN-32 dry storage cask for spent nuclear fuel. J. Acoust. Soc. Am.* **142**, 2517 (2017).

Two conference papers were published in Proceedings of Meetings on Acoustics:

- Lin, K. Y., Prather, W., Lu, Z., Mobley, J., Priyadarshan, G., Gladden, J. R. (2017) *Vibrometric characterization of an unloaded full-scale TN-32 dry storage cask for*

*spent nuclear fuel. Proceedings of Meetings on Acoustics, 31(1)*  
<https://doi.org/10.1121/2.0000678>

- Lin, K. Y., Prather, W., Lu, Z., Mobley, J., Priyadarshan, G., Gladden, J. R. (2017) *Vibrometric characterization of an intact and unloaded scaled model TN-32 dry storage cask for spent nuclear fuel. Proceedings of Meetings on Acoustics, 31(1)*  
<https://doi.org/10.1121/2.0000754>

One manuscript is in preparation:

- Lin, K. Y., Prather, W., Lu, Z., Mobley, J., Priyadarshan, G., Gladden, J. R. *Vibrational modes for the internal characterization of a full-scale Transnuclear-32 dry storage cask for spent nuclear fuel assemblies*

# Appendix A

Setup, Data and Analysis from 9/29/16 CHT Trip

# CHT TN-32 Test Cask Field Test 1

## Test Procedure 1

Sensor	Serial #	ADC box	ADC channel	Location	Mo
FMM 1	lw 211616	1,2	0,0	Source - Lower Trunnion at 180° face	FMI
AFMM 1	73598	1	1	Cask floor A1	AFF
AFMM 2	73596	1	2	Cask floor A2	AFF
AFMM 3	73602	1	3	Cask floor A3	AFF
CMM 1	60349	2	1	Lower Trunnion at 0° side	CM
CMM 2	73600	2	2	Upper Trunnion at 180° side	CM
CMM 3	73604	2	3	Upper Trunnion at 0° side	CM

## Test Procedure 2

Sensor	Serial #	ADC box	ADC channel	Location	Mo
FMM 1	LW211616	1,2	0,0	Source - Lower Trunnion at 0° face	FMI
AFMM 1	73598	1	1	Cask floor A1	AFF
AFMM 2	73596	1	2	Cask floor A2	AFF
AFMM 3	73602	1	3	Cask floor A3	AFF
CMM 1	60349	2	1	Lower Trunnion at 180° side	CM
CMM 2	73600	2	2	Upper Trunnion at 180° side	CM
CMM 3	73604	2	3	Upper Trunnion at 0° side	CM

## Test Procedure 3

Sensor	Serial #	ADC box	ADC channel	Location	Mo
FMM 1	lw 211616	1,2	0,0	Source - Upper Trunnion at 180° face	FMI
AFMM 1	73598	1	1	Cask floor A1	AFF
AFMM 2	73596	1	2	Cask floor A2	AFF
AFMM 3	73602	1	3	Cask floor A3	AFF
CMM 1	73600	2	1	Lower Trunnion at 0° side	CM
CMM 2	60349	2	2	Lower Trunnion at 180° side	CM
CMM 3	73604	2	3	Upper Trunnion at 0° side	CM

## Test Procedure 4

Sensor	Serial #	ADC box	ADC channel	Location	Mo
FMM 1	lw 211616	1,2	0,0	Source - Upper Trunnion at 0° face	FMI
AFMM 1	73598	1	1	Cask floor A1	AFF
AFMM 2	73596	1	2	Cask floor A2	AFF
AFMM 3	73602	1	3	Cask floor A3	AFF
CMM 1	60349	2	1	Lower Trunnion at 180° side	CM
CMM 2	73600	2	2	Upper Trunnion at 180° side	CM
CMM 3	73604	2	3	Lower Trunnion at 0° side	CM

## Test Procedure 5

Sensor	Serial #	ADC box	ADC channel	Location	Mo
FMM 1	lw 211616	1,2	0,0	Source - Lower Trunnion at 180° face	FMI
AFMM 1	73598	1	1	Cask floor B1	AFF
AFMM 2	73596	1	2	Cask floor B2	AFF
AFMM 3	73602	1	3	Cask floor B3	AFF
CMM 1	60349	2	1	Lower Trunnion at 0° side	CM
CMM 2	73600	2	2	Upper Trunnion at 180° side	CM
CMM 3	73604	2	3	Upper Trunnion at 0° side	CM

## Test Procedure 6

Sensor	Serial #	ADC box	ADC channel	Location	Mo
FMM 1	lw 211616	1,2	0,0	Source - Lower Trunnion at 0° face	FMI
AFMM 1	73598	1	1	Cask floor B1	AFF
AFMM 2	73596	1	2	Cask floor B2	AFF
AFMM 3	73602	1	3	Cask floor B3	AFF
CMM 1	60349	2	1	Lower Trunnion at 180o side	CM
CMM 2	73600	2	2	Upper Trunnion at 180o side	CM
CMM 3	73604	2	3	Upper Trunnion at 0o side	CM

#### **Test Procedure 7**

Sensor	Serial #	ADC box	ADC channel	Location	Mo
FMM 1	lw 211616	1,2	0,0	Source - Upper Trunnion at 180 ° face	FMI
AFMM 1	73598	1	1	Cask floor B1	AFF
AFMM 2	73596	1	2	Cask floor B2	AFF
AFMM 3	73602	1	3	Cask floor B3	AFF
CMM 1	60349	2	1	Lower Trunnion at 0o side	CM
CMM 2	73600	2	2	Lower Trunnion at 180o side	CM
CMM 3	73604	2	3	Upper Trunnion at 0o side	CM

#### **Test Procedure 8**

Sensor	Serial #	ADC box	ADC channel	Location	Mo
FMM 1	lw 211616	1,2	0,0	Source - Upper Trunnion at 0° face	FMI
AFMM 1	73598	1	1	Cask floor B1	AFF
AFMM 2	73596	1	2	Cask floor B2	AFF
AFMM 3	73602	1	3	Cask floor B3	AFF
CMM 1	60349	2	1	Lower Trunnion at 180o side	CM
CMM 2	73600	2	2	Upper Trunnion at 180o side	CM
CMM 3	73604	2	3	Lower Trunnion at 0o side	CM

#### **Test Procedure 9**

Sensor	Serial #	ADC box	ADC channel	Location	Mo
FMM 1	lw 211616	1,2	0,0	Source - Upper Trunnion at 180 ° face	FMI
AFMM 1	73598	1	1	Top Rim C1	FMI
AFMM 2	73596	1	2	Top Rim C2	FMI
AFMM 3	73602	1	3	Top Rim C3	FMI
CMM 1	73600	2	1	Lower Trunnion at 180o face	CM
CMM 2	73604	2	2	Upper Trunnion at 0o face	CM
CMM 3	60349	2	3	Lower Trunnion at 0o face	CM

#### **Test Procedure 10**

Sensor	Serial #	ADC box	ADC channel	Location	Mo
FMM 1	lw 211616	1,2	0,0	Source - Lower Trunnion at 180 ° face	FMI
AFMM 1	73598	1	1	Top Rim C1	FMI
AFMM 2	73596	1	2	Top Rim C2	FMI
AFMM 3	73602	1	3	Top Rim C3	FMI
CMM 1	73600	2	1	Upper Trunnion at 180o face	CM
CMM 2	73604	2	2	Upper Trunnion at 0o face	CM
CMM 3	60349	2	3	Lower Trunnion at 0o face	CM

#### **Test Procedure 11**

Sensor	Serial #	ADC box	ADC channel	Location	Mo
FMM 1	lw 211616	1,2	0,0	Source - Upper Trunnion at 180 ° face	FMI
AFMM 1	73598	1	1	Bottom Rim D1	FMI
AFMM 2	73596	1	2	Bottom Rim D2	FMI
AFMM 3	73602	1	3	Bottom Rim D3	FMI
CMM 1	73600	2	1	Lower Trunnion at 180o face	CM

CMM 2	73604	2	2	Upper Trunnion at 0o face	CM
CMM 3	60349	2	3	Lower Trunnion at 0o face	CM

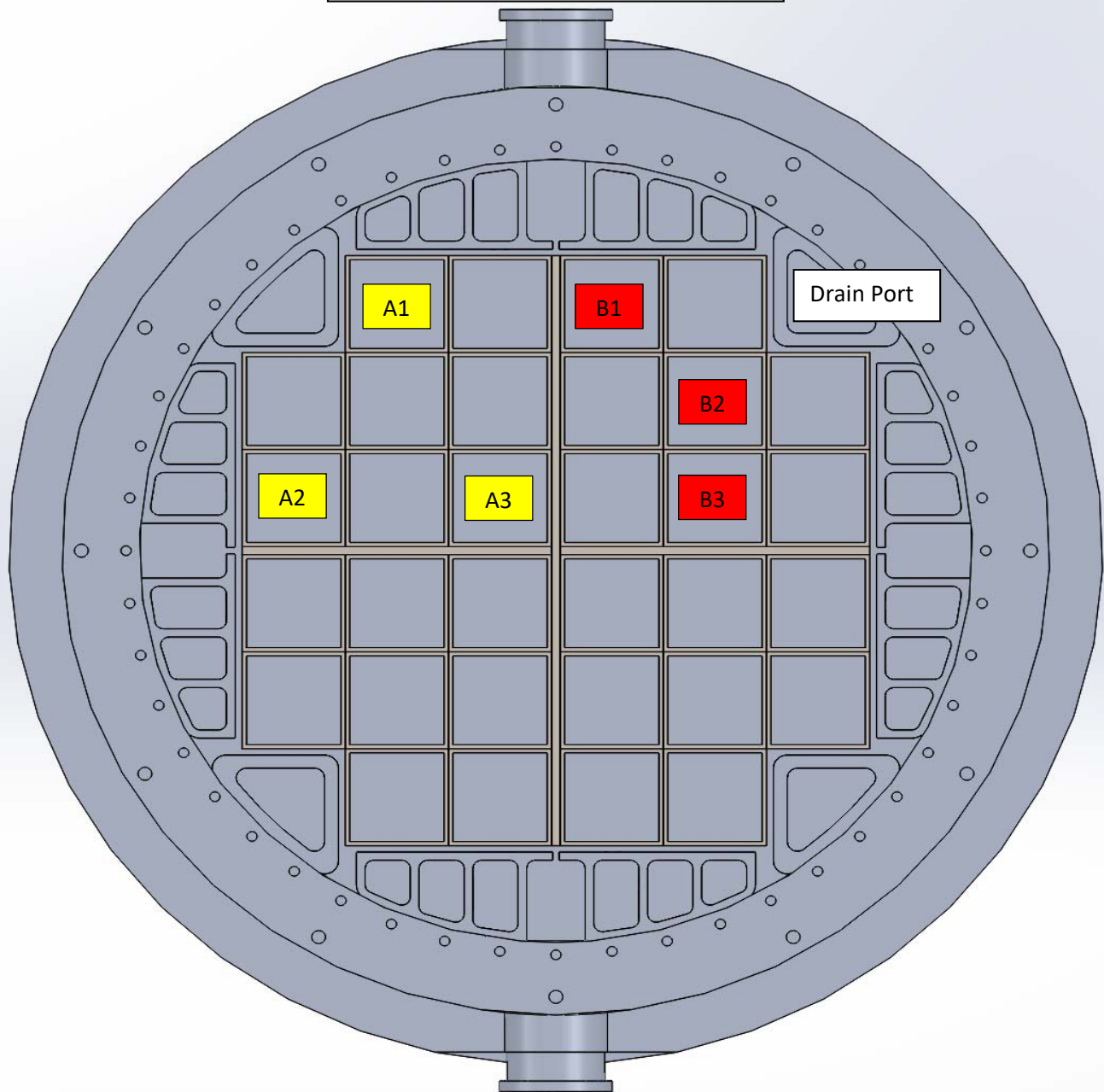
#### **Test Procedure 12**

Sensor	Serial #	ADC box	ADC channel	Location	Mo
FMM 1	lw 211616	1,2	0,0	Source - Lower Trunnion at 180° face	FMI
AFMM 1	73598	1	1	Bottom Rim D1	FMI
AFMM 2	73596	1	2	Bottom Rim D2	FMI
AFMM 3	73602	1	3	Bottom Rim D3	FMI
CMM 1	73600	2	1	Upper Trunnion at 180o face	CM
CMM 2	73604	2	2	Upper Trunnion at 0o face	CM
CMM 3	60349	2	3	Lower Trunnion at 0o face	CM

#### **Test Procedure 13**

Sensor	Serial #	ADC box	ADC channel	Location	Mo
FMM 1	lw 211616	1,2	0,0	Source - Lower Trunnion at 180° face	FMI
AFMM 1	73598	1	1	Shell Skin	FMI
AFMM 2	73596	1	2	Shell Skin	FMI
AFMM 3	73602	1	3	Shell Skin	FMI
CMM 1	73600	2	1	Upper Trunnion at 180o face	CM
CMM 2	73604	2	2	Upper Trunnion at 0o face	CM
CMM 3	60349	2	3	Lower Trunnion at 0o face	CM

Lower Trunnion, Upper Trunnion - 0°



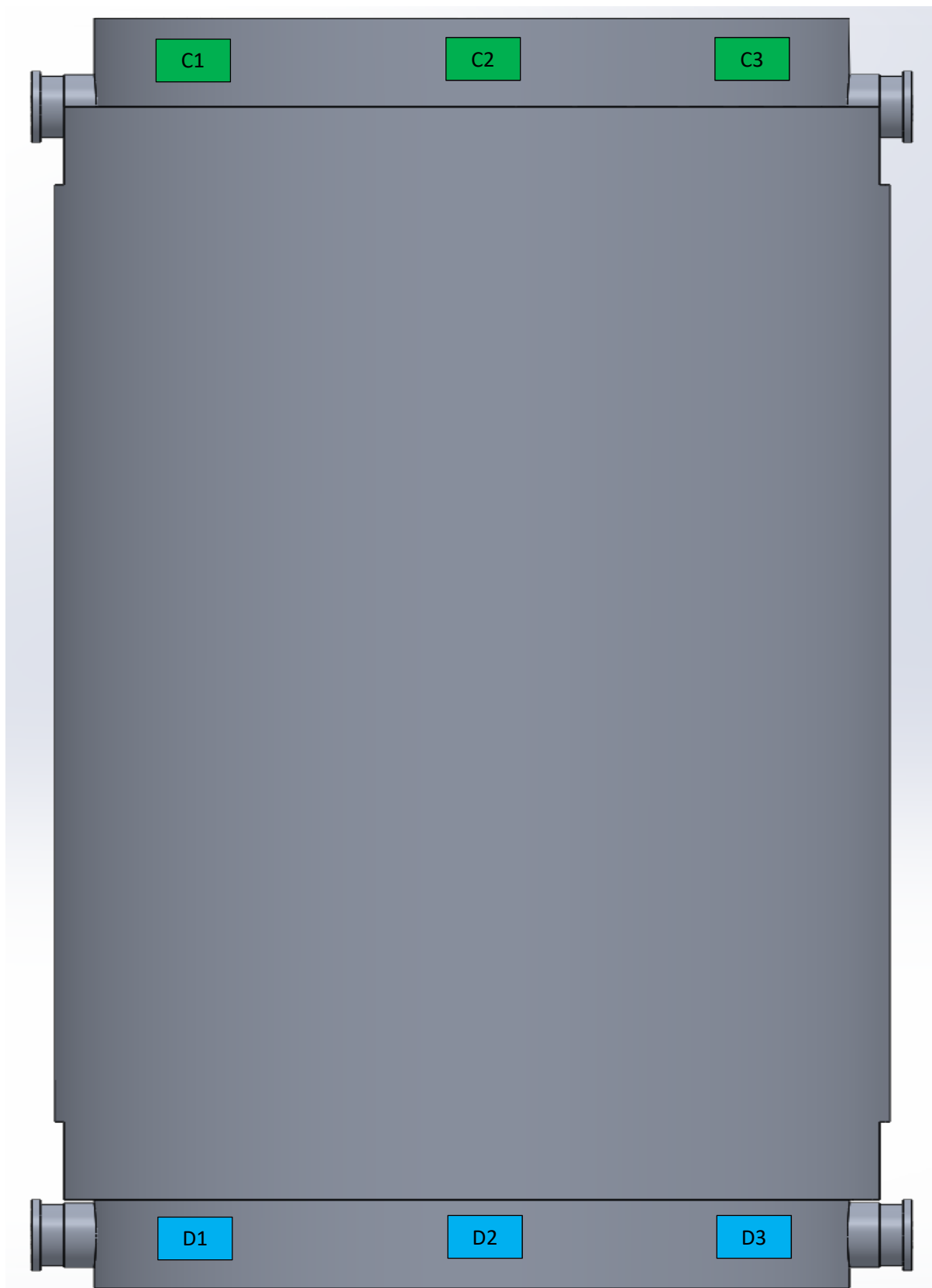
Drain Port

Lower Trunnion, Upper Trunnion - 180°



Upper Trunnion - 180°

Upper Trunnion - 0°



Lower Trunnion - 180°

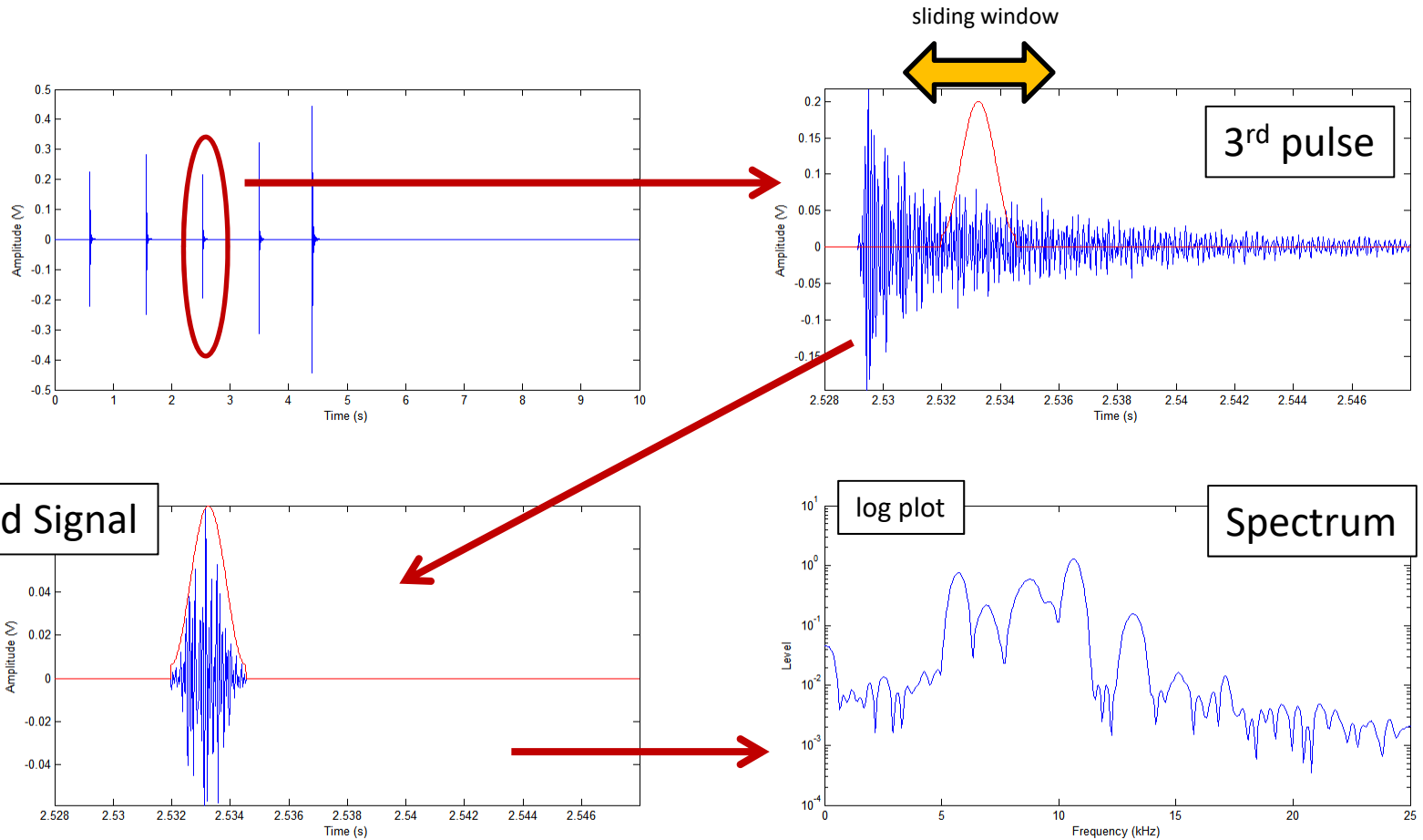
Lower Trunnion - 0°

# Time-Frequency Analysis of Impulse Data from CHT Study (9/29/16)

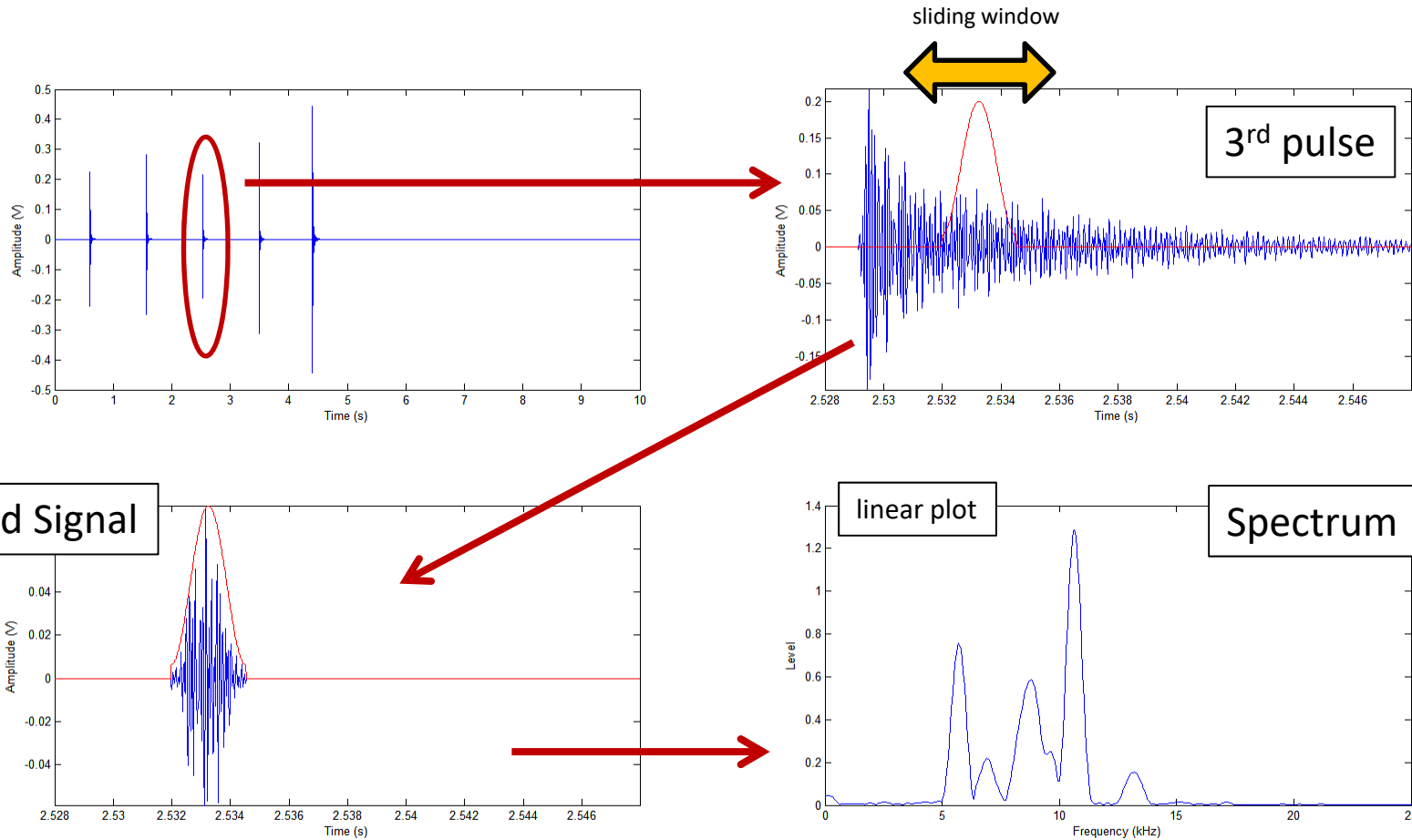
# Time Frequency Analysis of CHT Data

- Contains data from selected runs
  - Analyzed the 3<sup>rd</sup> signal in each set
- The time frequency analysis:
  - four settings
    - Range: Best frequency resolution to best time resolution
  - All four are shown for each sensor
  - Calculated using MATLAB's 'spectrogram' cmd
    - x-axis is Frequency (0-25 kHz)
    - y-axis is Time (0-200 ms)

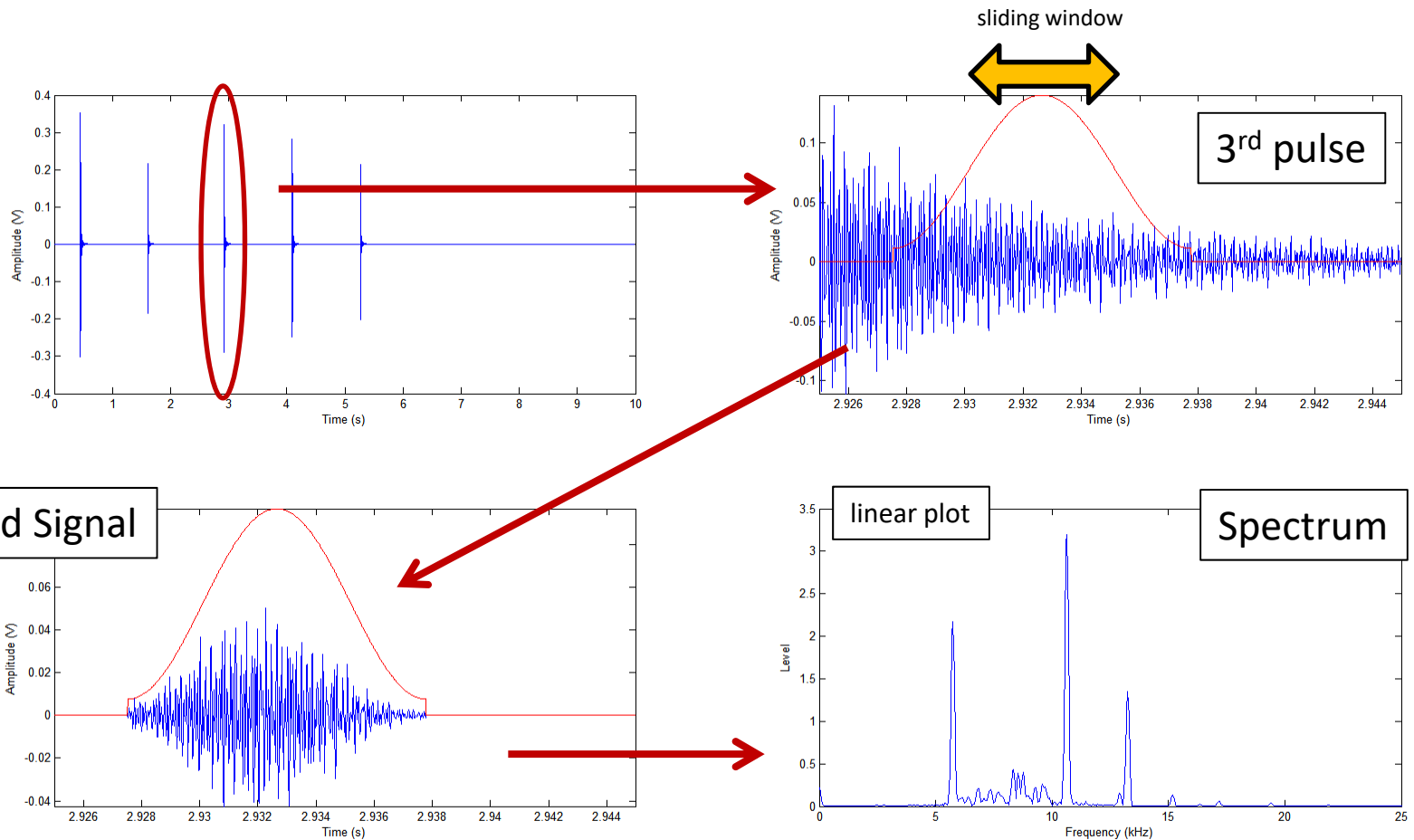
# From Signal to Spectrum



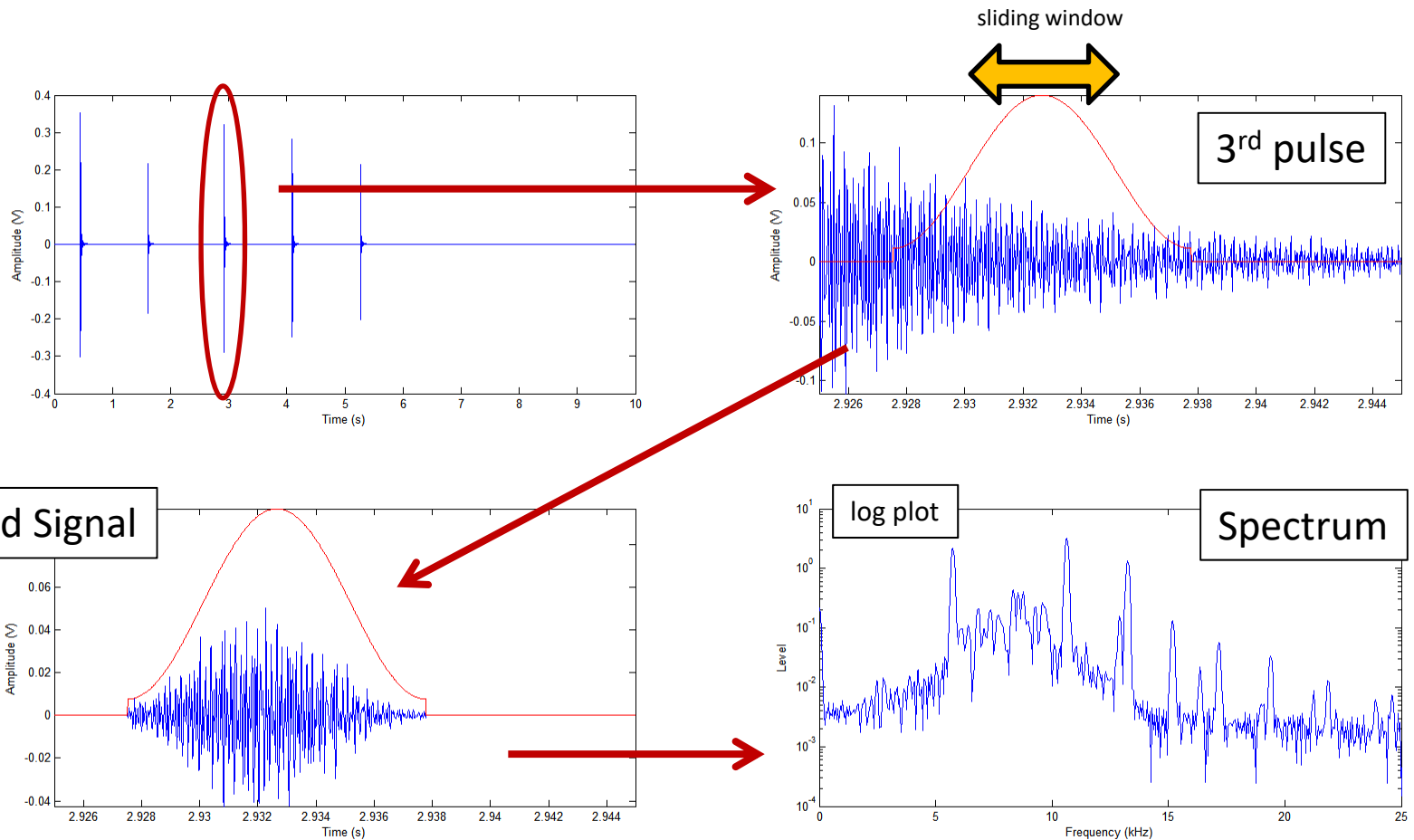
# From Signal to Spectrum



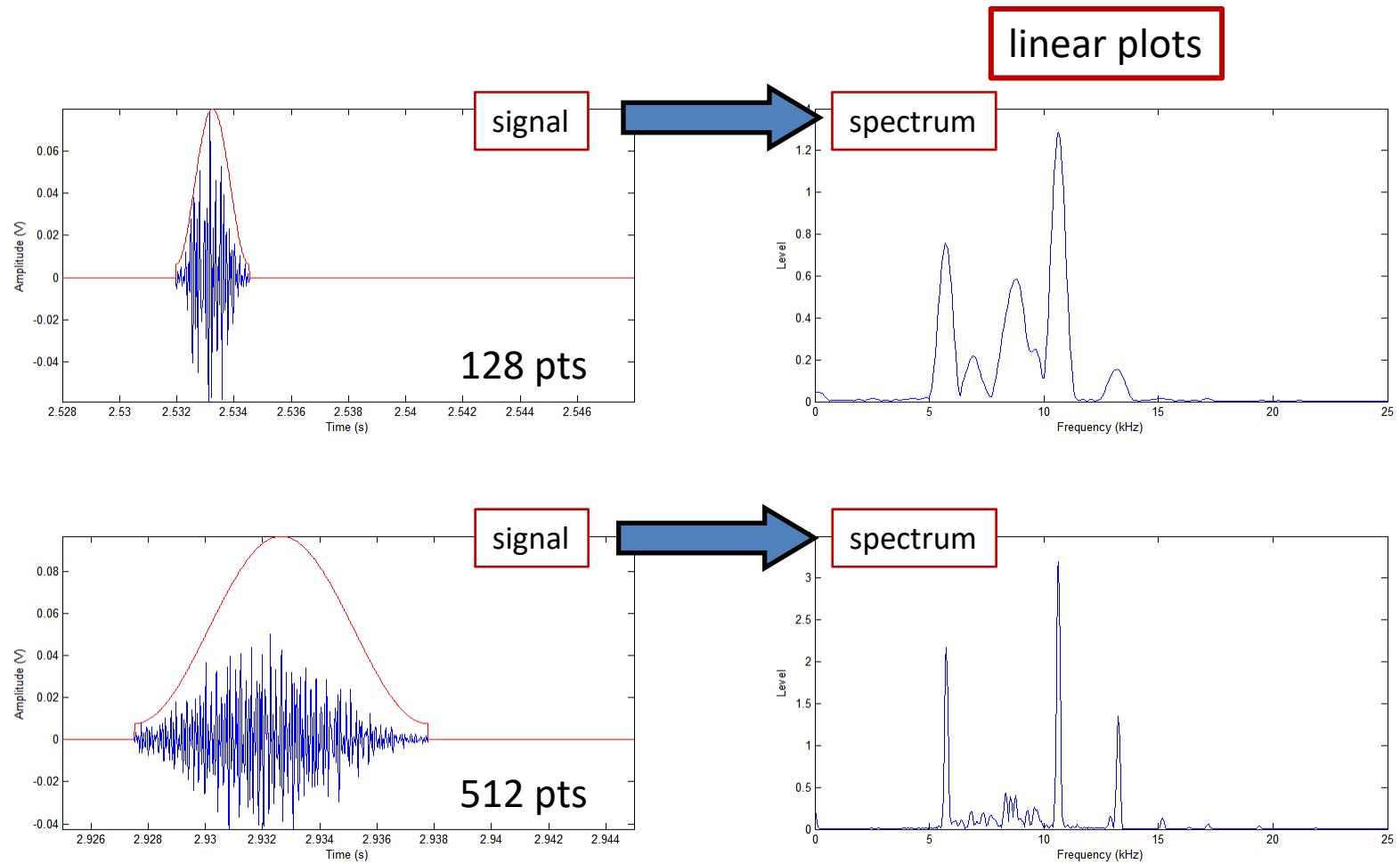
# From Signal to Spectrum (wider gate)



# From Signal to Spectrum (wider gate)

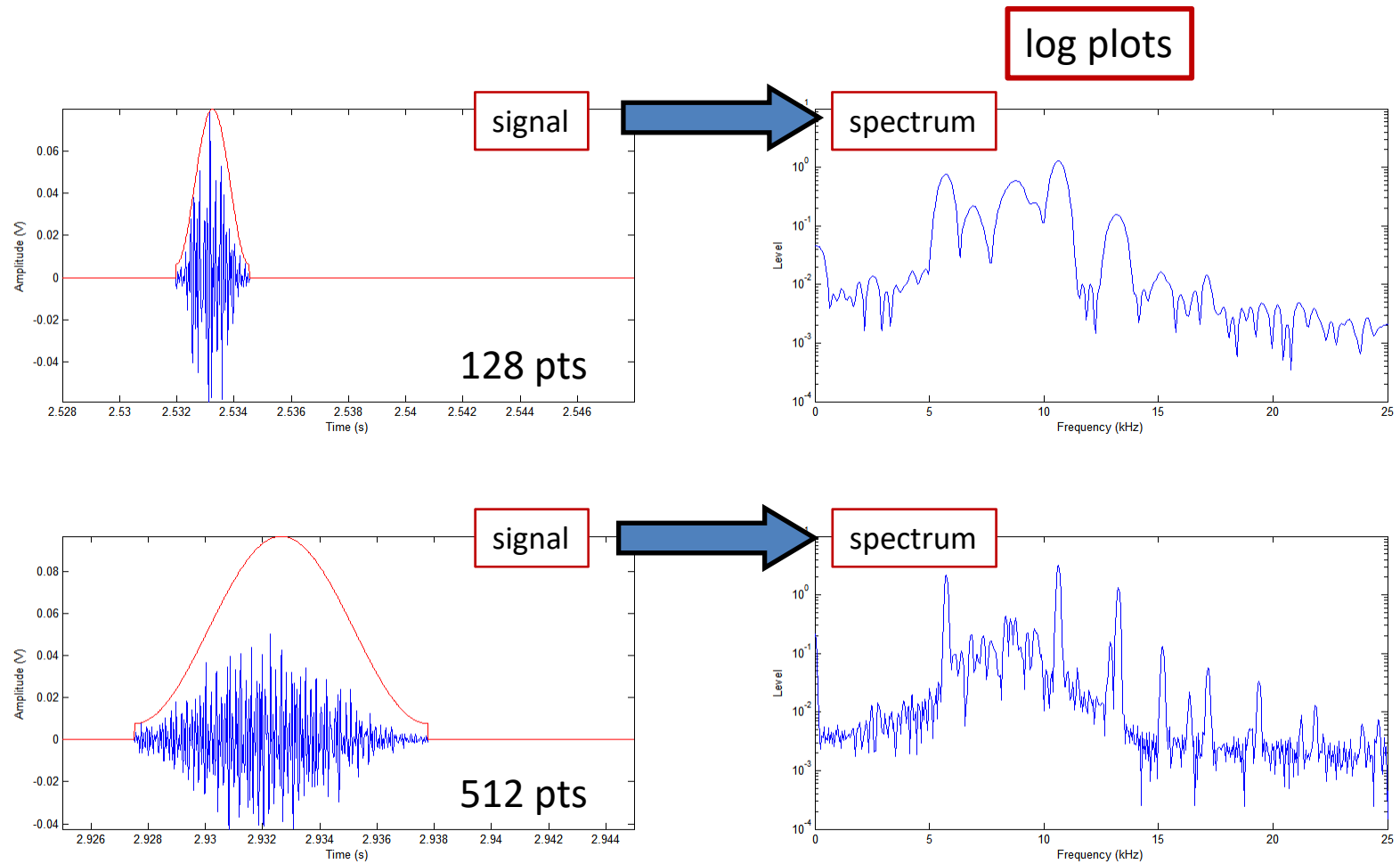


# Effect of gate length on spectra



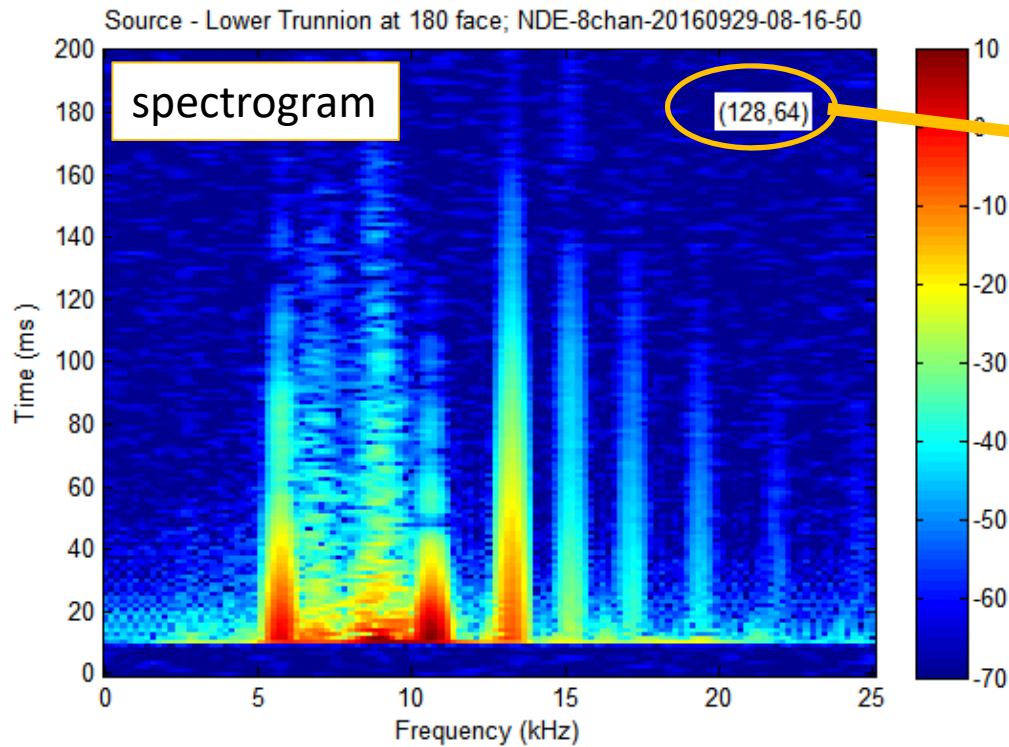
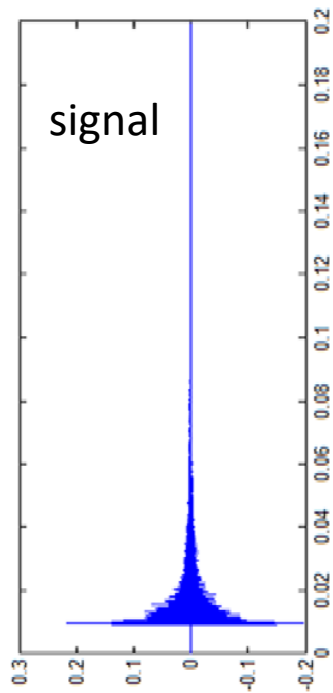


# Effect of gate length on spectra



# Example

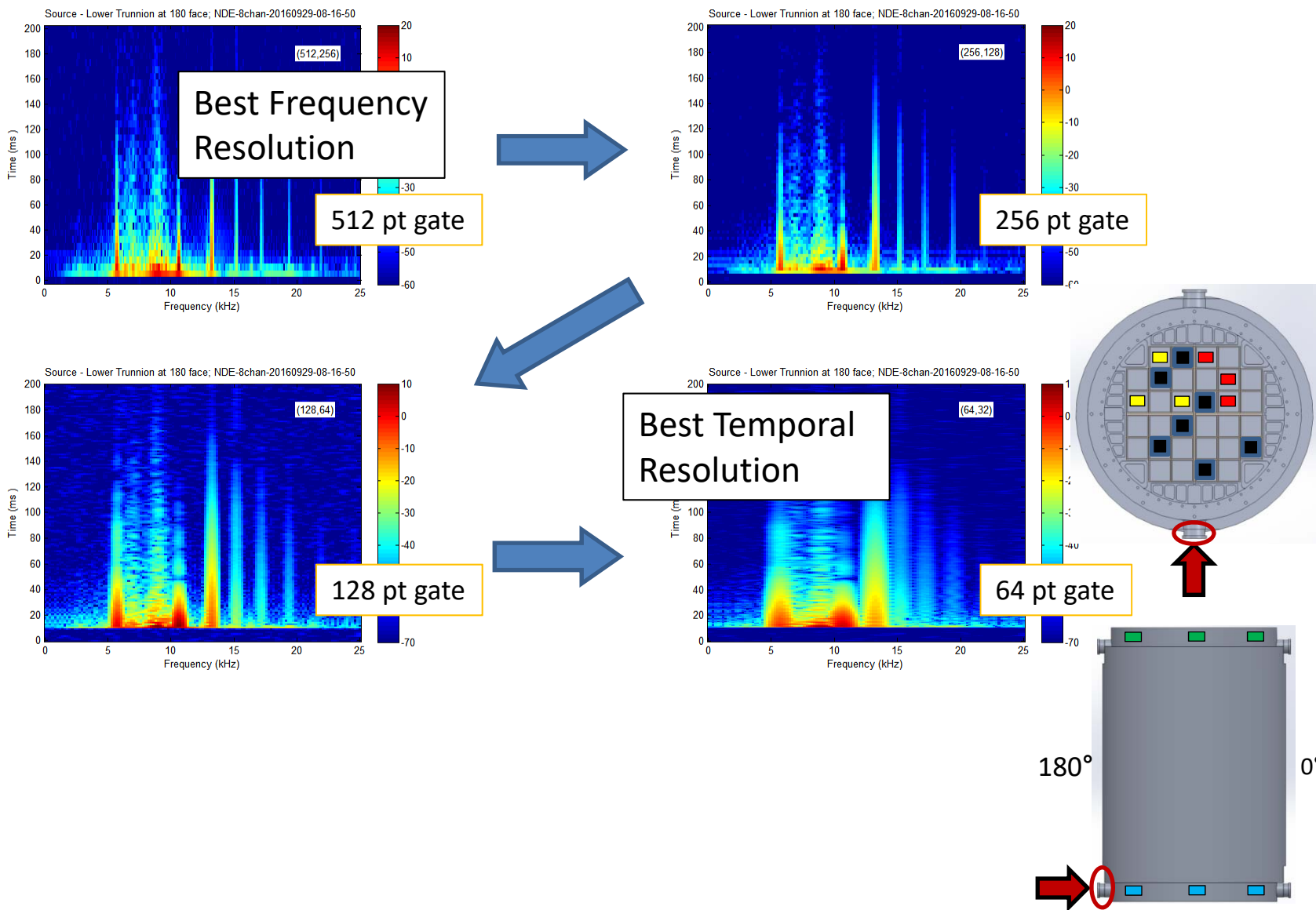
Color scale is in dB



128-point window

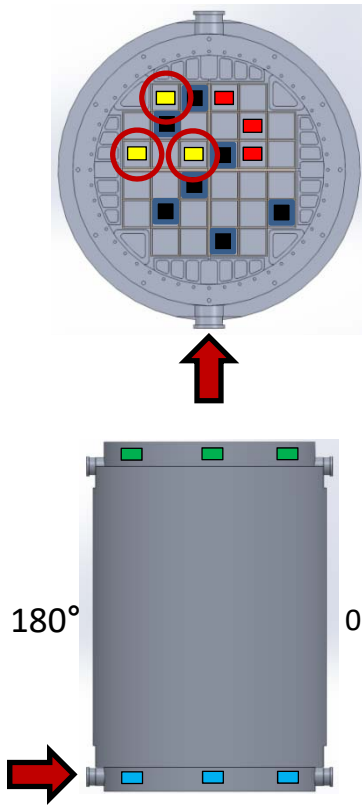
64-point overlap with adjacent windows for sliding gate

# Guide to the Figures

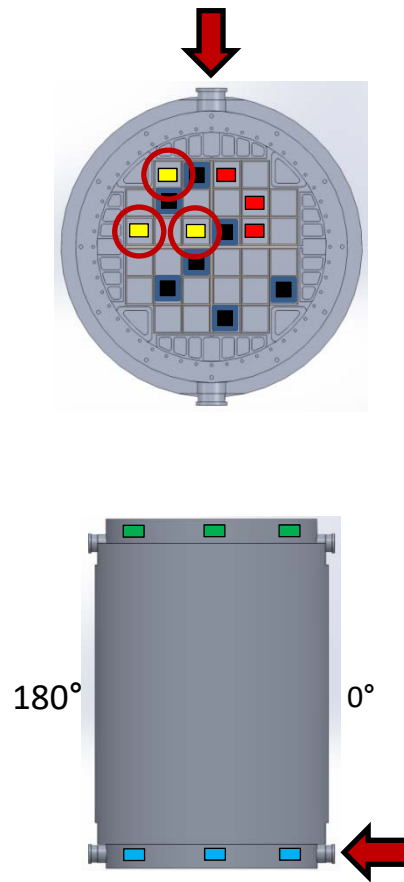


# Test Plans 1-4

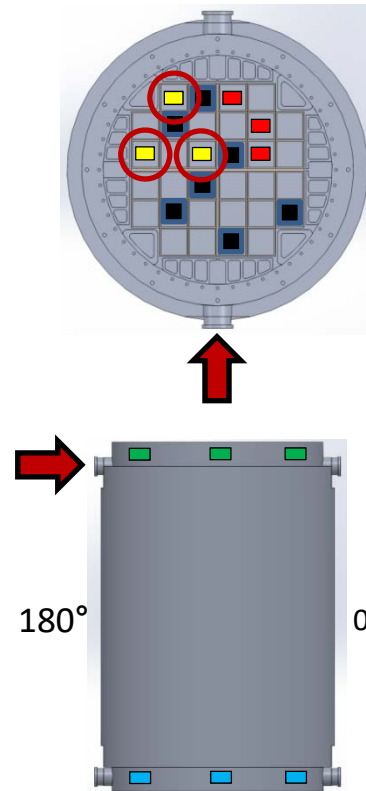
TP 01  
R01,02



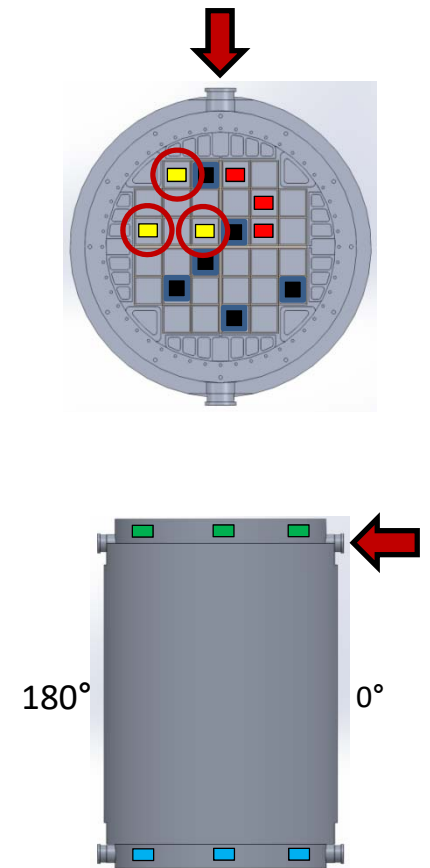
TP 02  
R03,04



TP 03  
R05,06

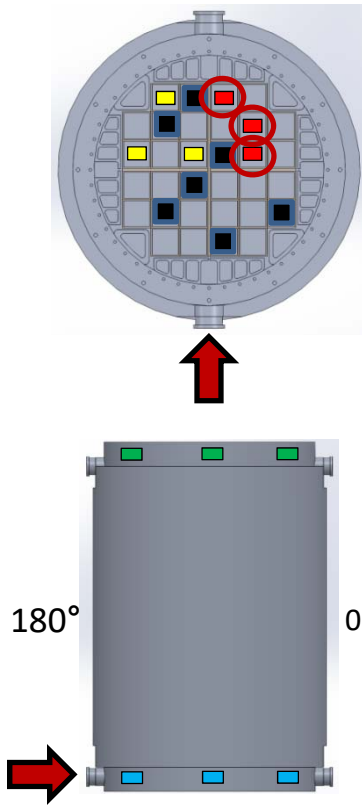


TP 04  
R07,08

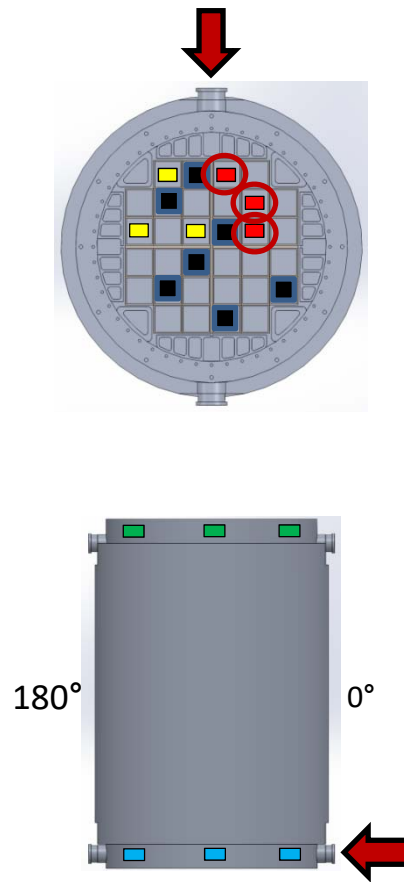


# Test Plans 5-8

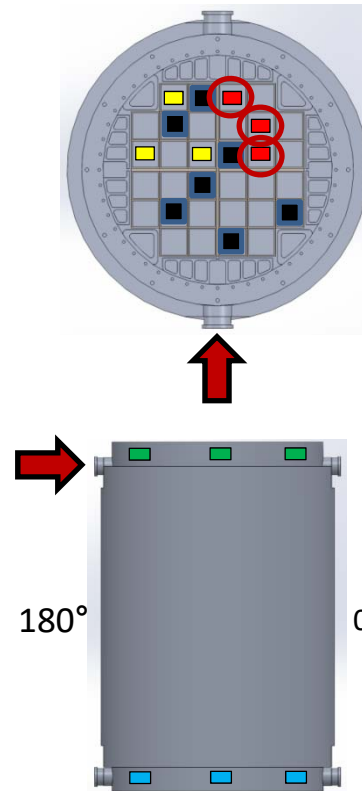
TP 05  
R09,10



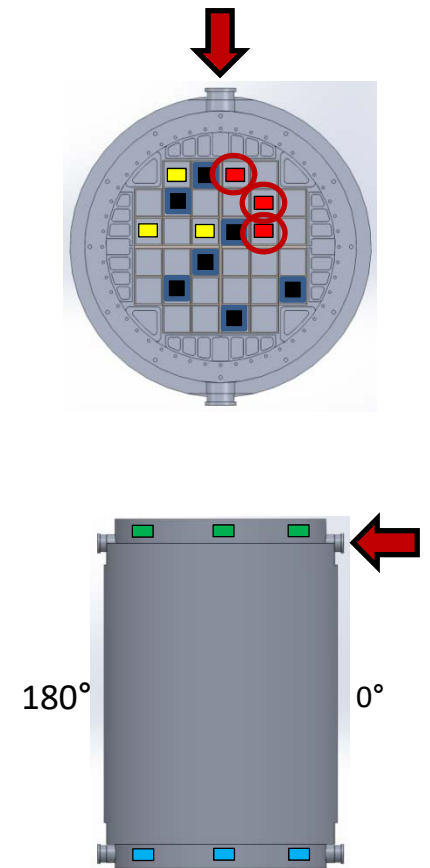
TP 06  
R11,12



TP 07  
R13,14

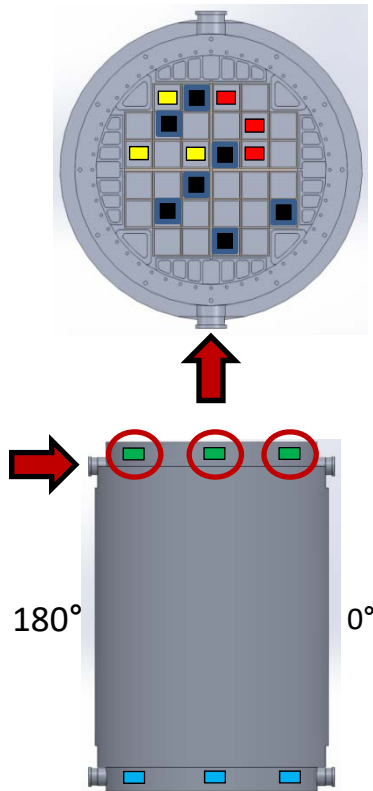


TP 08  
R15,16

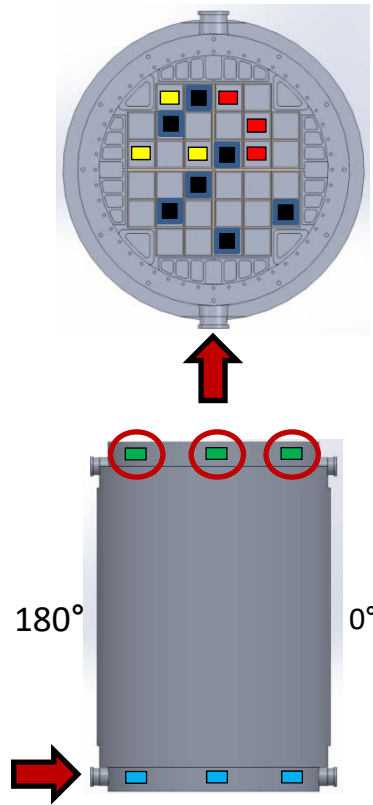


# Test Plans 9-12

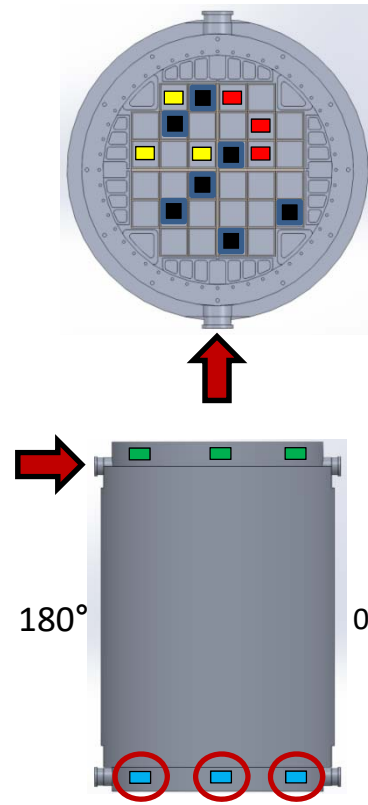
TP 09  
R17,18



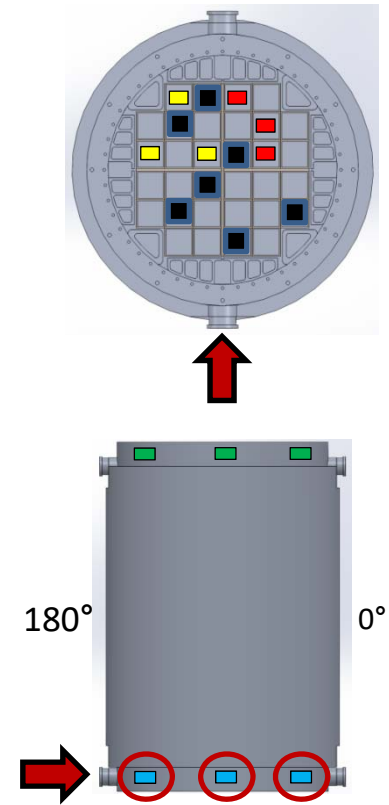
TP 10  
R19,20



TP 11  
R21,22

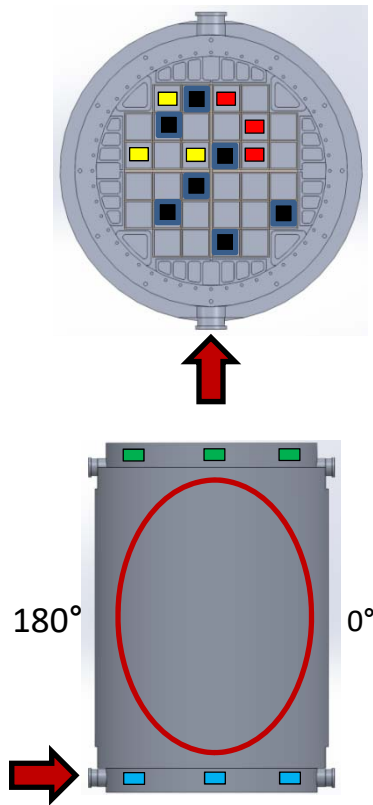


TP 12  
R23,24



# Test Plan 13

TP 13  
R25,26



NDE-8chan-20160929-08\_16\_50 Binary.bin

theLabel =

'Source - Lower Trunnion at 180 face'

'Cask floor A1'

'Cask floor A2'

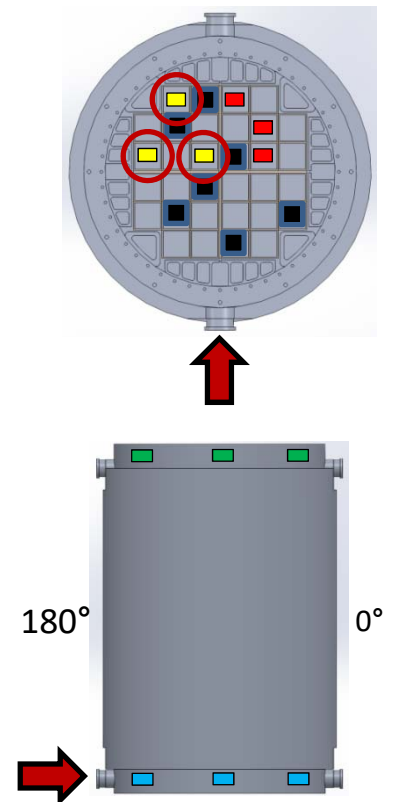
'Cask floor A3'

'Source - Lower Trunnion at 180 face'

'Lower Trunnion at 0 side'

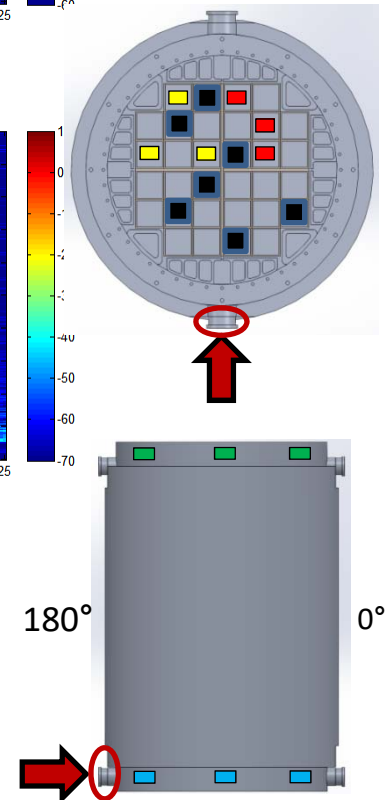
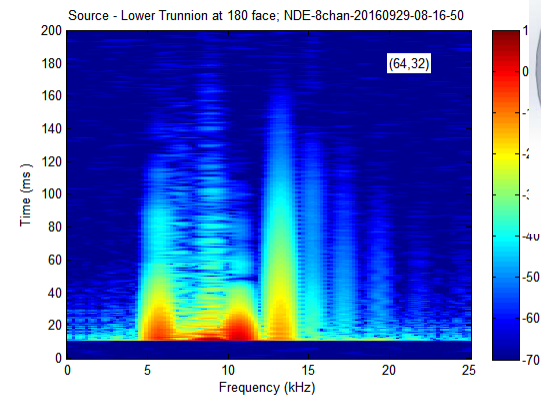
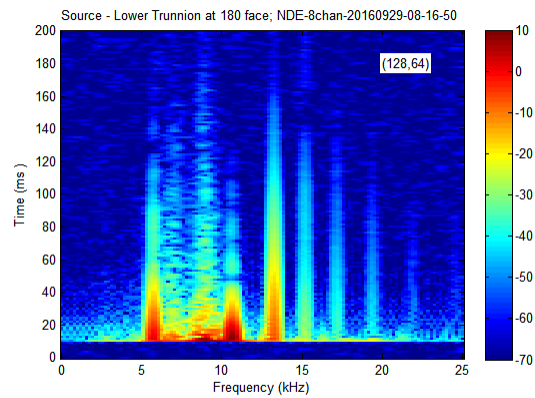
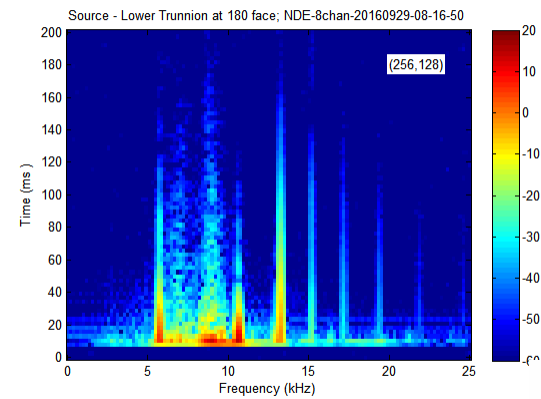
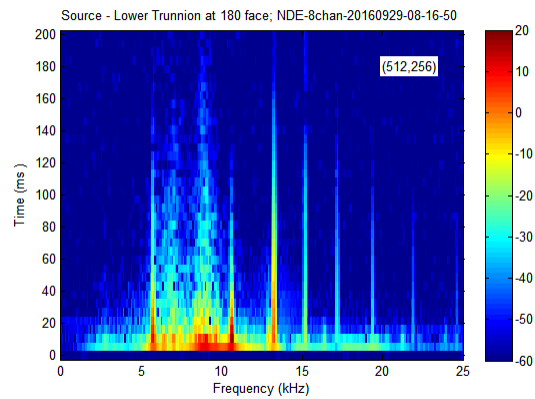
'Upper Trunnion at 180 side'

'Upper Trunnion at 0 side'

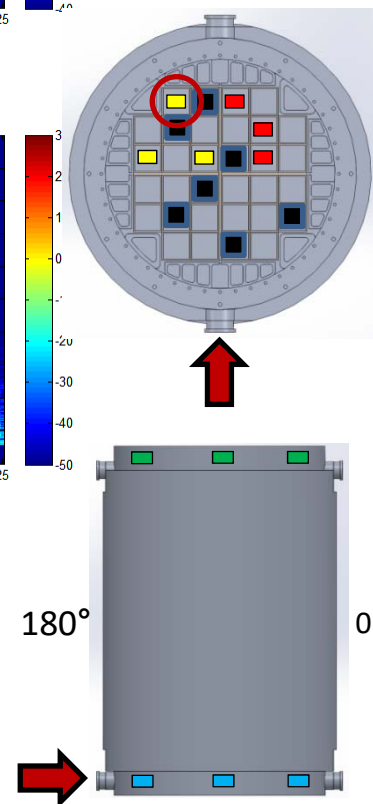
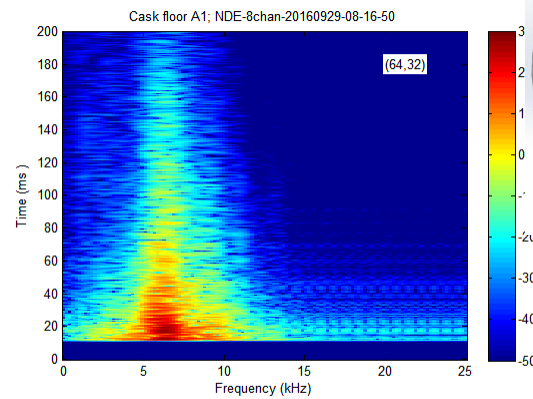
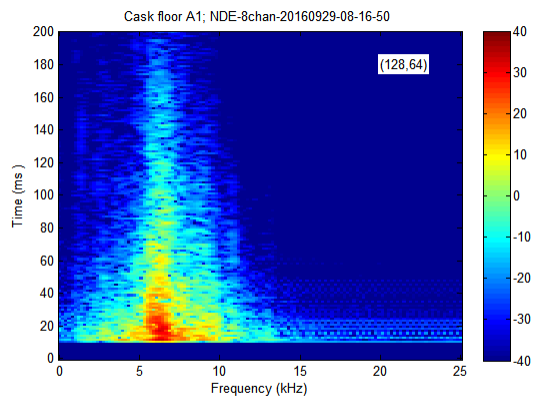
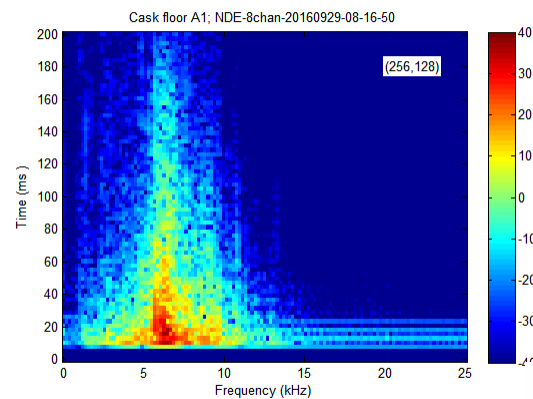
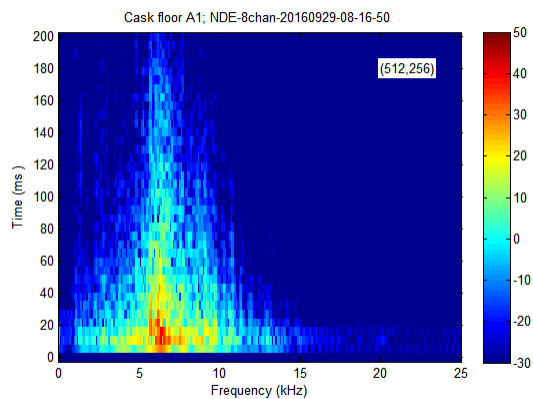




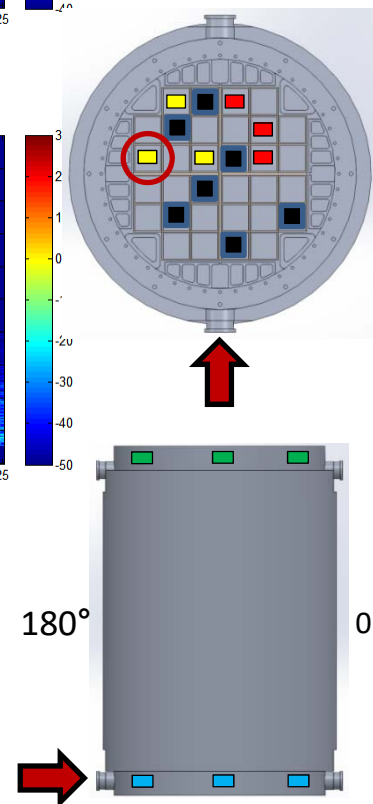
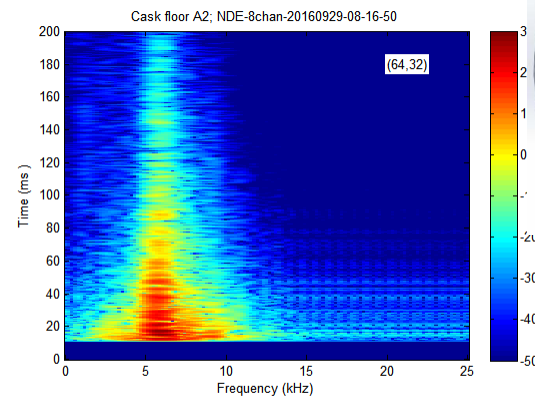
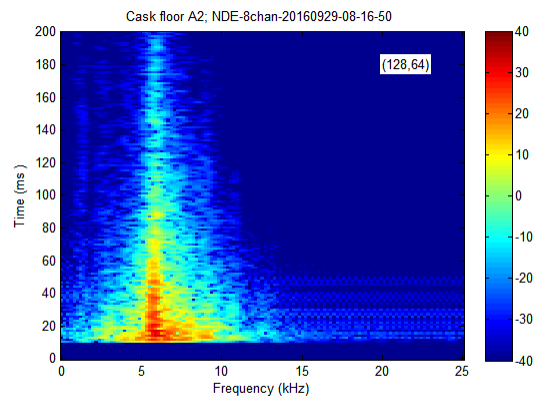
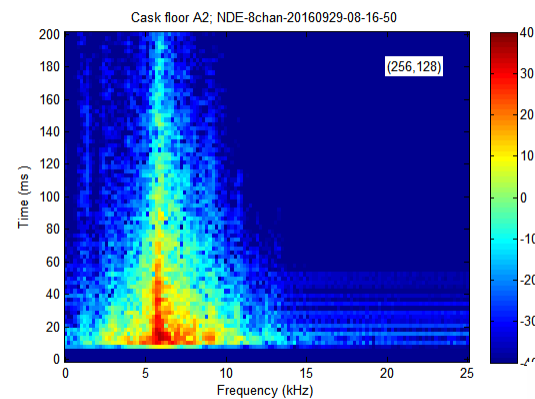
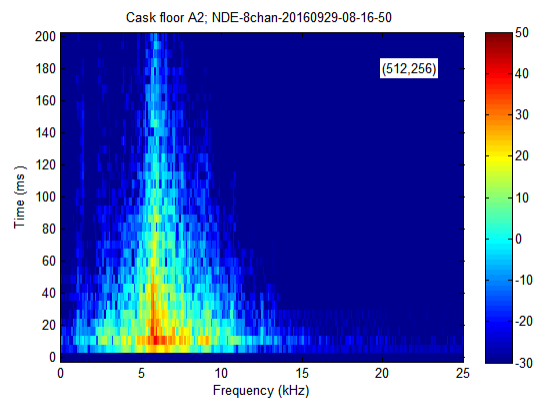
# Trunnion (Low) :Trigger



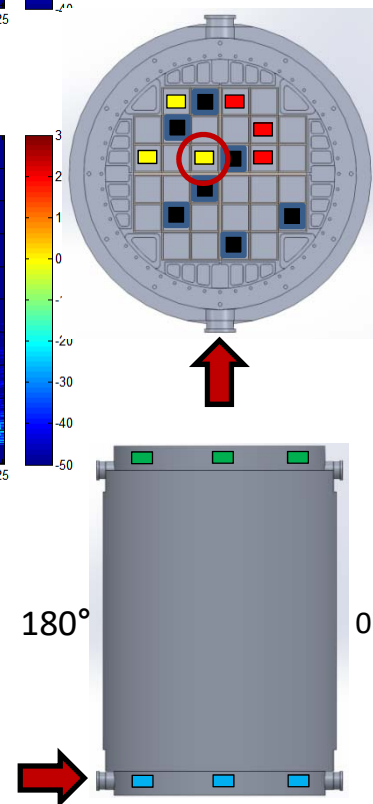
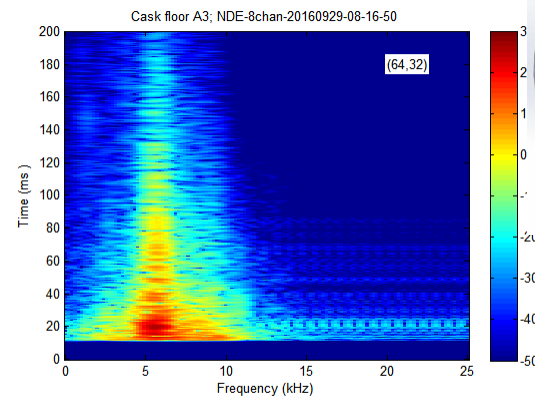
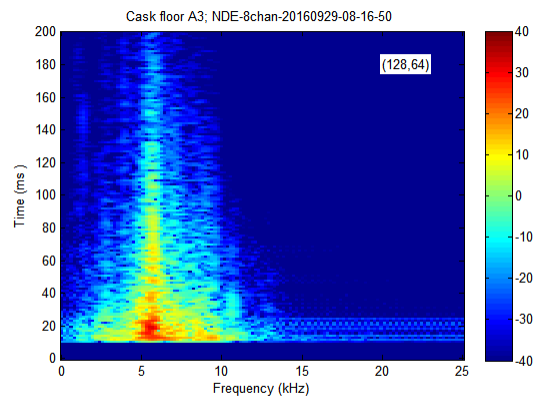
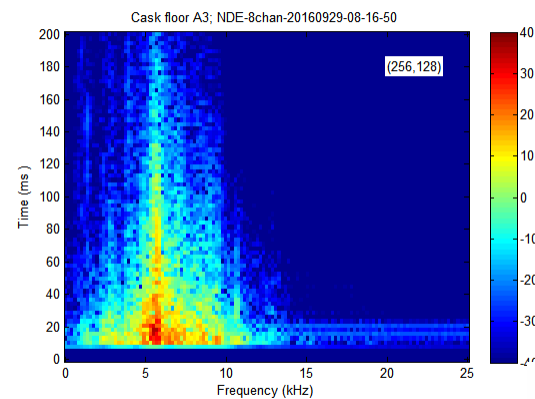
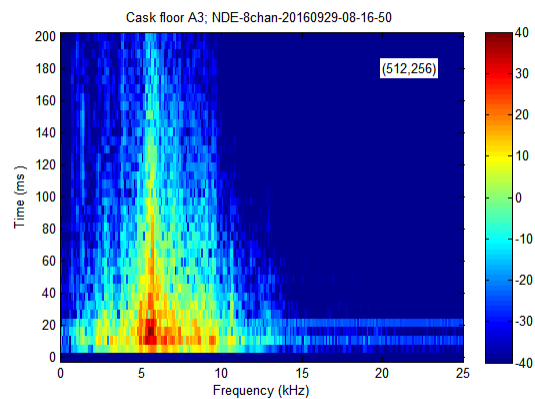
# Floor A1



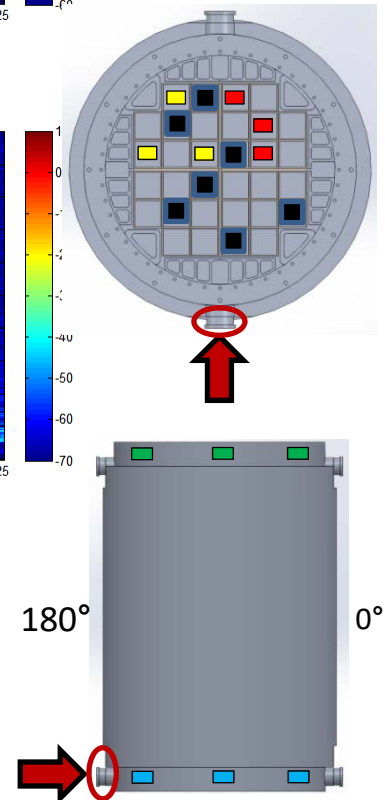
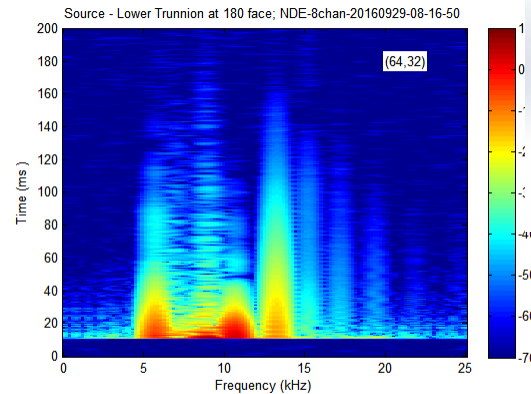
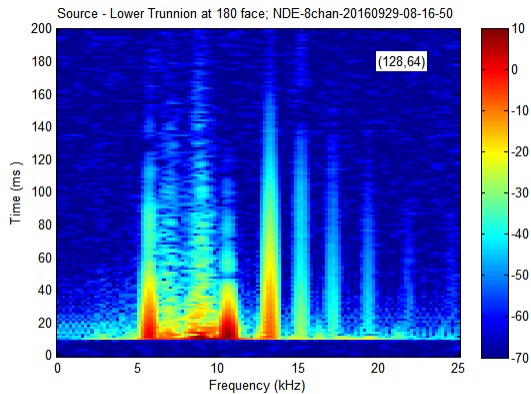
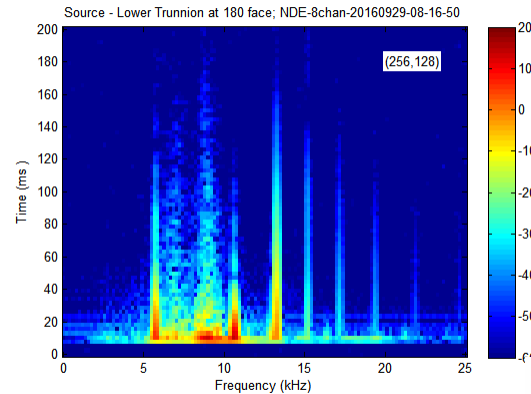
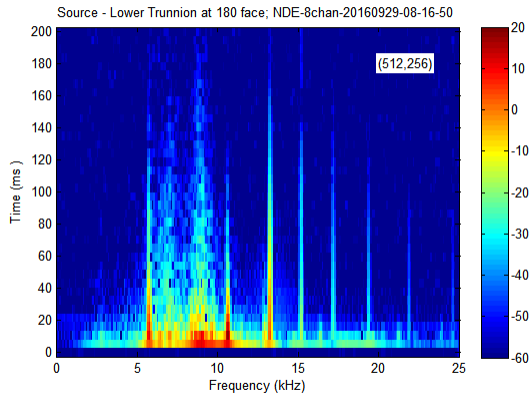
# Floor A2



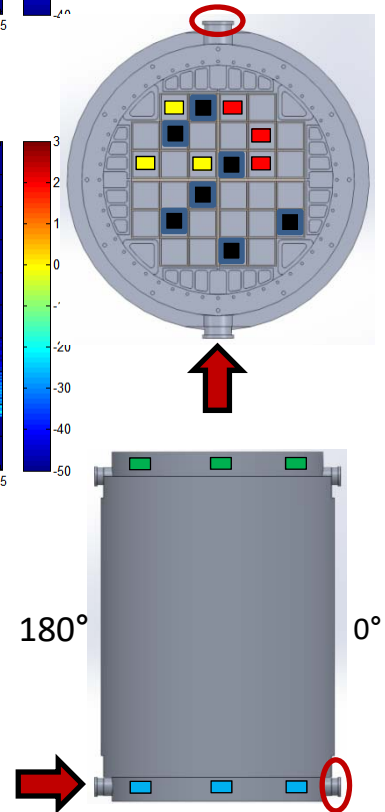
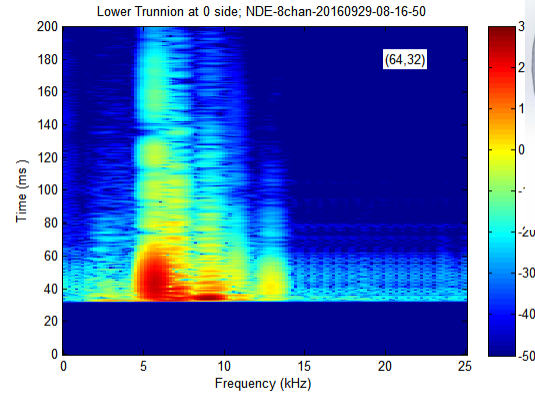
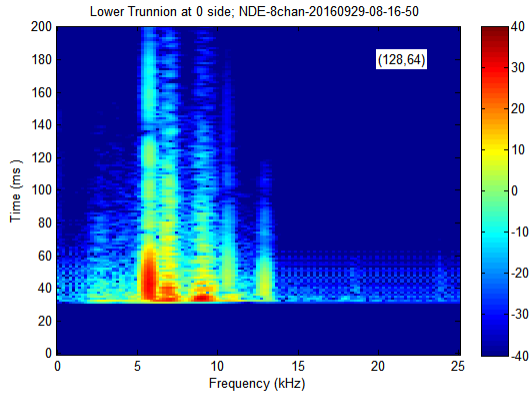
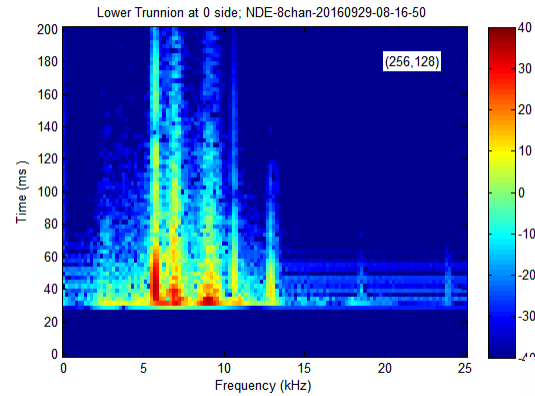
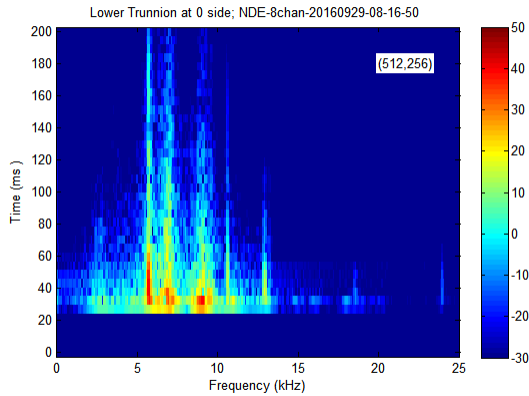
# Floor A3



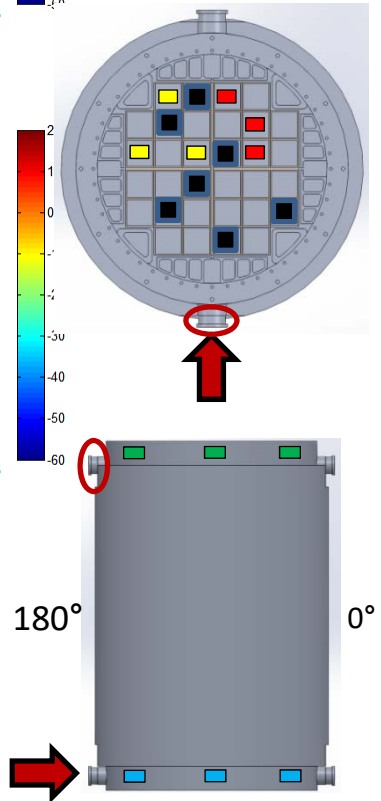
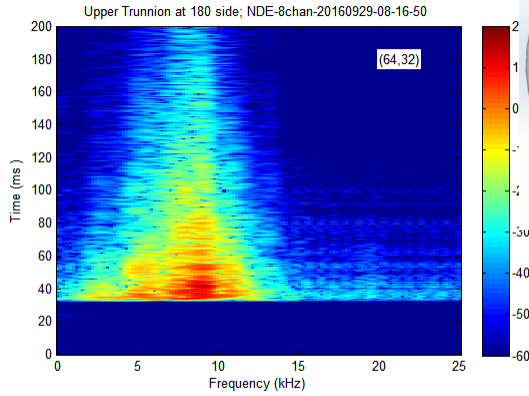
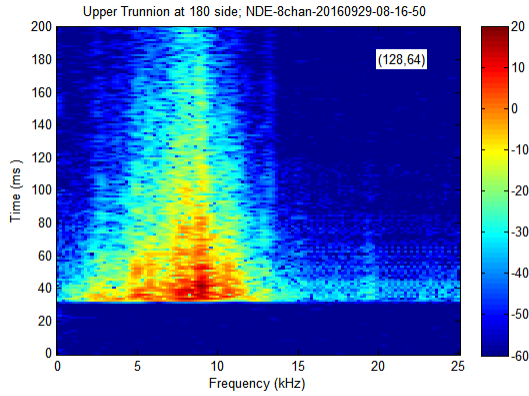
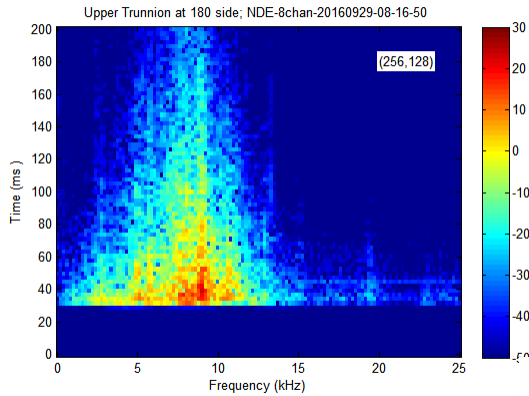
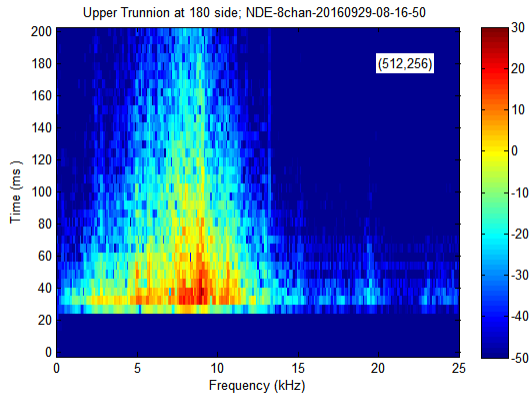
# Trunnion (Low):Trigger (Box 2)



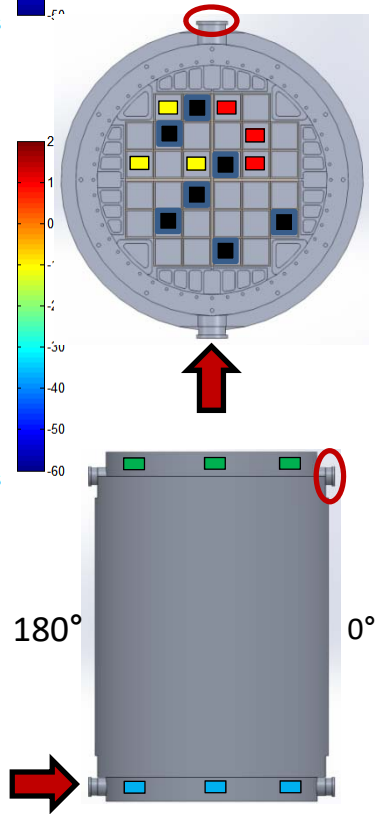
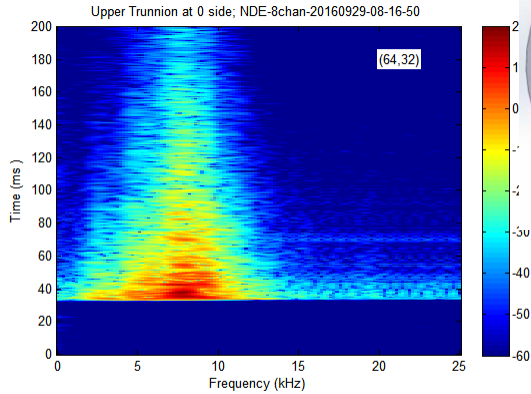
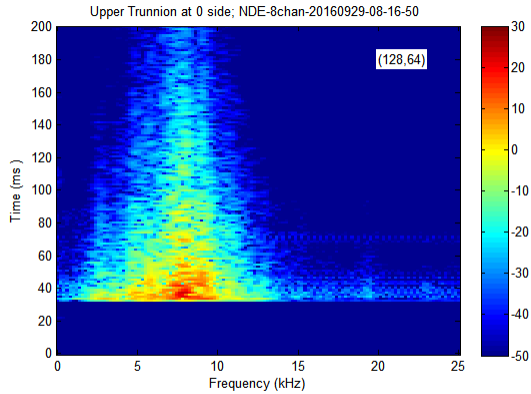
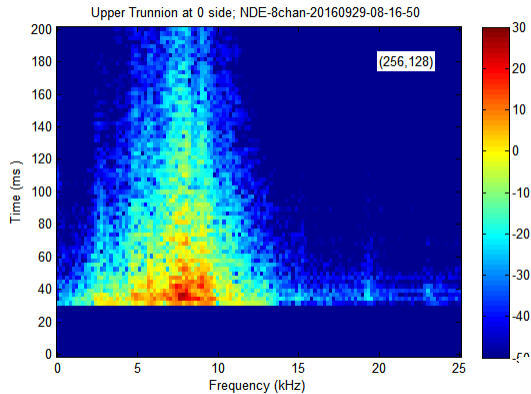
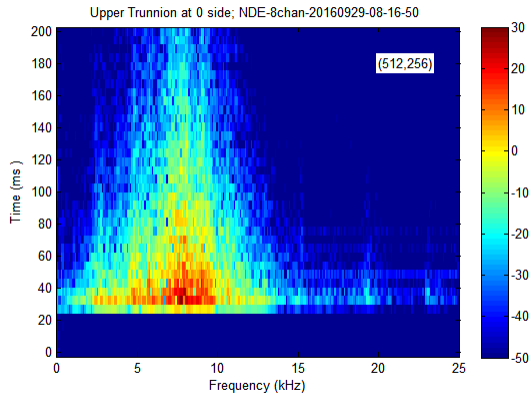
# Trunnion: Proximal



# Trunnion: Same Side



# Trunnion: Distal





NDE-8chan-20160929-08\_17\_44 Binary.bin

theLabel =

'Source - Lower Trunnion at 180 face'

'Cask floor A1'

'Cask floor A2'

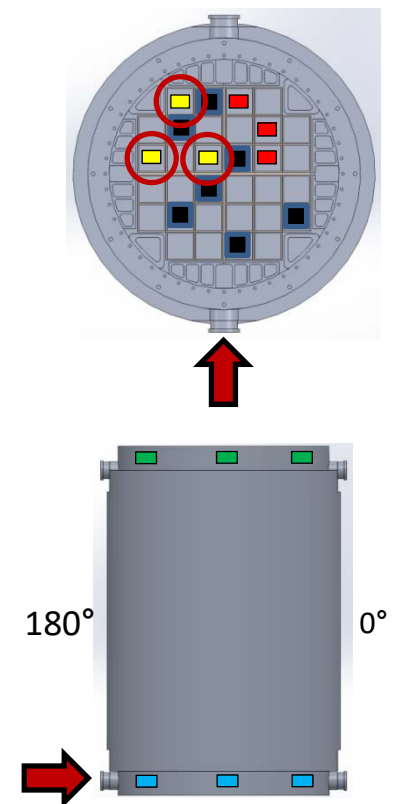
'Cask floor A3'

'Source - Lower Trunnion at 180 face'

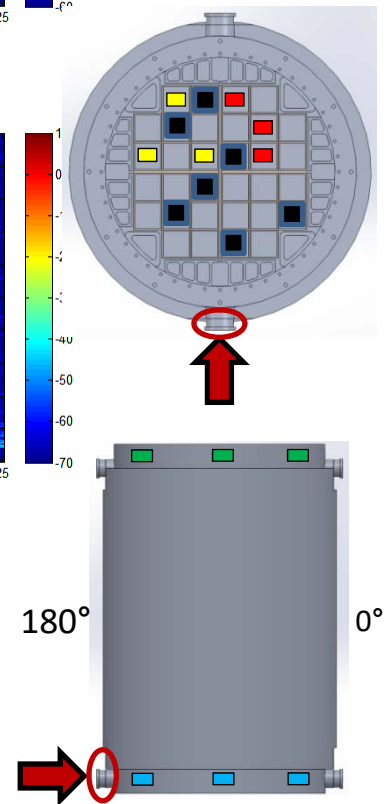
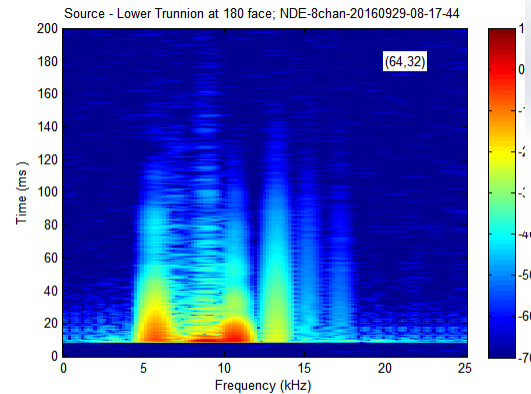
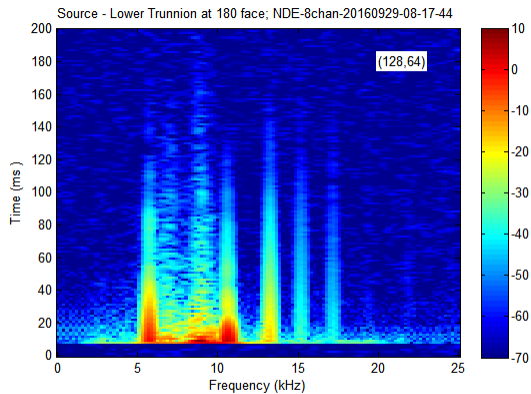
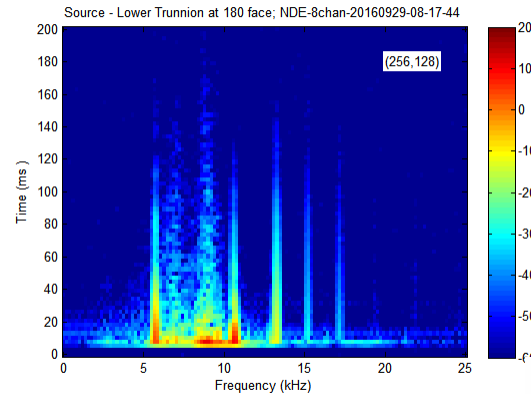
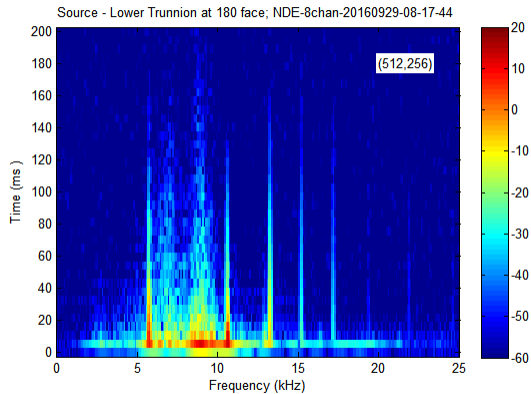
'Lower Trunnion at 0 side'

'Upper Trunnion at 180 side'

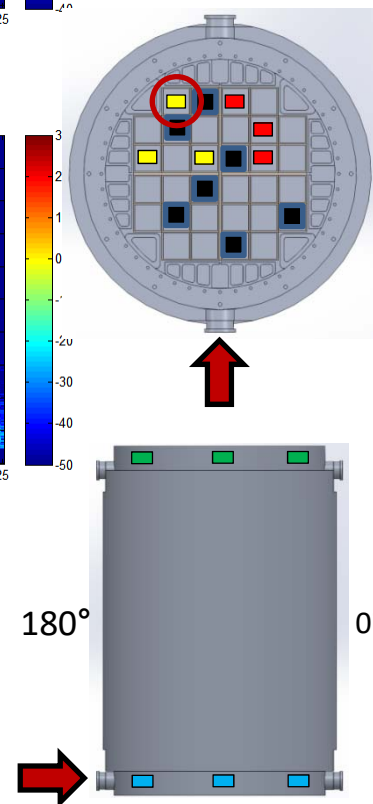
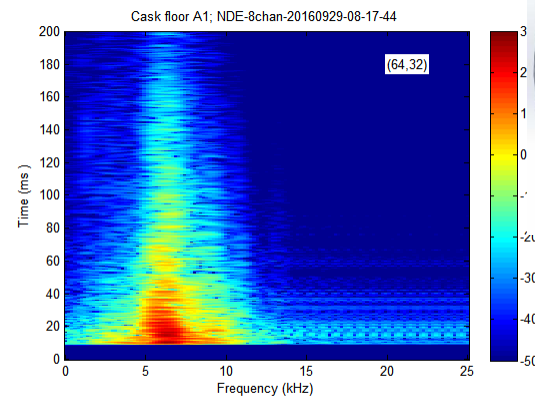
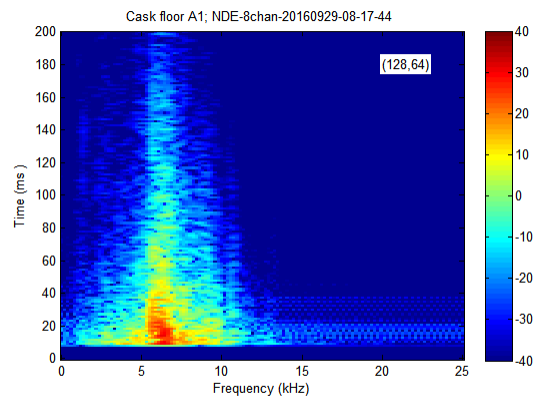
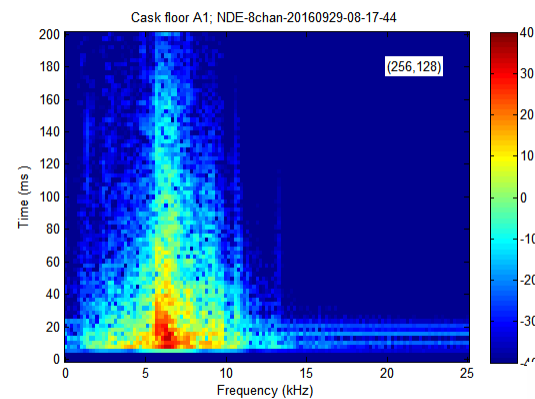
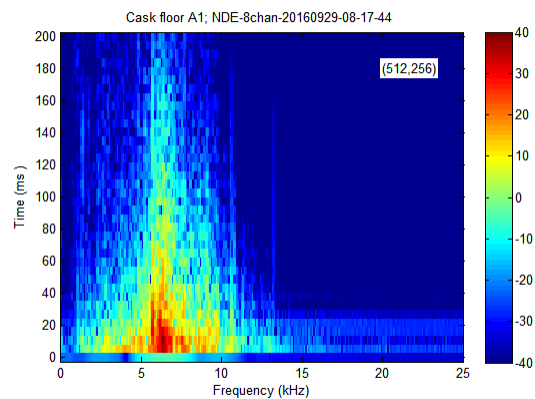
'Upper Trunnion at 0 side'



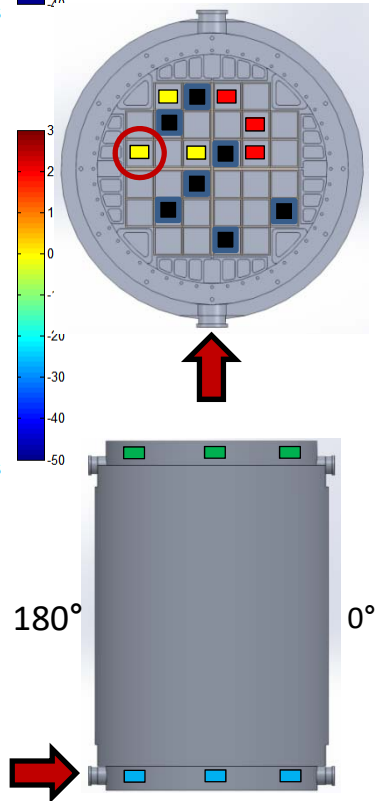
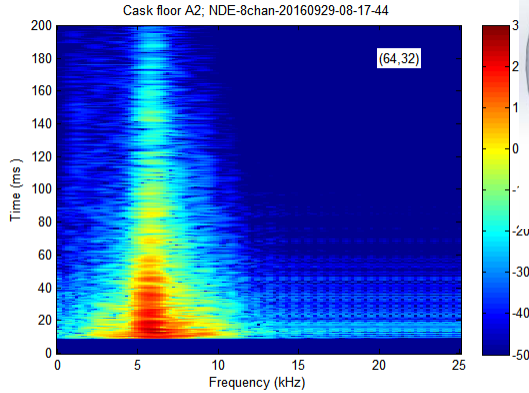
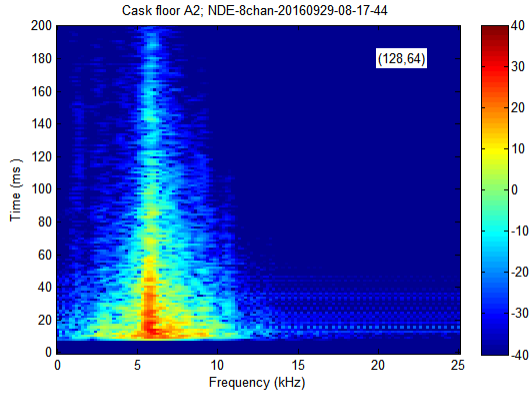
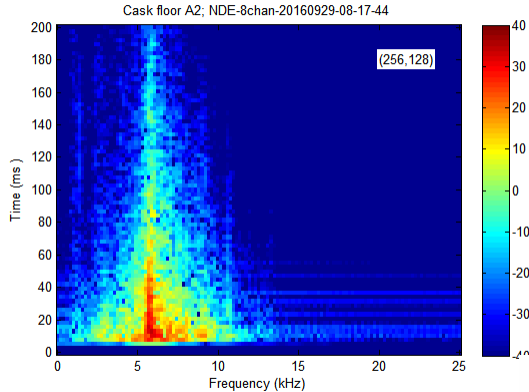
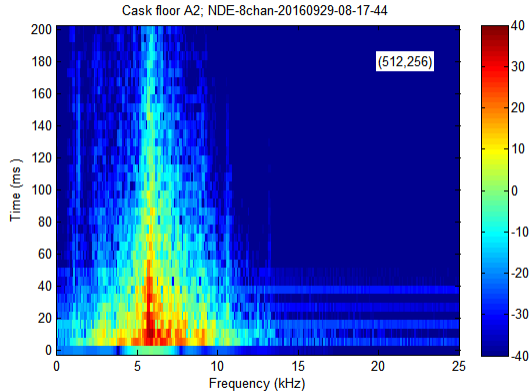
# Trunnion (Low): Trigger



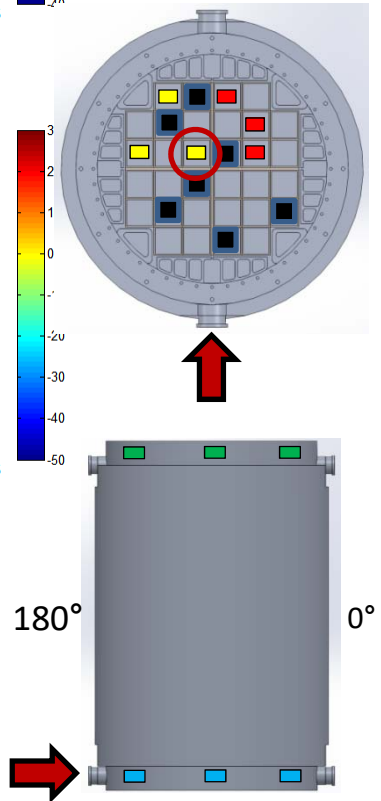
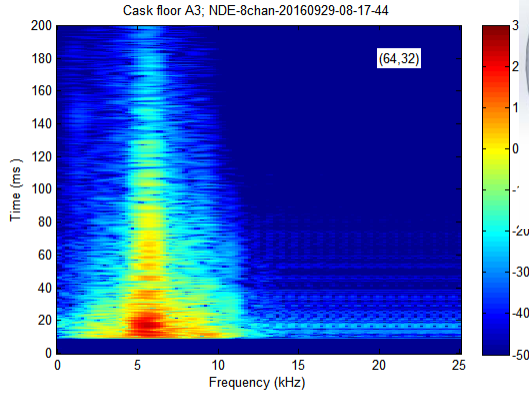
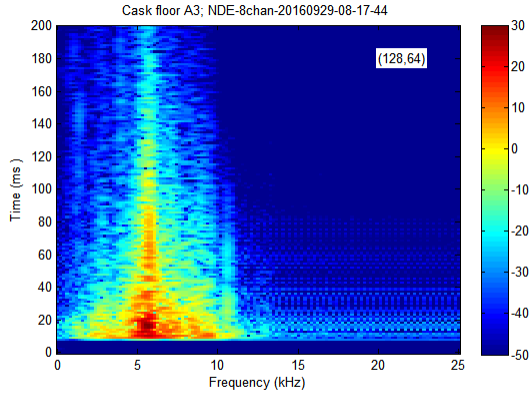
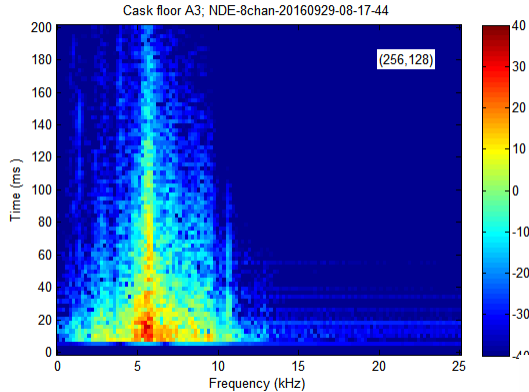
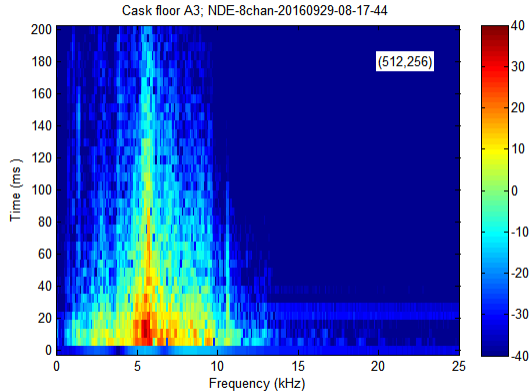
# Floor A1



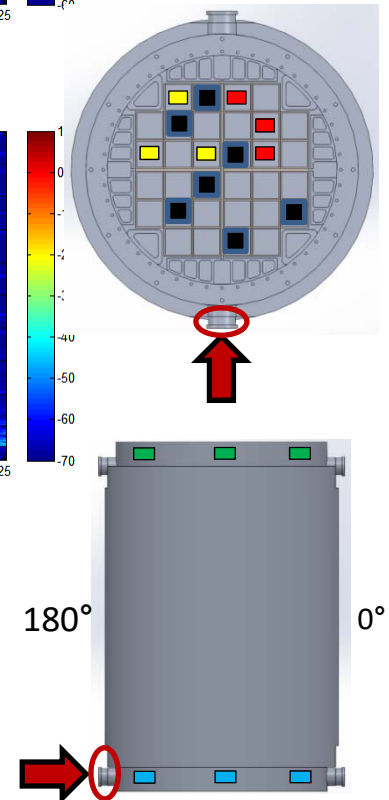
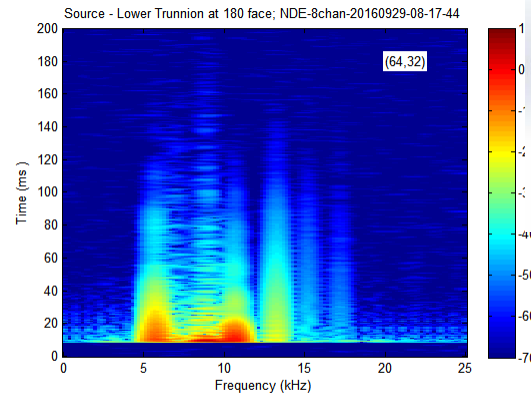
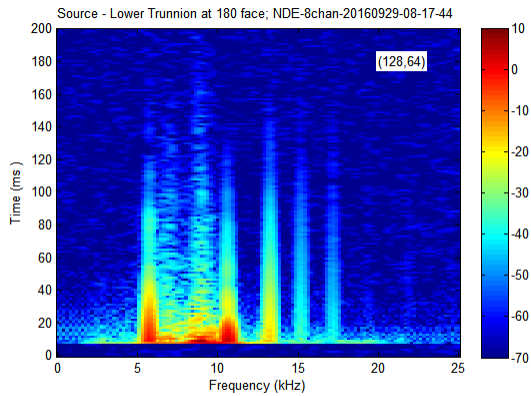
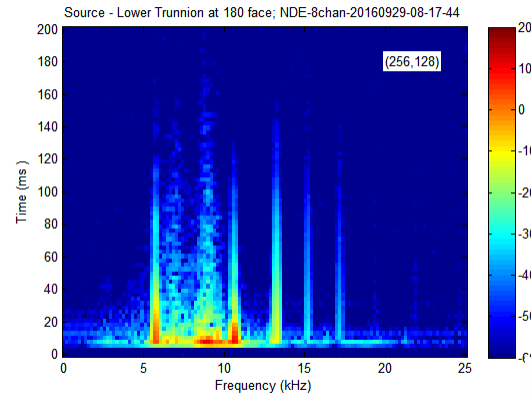
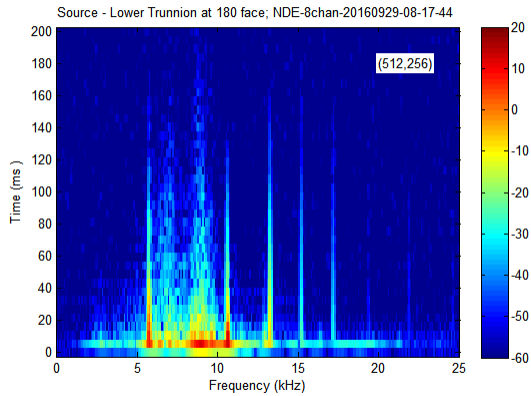
# Floor A2



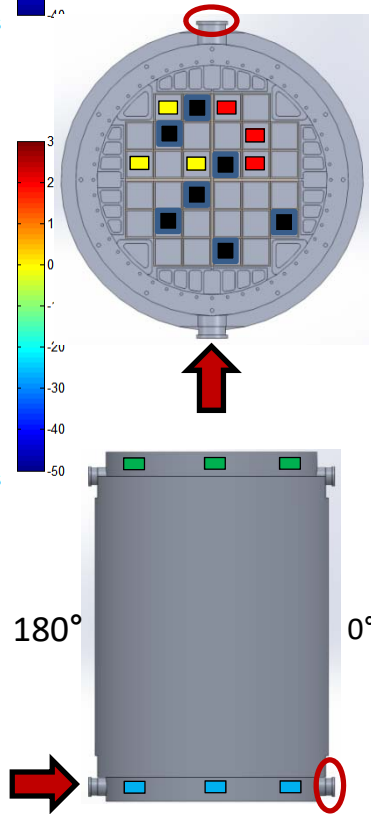
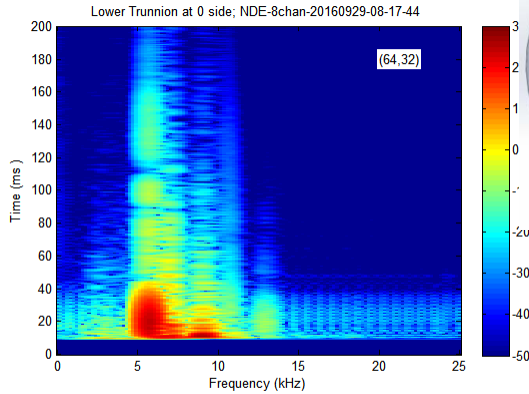
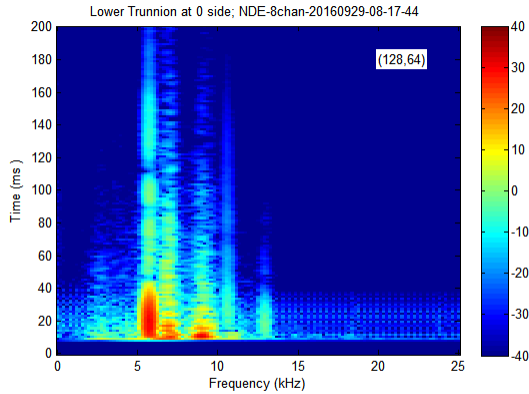
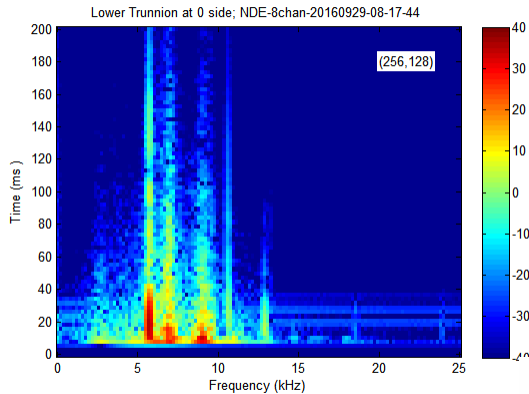
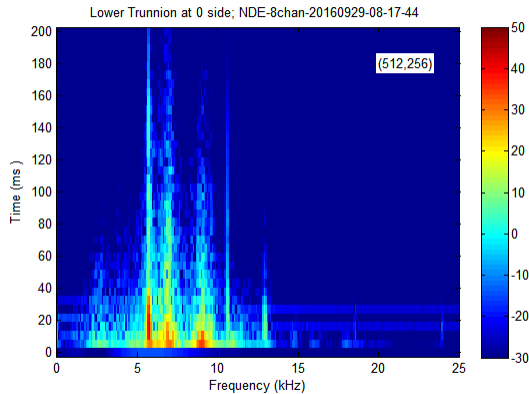
# Floor A3



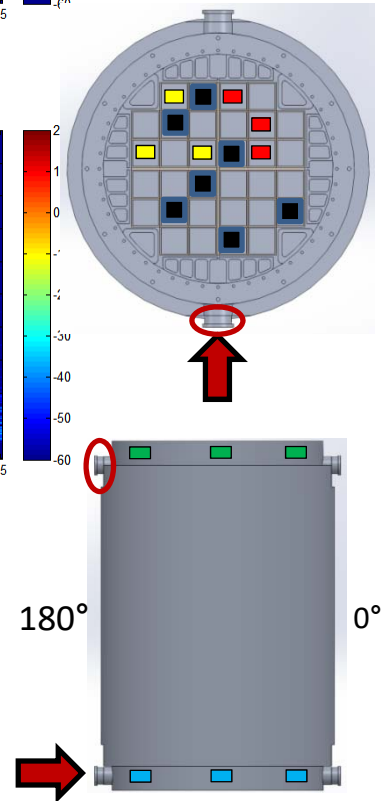
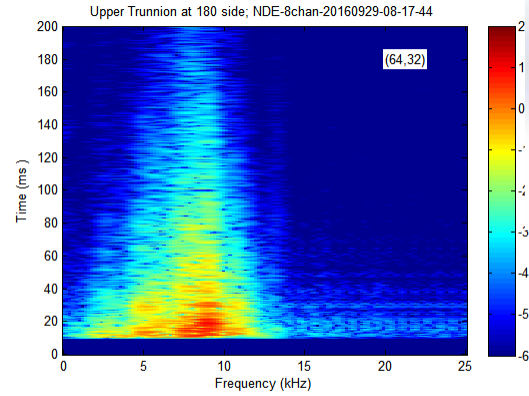
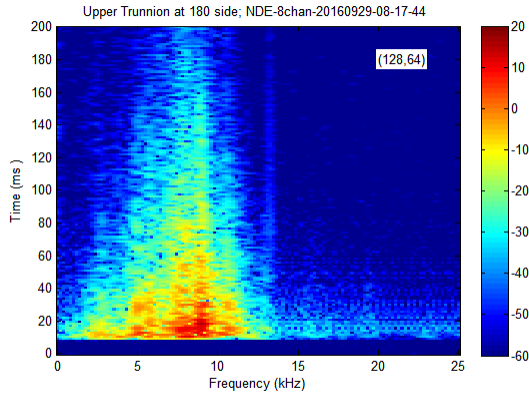
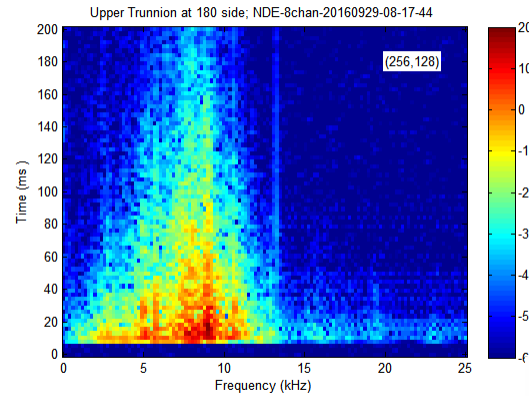
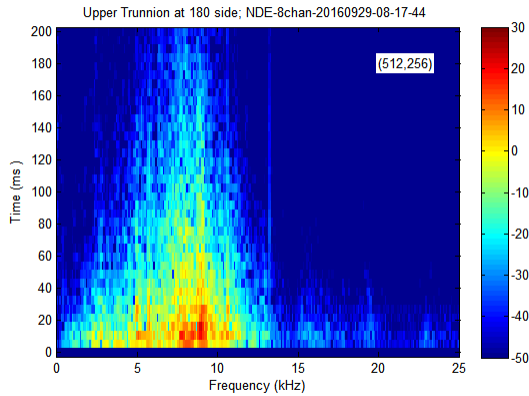
# Trunnion (Low): Trigger (Box 2)



# Trunnion: Proximal

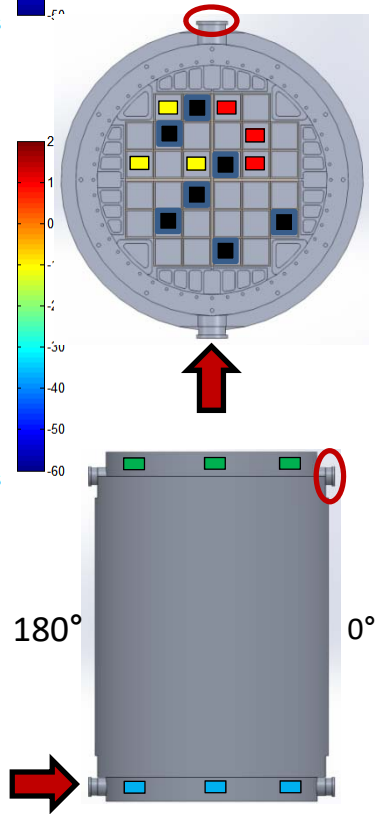
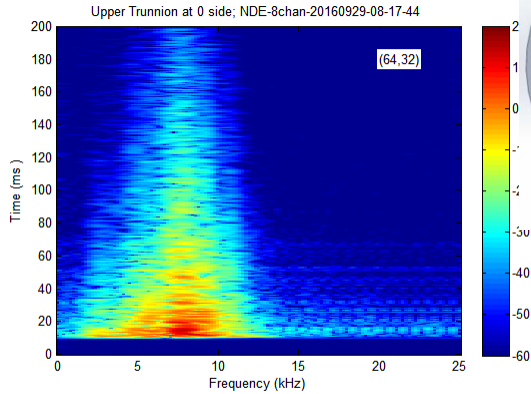
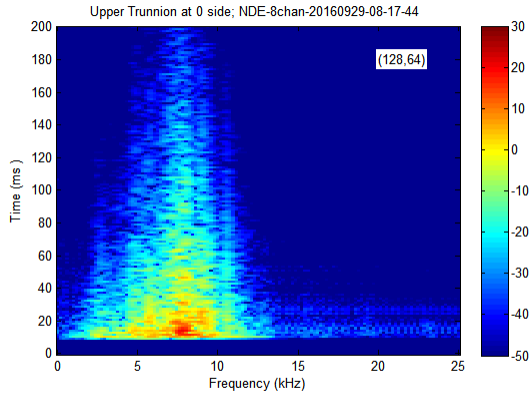
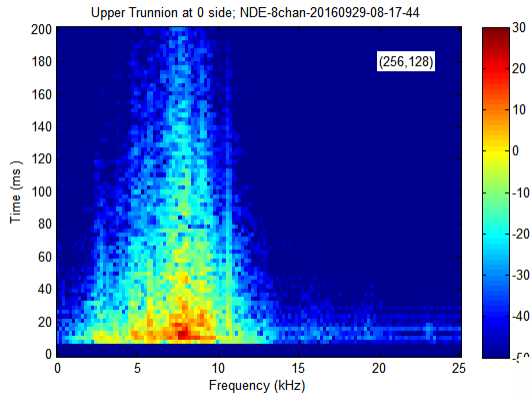
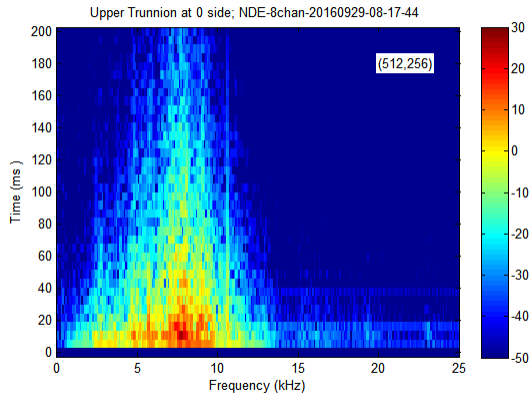


# Trunnion: Same Side





# Trunnion: Distal



NDE-8chan-20160929-08\_43\_56 Binary.bin

theLabel =

'Source - Upper Trunnion at 180 face'

'Cask floor A1'

'Cask floor A2'

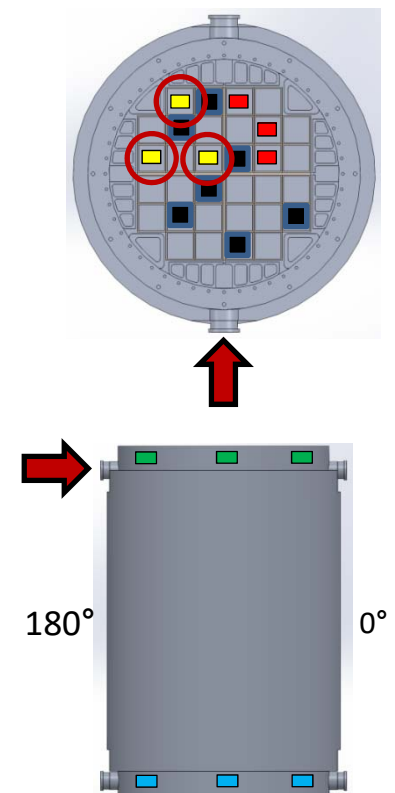
'Cask floor A3'

'Source - Upper Trunnion at 180 face'

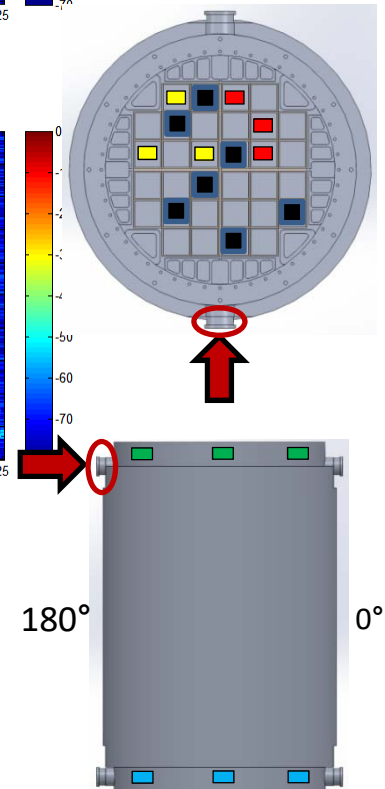
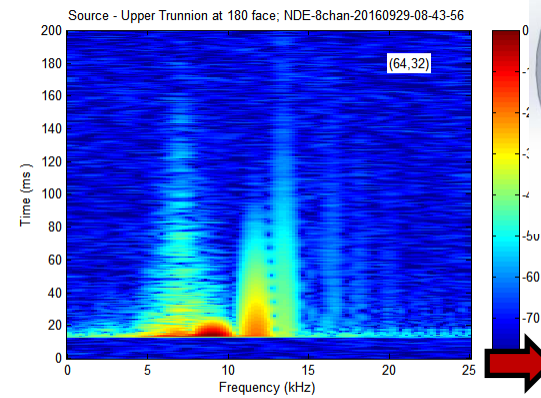
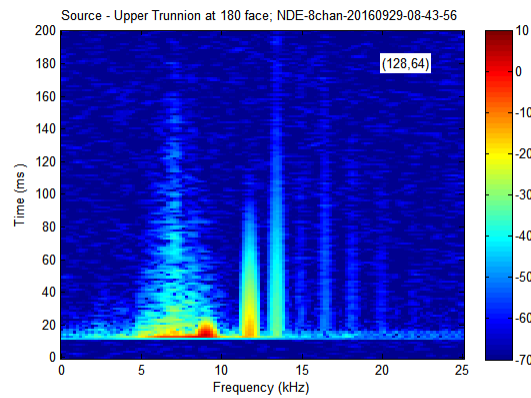
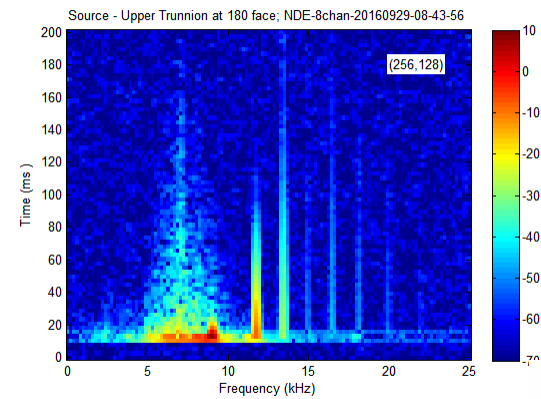
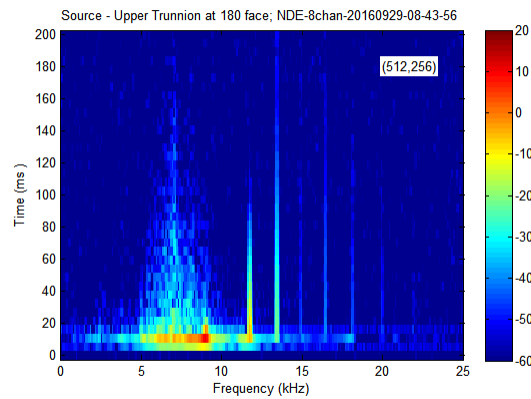
'Lower Trunnion at 0 side'

'Lower Trunnion at 180 side'

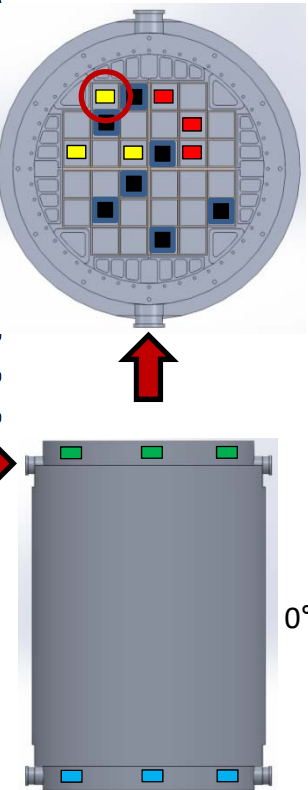
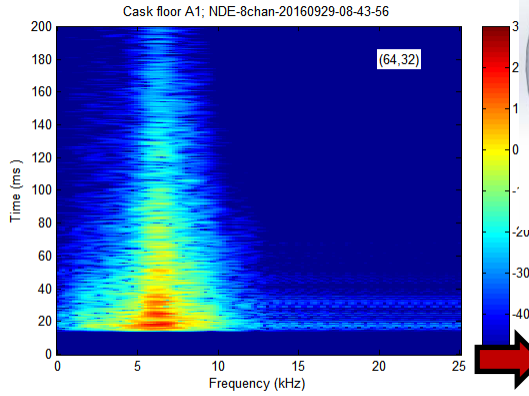
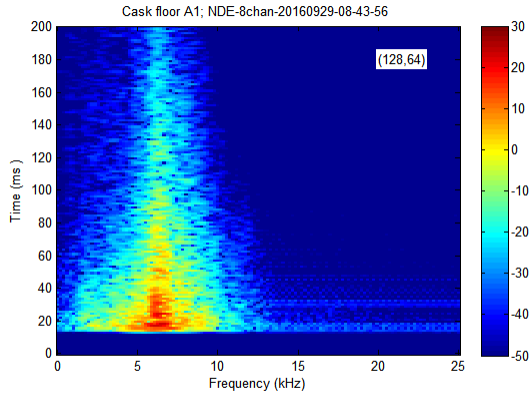
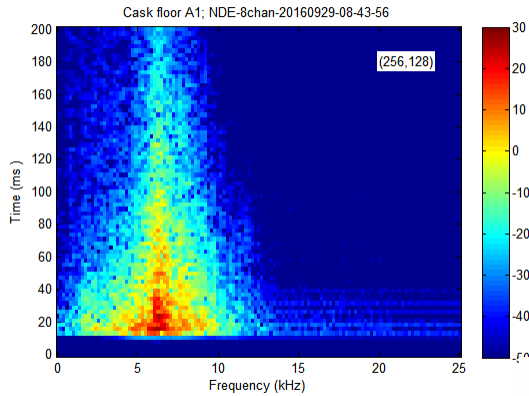
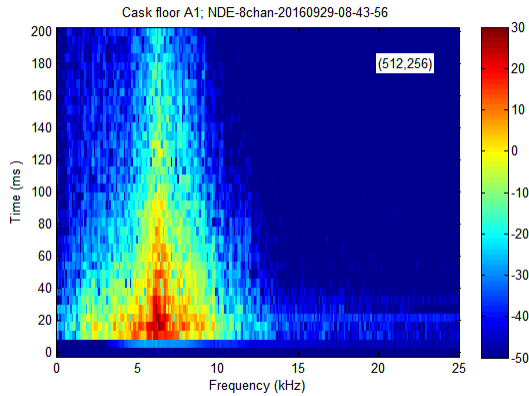
'Upper Trunnion at 0 side'



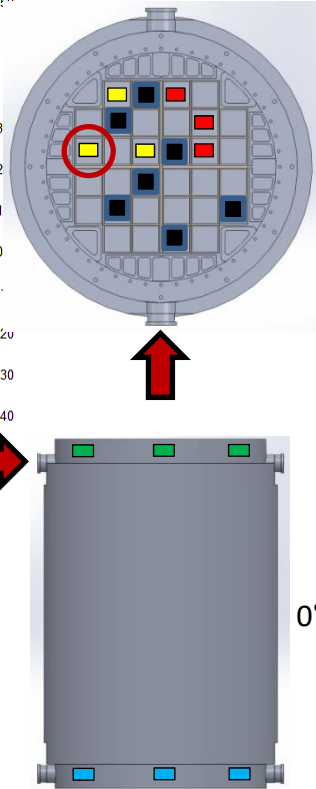
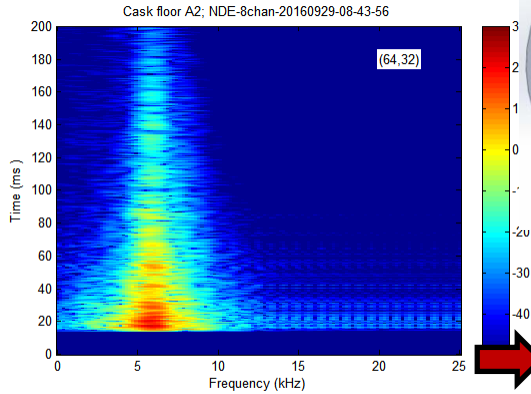
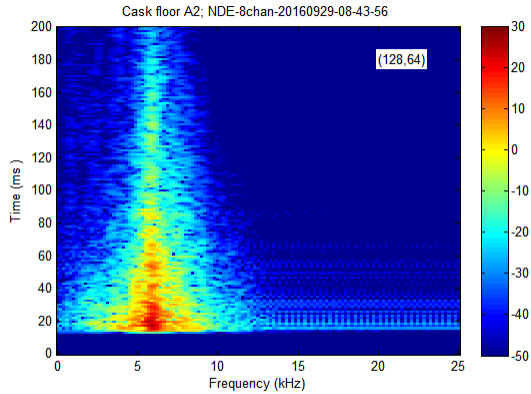
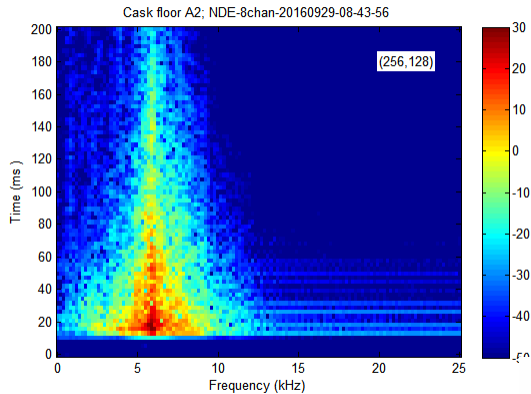
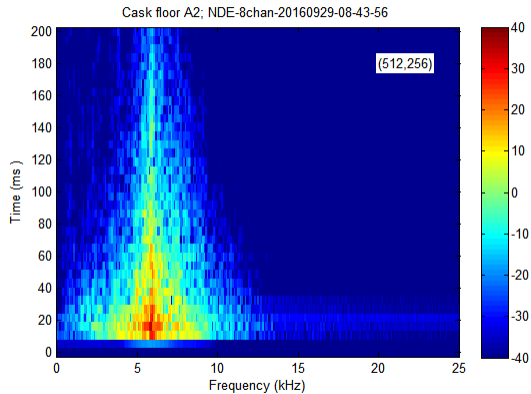
# Trunnion (High): Trigger



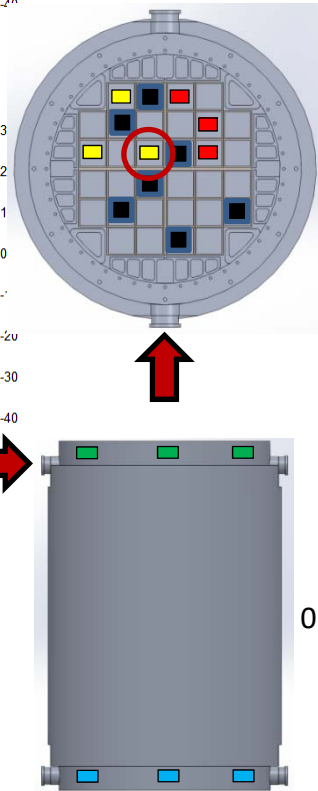
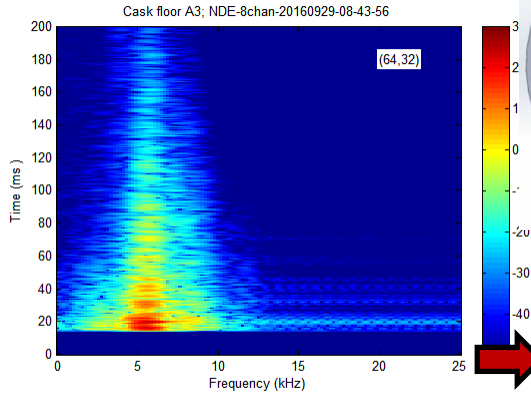
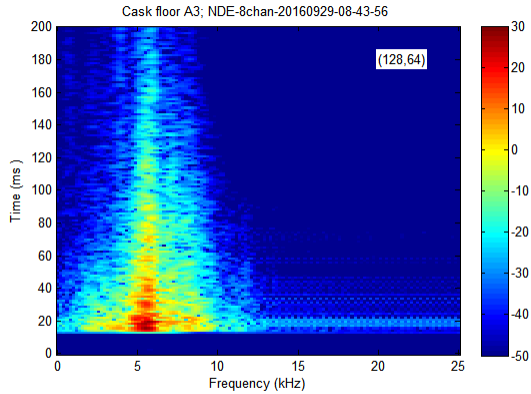
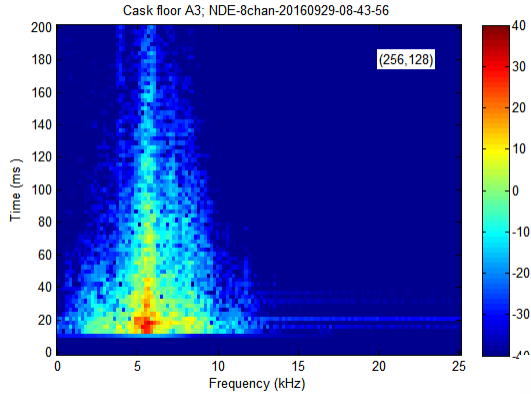
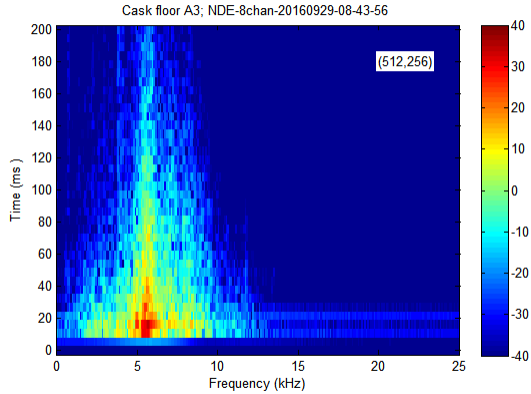
# Floor A1



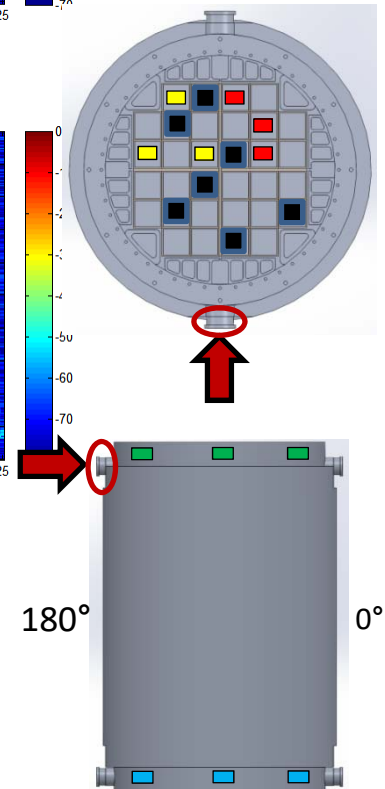
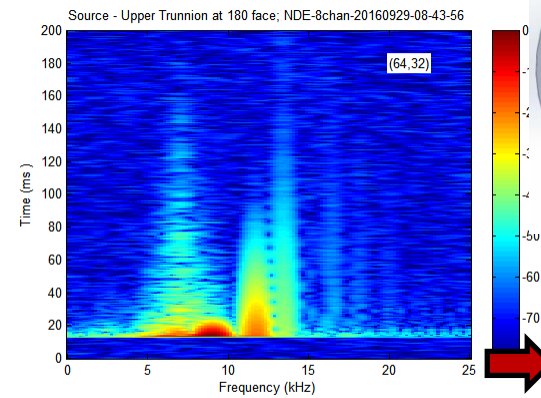
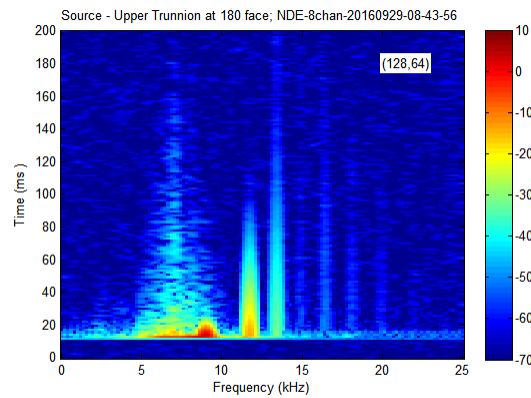
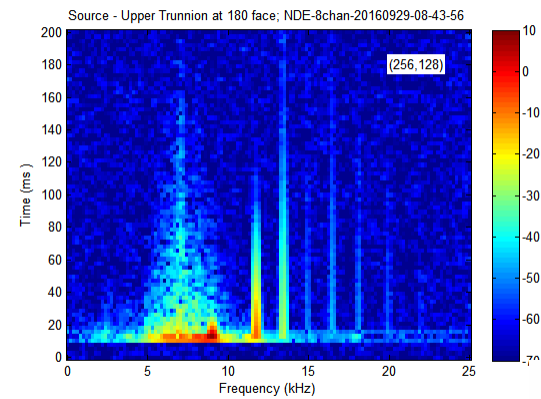
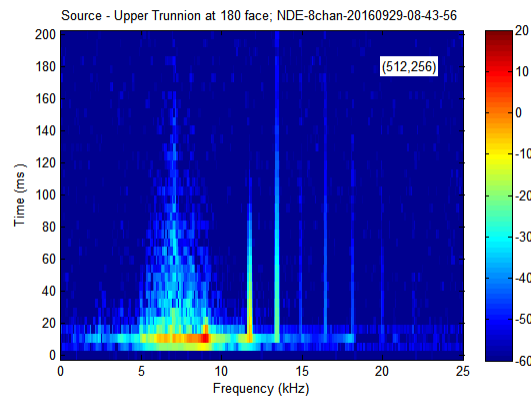
# Floor A2



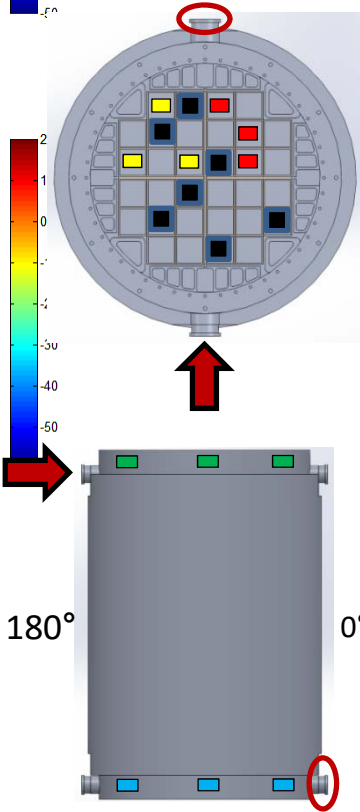
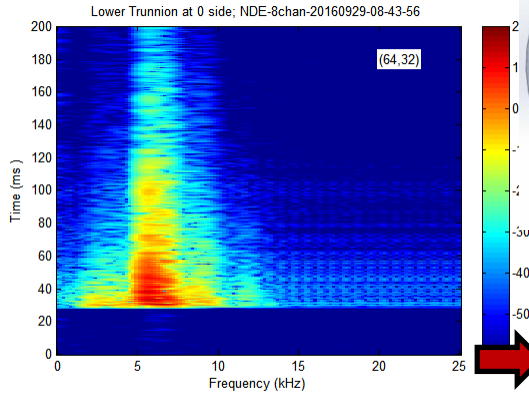
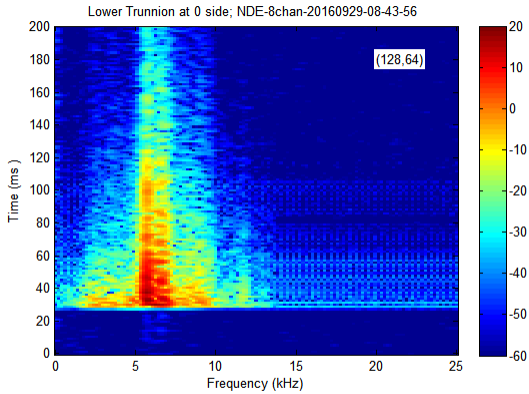
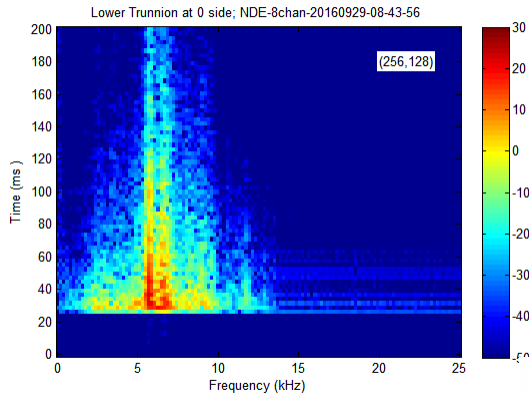
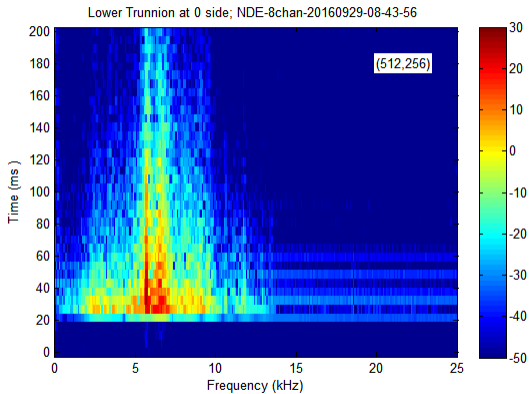
# Floor A3



# Trunnion (High): Trigger

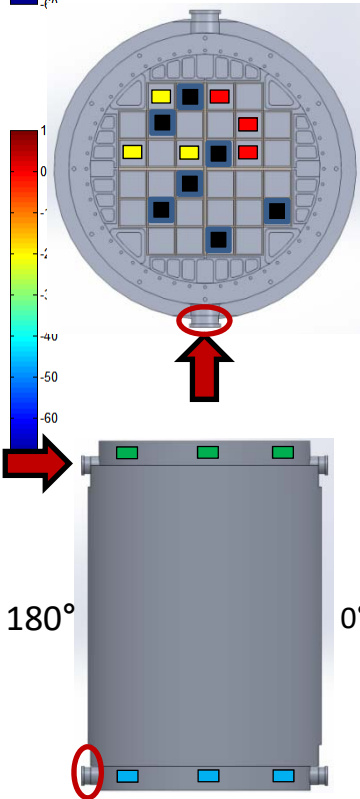
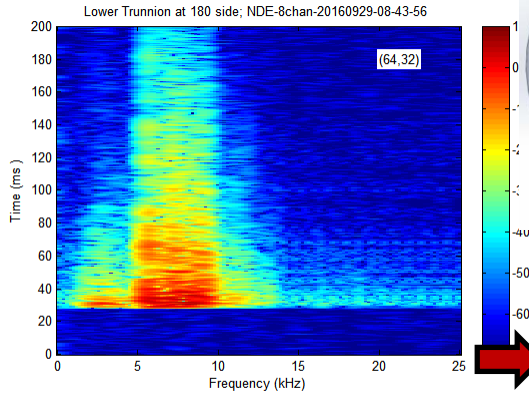
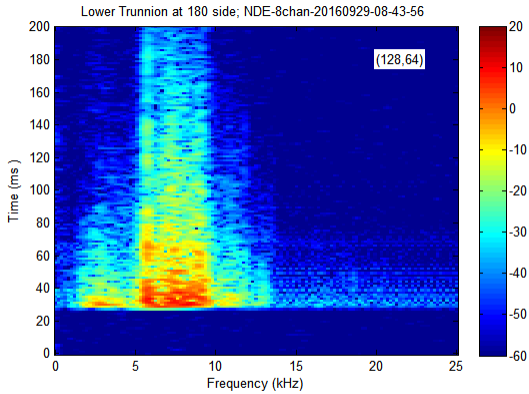
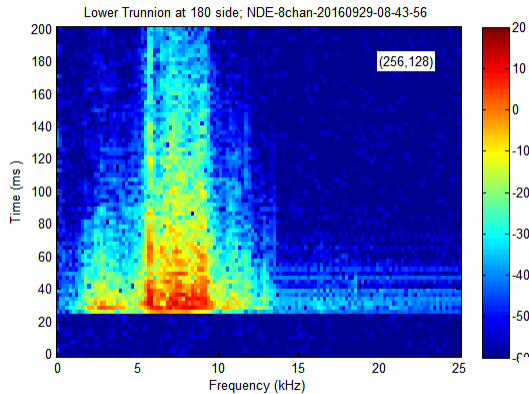
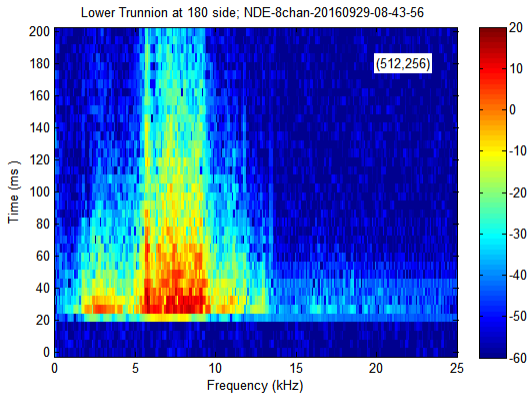


# Trunnion: Distal

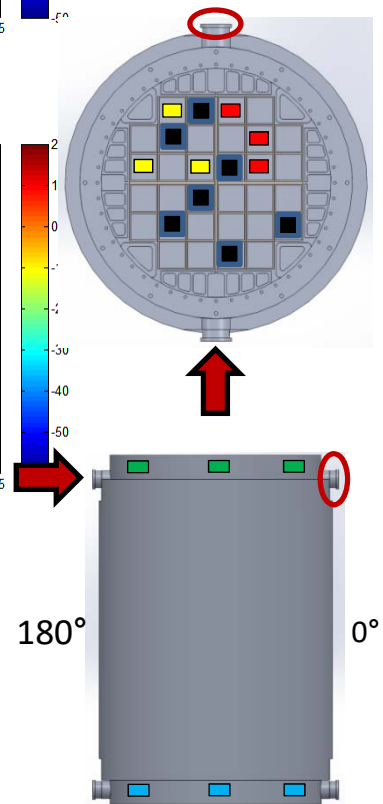
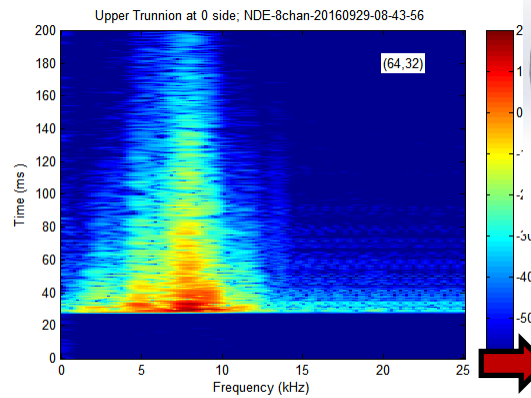
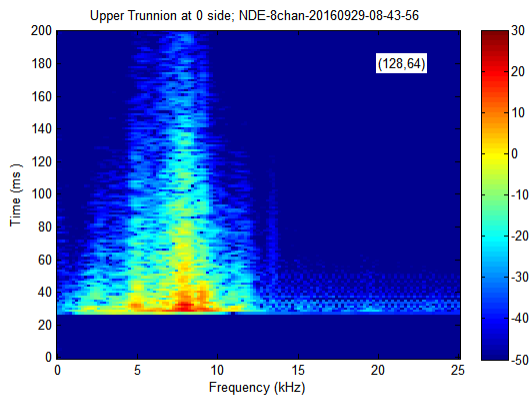
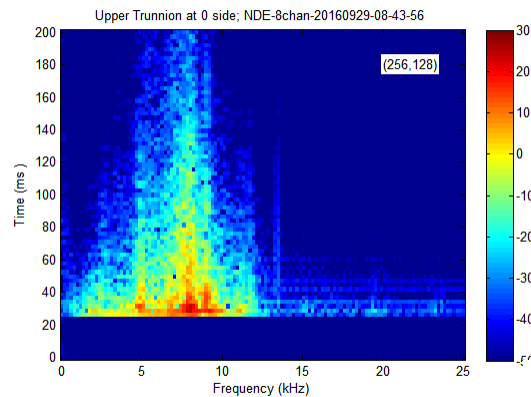
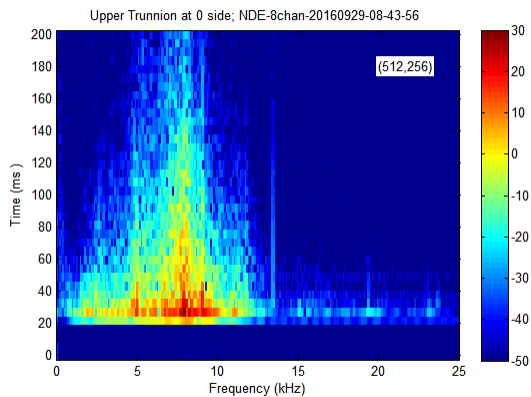




# Trunnion: Same Side



# Trunnion: Proximal



NDE-8chan-20160929-09\_44\_46 Binary.bin

theLabel =

'Source - Lower Trunnion at 180 face'

'Cask floor B1'

'Cask floor B2'

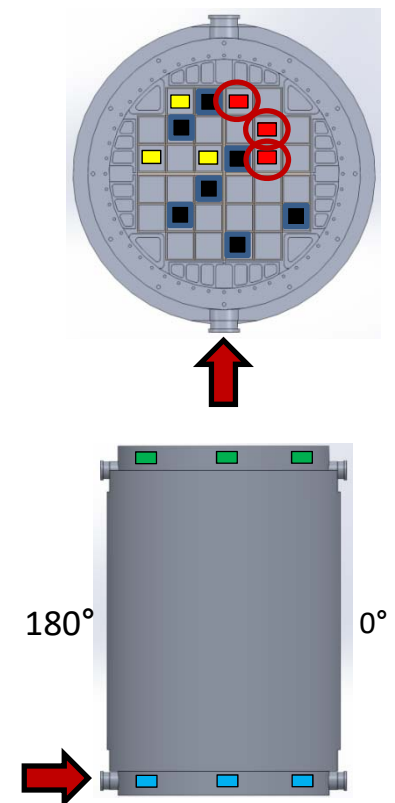
'Cask floor B3'

'Source - Lower Trunnion at 180 face'

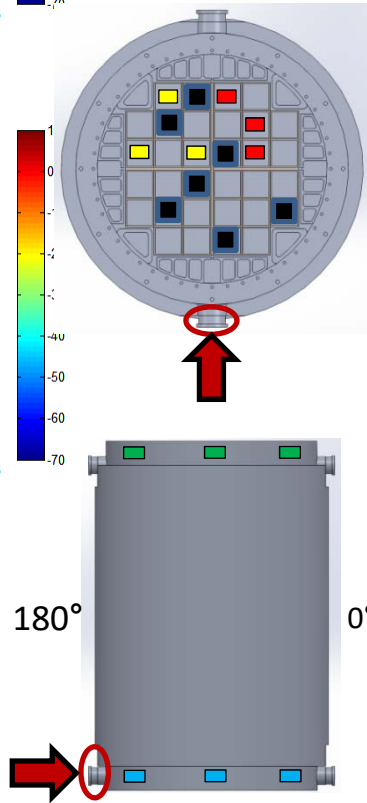
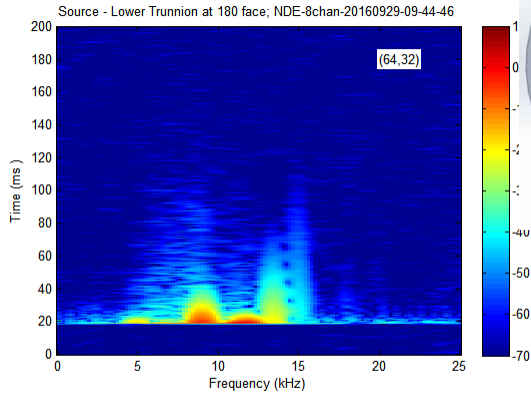
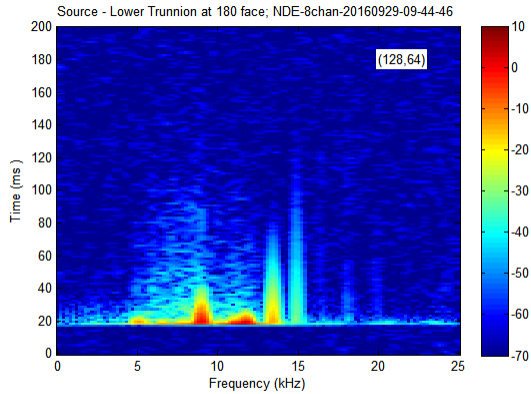
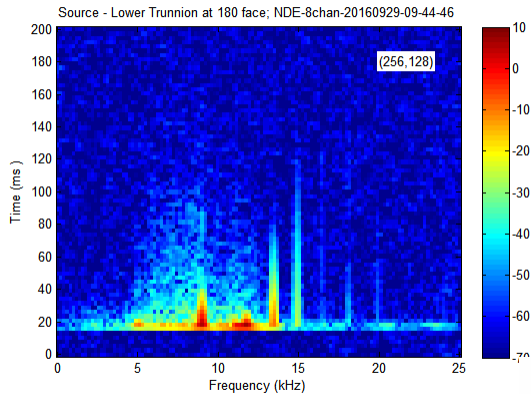
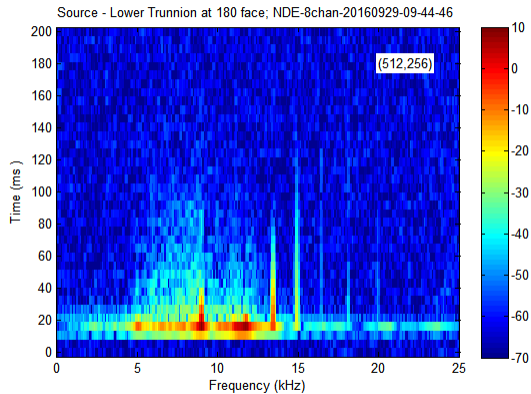
'Lower Trunnion at 0 side'

'Upper Trunnion at 180 side'

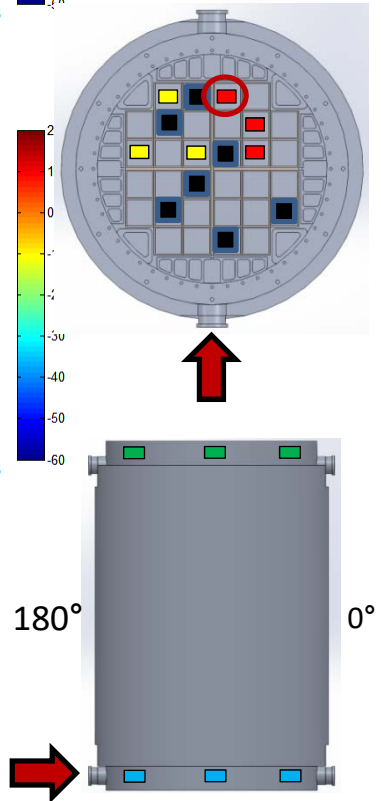
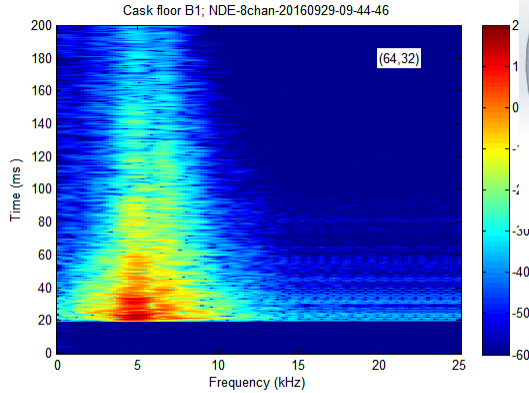
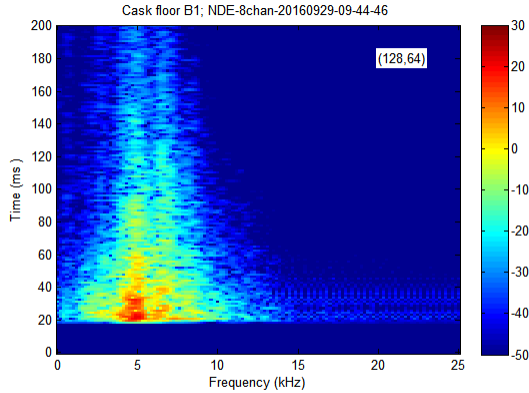
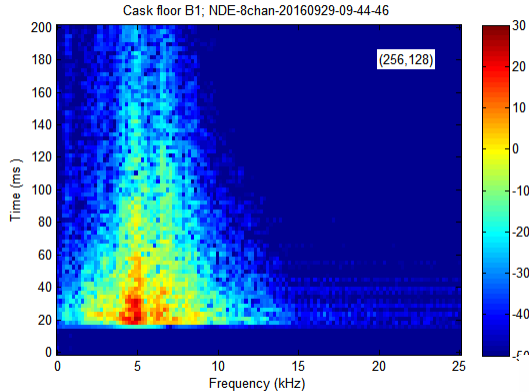
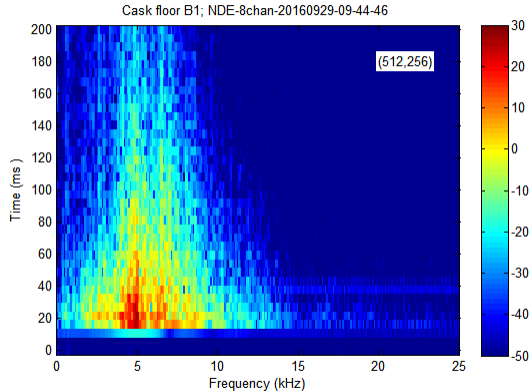
'Upper Trunnion at 0 side'



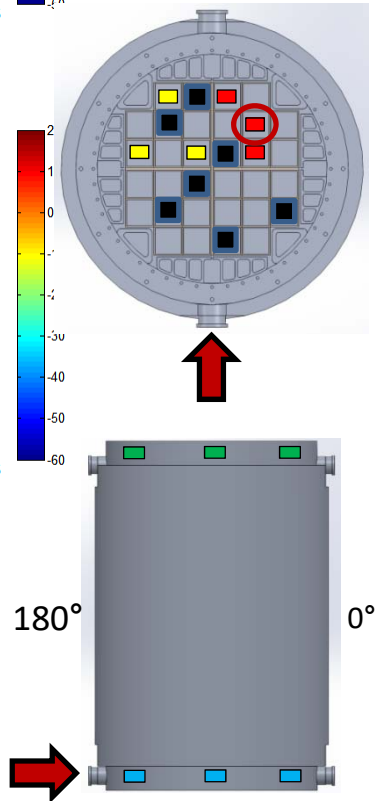
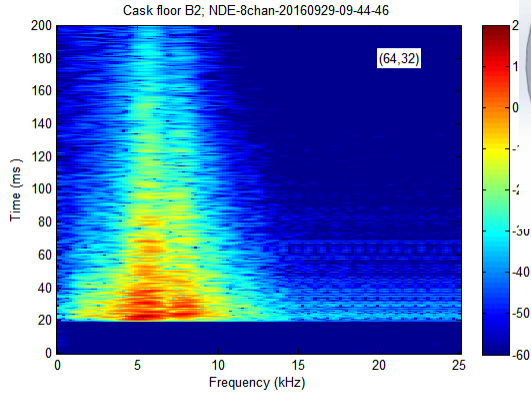
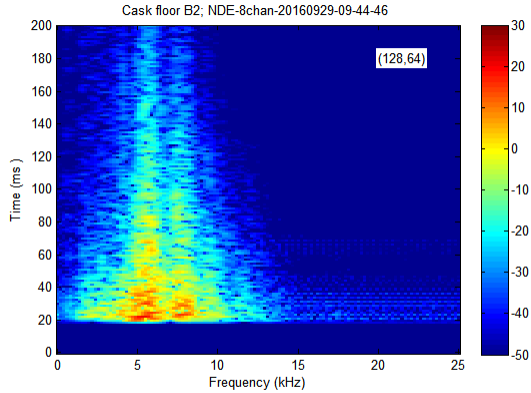
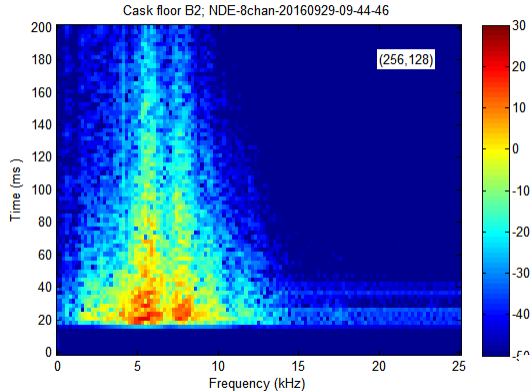
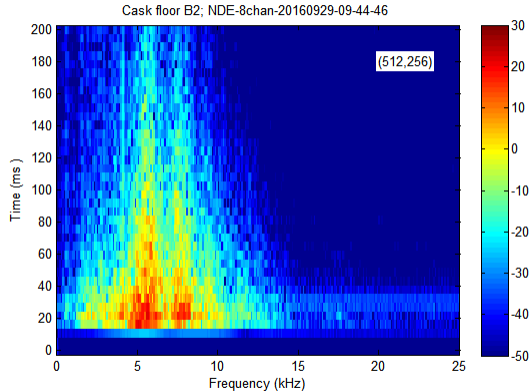
# Trunnion (Low) :Trigger



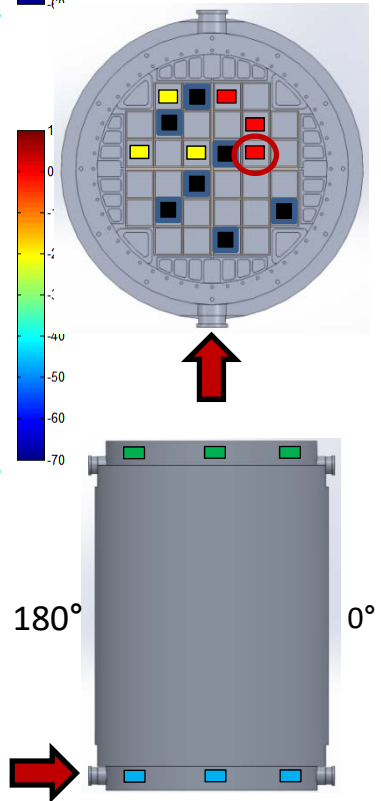
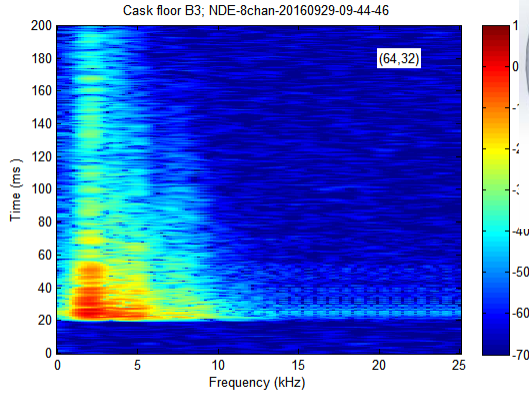
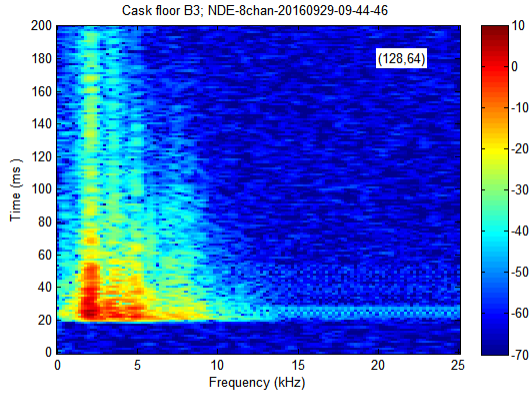
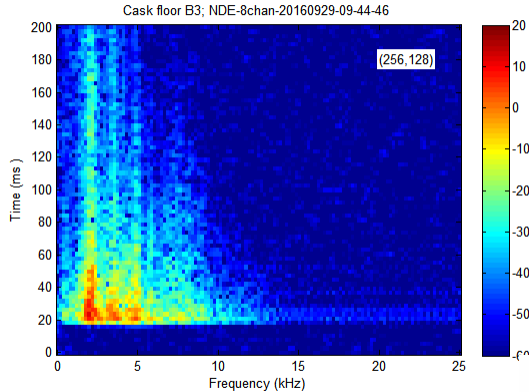
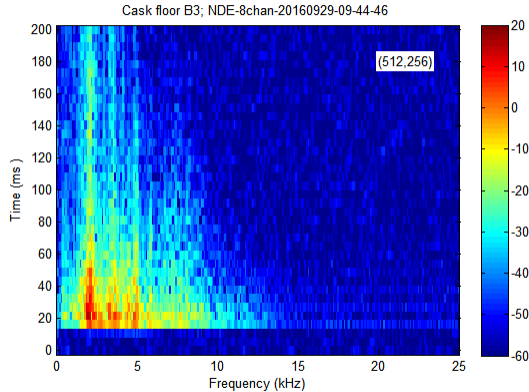
# Floor B1



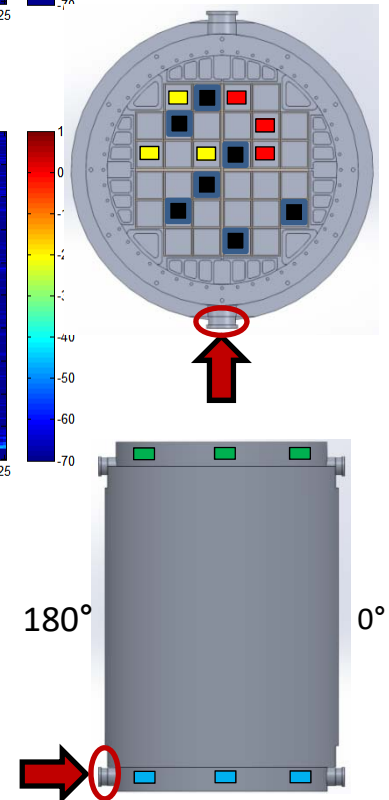
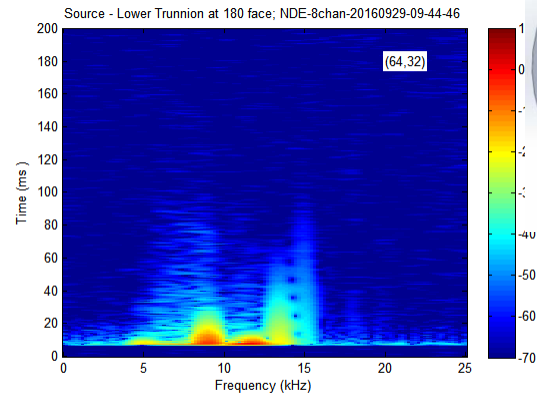
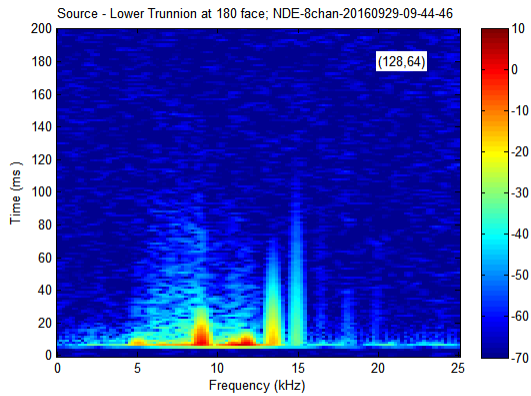
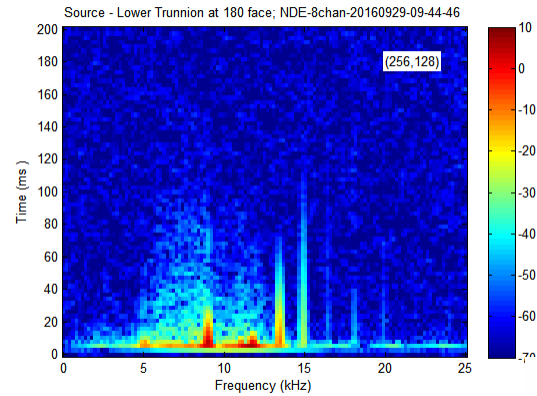
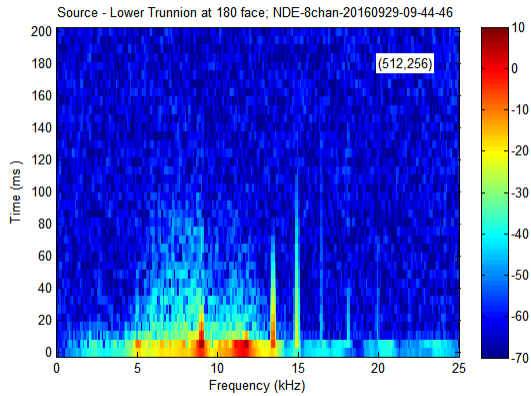
# Floor B2



# Floor B3

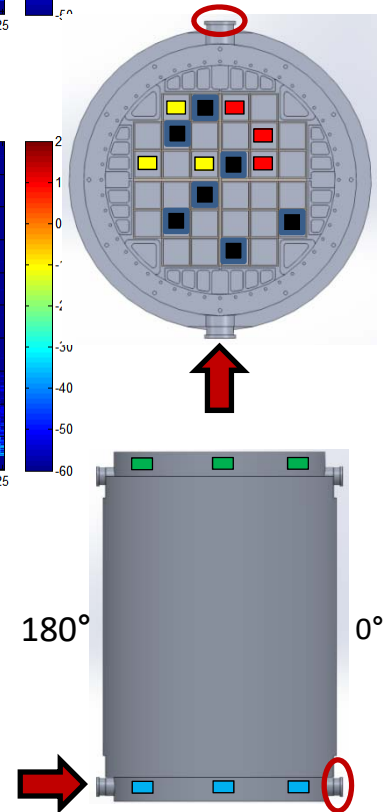
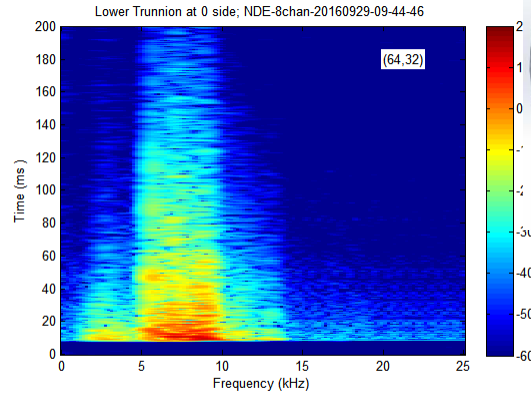
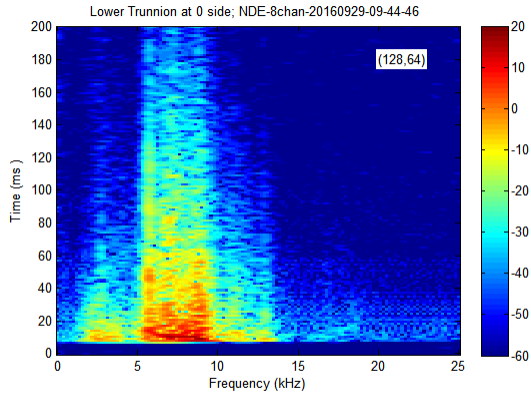
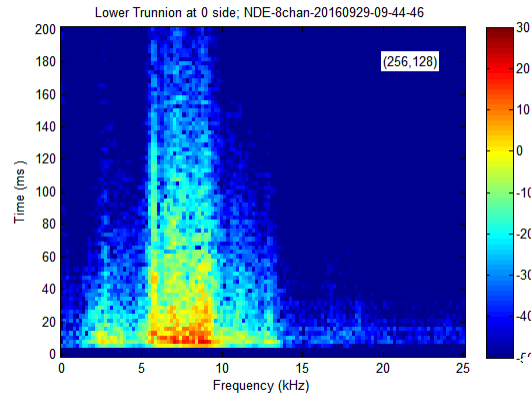
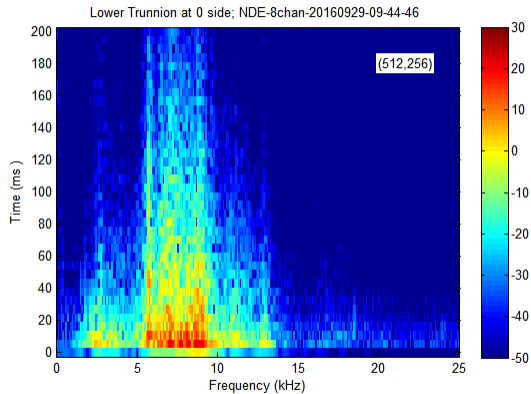


# Trunnion (Low) :Trigger (Box 2)

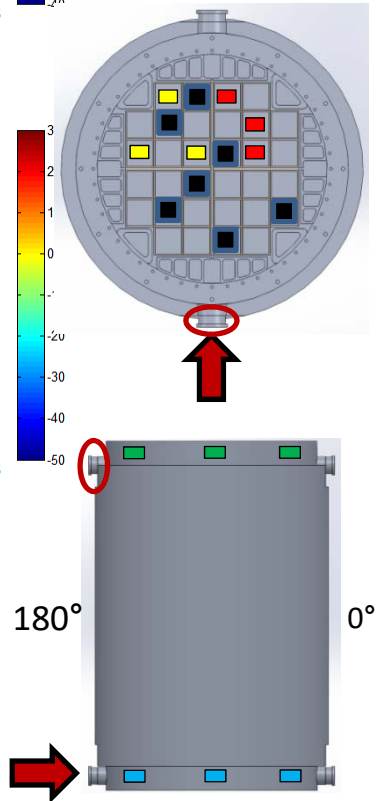
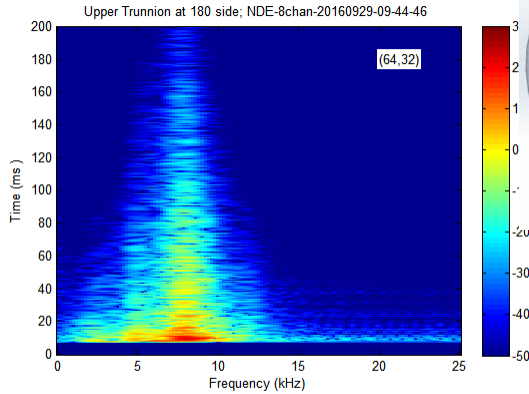
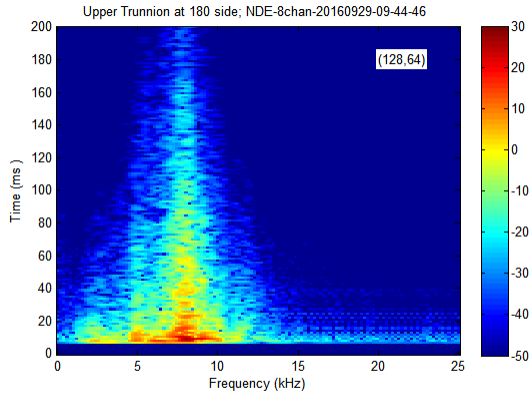
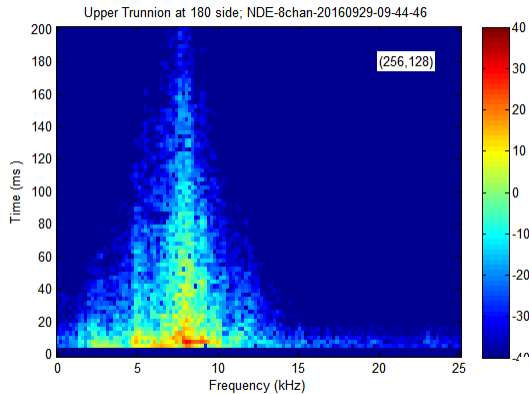
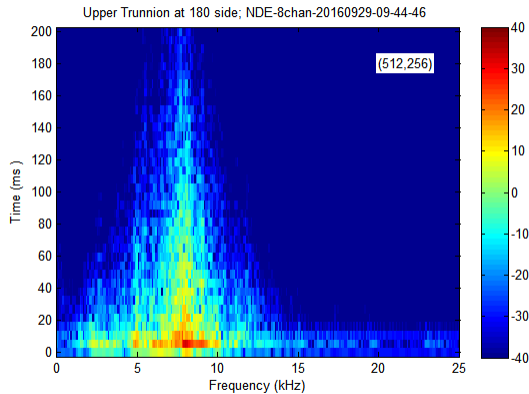




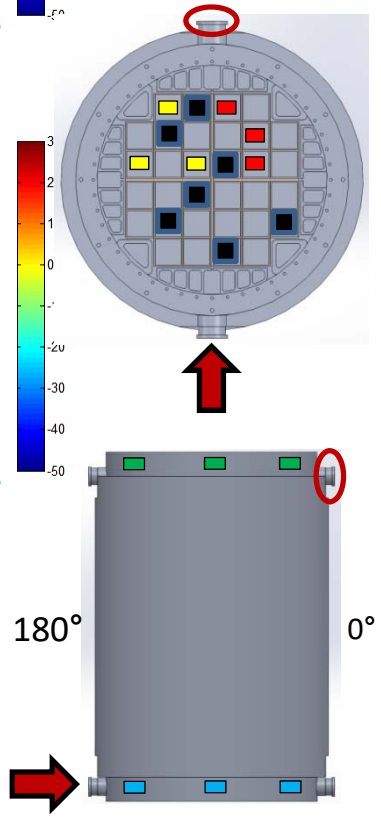
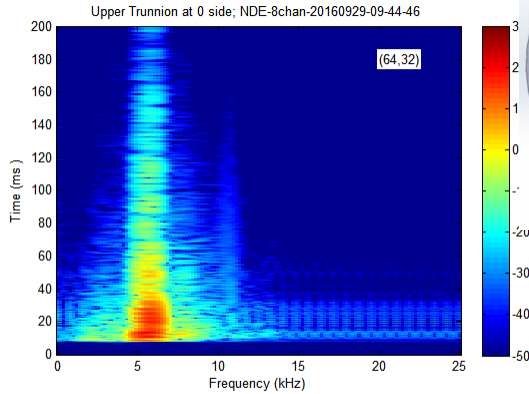
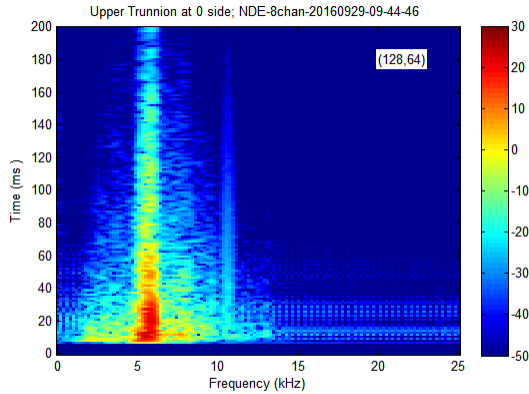
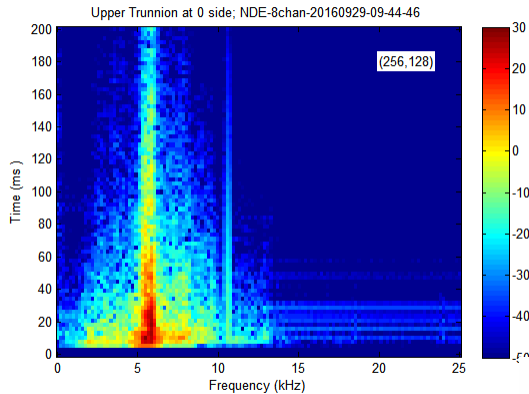
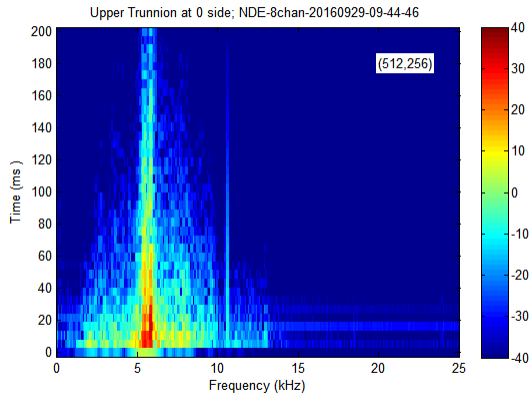
# Trunnion: Proximal



# Trunnion: Same Side



# Trunnion: Distal



NDE-8chan-20160929-09\_51\_11 Binary.bin

theLabel =

'Source - Lower Trunnion at 0 face'

'Cask floor B1'

'Cask floor B2'

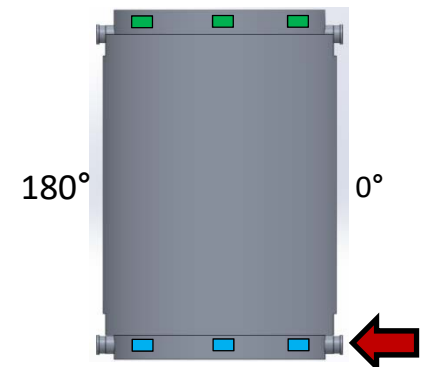
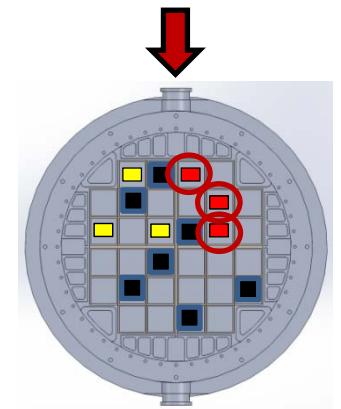
'Cask floor B3'

'Source - Lower Trunnion at 0 face'

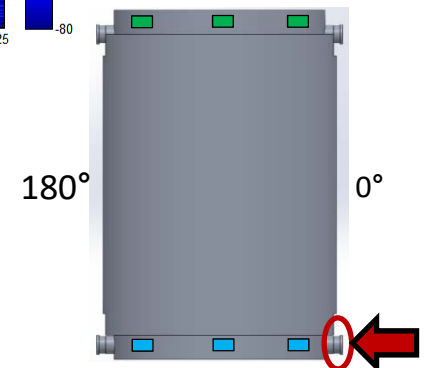
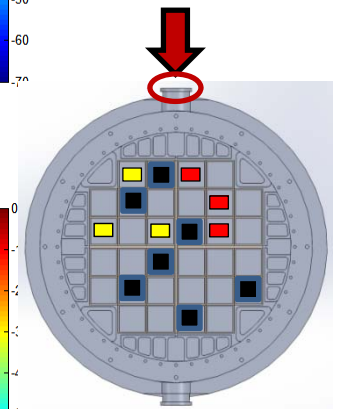
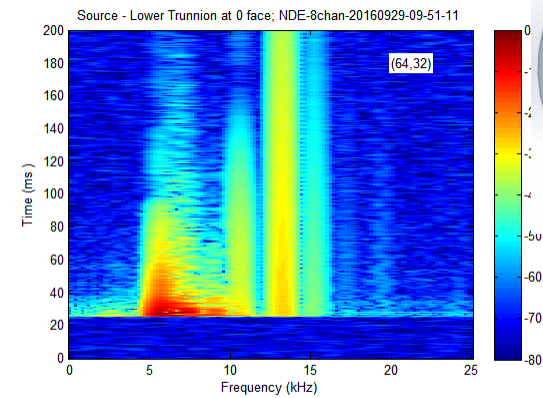
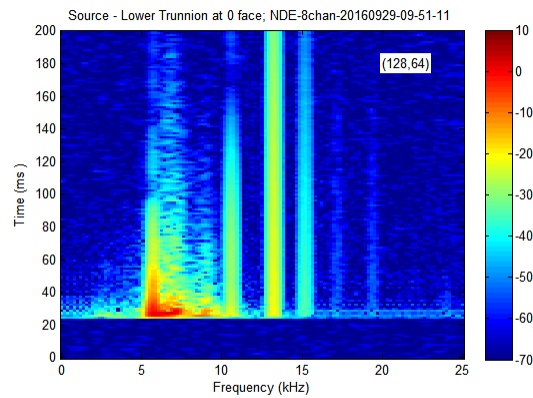
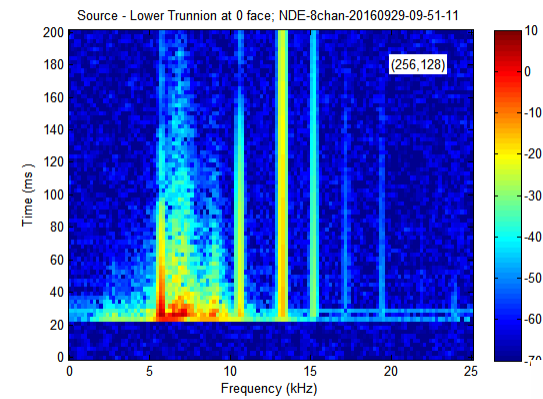
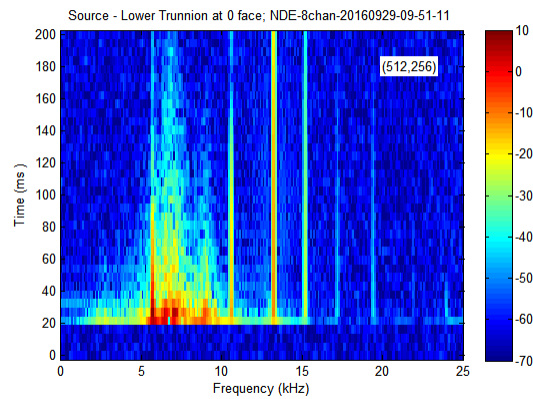
'Lower Trunnion at 180 side'

'Upper Trunnion at 180 side'

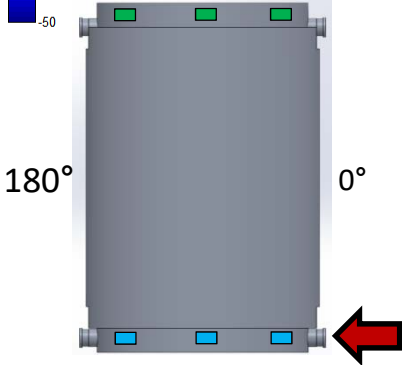
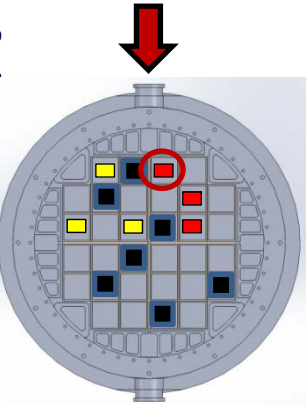
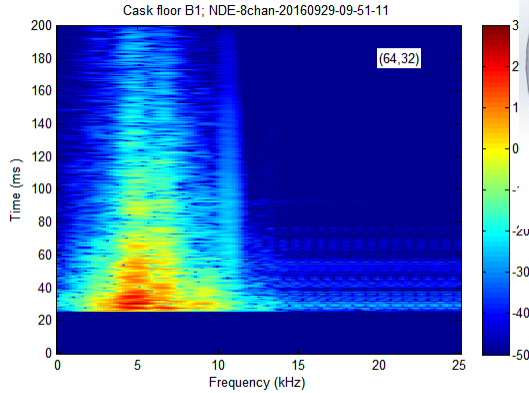
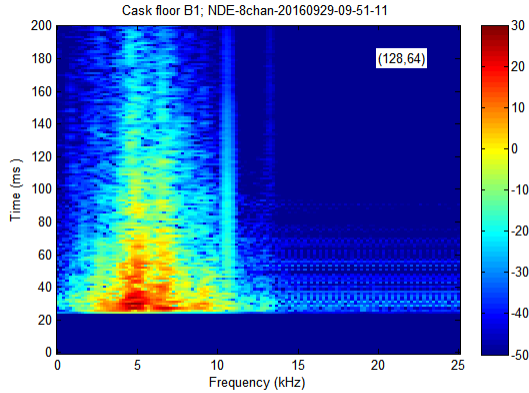
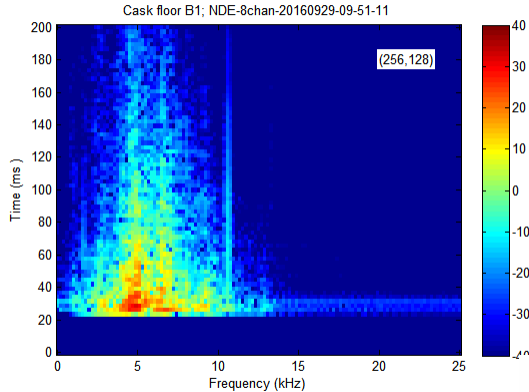
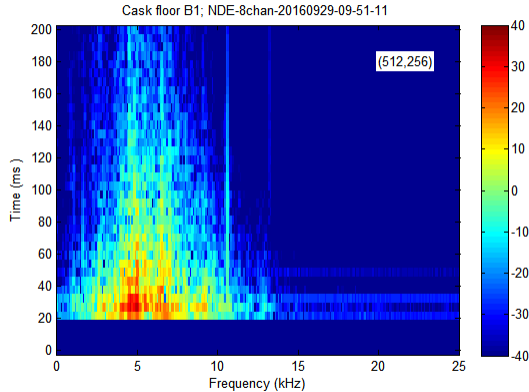
'Upper Trunnion at 0 side'



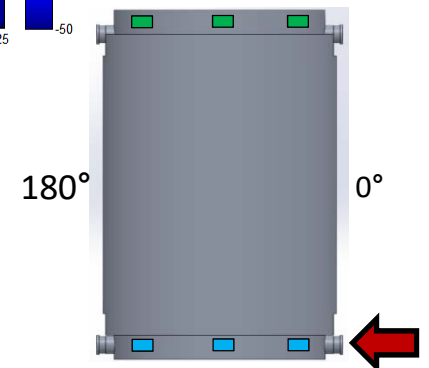
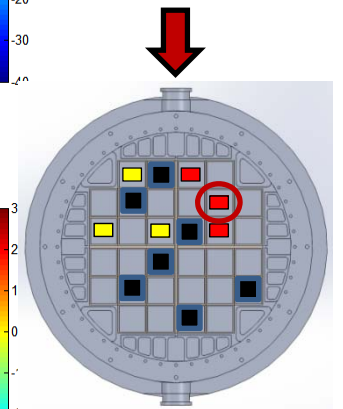
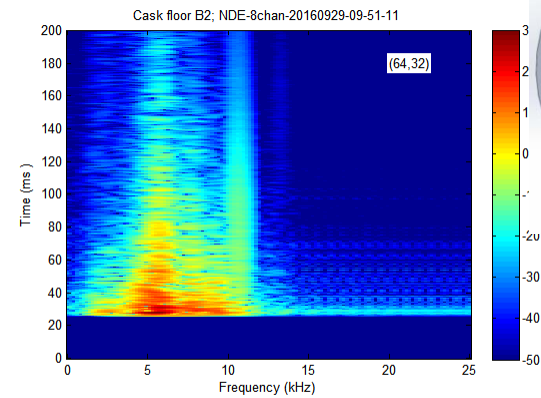
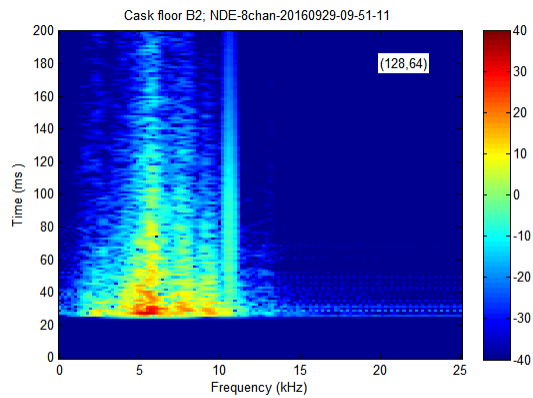
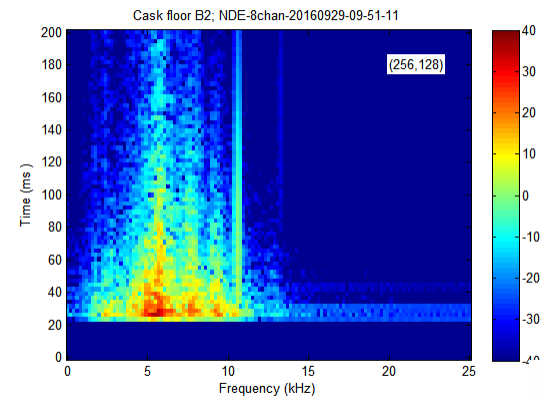
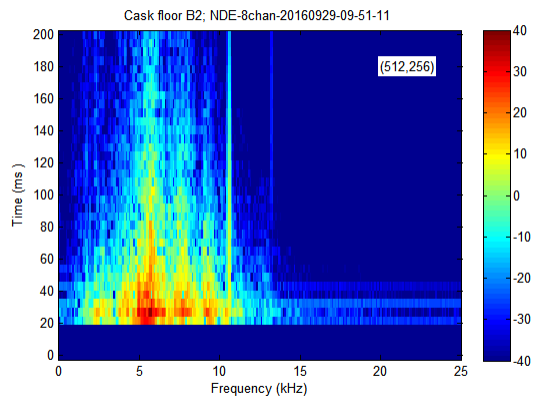
# Trunnion (Low) :Trigger



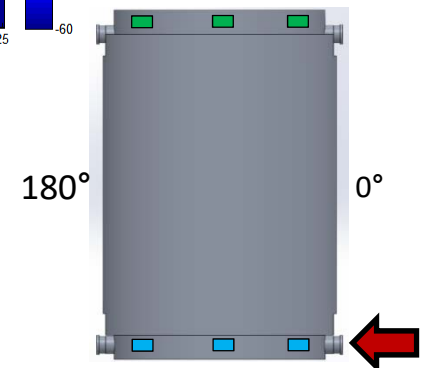
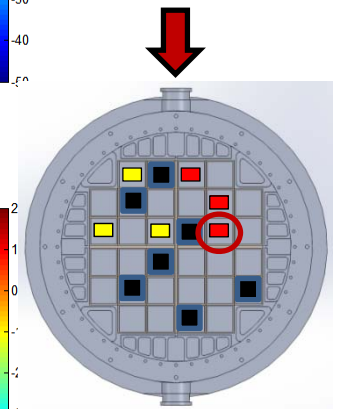
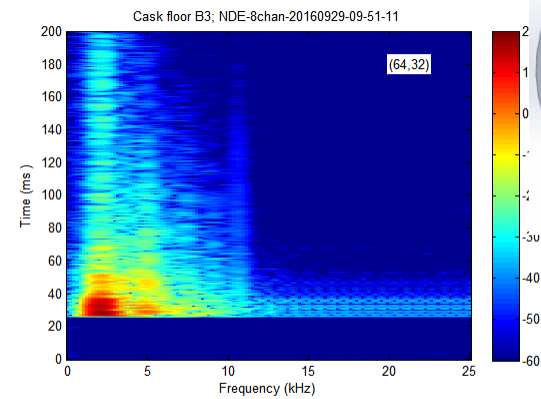
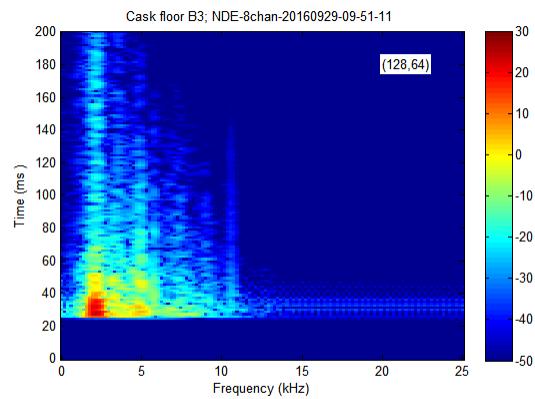
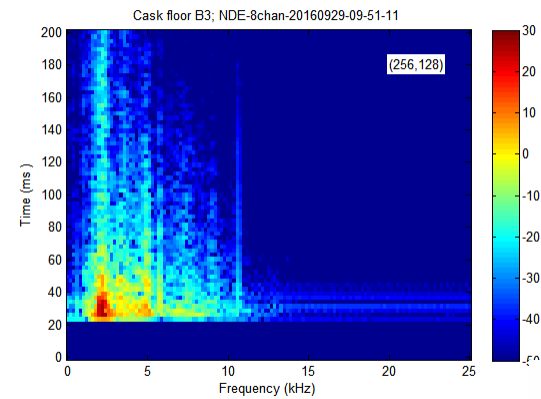
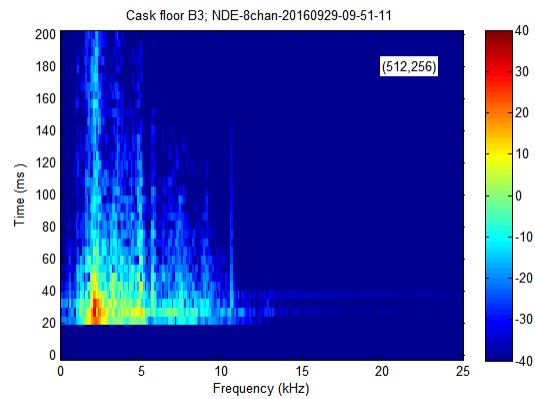
# Floor B1



# Floor B2

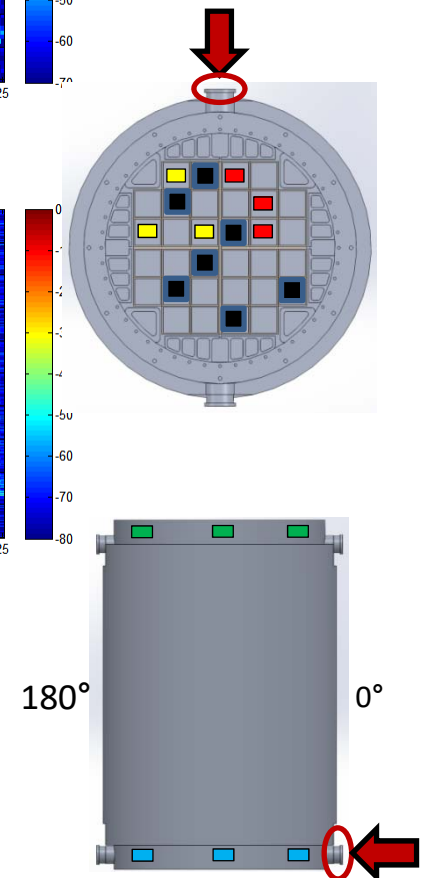
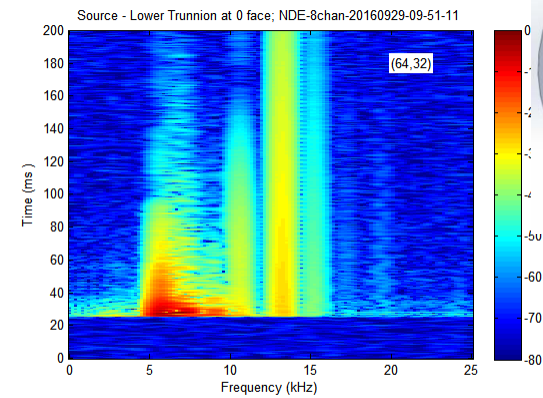
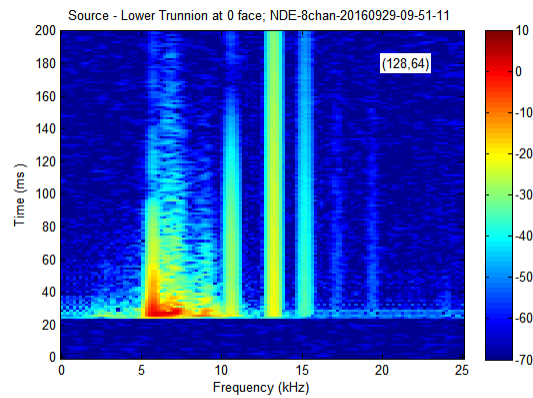
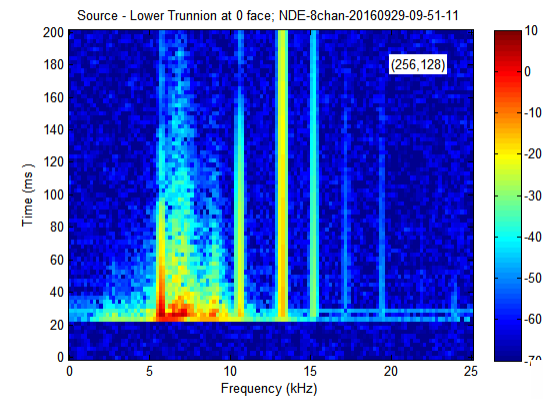
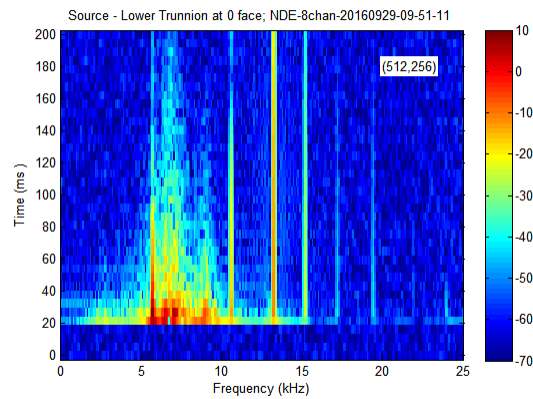


# Floor B3

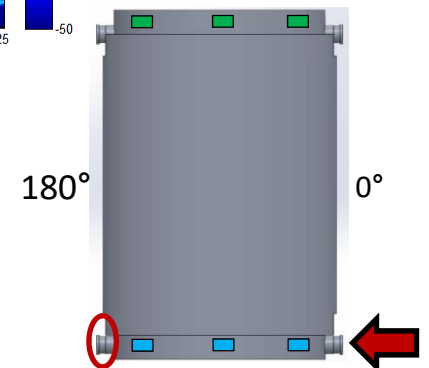
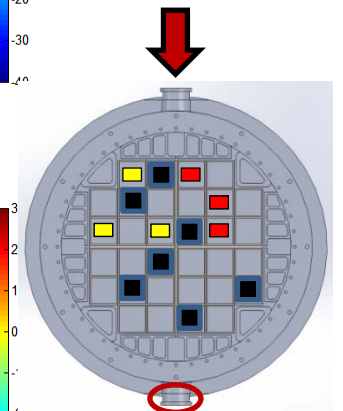
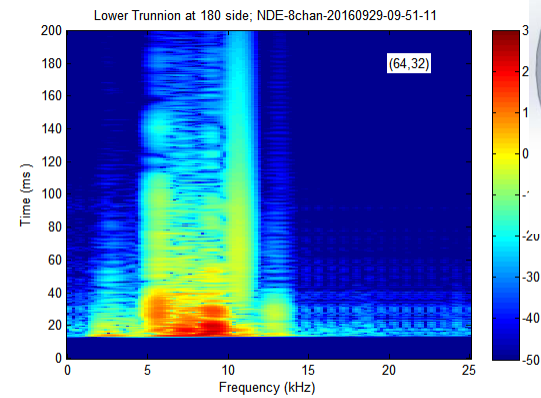
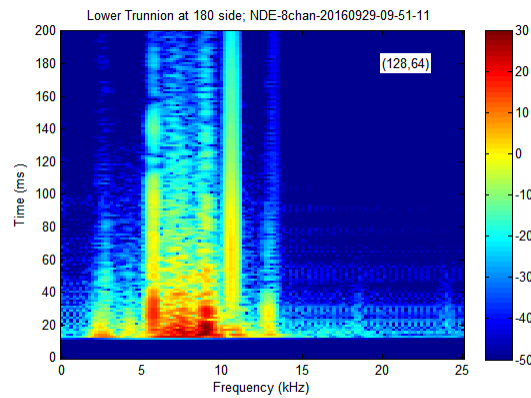
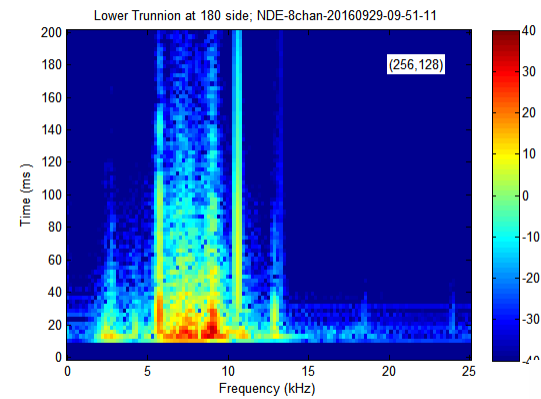
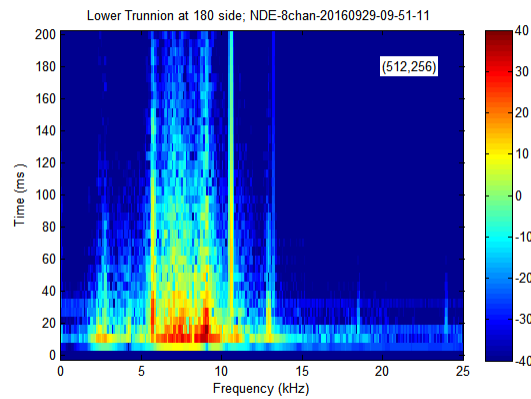




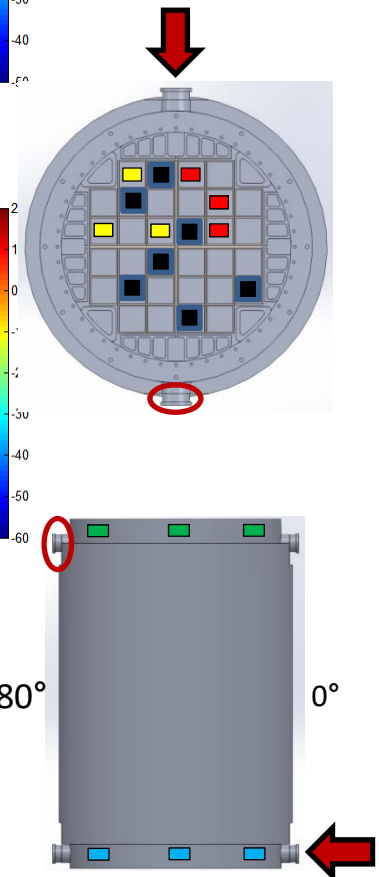
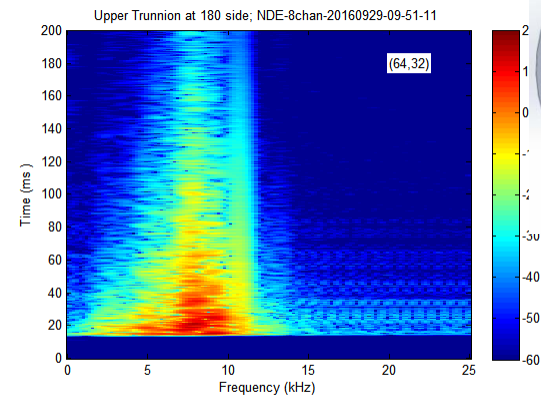
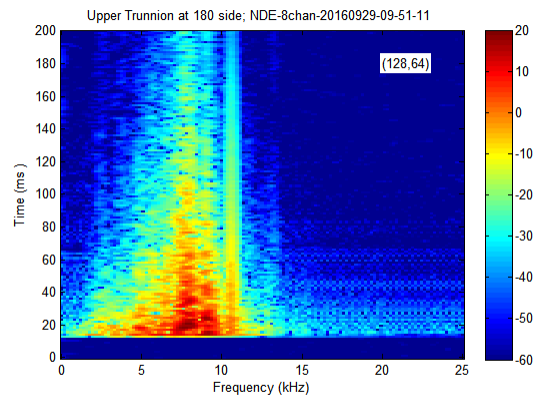
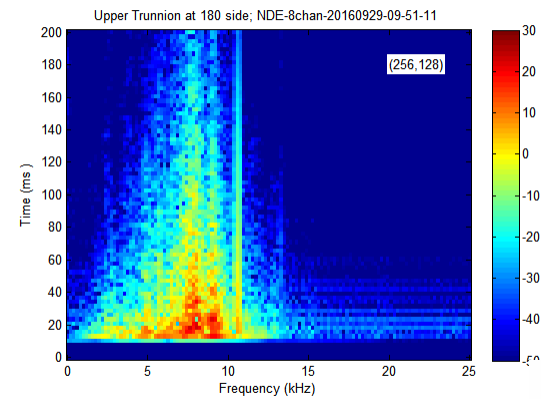
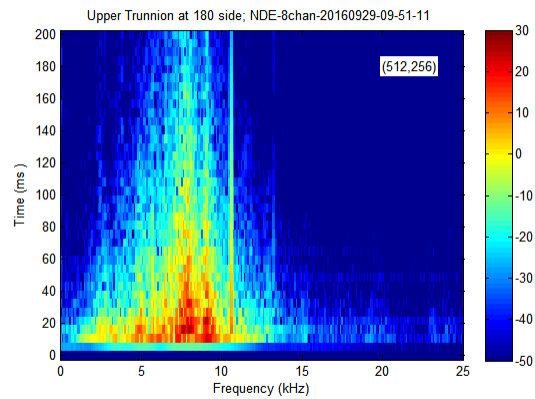
# Trunnion (Low) :Trigger (Box 2)



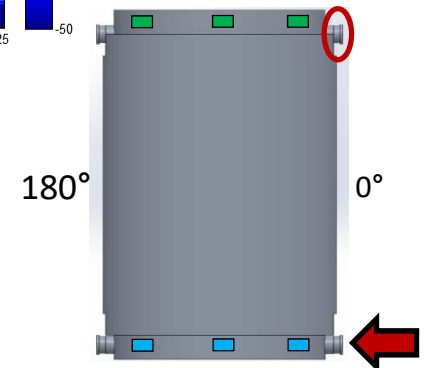
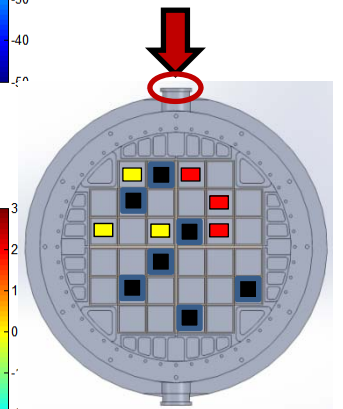
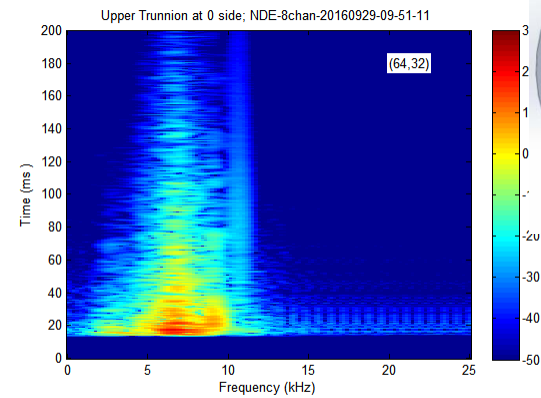
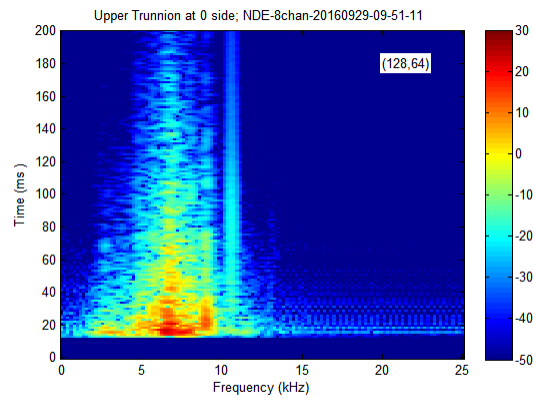
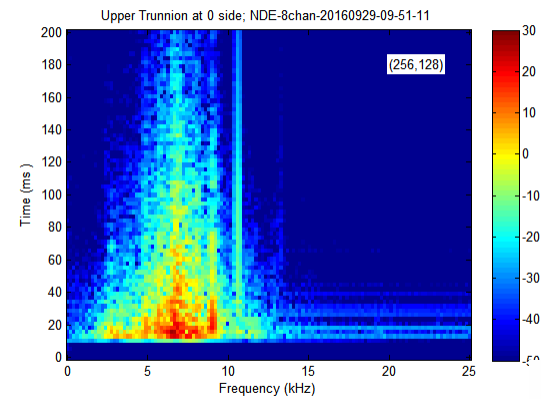
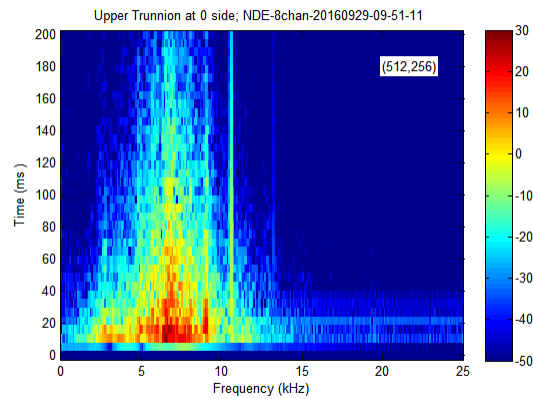
# Trunnion: Proximal



# Trunnion: Distal



# Trunnion: Same Side



NDE-8chan-20160929-10\_47\_52 Binary.bin

theLabel =

'Source - Lower Trunnion at 180 face'

'Bottom Rim D1'

'Bottom Rim D2'

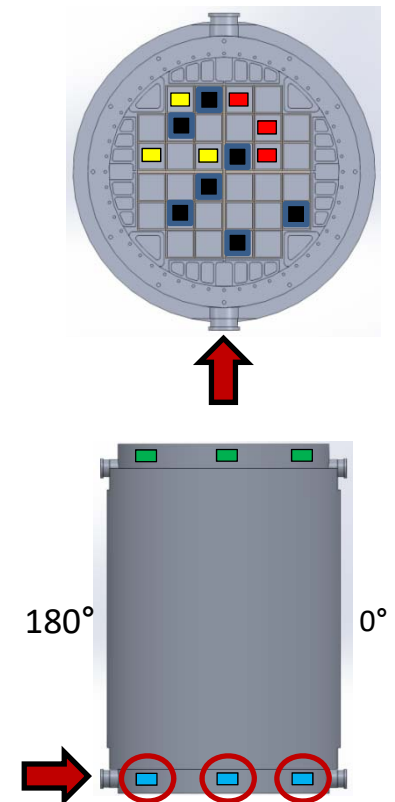
'Bottom Rim D3'

'Source - Lower Trunnion at 180 face'

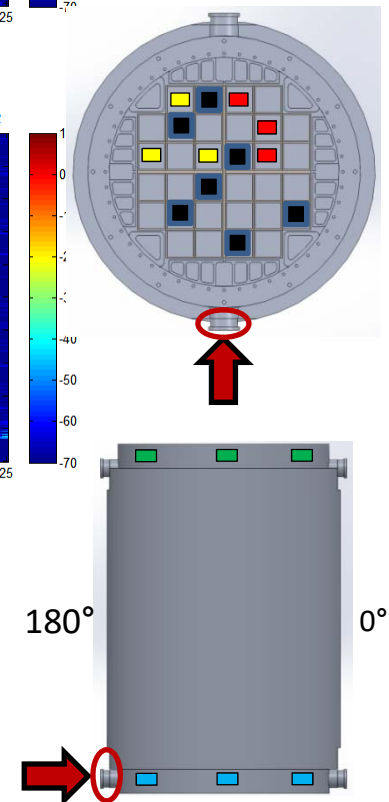
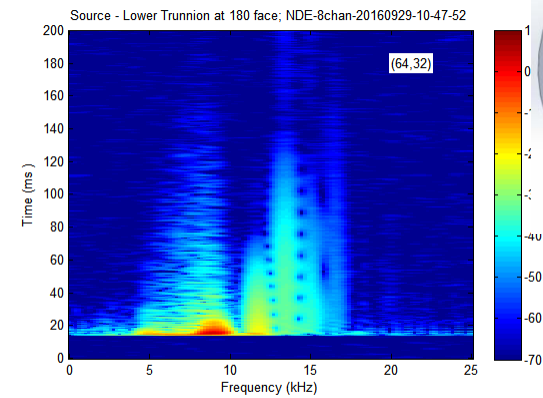
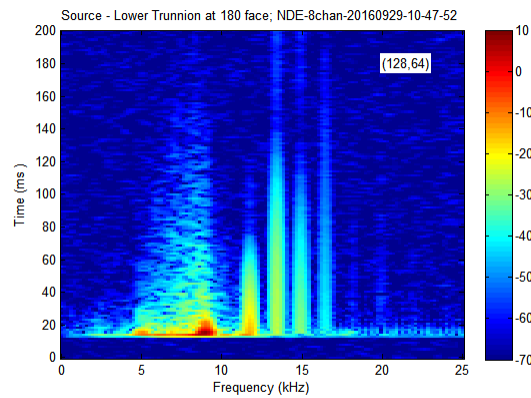
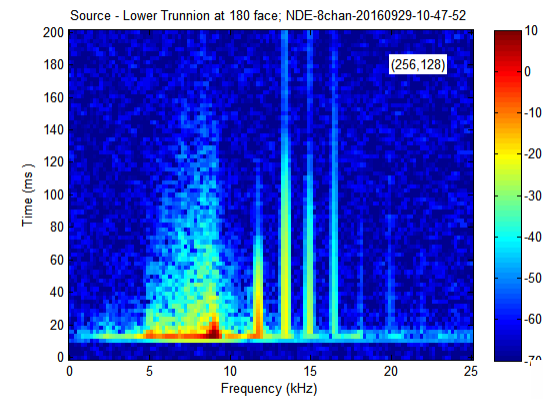
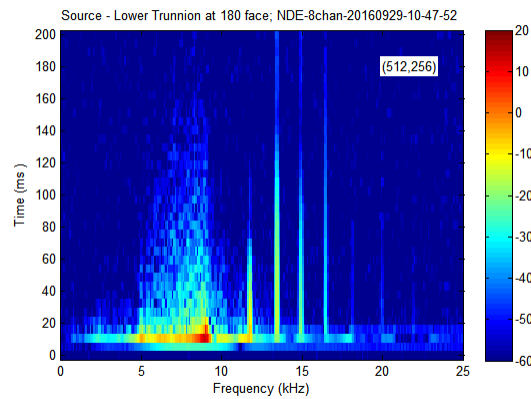
'Upper Trunnion at 180 face'

'Upper Trunnion at 0 face'

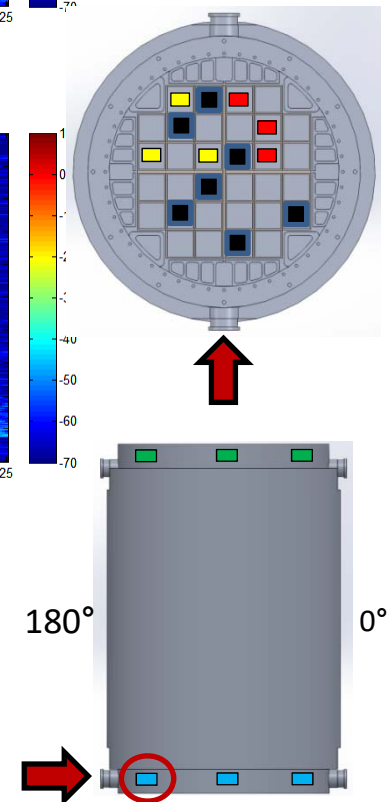
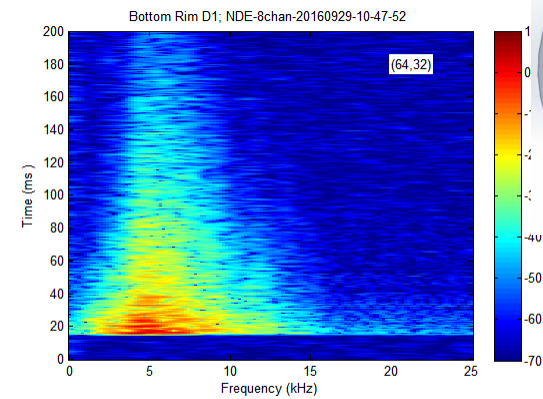
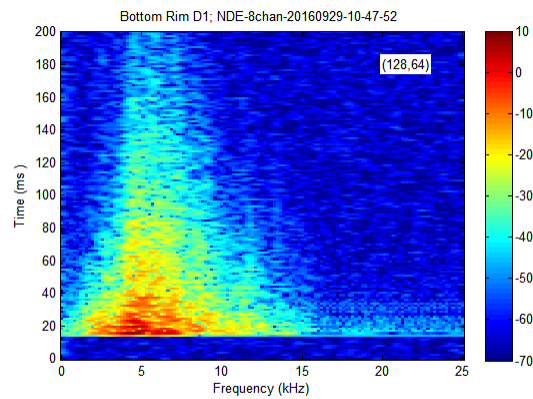
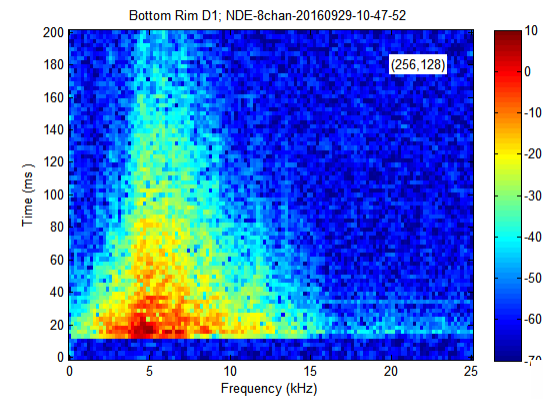
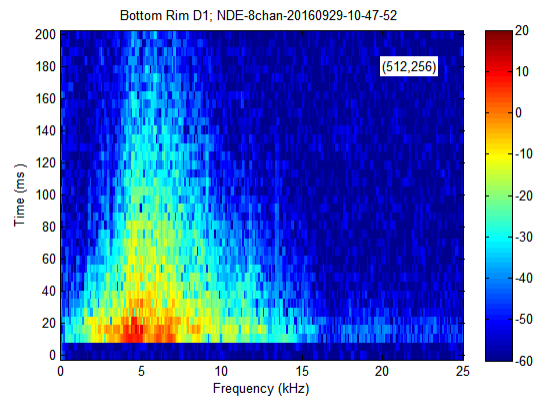
'Lower Trunnion at 0 face'



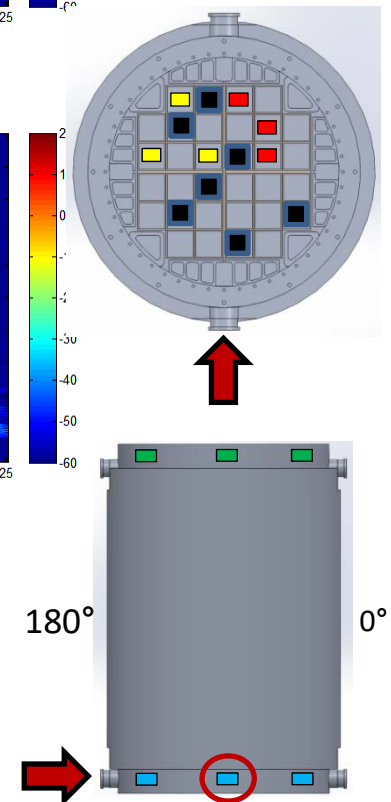
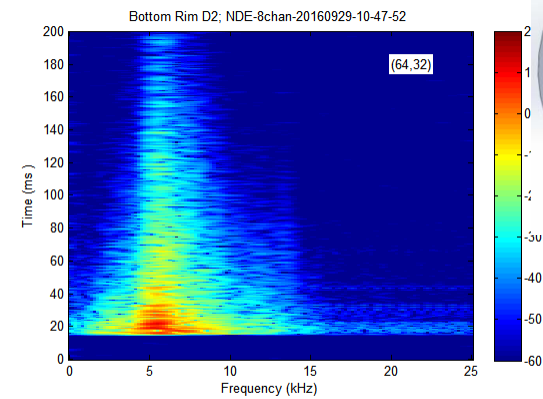
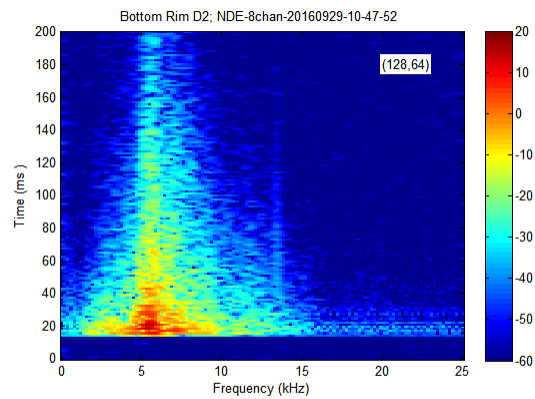
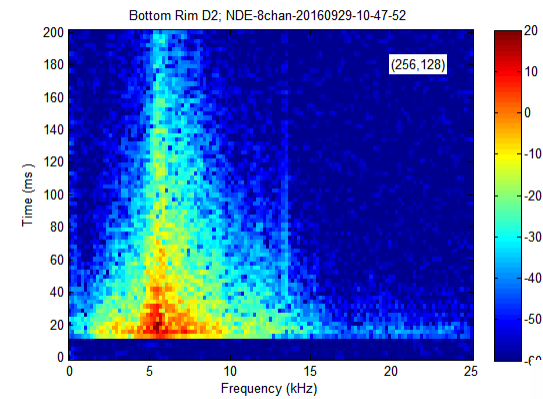
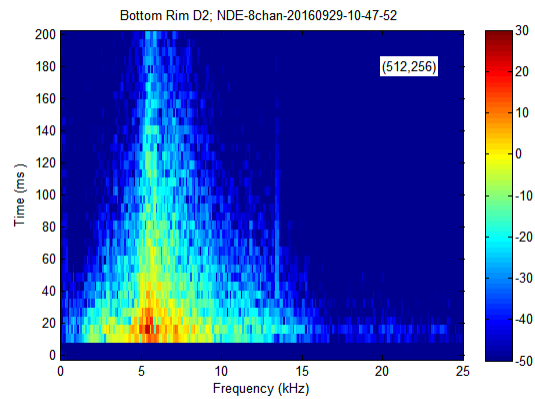
# Trunnion (Low) :Trigger



# Bottom Rim 1

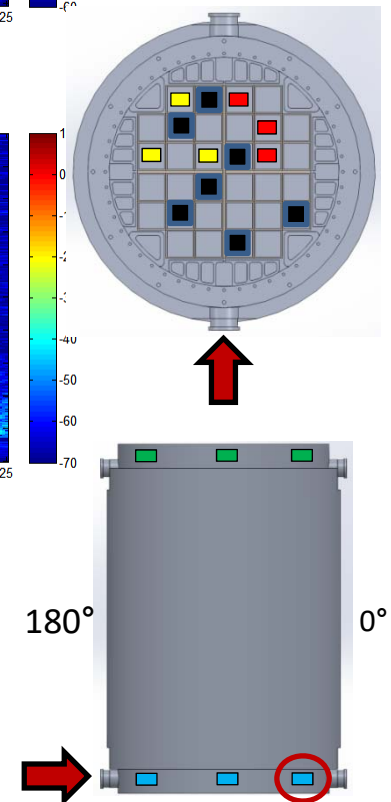
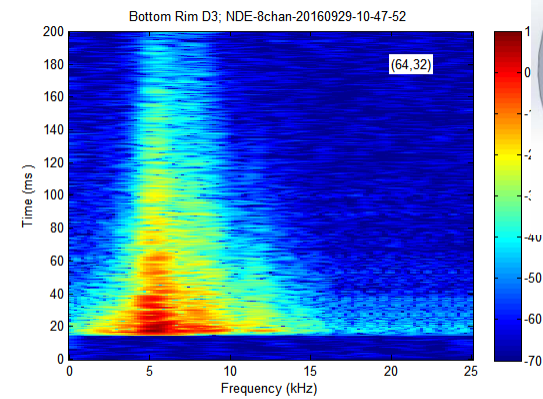
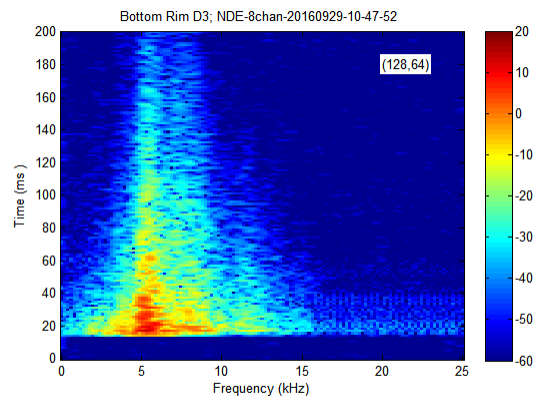
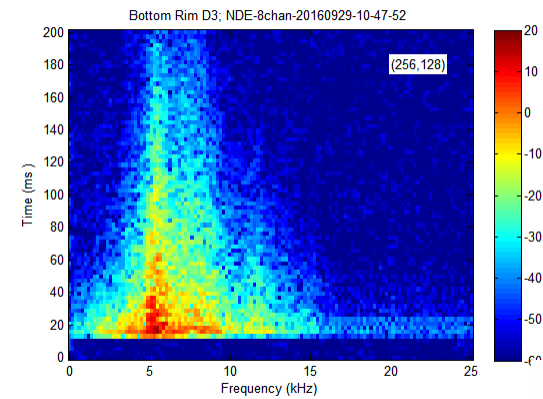
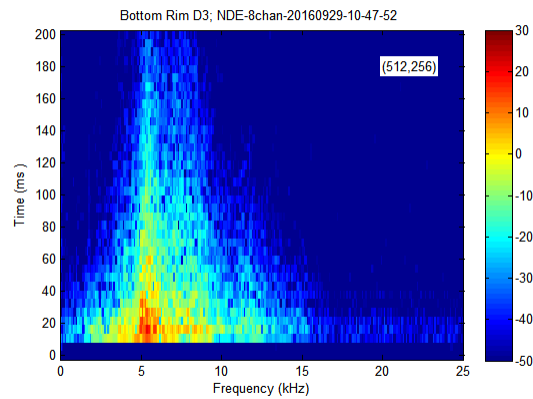


# Bottom Rim 2

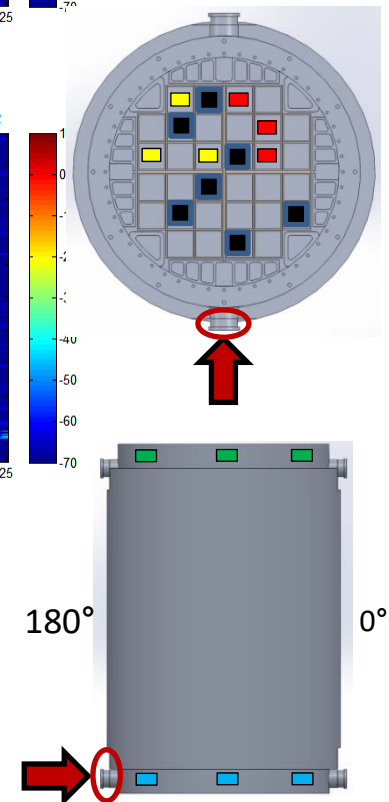
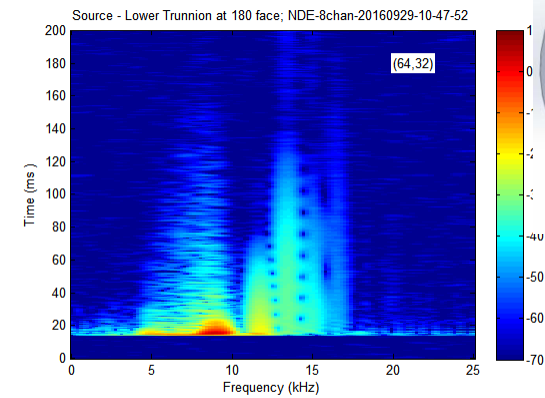
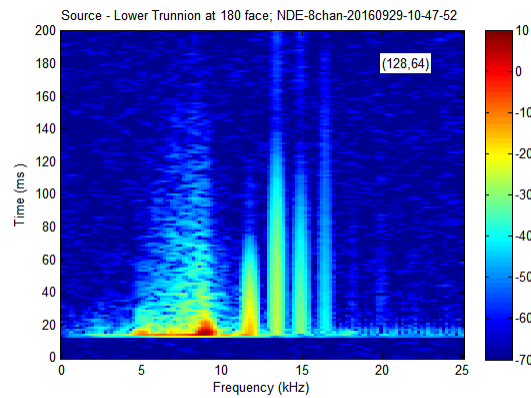
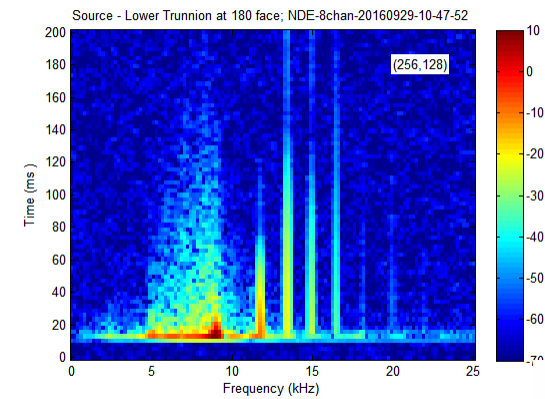
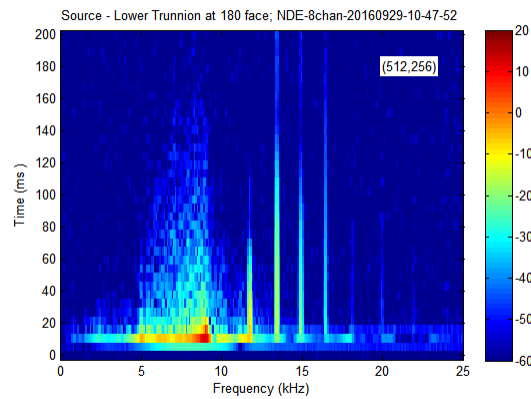




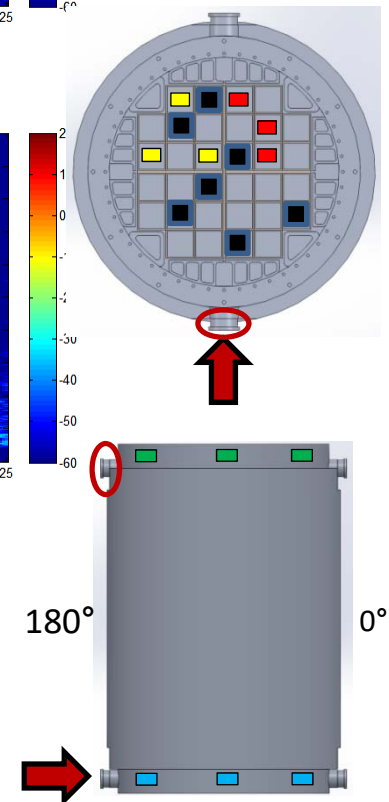
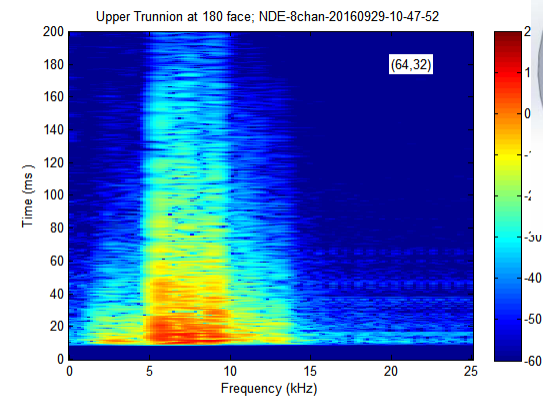
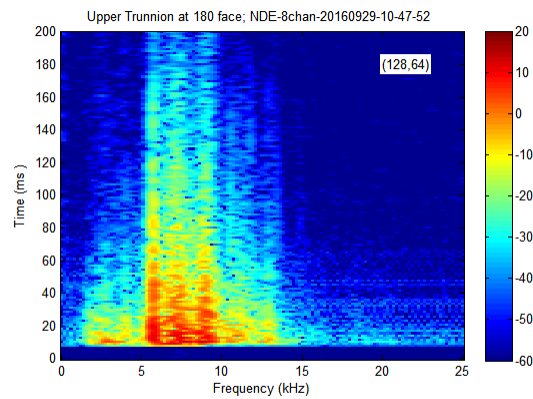
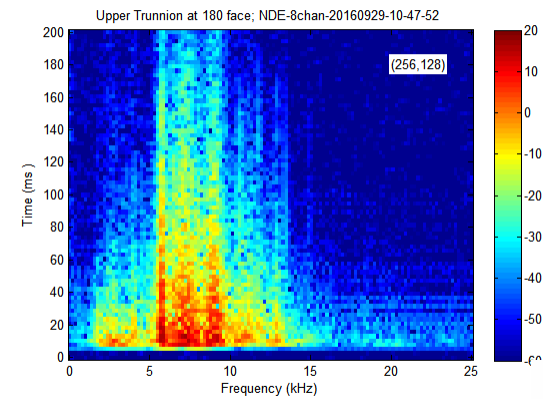
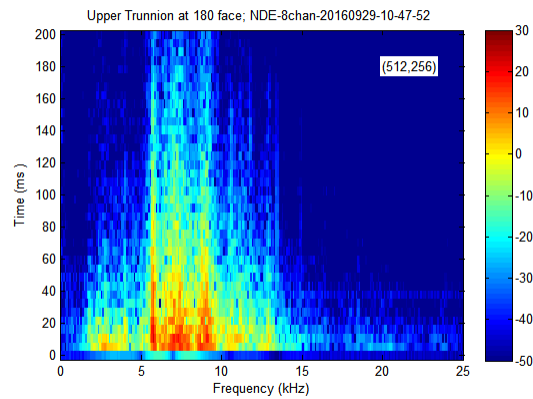
# Bottom Rim 3



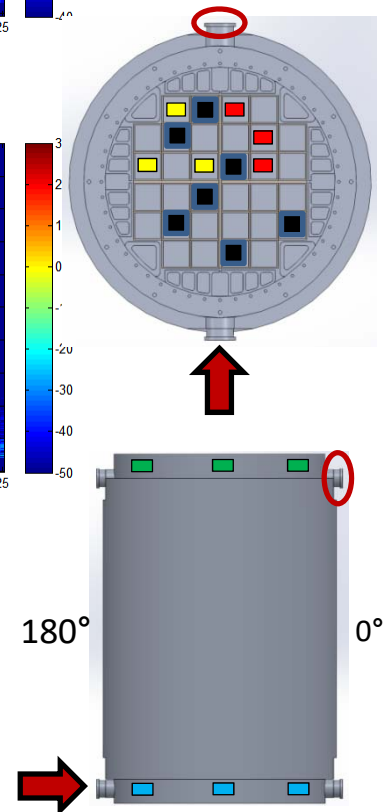
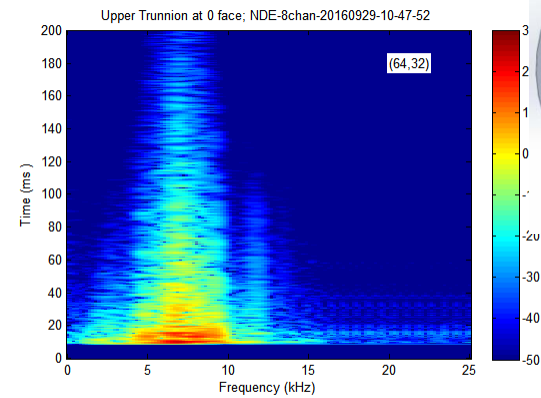
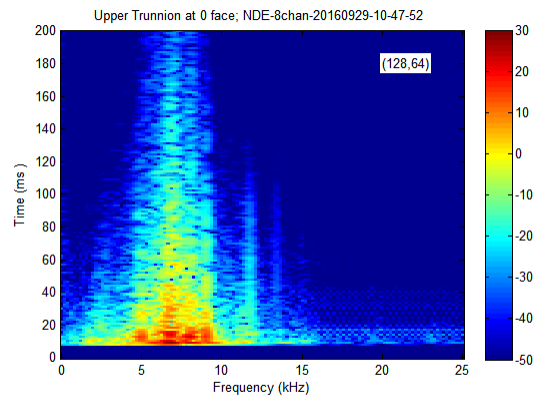
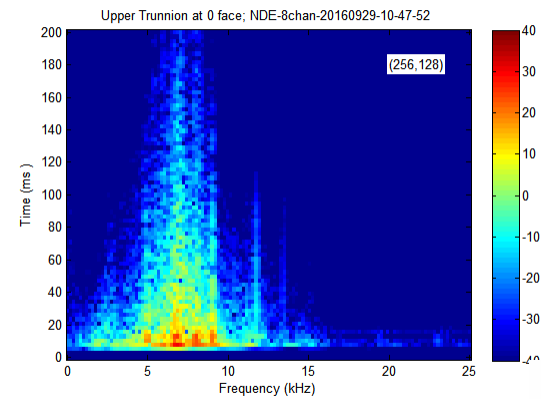
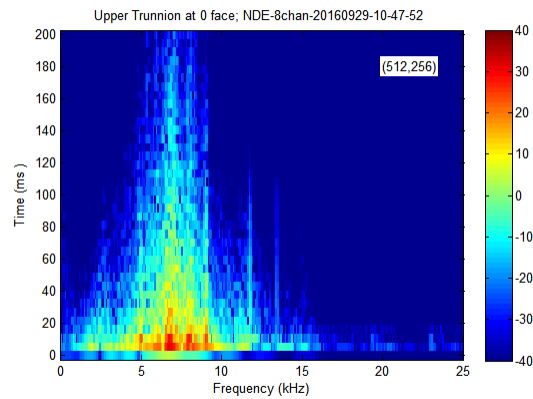
# Trunnion (Low) :Trigger (Box 2)



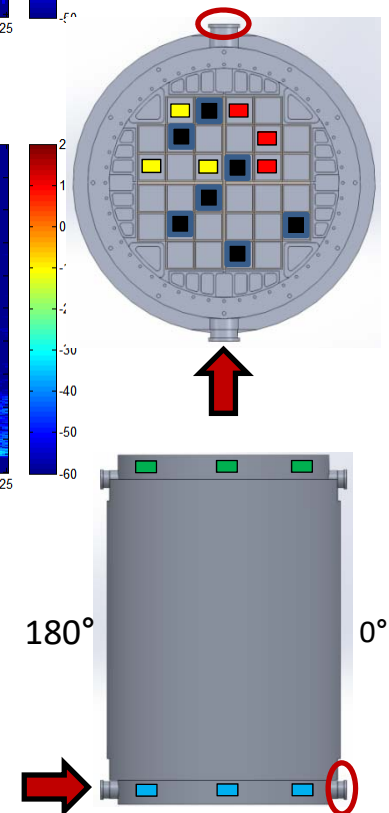
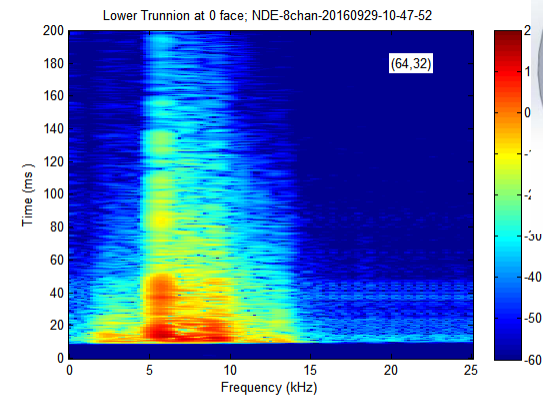
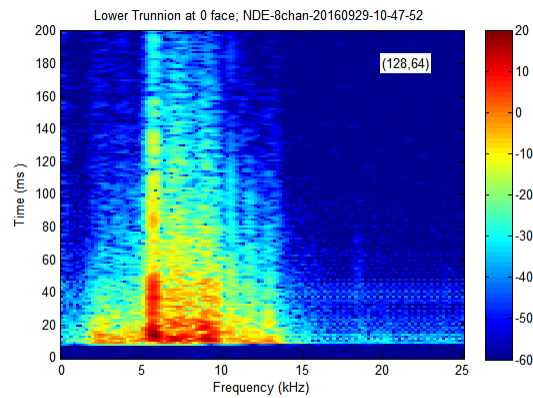
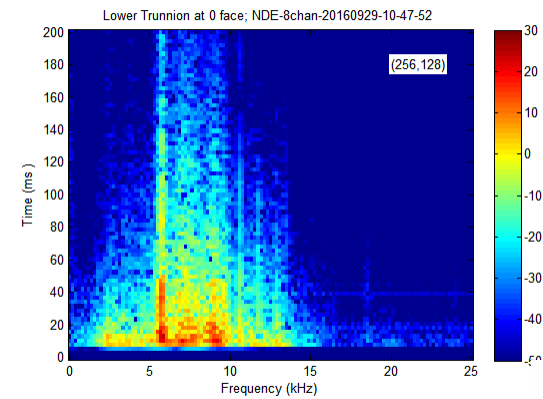
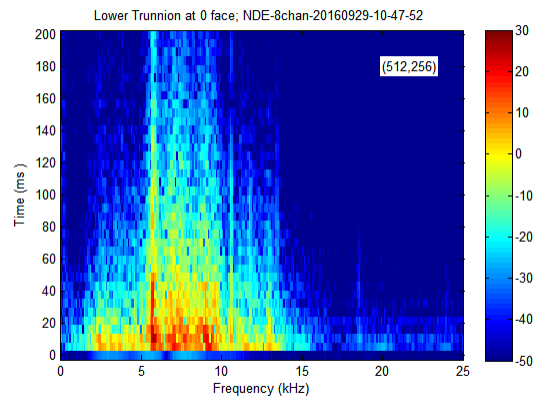
# Trunnion: Same Side



# Trunnion: Distal



# Trunnion: Proximal



# Appendix B

Setup, Data and Analysis from 2/22/17 CHT Trip

# CHT TN-32 Test Cask Field Test 2

## Test Procedure 1

Sensor	Serial #	ADC box	ADC channel	Location	Mo
Lock In - Out	LW211616	1,2	0,0	Source - Lower Trunnion 180 °, t4 box 2	Dir
AFMM 1	73600	1	1	Lower Rim D1	AFF
AFMM 2	73602	1	2	Lower Rim D2 (Lock-in input)	AFF
AFMM 3	60345	1	3	Lower Rim D3	AFF
CMM 1	73598	2	1	Lower Trunnion at 0° side	CM
CMM 2	60348	2	2	Upper Trunnion at 180° side	CM
CMM 3	60349	2	3	Upper Trunnion at 0° side	CM

## Test Procedure 2

Sensor	Serial #	ADC box	ADC channel	Location	Mo
Lock In - Out	LW211616	1,2	0,0	Source - Lower Trunnion 180 °, t4 box 2	Dir
AFMM 1	73600	1	1	Upper Rim D1	AFF
AFMM 2	73602	1	2	Upper Rim D2 (Lock-in input)	AFF
AFMM 3	60345	1	3	Upper Rim D3	AFF
CMM 1	73598	2	1	Lower Trunnion at 0° side	CM
CMM 2	60348	2	2	Upper Trunnion at 180° side	CM
CMM 3	60349	2	3	Upper Trunnion at 0° side	CM

## Test Procedure 3

Sensor	Serial #	ADC box	ADC channel	Location	Mo
Lock In - Out	LW211616	1,2	0,0	Source - Upper Trunnion 180 °, t4 box 2	Dir
AFMM 1	73600	1	1	Upper Rim D1	AFF
AFMM 2	73602	1	2	Upper Rim D2 (Lock-in input)	AFF
AFMM 3	60345	1	3	Upper Rim D3	AFF
CMM 1	73598	2	1	Lower Trunnion at 0° side	CM
CMM 2	60348	2	2	Lower Trunnion at 180° side	CM
CMM 3	60349	2	3	Upper Trunnion at 0° side	CM

## Test Procedure 4

Sensor	Serial #	ADC box	ADC channel	Location	Mo
Lock In - Out	LW211616	1,2	0,0	Source - Upper Trunnion 180 °, t4 box 2	Dir
AFMM 1	73600	1	1	Lower Rim D1	AFF
AFMM 2	73602	1	2	Lower Rim D2 (Lock-in input)	AFF
AFMM 3	60345	1	3	Lower Rim D3	AFF
CMM 1	73598	2	1	Lower Trunnion at 0° side	CM
CMM 2	60348	2	2	Lower Trunnion at 180° side	CM
CMM 3	60349	2	3	Upper Trunnion at 0° side	CM

## Test Procedure 5

Sensor	Serial #	ADC box	ADC channel	Location	Mo
AFMM 4	LW211616	1,2	0,0	Ping - Upper Trunnion 180	AFF
AFMM 1	73600	1	1	Lower Rim D1	AFF
AFMM 2	73602	1	2	Lower Rim D2	AFF
AFMM 3	60345	1	3	Lower Rim D3	AFF
CMM 1	73598	2	1	Lower Trunnion at 0° side	CM
CMM 2	60348	2	2	Lower Trunnion at 180° side	CM
CMM 3	60349	2	3	Upper Trunnion at 0° side	CM

**Test Procedure 6**

Sensor	Serial #	ADC box	ADC channel	Location	Mo
AFMM 4	LW211616	1,2	0,0	Upper Trunnion 180	AFF
AFMM 1	73600	1	1	Lower Rim D1	AFF
AFMM 2	73602	1	2	Lower Rim D2	AFF
AFMM 3	60345	1	3	Lower Rim D3	AFF
CMM 1	73598	2	1	Lower Trunnion at 0° side	CM
CMM 2	60348	2	2	Lower Trunnion at 180° side	CM
CMM 3	60349	2	3	Upper Trunnion at 0° side	CM

**Test Procedure 7**

Sensor	Serial #	ADC box	ADC channel	Location	Mo
AFMM 4	LW211616	1,2	0,0	Ping - Lower Trunnion 180	AFF
AFMM 1	73600	1	1	Lower Rim D1	AFF
AFMM 2	73602	1	2	Lower Rim D2	AFF
AFMM 3	60345	1	3	Lower Rim D3	AFF
CMM 1	73598	2	1	Lower Trunnion at 0° side	CM
CMM 2	60348	2	2	Upper Trunnion at 180° side	CM
CMM 3	60349	2	3	Upper Trunnion at 0° side	CM

**Test Procedure 8**

Sensor	Serial #	ADC box	ADC channel	Location	Mo
AFMM 4	LW211616	1,2	0,0	Lower Trunnion 180°	AFF
AFMM 1	73600	1	1	Lower Rim D1	AFF
AFMM 2	73602	1	2	Lower Rim D2	AFF
AFMM 3	60345	1	3	Lower Rim D3	AFF
CMM 1	73598	2	1	Lower Trunnion at 0° side	CM
CMM 2	60348	2	2	Upper Trunnion at 180° side	CM
CMM 3	60349	2	3	Upper Trunnion at 0° side	CM

**Test Procedure 9**

Sensor	Serial #	ADC box	ADC channel	Location	Mo
AFMM 4	LW211616	1,2	0,0	Ping - Lower Trunnion 180°	AFF
AFMM 1	73600	1	1	Upper Rim D1	AFF
AFMM 2	73602	1	2	Upper Rim D2	AFF
AFMM 3	60345	1	3	Upper Rim D3	AFF
CMM 1	73598	2	1	Lower Trunnion at 0° side	CM
CMM 2	60348	2	2	Upper Trunnion at 180° side	CM
CMM 3	60349	2	3	Upper Trunnion at 0° side	CM

**Test Procedure 10**

Sensor	Serial #	ADC box	ADC channel	Location	Mo
AFMM 4	LW211616	1,2	0,0	Lower Trunnion 180°	AFF
AFMM 1	73600	1	1	Upper Rim D1	AFF
AFMM 2	73602	1	2	Upper Rim D2	AFF
AFMM 3	60345	1	3	Upper Rim D3	AFF
CMM 1	73598	2	1	Lower Trunnion at 0° side	CM
CMM 2	60348	2	2	Upper Trunnion at 180° side	CM
CMM 3	60349	2	3	Upper Trunnion at 0° side	CM

**Test Procedure 11**

Sensor	Serial #	ADC box	ADC channel	Location	Mo
AFMM 4	LW211616	1,2	0,0	Ping - Upper Trunnion 180°	AFF
AFMM 1	73600	1	1	Upper Rim D1	AFF
AFMM 2	73602	1	2	Upper Rim D2	AFF

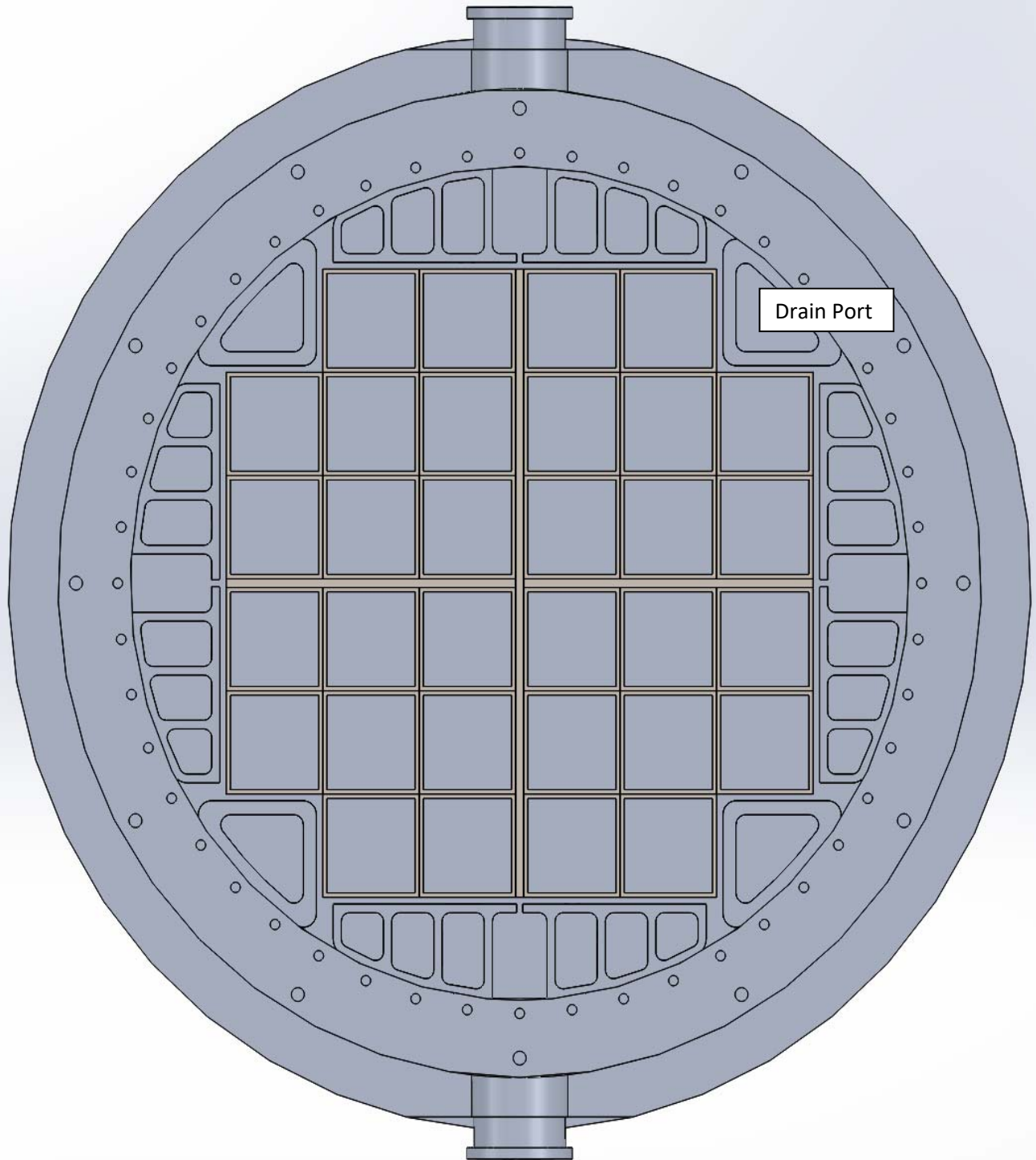


AFMM 3	60345	1	3	Upper Rim D3	AFF
CMM 1	73598	2	1	Lower Trunnion at 0° side	CM
CMM 2	60348	2	2	Lower Trunnion at 180° side	CM
CMM 3	60349	2	3	Upper Trunnion at 0° side	CM

#### **Test Procedure 12**

<b>Sensor</b>	<b>Serial #</b>	<b>ADC box</b>	<b>ADC channel</b>	<b>Location</b>	<b>Mo</b>
AFMM 4	LW211616	1,2	0,0	Upper Trunnion 180 °	AFF
AFMM 1	73600	1	1	Upper Rim D1	AFF
AFMM 2	73602	1	2	Upper Rim D2	AFF
AFMM 3	60345	1	3	Upper Rim D3	AFF
CMM 1	73598	2	1	Lower Trunnion at 0° side	CM
CMM 2	60348	2	2	Lower Trunnion at 180° side	CM
CMM 3	60349	2	3	Upper Trunnion at 0° side	CM

Lower Trunnion, Upper Trunnion - 0°

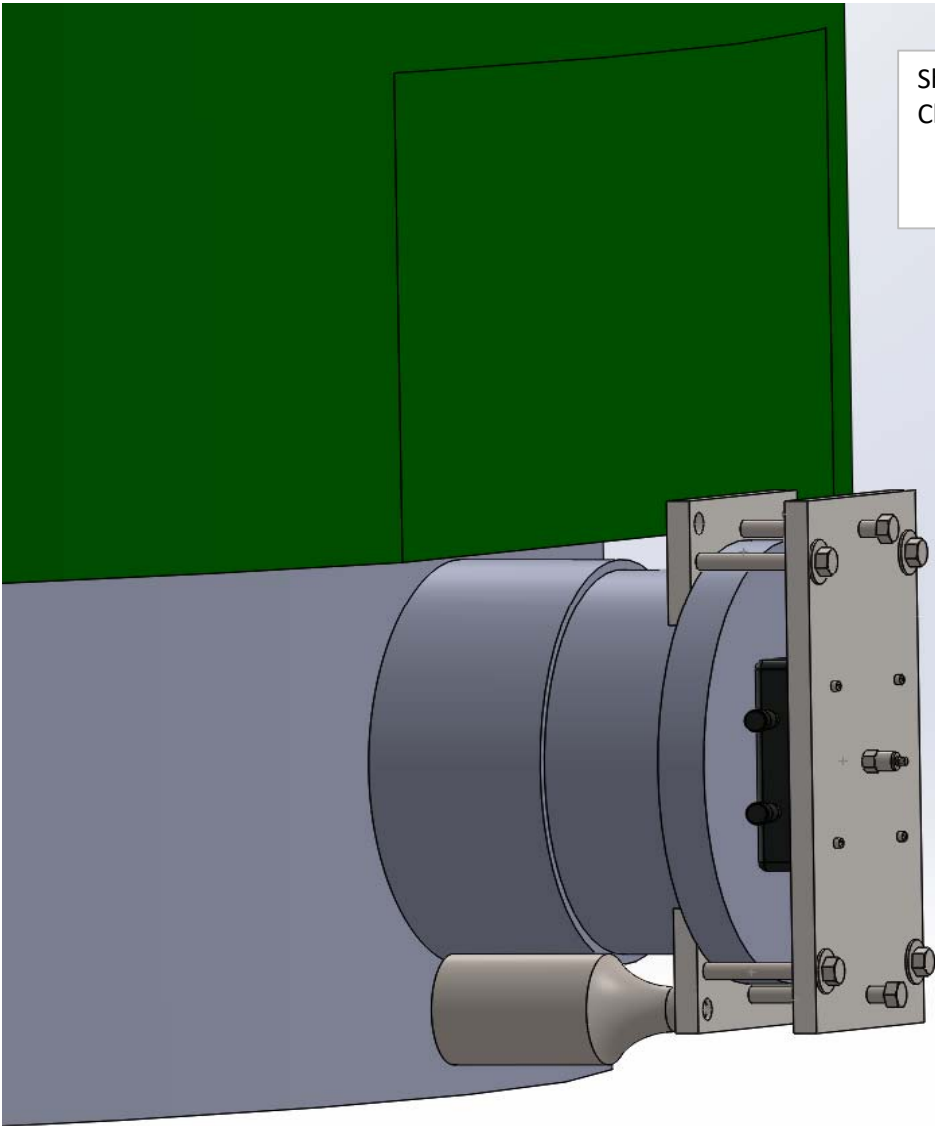


Drain Port

Lower Trunnion, Upper Trunnion - 180°



Shaker Mounting using Trunnion  
Clamp



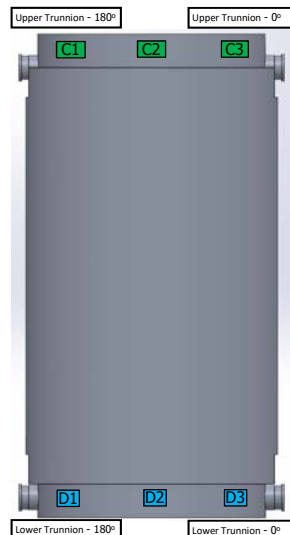


# TN-32 CHT Acoustic Test

## February 22, 2017



- Impulsive & Continuous Sources
- 7 accelerometer broadband data acquisition system
- 12 source/sensor arrangements
  - Sensor placement
    - ◆ Trunnions
    - ◆ Rims

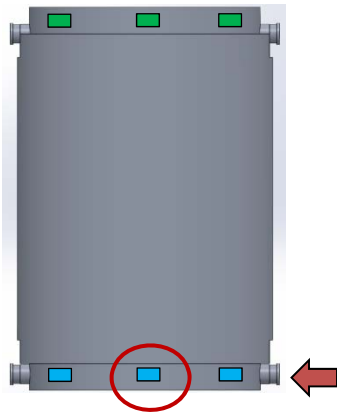


Impulsive  
Source



Continuous  
Source

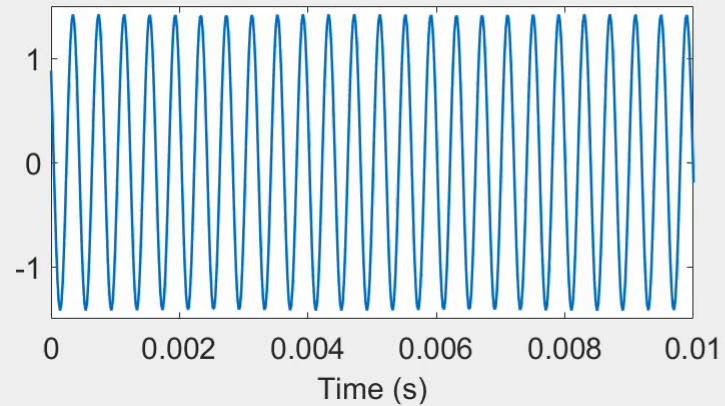




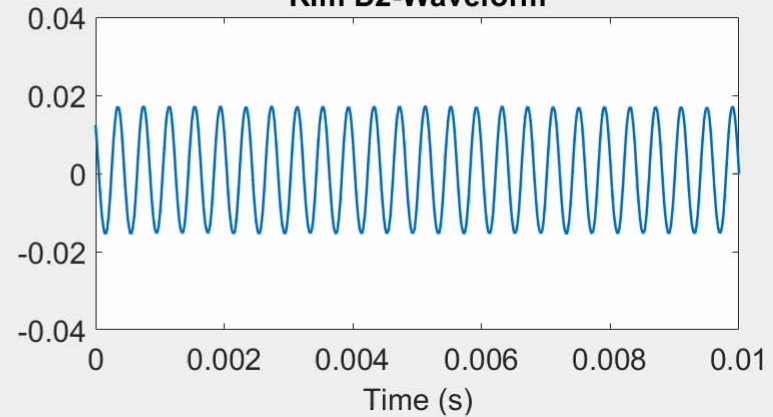
# Continuous Source Data



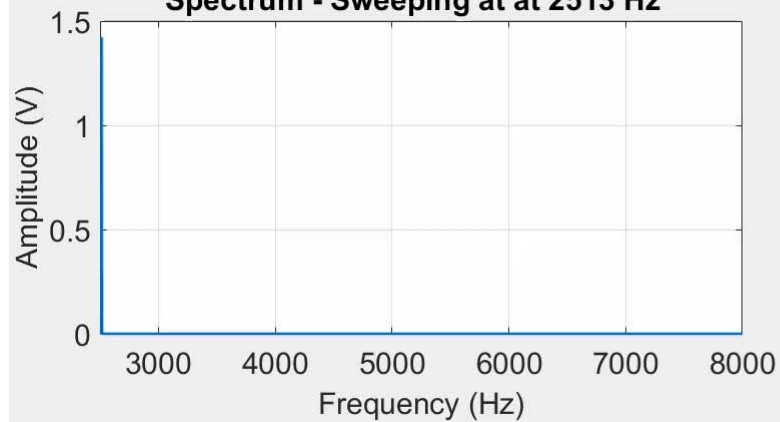
Source-Waveform



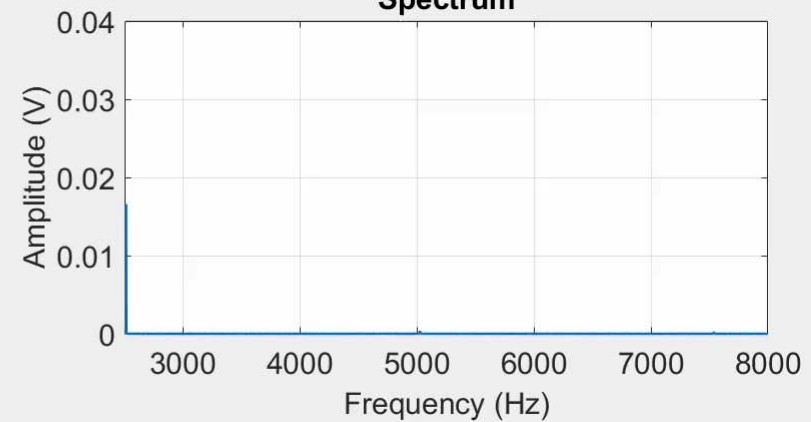
Rim D2-Waveform

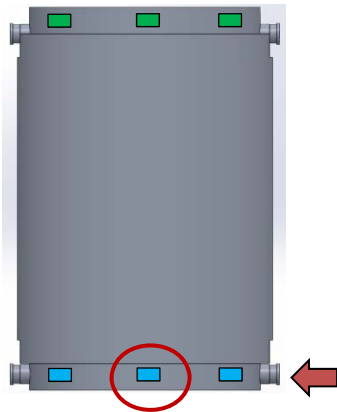


Spectrum - Sweeping at at 2513 Hz



Spectrum

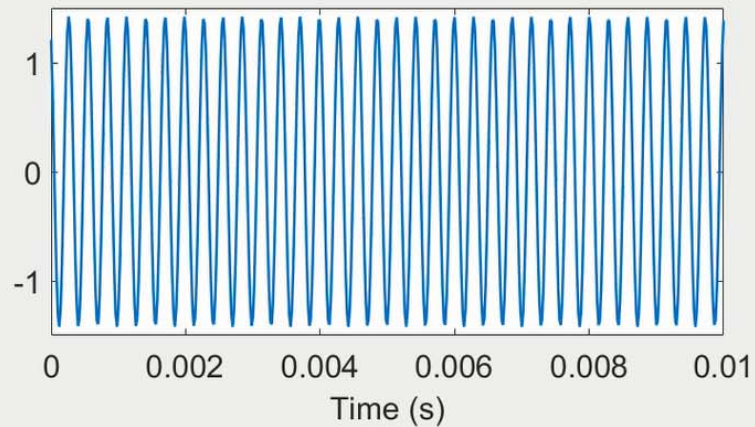




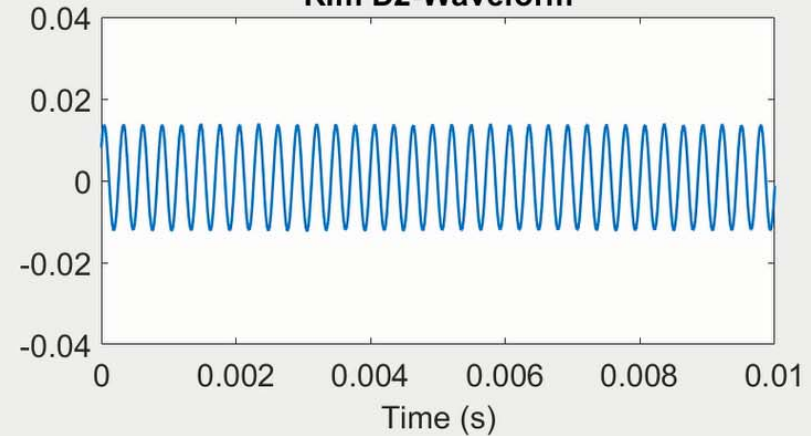
# Continuous Source Data



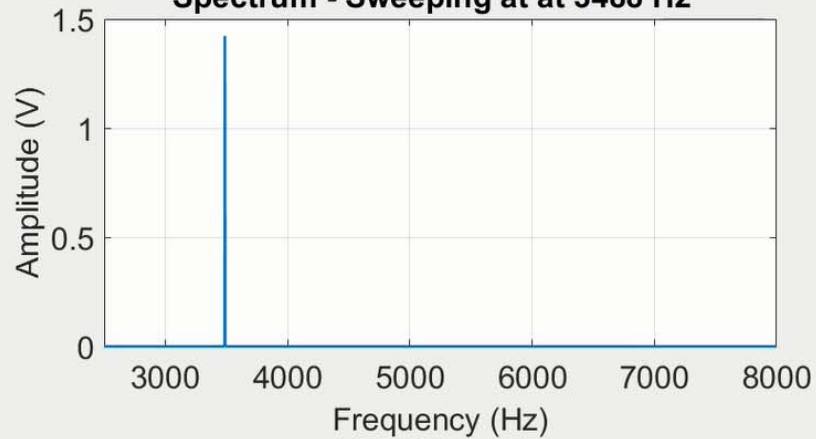
Source-Waveform



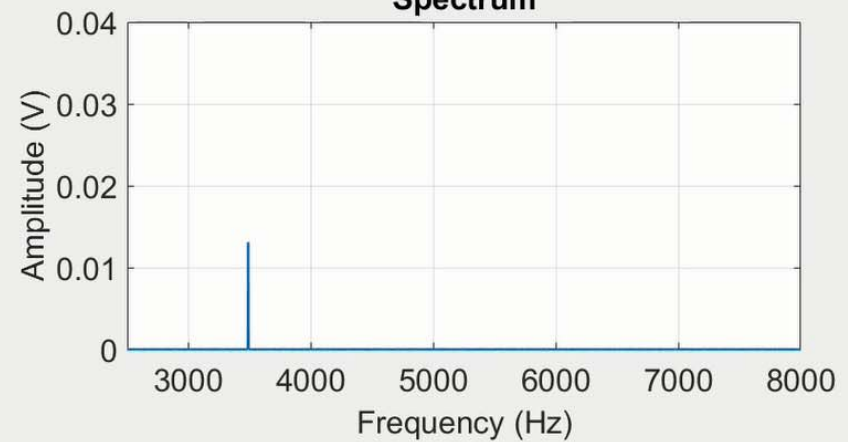
Rim D2-Waveform



Spectrum - Sweeping at at 3488 Hz



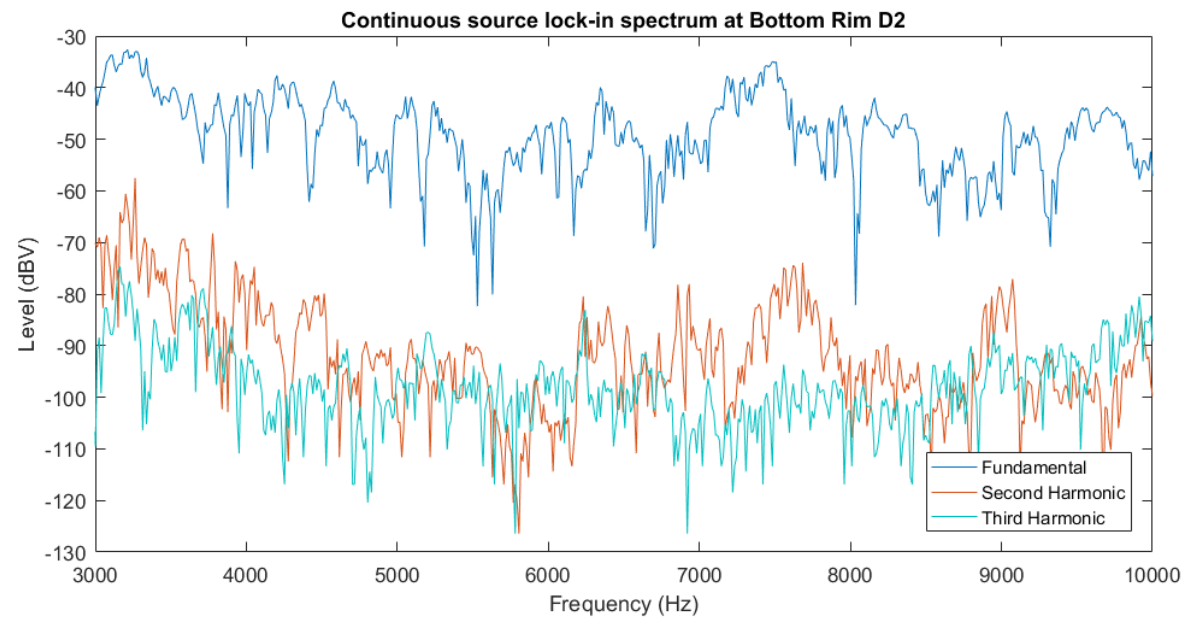
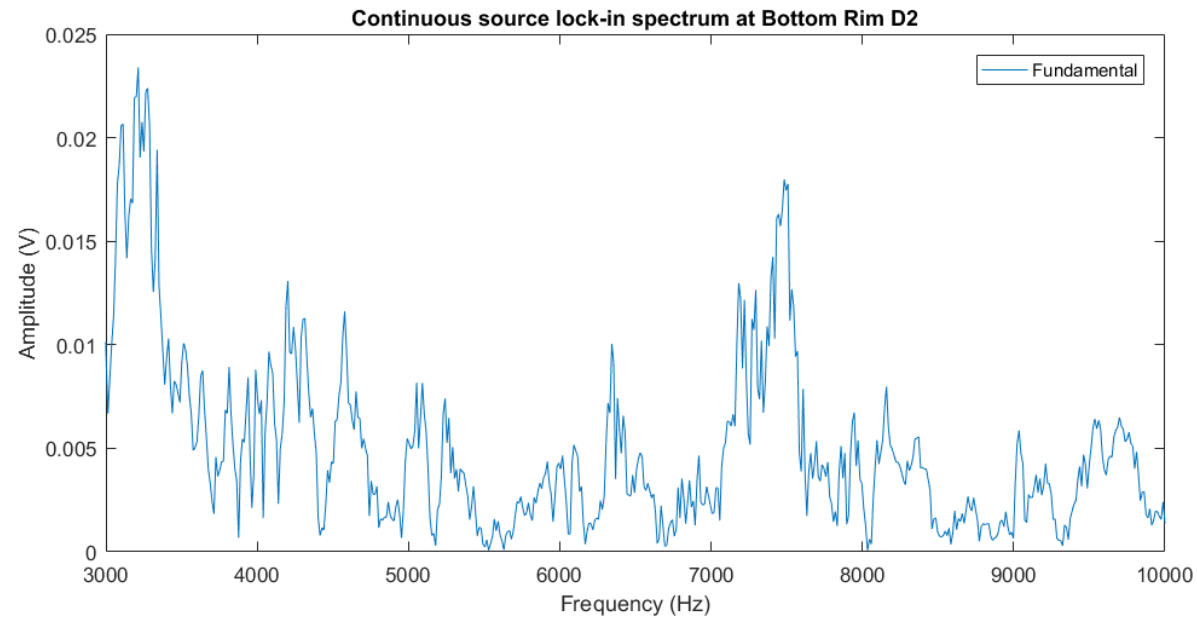
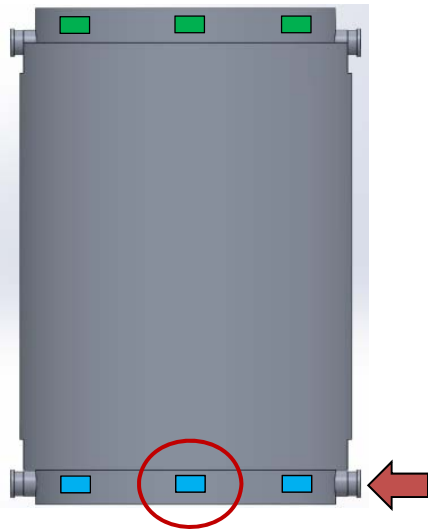
Spectrum







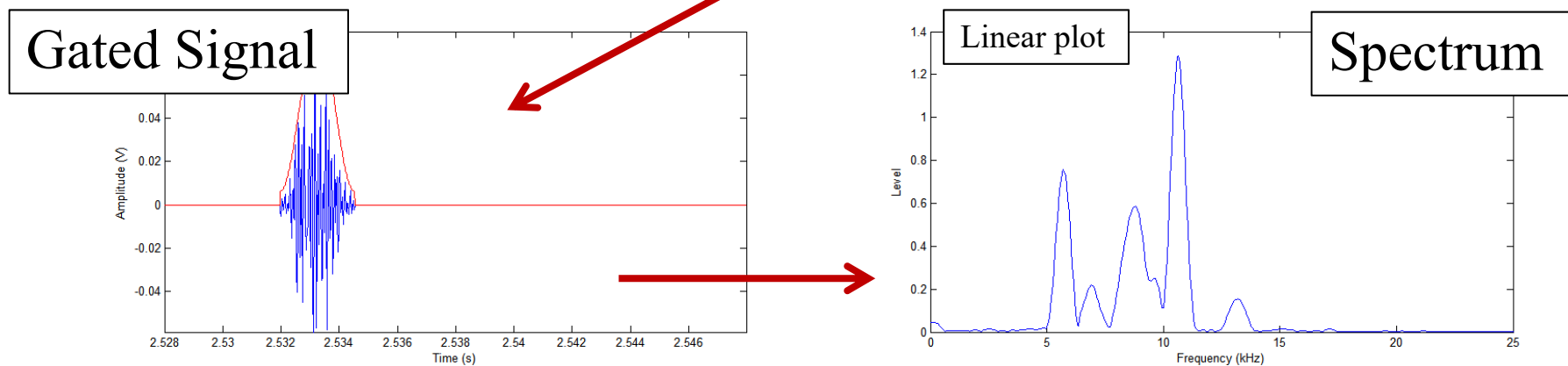
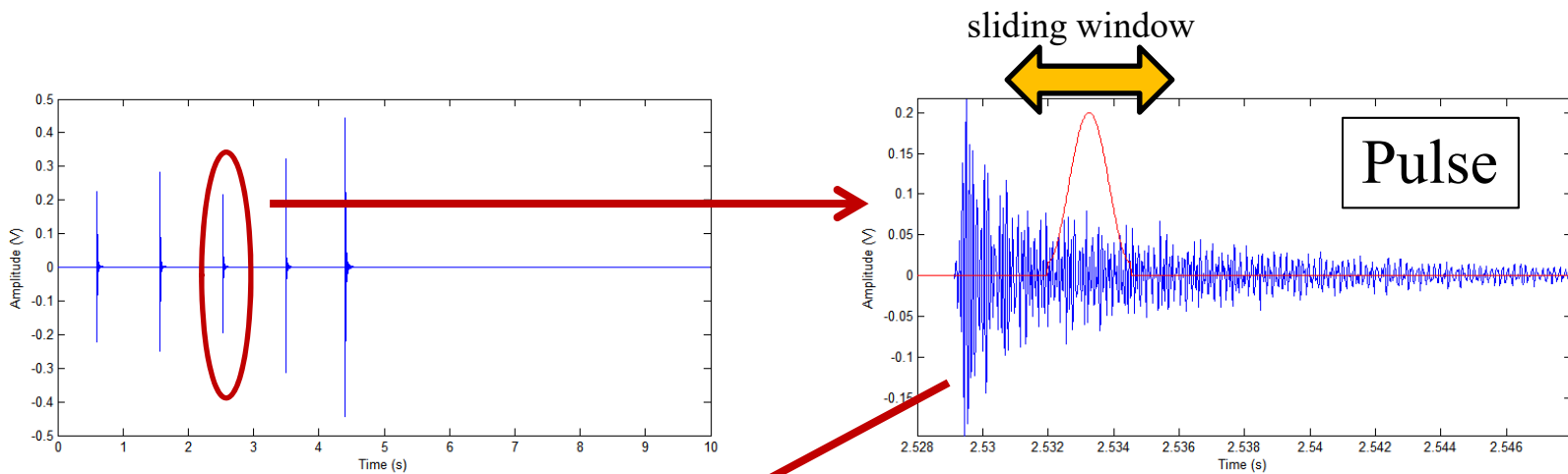
# Continuous Source Data





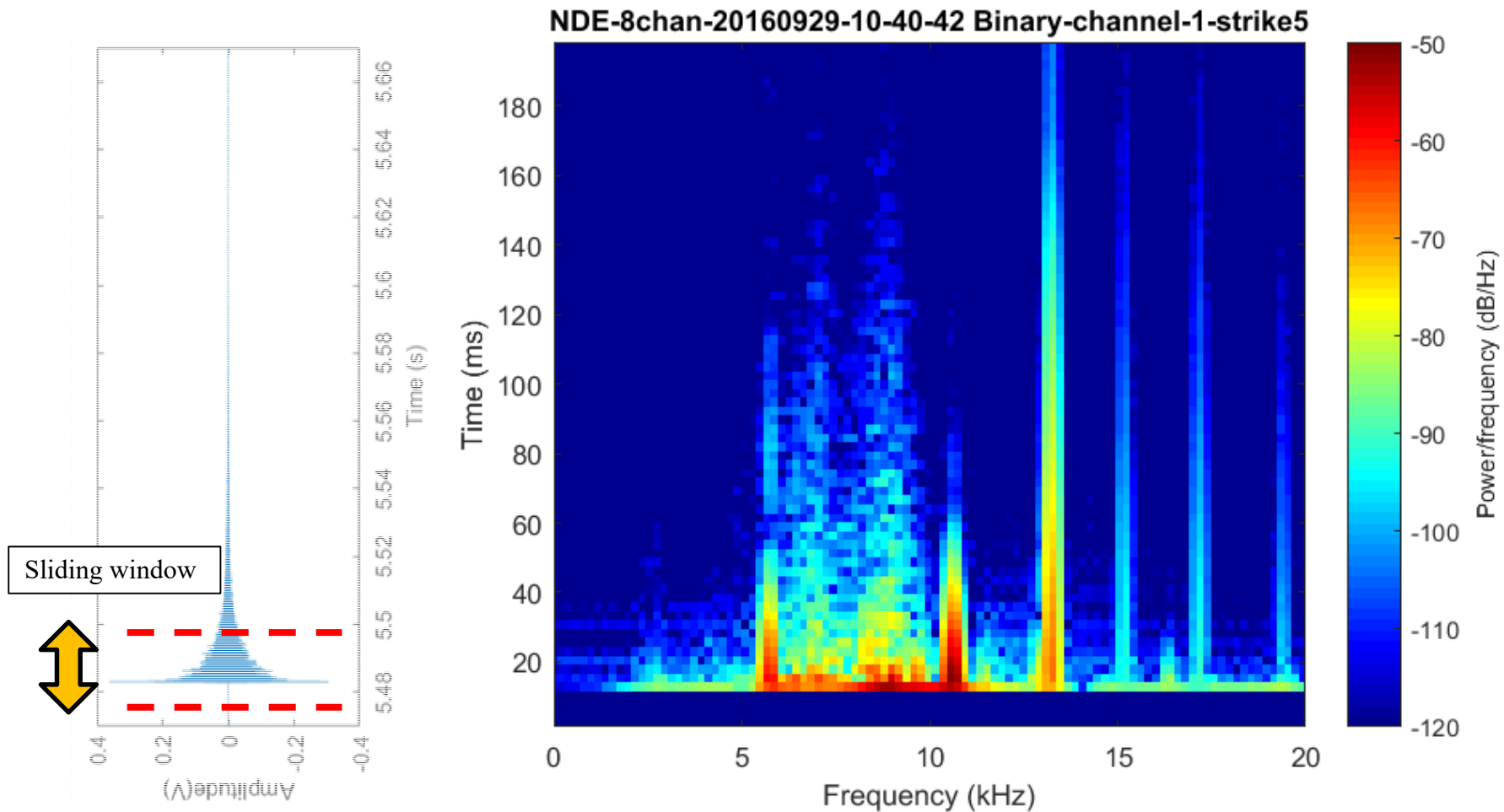


# Time-Frequency Technique on Impulse Data





# Spectrogram



Lower Trunnion – Impact Source



# Mode Identification and Quality Factor

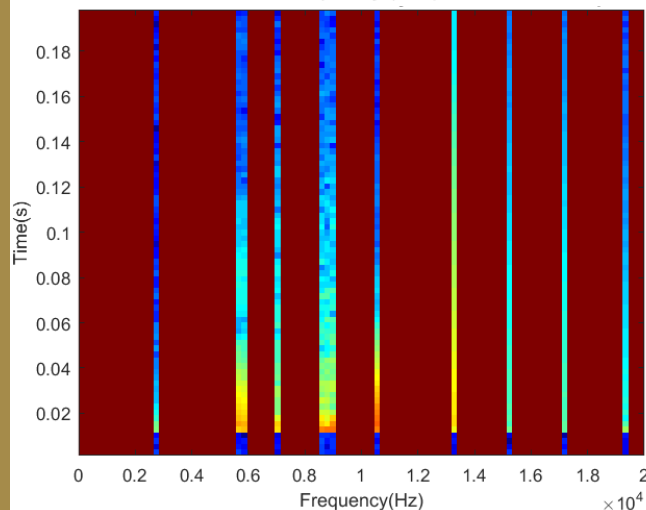
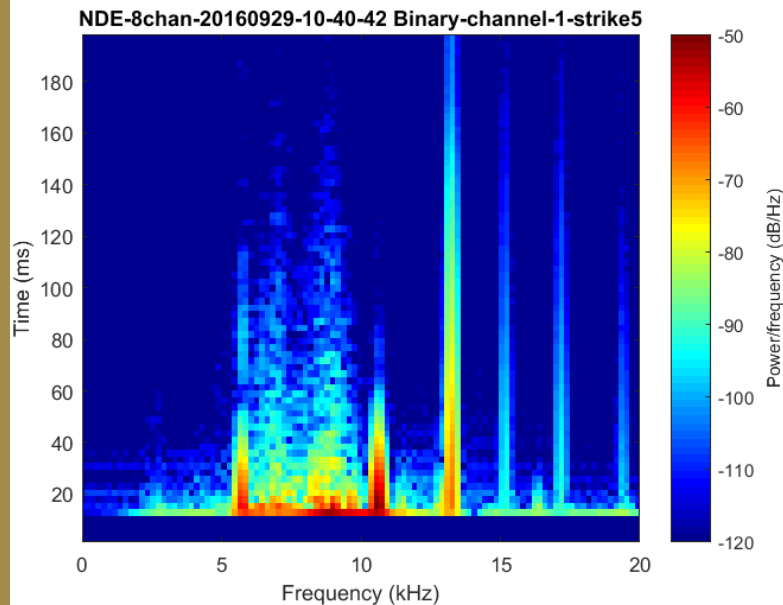


## Goals:

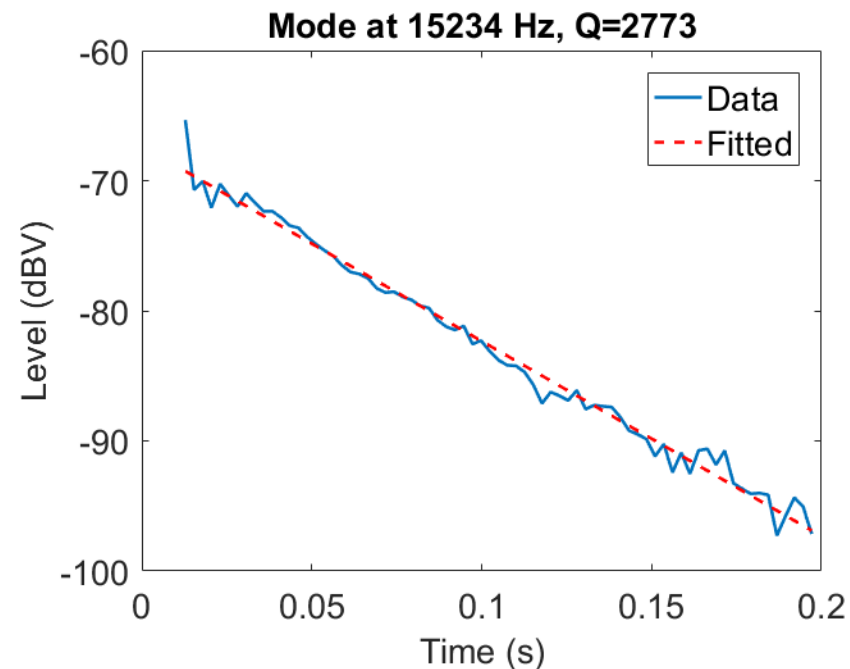
- Identify modes from impulse data
- Time evolution of modes (Q-value)

## Work in progress:

- Algorithm for mode identification
- Comparison with FEM



Lower Trunnion – Impact Source





# Mode Identification and Quality Factor

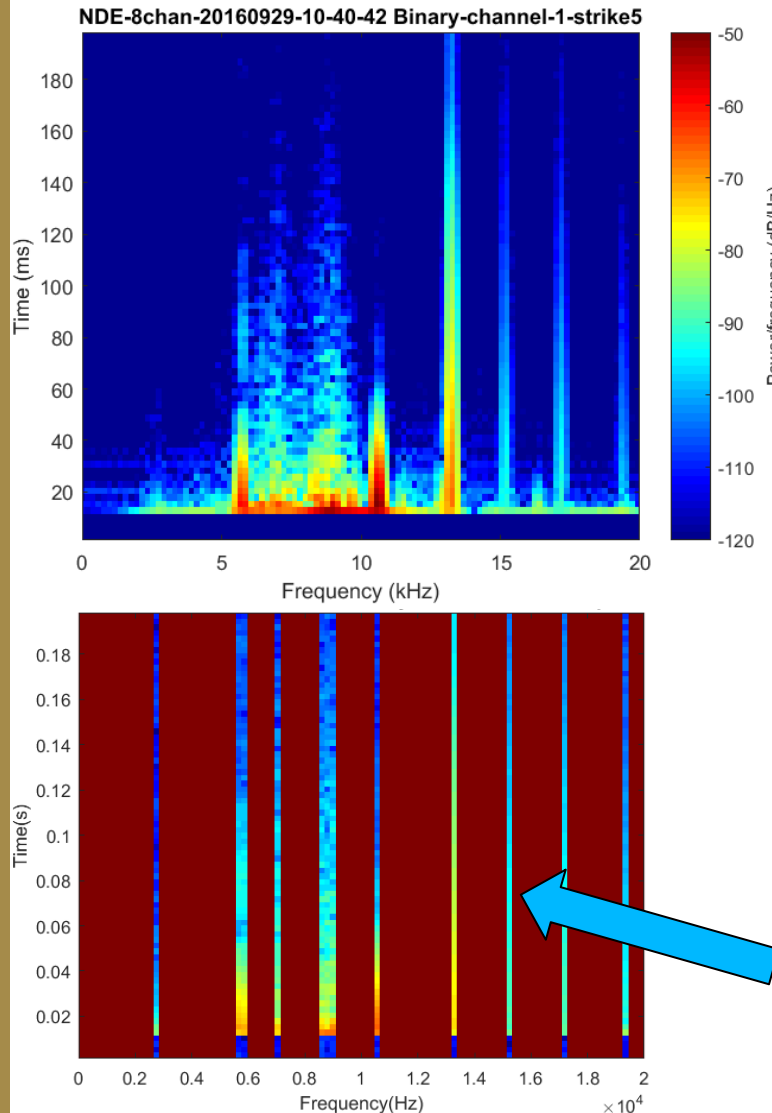


## Goals:

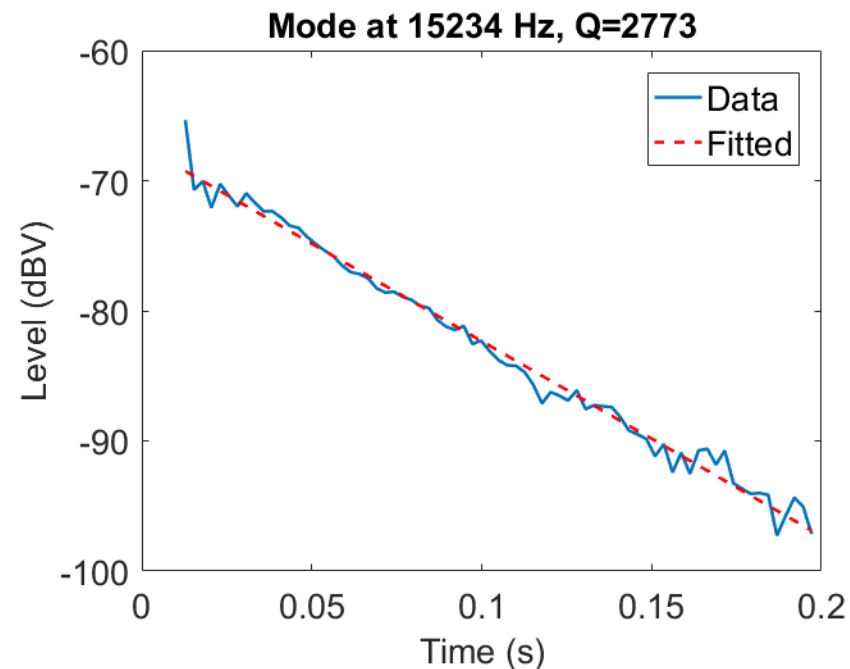
- Identify modes from impulse data
- Time evolution of modes (Q-value)

## Work in progress:

- Algorithm for mode identification
- Comparison with FEM



Lower Trunnion – Impact Source

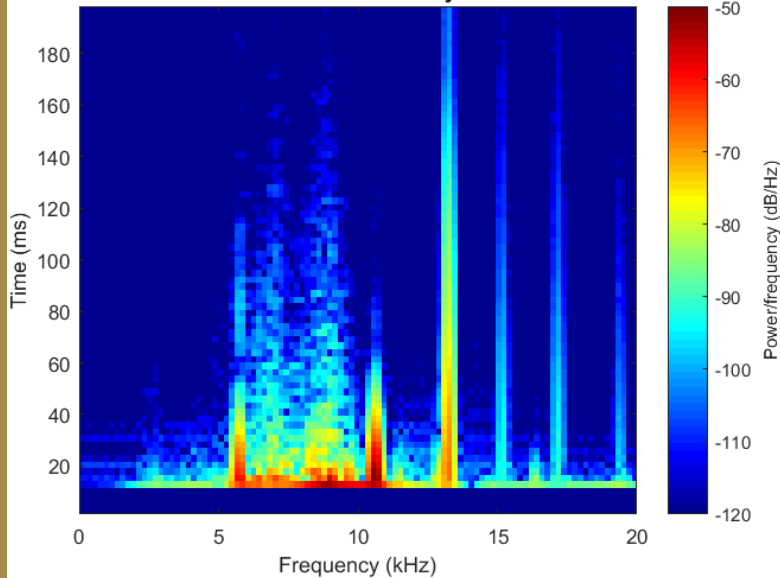




# Mode Identification and Quality Factor

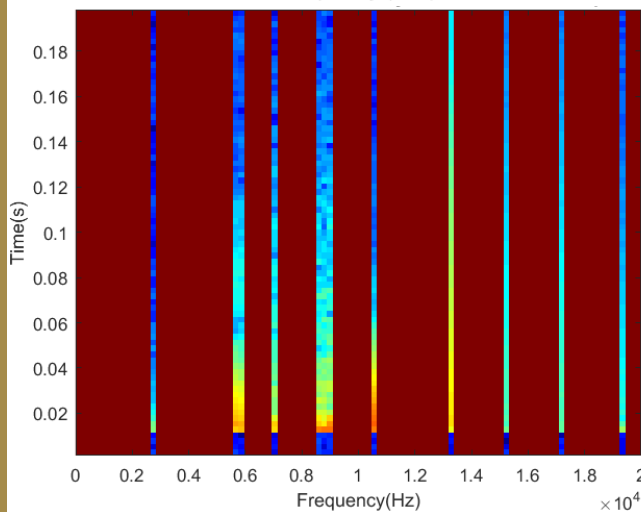


NDE-8chan-20160929-10-40-42 Binary-channel-1-strike5



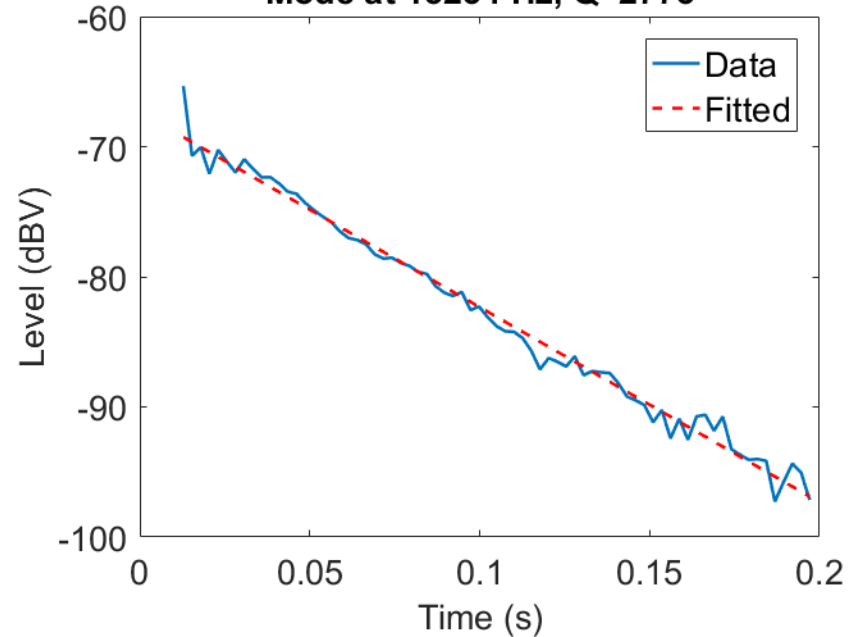
Modes:

Frequency (Hz)	2734	5762	7031	8789	10547
Q	126	480	712	901	450
Frequency (Hz)	13281	15234	17188	19336	21875
Q	1730	2773	3055	3108	3287



Lower Trunnion – Impact Source

Mode at 15234 Hz, Q=2773



# Appendix C

Setup and photo from 9/19/17 CHT Trip

# CHT TN-32 Test Cask Field Test 3 (Final)

Everything is driven at 21.8V output from the amplifier

## Test Procedure 1

Sweep

Sensor	Serial #	ADC box	ADC channel	Location
Shaker	LW211616	1,2	0,0	Source - Lower Trunnion 180°
CMM 1		1	1	Sine out
CMM 2	73598	1	2	Lower Rim D2
CMM 3	73604	1	3	Lower Rim D3
AFMM 1	73600	2	1	Lower Rim D4
AFMM 2	60349	2	2	Lower Rim D5
AFMM 3	60345	2	3	Lower Trunnion at 0° side
	73596			Lower Rim D1 (to lock-in)

## Test Procedure 2

Ping, Dead Blow

Sensor	Serial #	ADC box	ADC channel	Location
Shaker	LW211616	1,2	0,0	Upper Rim C3
CMM 1	73596	1	1	Upper Rim C1
CMM 2	73598	1	2	Upper Rim C2
CMM 3	73604	1	3	Lower Trunnion 180°
AFMM 1	73600	2	1	Upper Rim C4
AFMM 2	60349	2	2	Upper Rim C5
AFMM 3	60345	2	3	Upper Trunnion at 0° side

## Test Procedure 3

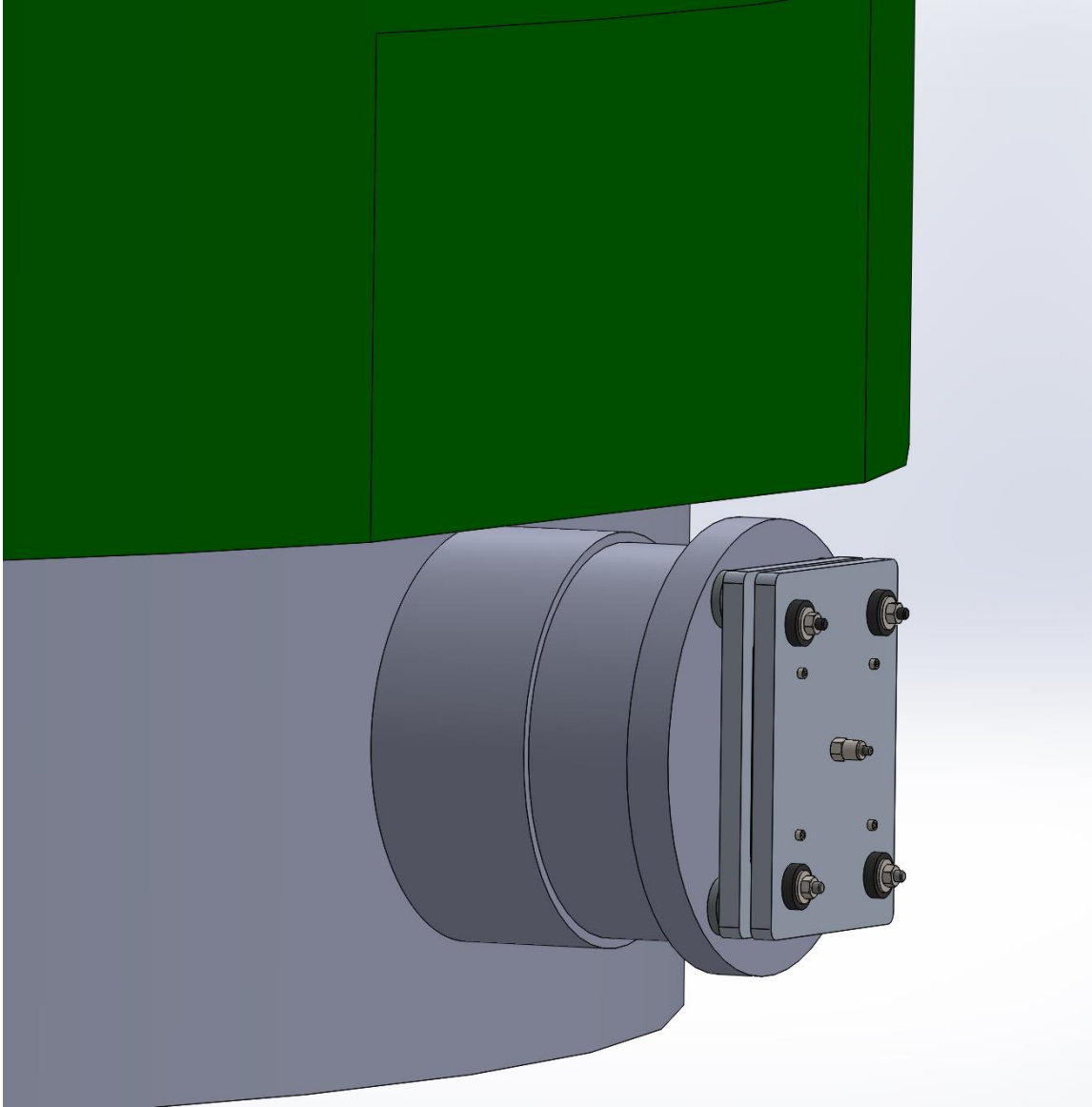
Sweep

Sensor	Serial #	ADC box	ADC channel	Location
Shaker	LW211616	1,2	0,0	Source - Lower Trunnion 180°
CMM 1	73596	1	1	Upper Rim C1
CMM 2		1	2	Sine out
CMM 3	73604	1	3	Upper Rim C3
AFMM 1	73600	2	1	Upper Rim C4
AFMM 2	60349	2	2	Upper Rim C5
AFMM 3	60345	2	3	Upper Trunnion at 0° side
	73598			Upper Rim C2

## Test Procedure 4

Ping, Dead Blow

Sensor	Serial #	ADC box	ADC channel	Location
Shaker	LW211616	1,2	0,0	Lower Trunnion 180°
CMM 1	73596	1	1	Lower Rim D1
CMM 2	73598	1	2	Lower Rim D2
CMM 3	73604	1	3	Lower Rim D3
AFMM 1	73600	2	1	Lower Rim D4
AFMM 2	60349	2	2	Lower Rim D5
AFMM 3	60345	2	3	Lower Trunnion at 0° side

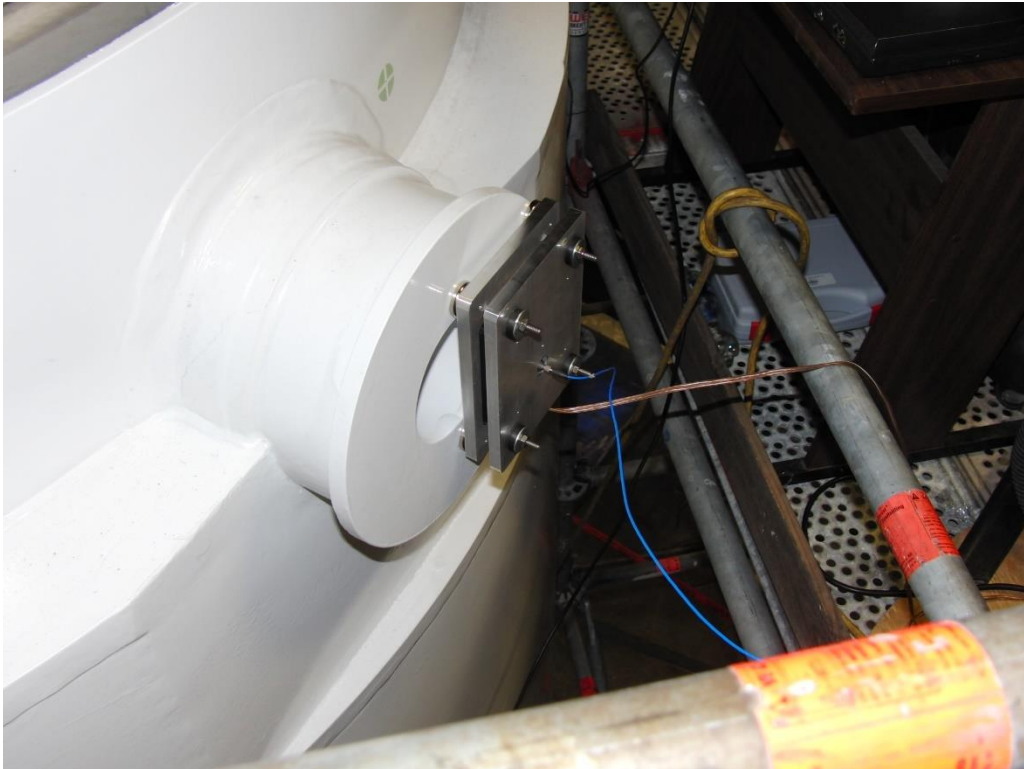
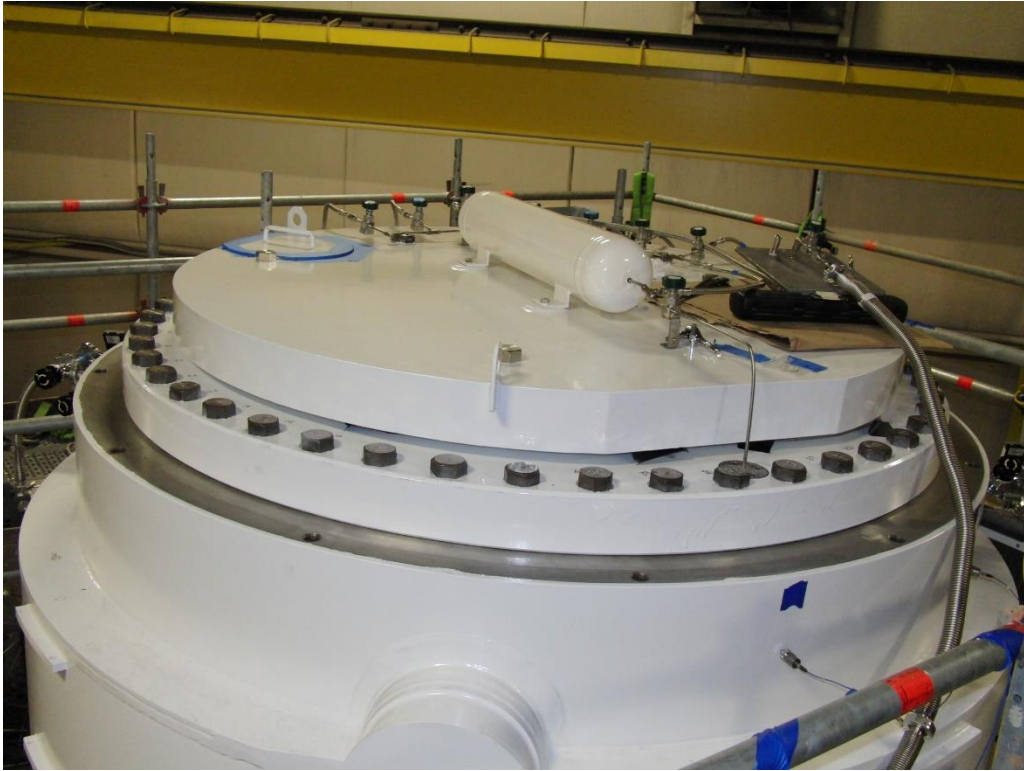


Custom magnetic mount





Sensor locations





# Appendix D

Setup and photo from 10/10/17 CHT Trip

# CHT TN-32 Test Cask Field Test 4 (Final)

Everything is driven at 21.5V output from the amplifier

## Test Procedure 1

Ping(metal/deadblow)

Sensor	Serial #	ADC box	ADC channel	Location
Shaker	LW211616	1,2	0,0	Lower Trunnion 180°
CMM 1	73596	1	1	Lower Rim D1
CMM 2	60345	1	2	Lower Rim D2
CMM 3	73598	1	3	Lower Rim D3 (to lock-in)
AFMM 1	60349	2	1	Lower Rim D4
AFMM 2	73600	2	2	Lower Rim D5
AFMM 3	73604	2	3	Lower Trunnion at 0° side

## Test Procedure 2

Sweep

Sensor	Serial #	ADC box	ADC channel	Location
Shaker	LW211616	1,2	0,0	Source - Lower Trunnion 180°
CMM 1	73596	1	1	Lower Rim D1
CMM 2	60345	1	2	Lower Rim D2
CMM 3	73598	1	3	Lower Rim D3 (to lock-in)
AFMM 1	60349	2	1	Lower Rim D4
AFMM 2	73600	2	2	Lower Rim D5
AFMM 3	73604	2	3	Lower Trunnion at 0° side

## Test Procedure 3

Ping(metal/deadblow)

Sensor	Serial #	ADC box	ADC channel	Location
Shaker	LW211616	1,2	0,0	Upper Trunnion 180°
CMM 1	73596	1	1	Lower Rim D1
CMM 2	60345	1	2	Lower Rim D2
CMM 3	73598	1	3	Lower Rim D3 (to lock-in)
AFMM 1	60349	2	1	Lower Rim D4
AFMM 2	73600	2	2	Lower Rim D5
AFMM 3	73604	2	3	Lower Trunnion at 0° side

## Test Procedure 4

Ping(metal/deadblow)

Sensor	Serial #	ADC box	ADC channel	Location
Shaker	LW211616	1,2	0,0	Upper Trunnion 180°
CMM 1	73596	1	1	Upper Rim D1
CMM 2	73598	1	2	Upper Rim D2
CMM 3	73604	1	3	Upper Rim D3 (to lock-in)
AFMM 1	73600	2	1	Upper Rim D4

AFMM 2	60349	2	2	Upper Rim D5
AFMM 3	60345	2	3	Upper Trunnion at 0° side

#### **Test Procedure 5**

<b>Sensor</b>	<b>Serial #</b>	<b>Sweep ADC box</b>	<b>ADC channel</b>	<b>Location</b>
Shaker	LW211616	1,2	0,0	Source - Upper Trunnion 180°
CMM 1	73596	1	1	Upper Rim D1
CMM 2	73598	1	2	Upper Rim D2
CMM 3	73604	1	3	Upper Rim D3 (to lock-in)
AFMM 1	73600	2	1	Upper Rim D4
AFMM 2	60349	2	2	Upper Rim D5
AFMM 3	60345	2	3	Upper Trunnion at 0° side

#### **Test Procedure 6**

<b>Sensor</b>	<b>Serial #</b>	<b>Sweep ADC box</b>	<b>ADC channel</b>	<b>Location</b>
Shaker	LW211616	1,2	0,0	Source - Upper Trunnion 180°
CMM 1	73596	1	1	Lower Rim D1
CMM 2	60345	1	2	Lower Rim D2
CMM 3	73598	1	3	Lower Rim D3 (to lock-in)
AFMM 1	60349	2	1	Lower Rim D4
AFMM 2	73600	2	2	Lower Rim D5
AFMM 3	73604	2	3	Lower Trunnion at 0° side



Sensor locations









# Appendix E

Custom Shaker Mount Design

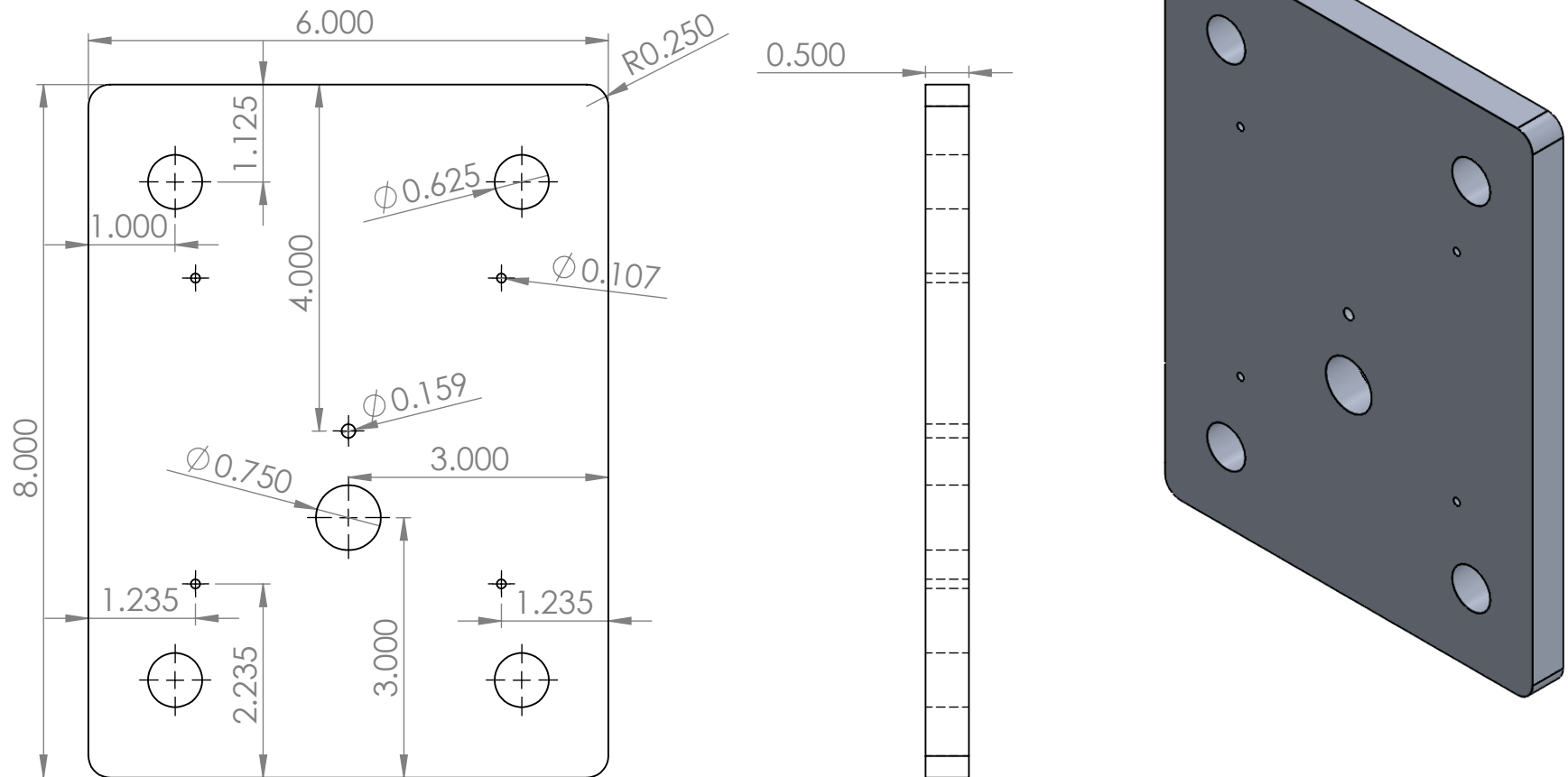
(dimensions in inches)  
(all unmarked dimensions derived from symmetry)

(all unmarked dimensions derived from symmetry)



# Shaker Magnetic Mount Plate

(dimensions in inches)  
(all unmarked dimensions derived from symmetry)



# University of South Carolina

## Acoustic Emissions and Ultrasonic Investigation

Dr. Lingyu Yu - PI

### **1 Summary**

This research conducted at University of South Carolina aims to investigate the challenging task of monitoring the conditions of spent fuel casks without physically penetrating the spent fuel container. We use acousto-ultrasonic technique, which strategically combines the advantages of passive online monitoring and active on-demand interrogation. To achieve such a goal, extensive researches have been performed in this project to perform numerical modeling to understand the essential properties of waves propagating in the subject materials, to develop appropriate diagnostic algorithms, and to investigate the applicability toward field deployment.

### **2 Hybrid Global-Local Modeling of Wave propagation**

#### **2.1 Goal of the work**

Based on the modeling and simulation fundamental studies that have been done in the project, our goal here is to develop a novel hybrid global-local method to analyze AE source from a crack growth in a structure. The derivation of Lamb wave equation is provided by solving elastodynamic equations for generalized excitation potentials. In this derivation straight crested Lamb wave is considered. Local analysis of AE waves from a source is conducted to estimate amount of energy release due to extension of a crack as potentials. The time dependent excitation potentials are the true description of time dependent energy release from a crack. Therefore, the total released energy from a crack can be decomposed as pressure potential and shear potential. Each potential has contribution to different wave modes. Out of plane displacement was calculated numerically at certain distance from excitation point on top surface of the plate. Numerical simulation was conducted for 2mm, 6.35 mm and 12.7 mm stainless steel plate. In addition, we want to discover the convergence differences in the codes to show the necessary convergence characteristics to simulate the thick structure in the dry cask like TN32.

#### **2.2 Accomplishment under this goal**

FEM requires extensive computation for detecting crack in large structure to analysis and it is difficult to attain computational accuracy. To overcome the problem a hybrid global local (HGL) analysis will be used (Figure 1). In the HGL method a combined global analytical and local analysis will be used. HGL method for AE is advantageous in two regards.

1. Instead of supplying energy to the object under examination, sensors can capture the event for the energy released by the crack.
2. HGL for AE can be performed on structures while in operation, as this provides adequate loading for propagating defects and triggering acoustic emissions. This method will be very useful to inspect large structure while in operation.

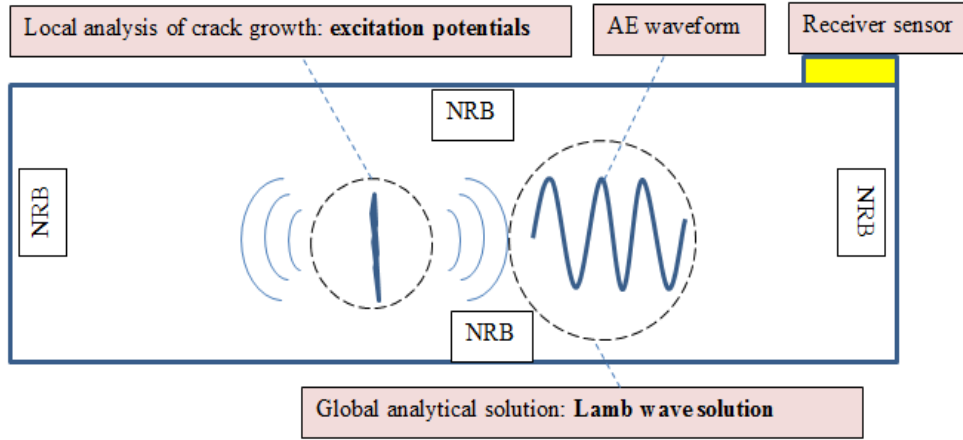


Figure 19 Overview of combined HGL approach

### 2.2.1 Local analysis: Formation of pressure and shear excitation potential

In fracture mechanics, energy is released due to crack extension from the tip of the crack. The amount of energy that must be released from a crack tip for it to grow must be balanced by the amount of energy dissipated due to the formation of new surfaces and other dissipative processes such as plasticity. Elastic waves emission from a crack growth due to energy release can be correlated by concentrated excitation force. According to Helmholtz decomposition, the exciting force can be decomposed further in to excitation potentials. If the excitation force is present, then the Navier-Lame equation can be written as follow [1-3]

$$(\lambda + \mu)\vec{\nabla}(\vec{\nabla} \cdot \vec{u}) + \mu\nabla^2\vec{u} + \rho\vec{f} = \rho\ddot{\vec{u}} \quad (1)$$

Helmholtz decomposition states that, any vector can be resolved into the sum of an irrotational (curl-free) vector field and a solenoidal vector field, where an irrotational vector field has a scalar potential and a solenoidal vector field has a vector potential. Equations below are the wave equations for the pressure potential and the shear potential respectively with the presence of excitation potentials. These potential can be calculated from the energy release during a crack growth.

$$c_p^2\nabla^2\Phi + A = \ddot{\Phi}, \quad c_s^2\nabla^2\vec{H} + \vec{B} = \ddot{\vec{H}} \quad \text{with} \quad c_p^2 = \frac{\lambda + 2\mu}{\rho}; c_s^2 = \frac{\mu}{\rho} \quad (2)$$

### 2.2.2 Developing global solution due to excitation potentials

A global solution is need to be developed from equation (2). A Dirac delta function can be used to represent the concentrated excitation force or potentials. In global analytical analysis guided waves propagating in a plate of thickness  $h=2d$ . The assumption of straight-crested waves makes the problem  $z$ -invariant. The  $z$ -invariant problem can be split into two separate cases, (1) SH waves and (2) P+SV waves. The P waves and SV waves give rise to the Lamb waves, which consist of a pattern of standing waves in the thickness  $y$  direction (Lamb wave modes) behaving like traveling waves in the  $x$  direction. Equations of Lamb wave equations can be found in project deliverables in details.

### 2.2.3 Coupled local-global numerical representation

The excitation time rate of potentials/energy release can be assumed as a pulse (Gaussian) signal. Lamb wave will be generated due to excitation potentials. Out of plane velocity can be calculated at certain distance from the source on top of the plate. This out of plane velocity can be captured by AE sensor installed on the surface of the structure. A numerical solution is obtained due to excitation potential by using global solution in plate. Elastic waves emission from a crack growth due to energy release is represented by concentrated excitation potentials where the global solution carries the information all the way to receiver sensor.

For small incremental increase of crack length, it releases certain amount of strain energy. The incremental strain energy can be released at different time rate at different time depending on crack growth. If time rate of energy released is known, then after integrating the time rate of potential with respect to time gives the time profile of released energy. The time dependent excitation potentials are the true description of time dependent energy release from a crack. Therefore, the total released energy from a crack can be decomposed as pressure potential and shear potential.

### 2.2.4 Simulation results

Figure 2 (a) and (b) show the A0 and S0 signal for 2 mm 304-steel plate. It can be seen that for 2 mm plate A0 is more dispersive than S0. And the amplitude of the A0 signal is higher than the S0 signal. Dispersive behavior of S0 can be seen due to high frequency response. Figure 3 (a) and (b) show the S0 and A0 signal for 6.35 mm 304-steel plate. It can be seen that S0 for 6.35 mm plate is more dispersive than 2 mm plate. And still A0 is more dispersive than S0. The amplitude of the A0 signal is higher than the S0 signal. Figure 4 (a) and (b) show the S0 and A0 signal for 12.7 mm 304-steel plate. It can be seen that both S0 and A0 is more non dispersive than 6.35 mm plate. At this thickness, the amplitude of the A0 signal is similar to S0 signal. Details of the simulation and codes can be found in the project deliverables.

### 2.2.5 Convergence study

A thick steel plate of 12.7 mm thickness (AISI steel 4340) was analyzed for pitch catch simulation. Analysis is done with free edge boundary conditions on the plate. The reflected signals were clearly visible at the plate edges. A convergence study of the ANSYS model was performed by changing the mesh size of plate element size and mesh size of non-reflective boundary element size. First the non-reflective element boundary mesh density, boundary length and damping coefficients are kept constant. The mesh density of plate and PWAS is changed from a lower value to higher value.

We can observe that, the mesh size has negligible effect on the first signal received at receiver PWAS. But the reflected signal from the boundaries is affected by mesh density. On analyzing the signals we can understand that, higher mesh density of plate and PWAS gives better damping effectiveness of non-reflective boundaries. This is due to the fact that the finer mesh on plate gives better interaction with non-reflective boundaries and which leads to better damping. A plot of mesh density vs amplitude of the reflected wave is plotted and is shown below. By considering the computational efforts as well, we can propose a mesh density of 4000 as an optimum mesh density. The plot of mesh density vs amplitude curve of reflected wave is shown in the Figure 5 on the right.

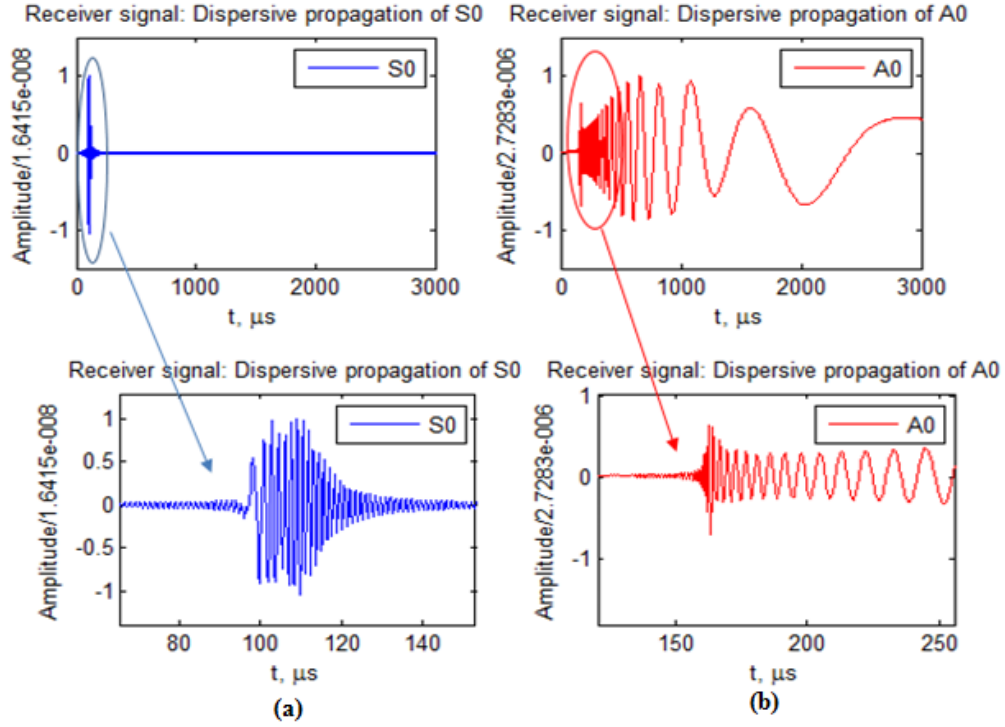


Figure 20 Dispersive wave propagation at 500 mm distance in 2 mm 304 steel plate (a) S0 wave (b) A0 wave

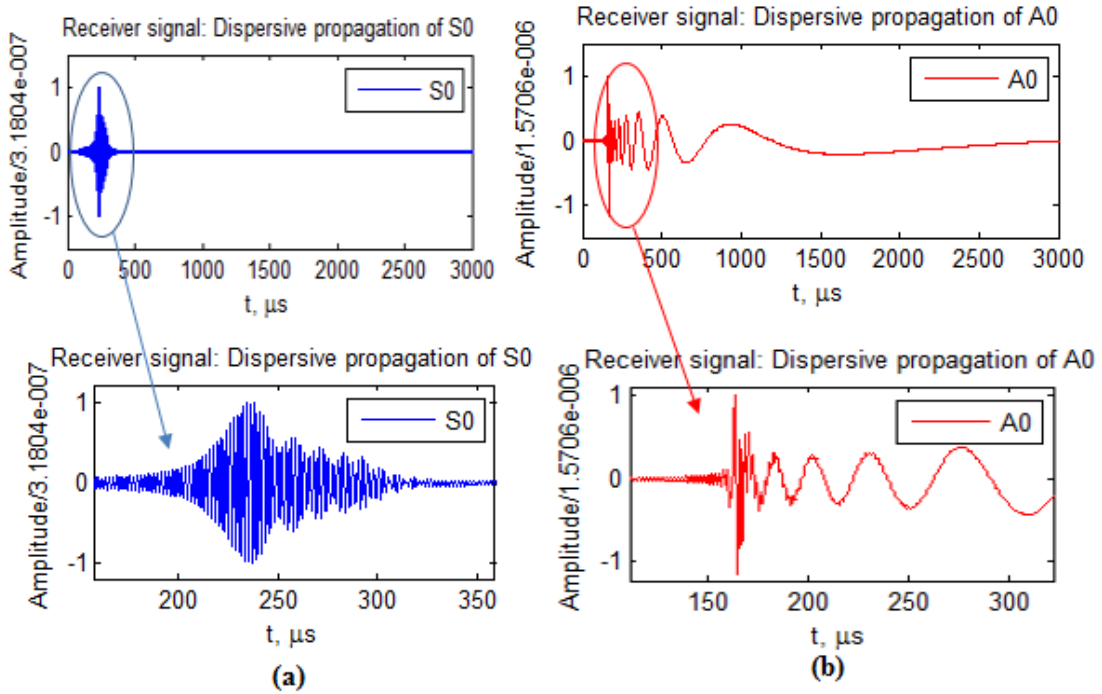


Figure 21 Dispersive wave propagation at 500 mm distance in 6.35 mm 304 steel plate (a) S0 wave (b) A0 wave



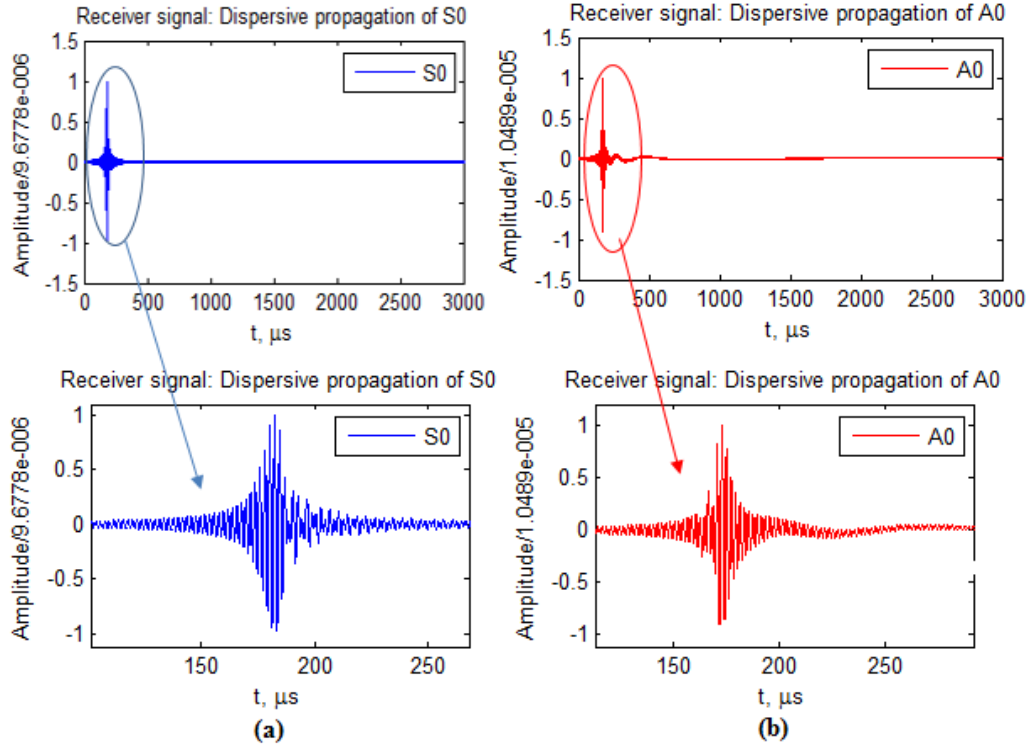


Figure 22 Dispersive wave propagation at 500 mm distance in 12.7 mm 304 steel plate (a) S0 wave (b) A0 wave

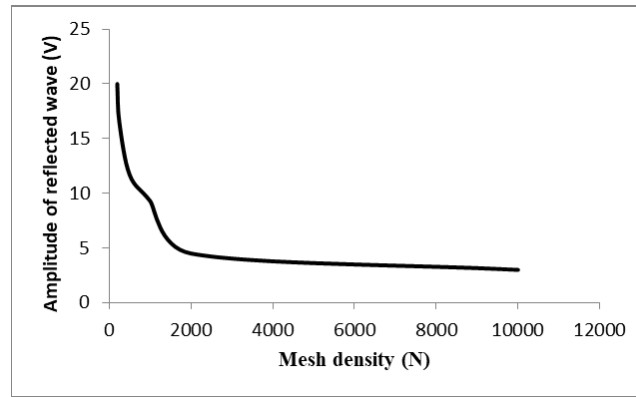


Figure 23 Convergence study on mesh density

### 3 Active UI methodology

#### 3.1 Goal of the work

Non-contact methodology has attracted a lot of attention due to its potential for applications on hazardous environments. A fully non-contact ultrasonic inspection (UI) method is therefore developed in this project, accompanied with damage detection algorithms that can designate a damage signature to be correlated to the degradation of structure. The algorithm can achieve the following objectives:

- Detect the damage if occurs
- Identify damage location and if possible evaluate its size

- Be correlated to evolution of damage growth (i.e. structural degradation)

From the work we have performed using time and/or frequency and/or wavenumber information, an effective algorithm based on wave energy distribution map was successfully developed.

## 3.2 Accomplishment under this goal

### 3.2.1 Fully non-contact ACT-SLDV system setup

We have successfully configured and set up a fully non-contact ACT-SLDV system for UI of metallic structural components. A typical laboratory setup of the system is shown in Figure 6. Several parameters have been found critical for successful implementation of GW inspection when using this system, including (as shown in Figure 6):

- ACT incident angle  $\theta$
- ACT distance to the plate along its center axis  $d$

The test plate used in this study is a large 1-mm thick aluminum 2024-T3 plate. To inspect this plate, the ACT is set to have incident angle  $\theta = 20^\circ$  and distance  $d = 25$  mm from previously conducted studies. We have also found that ACT actuated GW is highly directional, in the direction aligned with the center line of ACT. Therefore, the coordinates in the plate for studying GW have been defined in a way shown in Figure 6 where the strongest waves propagate along the  $x$ -axis.

In the ACT-SLDV system, ACT is used to actuate GW while SLDV is used to detect them. The ACT transducer used in this study is AS120Ti from QMI<sup>1</sup>, a resonant type transducer with extremely narrow bandwidth and with a resonant frequency at 120 kHz. Our study has found out that ACT can actuate pure A0 GW mode in plate which reduced the complexity of subsequent data analysis. On the other hand, the SLDV is a scanning laser vibrometer based on Doppler effect and can measure the waves' out of plane motion when placed normal to the plate (as shown in Figure 6a). The scanning vibrometer therefore can measure waves in terms of the out of plane velocities at multiple points over a user defined grid which can be configured as line (for 1D wave propagation), or planar rectangular, circular, etc. (for 2D wave propagation). The output signal when plotted as spatial distances is known as multidimensional wavefield data including both time and space information. In this study, we have set up the 2D wavefield data sensing over a rectangular grid with a spatial resolution 1 mm.

### 3.2.2 Damage detection algorithm development

When waves propagate in structure and arrive at a structural discontinuity such as boundary, structural feature, or defect, waves will interact with it as waves are reflected, transmitted, or scattered. In that way, the wave energy distribution in the plate is redistributed based on the location and size of the damage. An image of the plate that is based on the wave energy distribution in the plate can therefore be used as an effective way for damage detection and evaluation.

For 2D wave propagation, the wavefield data are recorded as a function of both  $x$  and  $y$  directions as well as time, as a three dimensional data set  $u(x, y, t)$ . Plot of the wavefield data

---

<sup>1</sup> Quality Material Inspection, Inc. <https://www.qmi-inc.com/airscan.php>

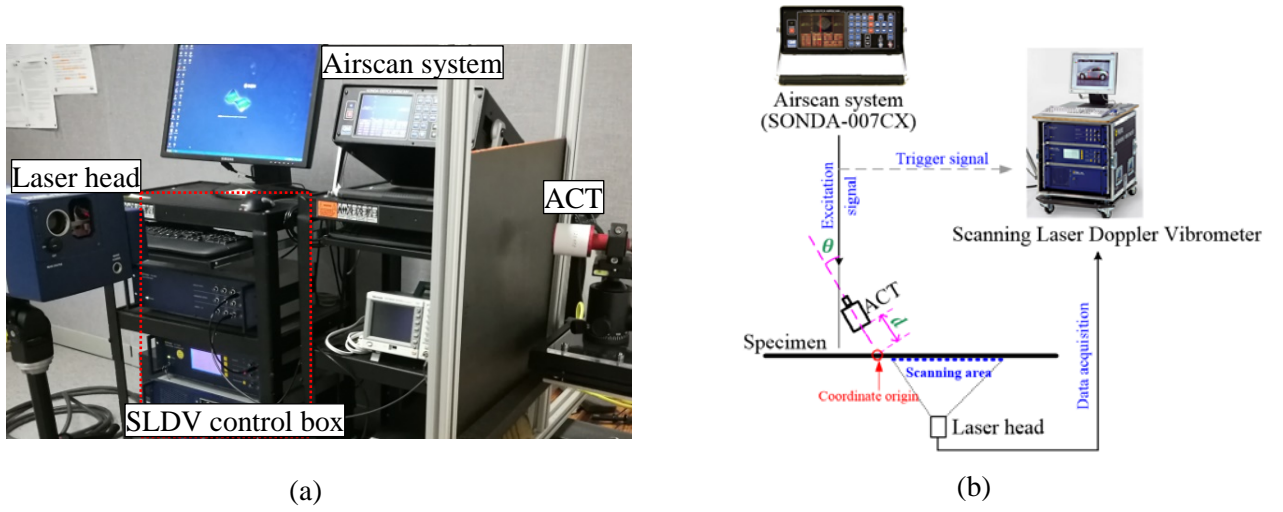


Figure 24 Typical laboratory setup of the ACT-SLDV system. (a) the overall ACT-SLDV experimental setup, (b) the schematic of the overall ACT-SLDV setup

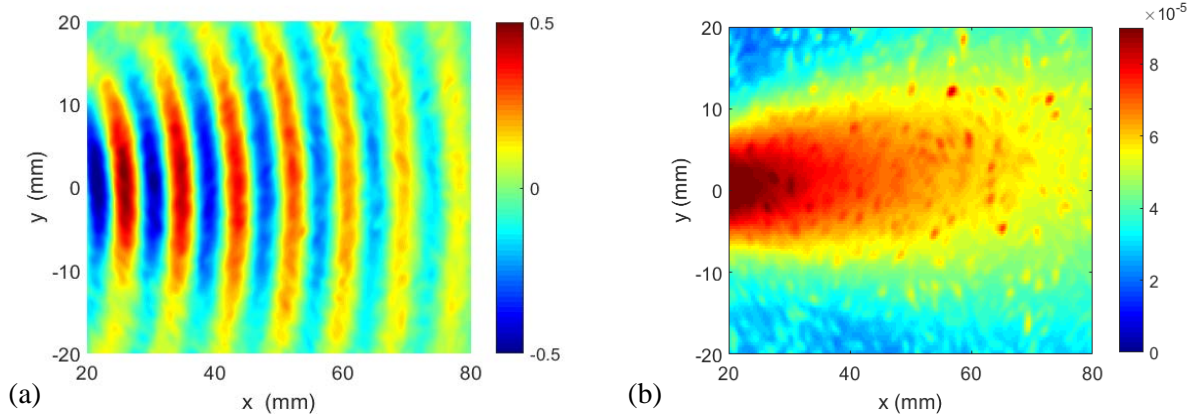


Figure 25 2-D wavefield of ACT-GW propagation in 1-mm aluminum test plate. (a) Wavefield recorded at 60  $\mu$ s in pristine condition (no damage), (b) its energy map

recorded at 60  $\mu$ s after wave started propagating over the  $x$ - $y$  plane is shown in Figure 7a. The wave energy at a location  $(x, y)$  in the plate can hence be acquired using the waveform recorded at this location retrieved from the 2D wavefield data. Various ways can be used to calculate or indicate the energy of a signal. Among them, root mean square (RMS) value is one of the popular methods and is adopted in the present study. Hence, the wave energy  $E(x, y)$  at location  $(x, y)$  can be determined as:

$$E(x, y) = \sqrt{\frac{1}{N} \sum_{n=1}^N |S_n|^2}, \quad n = 1, 2, 3 \dots N \quad (3)$$

Here  $\{S_n\}$  are the sample data; and  $N$  is the total number of samples of the signal. By obtaining the energy values over the entire wave propagation plane, the energy distribution for the wave propagation can therefore be obtained. It can be further plotted over the  $x$ - $y$  plane to generate an inspection image. When discontinuity such as defect is present in the plate, the energy

distribution will be modified and therefore can be seen in the energy image. The energy image of the test plate in pristine condition (no damage) is given in Figure 7b. It can be seen that:

- The wave energy gradually decreased as the waves propagate away from the source.
- The ACT-GW maximum energy is aligned along the direction of the ACT axis ( $x$ -axis), known as the “directional GW actuation”.

### 3.2.3 Damage detection and growth monitoring: case 1

The first case of study uses quartz rod of various sizes (4, 8, 10, 12 mm in diameter, shown in Figure 8) to simulate hole type defect and to represent its growth (enlargement in diameter), a.k.a. the degradation of the overall structural integrity. The rods are located at  $x=70$  mm in this test. 2D wavefield are collected over the rectangular grid defined with 1 mm spatial resolution in both  $x$  and  $y$  direction and 1800 measurement points in total. Wavefields for each damage level (diameter size) at 60  $\mu$ s are given in Figure 9. By comparing these 2D wavefields to the pristine wavefield (Figure 7):

- The ACT-GW exhibit strong interactions around the locations where damages are present (roughly at 70 mm), manifesting the damage modified the GW propagation.
- As the damage size increases, the interaction becomes stronger.

Although the 2D wavefield can be obtained and the interactions of the GW and the damage can be observed, it is difficult for damage localization and quantification, due to the fact 2D wavefield only represent the wave distribution at specific recording time. Wave energy, which is the accumulated over the entire propagation time, can indicate better the changes in wave propagation pattern at damage. Therefore, energy distribution imaging based on energy distribution over the entire propagation plane will be further used to evaluate the damage.

The energy images for these various damage sizes were obtained by the method given in Eq.(3) and the results are given in Figure 10. In Figure 10, the black circle represents the actual damage size and location. It shows when the waves arrive at the defect, the energy was nearly all blocked off for further transmission through by the defect, resulting in “dark blue area” at and after the location of the damage. Indeed, the energy is reflected back toward the source, making the energy right before the damage become significant. The wave interactions and energy distribution show:

- All defects at different sizes were detected successfully.
- The damage modified the wave energy distribution. The energy was majorly reflected; as a result, the wave energy at the location before the defect increased and the transmission wave energy significantly reduced.

The energy distribution pattern is related to the size of the defect. The larger the defect, the more waves will be blocked from transmitting through (i.e. low energy area where the damage is located). Moreover, more energy will be reflected by larger damage, resulting in more energy right before the damage location. As we have observed, the energy distribution is highly related to the damage location and damage size. Therefore, damage evaluation was further studied for damage localization and quantification. Damage localization was based on the detected damage center. And the detected damage center was obtained through the edge of the “dark blue area” plus the radius of the actual damage size. By using the same method, damage localization and quantification evaluation results for each damage level (diameter size) were obtained and listed in Table 1.

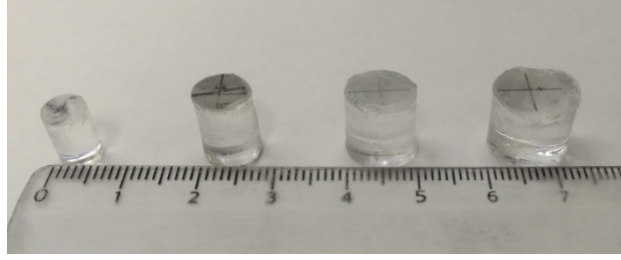


Figure 26 Quartz rods of different sizes (4, 8, 10, 12 mm diameters, from left to right) used in this study for simulating damage

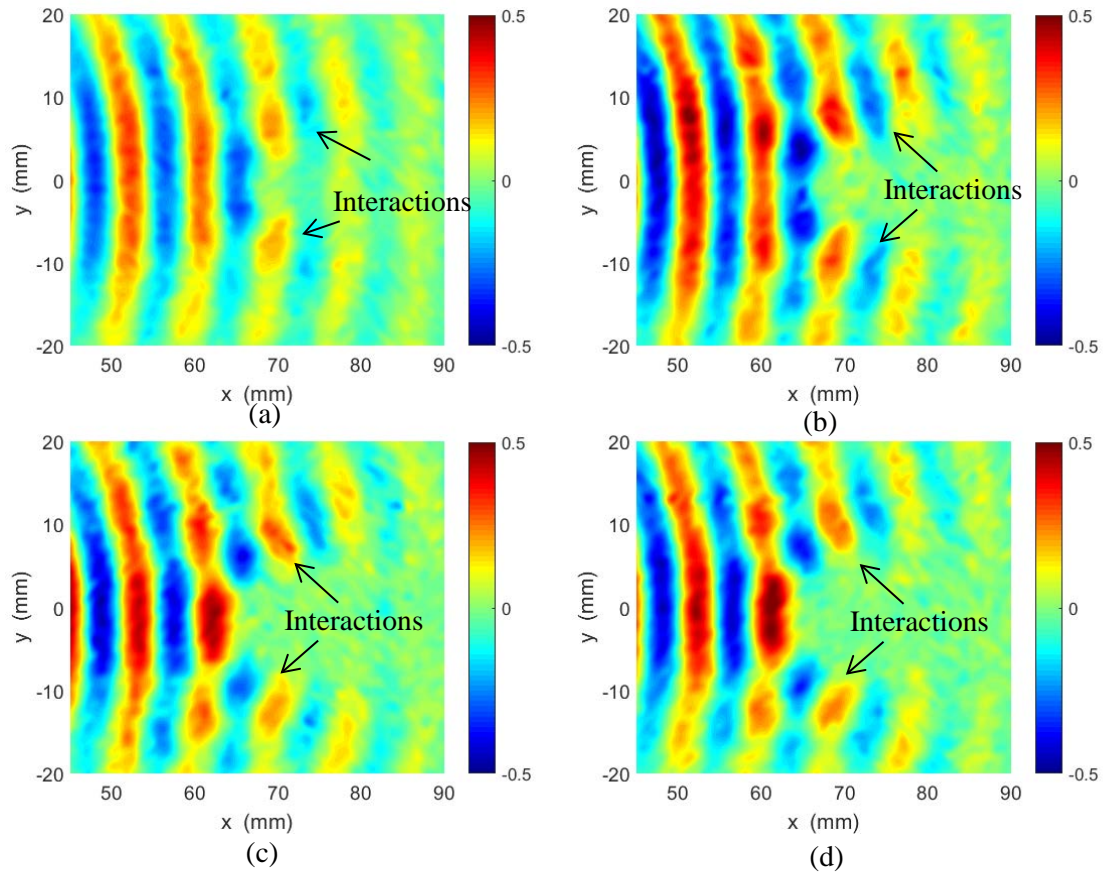


Figure 27 2D wavefields recorded at  $60\ \mu\text{s}$  at each damage level. (a)  $d = 4\ \text{mm}$ , (b)  $d = 8\ \text{mm}$ , (c)  $d = 10\ \text{mm}$ , and (d)  $d = 12\ \text{mm}$ .

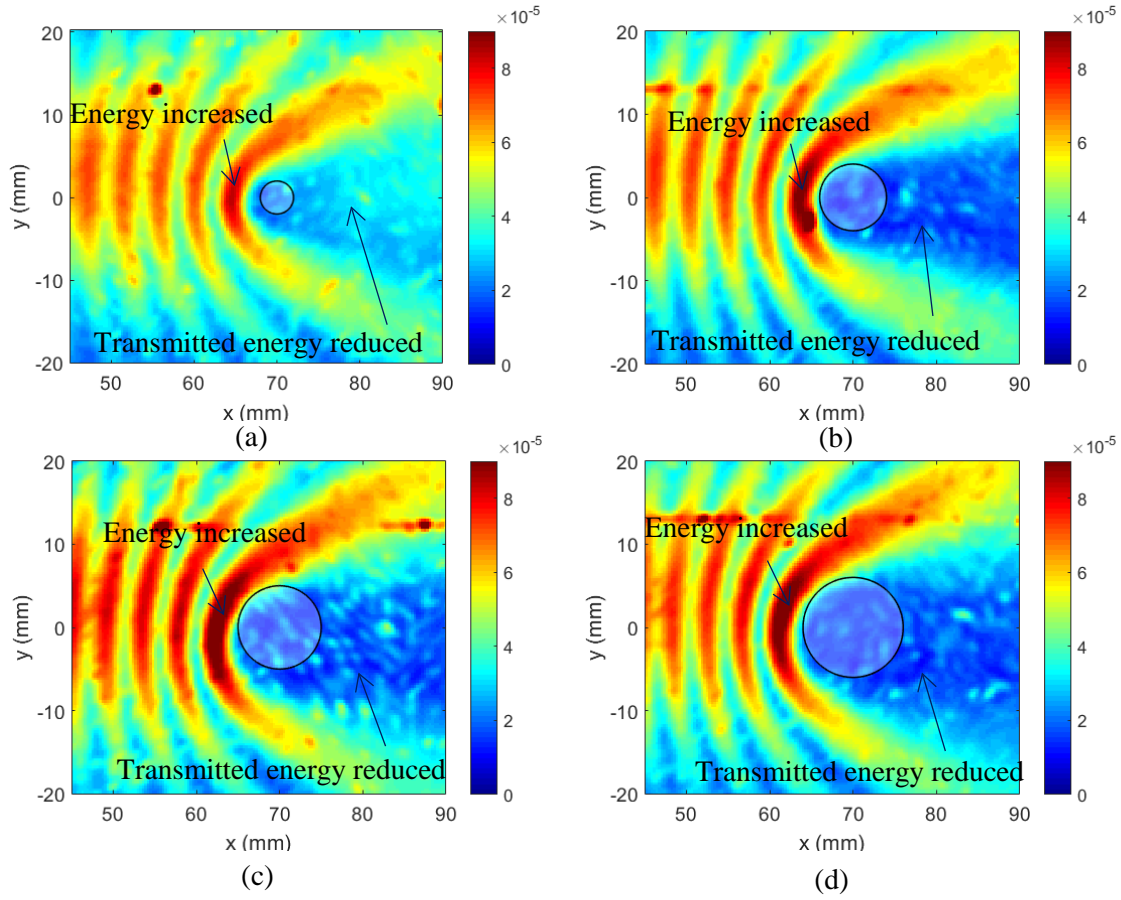


Figure 28 Damage detection results based on energy image at each level damage. (a)  $d = 4$  mm, (b)  $d = 8$  mm, (c)  $d = 10$  mm, and (d)  $d = 12$  mm. Black circle represents the actual damage



From Table 1, we can draw a conclusion that the energy image method can locate the damage with 0.14% error and evaluate their size with 23.3% error.

Table 5 Damages evaluation of results

Actual damage size: $d$ (mm)	Detected location: center location (mm)	Estimated location error (%)	Estimated size (mm)	Estimated quantification error (%)
$d = 4$	69.1	1.29	6.2	55
$d = 8$	70.1	0.14	10.2	27.5
$d = 10$	70.5	0.71	13.3	33
$d = 12$	69.7	0.43	14.8	23.3

### 3.2.4 Damage detection and growth monitoring: case 2

The second case of study uses a quartz rod of 4 mm diameter to simulate a crack tip (perfect wave scatterer) and then move its location toward the GW source to resemble the crack growth (crack tip movement), a.k.a. the degradation of the overall structural integrity. The quartz was first located at  $x=60$  mm and then moved toward  $x = 50$ , and 40 mm with 10 mm crack increment.

First 2D wavefields were collected over the rectangular grid defined with 1 mm spatial resolution in both  $x$  and  $y$  direction and 1800 measurement points in total. The energy images for these various damage sizes were then obtained by the method given in Eq.(3) and the results are given in Figure 11. In Figure 11, the black circle represents the actual damage and location. It shows that all damages at different locations were detected successfully. When the waves arrive at the defect, the energy was nearly all blocked off for further transmission through by the defect, resulting in “dark blue area” at and after the location of the damage. And the energy was majorly reflected; as a result, the wave energy at the location before the defect increased. What’s more, as the damage get closer to the source, the wave energy at the location before the defect increased more due to the stronger reflection. The crack growth detection evaluation results were listed in Table 2. From Table 2, we can draw a conclusion that the energy image method can detect the crack tip location with 0.2% error and detect the crack tip growth with 3% error.

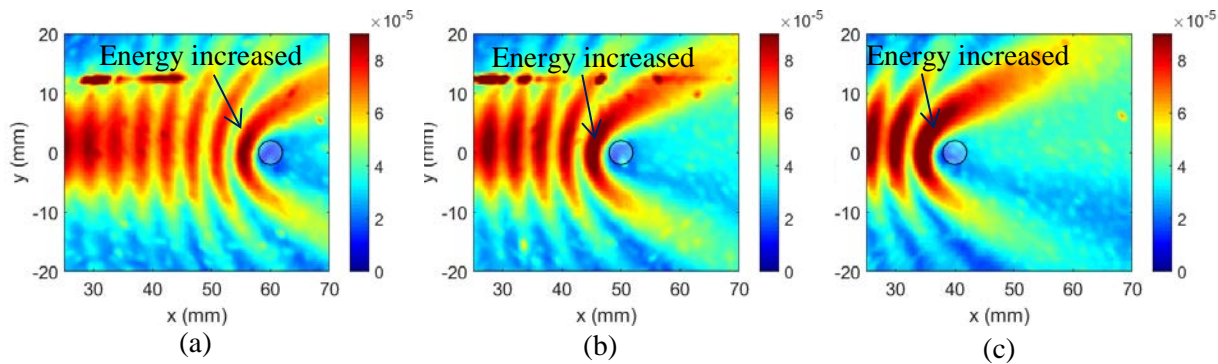


Figure 29 Damage detection results based on energy image for damage ( $d = 4$  mm) at different locations (a)  $x = 60$  mm, (b)  $x = 50$  mm, and (c)  $x = 40$  mm. Black circle represents the actual damage

Table 6 Case 2: crack growth detection evaluation results

Actual damage location (mm)	Detected location: center location (mm)	Estimated location error (%)	Actual crack growth (mm)	Estimated crack growth (mm)	Estimated crack increment error (%)
60	59.9	0.2			
50	49.4	1.2	10	10.5	5
40	39.1	2.3	10	10.3	3

## 4 Integration of passive-active ultrasonic inspection

### 4.1 Goal of the work

The goal of this part of work is to integrate the passive AE method for real time monitoring of active degradation events and the active ACT based ultrasonic inspection for further offline confirmation and/or quantitative evaluation of the defect. A fatigue loading test on a stainless steel sample using similar material as in TN 32 dry cask storage was therefore performed to result in crack generation and growth. With that, the AE sensing capability of PWAS in steel structure was investigated and the localization of AE source based on those AE signals were performed. After performing the passive AE monitoring, ultrasonic inspection based on the developed ACT method on the subject specimen was performed to confirm the presence or growth of the crack.

### 4.2 Accomplishment under this goal

A stainless steel 304 specimen with 103 mm width and 305 mm length and 1 mm thickness has been prepared. An 1 mm hole was drilled at the geometric center of the specimen to initiate pre crack during fatigue experiment. For the pre crack of 6 mm tip to tip length generation fatigue loading from 30 kN to 3.3 kN at a frequency of 4 Hz was applied. After growing the initial crack, PWAS sensors were installed on the steel specimen. The fatigue loading was varied between 18 kN and 1.8 kN (corresponding to 80 % and 8 % of the yield strength of the material) with a loading rate of 0.5 Hz.

#### 4.2.1 Passive AE detection during fatigue crack growth

During the fatigue loading, AE signals were captured by PWAS and analyzed. The experimental set up for capturing AE signal from a fatigue crack growth event is presented in Figure 12. AE signals during crack growth event was captured by four PWAS network (Figure 13) installed at a distance 40 mm from the hole as shown on the right. The PWAS transducer was connected to acoustic pre- amplifier. The acoustic preamplifier is a band pass filter which filter out signals between 30 to 700 kHz. The pre- amplifier is then connected to 4 channel Mistras AE system for processing the signals. The peak amplitude of the AE PWAS signal collected is found to be approximately 27000 mV, while the peak frequencies at 35, 135, 322 kHz, respectively. All the AE signals recorded during fatigue crack event had a dominant peak frequency at low frequency.

To determine the origin of AE signals, AE source localization was performed using Mistras AE system source localization tool. Mistras AE system has an in built source localization tool in which the system localizes the AE source based on arrival time of AE signals at multiple



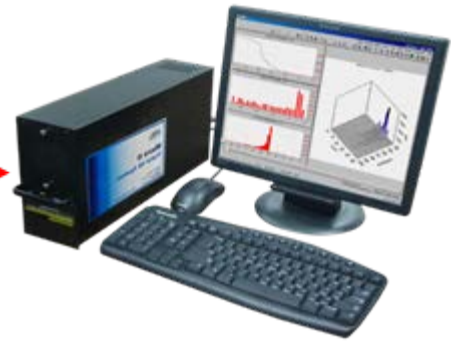
AE sensors [4]. Key input parameters to the system are the location of PWAS, material properties of the specimen in which AE source localization needs to be done and Rayleigh wave speed of the material. For providing location of PWAS sensors, PWAS 1 location is considered as the origin and all other PWAS dimensions were given based on that. Steel 304 plate material properties and Rayleigh wave speed were given as input. At 0.5 Hz the experiment was run for 120 cycles. The strongest AE signal captured among 4 PWAS (for present two cases strongest signals were captured by PWAS 4) and corresponding source localization results are presented in Figure 14. The AE system with PWAS as AE sensor could able to localize the signals with acceptable accuracy.



**Test specimen  
mounted on  
MTS machine**



**Acoustic pre-  
amplifier**



**Mistras AE  
instrument**

Figure 30 Experimental set up for capturing fatigue AE signals

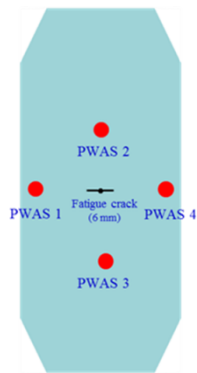


Figure 31 Layout of the piezoelectric sensor network for AE monitoring

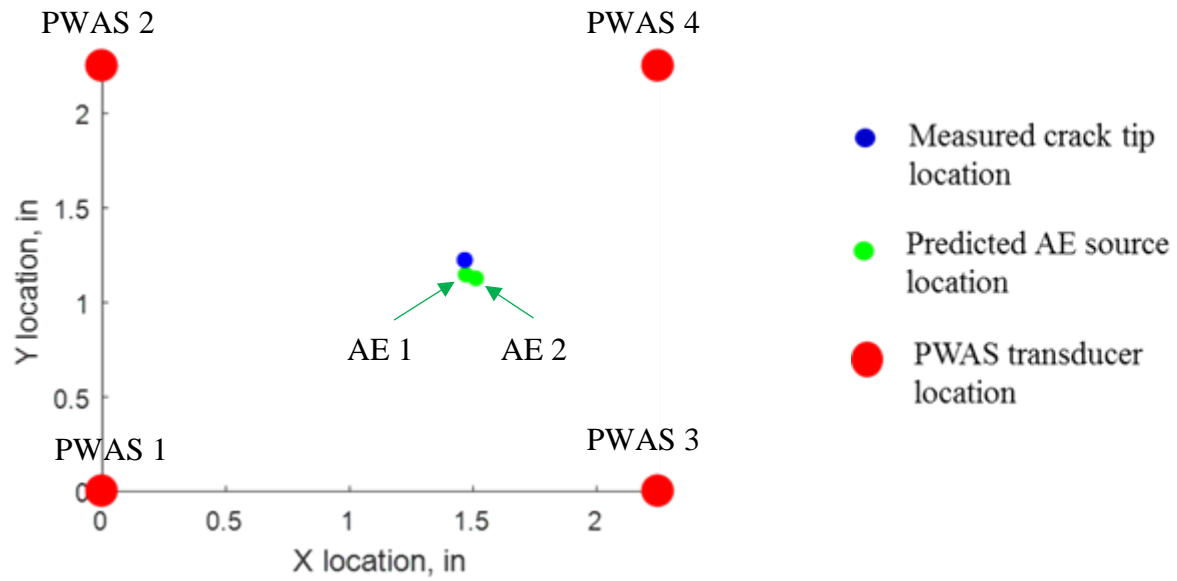
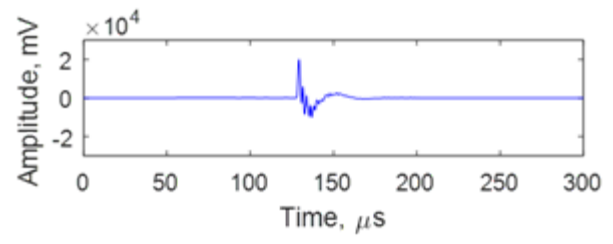
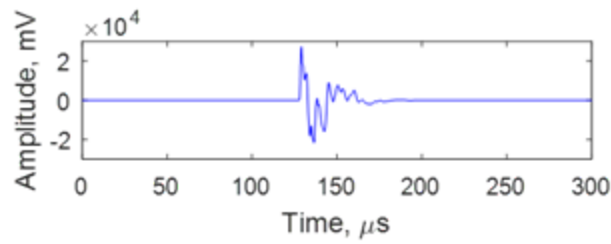


Figure 32 AE source localization predictions and exact crack tip location

#### 4.2.2 Active ultrasonic inspection by ACT system

As crack growth (i.e. increased crack size) being detected by AE, active ultrasonic inspection (UI) is called to (1) further confirm the presence of crack, and (2) quantitatively evaluate it in terms of the crack length in the proof-of-concept test. Using the ACT based UI we have shown that the fatigue crack at 5 mm and 10 mm length has been detected and the estimation of length is close to the actual size, respectively.

ACT UI scanning for the crack is illustrated in Figure 15. The ACT excitation is selected at 120 kHz with incident angle at 20 degree for actuation of A0 guided wave mode. The spatial resolution for scanning grid is set at 1 mm. The acquired wavefield data were then processed by our imaging method delivered previously, as given in Figure 16 and Figure 17. With zoom-in and thresholding, a quick estimation of the crack length can be generated, with 4.8 mm for the 5-mm crack (4% error) and 10.4 mm for the 10-mm crack (4% error), indicating a crack growth of 5.7 mm (14% error).

### 5 **Field Tests**

In order to develop effective guided waves based passive and active inspection on the subject TN-32 cask structures, the University of South Carolina (USC) team has made three field tests on a TN-32 at Columbiana Hi Tech, LLC in 2016 and 2017 (Figure 18):

1. Test 1: evaluating sensing capabilities on TN-32
2. Test 2: damage localization on TN-32
3. Test 3: test repetition and active sensing investigation

The results generated from these field tests show that (1) ultrasonic signals generated by simulated acoustic emission event (pencil lead break for cracking) and impact (hammer) can travel a long way in the complex canister structures to allow for using the ultrasonic methods for real time monitoring of the canister structural integrity. (2) with a network of sensors installed on selected locations on the canister, the locations of the events can be estimated. Localized network will provide better resolution compared to the global network where the sensors are installed on the trunnions. But the global network provides itself as a very accessible method for monitoring and provides very correct detection after all. (3) low profile piezoelectric wafer type sensors also have the potential for TN 32 applications.

In field test 1: ASNT standard pencil lead break (PLB) and hammer simulated passive events were made on various locations on TN32 including the outer wall, trunnions, and inside wall. All events were detected and signals were recorded. The results showed that ultrasonic waves can propagate through the complex TN32 canister structure. Moreover, the recorded signals are able to indicate the changes of the events, for example the hitting force of the impact as shown in Figure 19.

In field test 2: we performed localization tests of impact event using acoustic emission (AE) method during this field trip. The tests were performed as (a) localization on a small area on the canister wall with four AE sensors installed on the wall as well, and (b) localization on a large area (full canister) with four AE sensors installed on the four trunnions. The detection results are given in Figure 20. It can be seen that the local detection generates very good results with the detected locations being a few inches in proximity to the actual event locations; while the offset for the global detection being a few feet away. This is understandable since the full canister has very large dimension and very complex constructions, resulting very complicated ultrasonic wave propagation.

In field test 3: we not only repeated some passive sensing but also investigated the potential of active sensing using piezoelectric wafer active sensors. The sensors were installed on the four trunnions with one of them serving as the “ultrasonic wave actuator” to generate and send out ultrasonic signals for the rest sensors to detect. Our results show that strong signals at 350 kHz can be received throughout the tests.

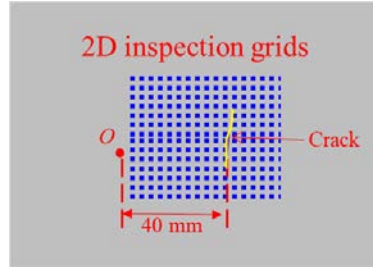


Figure 33 ACT UI on fatigue crack. Inspection line is normal to the crack and aligned with the initial hole

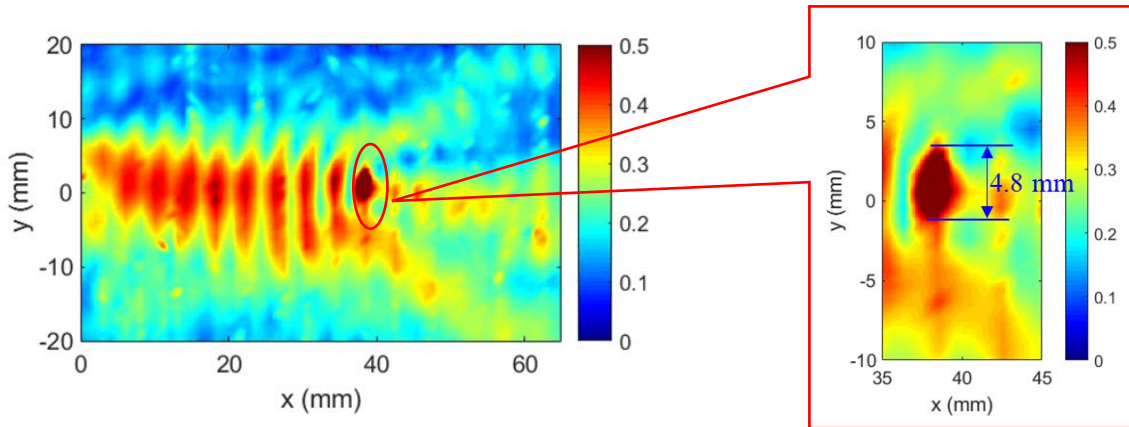


Figure 34 ACT UI imaging of the 5 mm crack

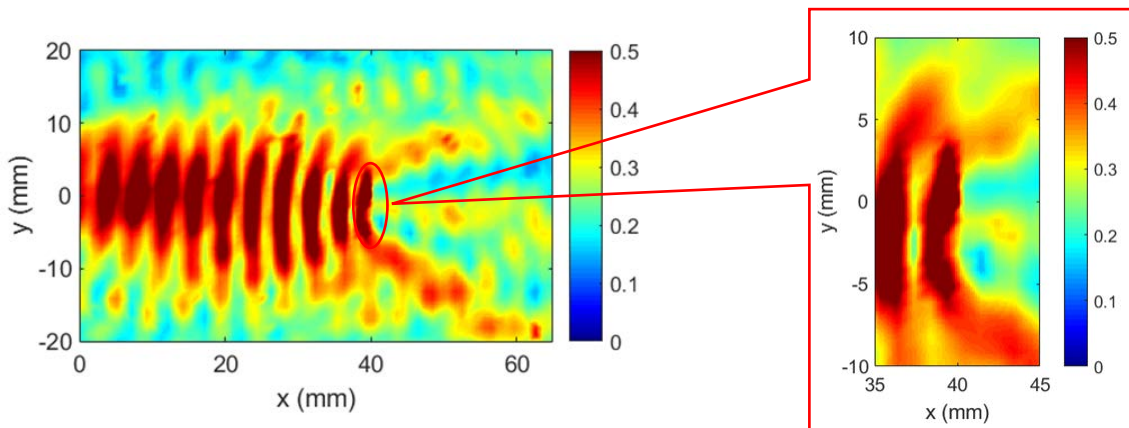


Figure 35 ACT UI imaging of the 10 mm crack



Project team



AE Experimental setup and testing



TN32 at CHT

Figure 36 TN32 field test at CHT

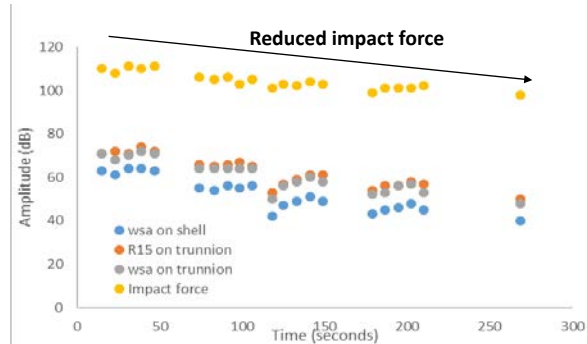


Figure 37 Passive events detection on various locations on TN 32 during field test 1

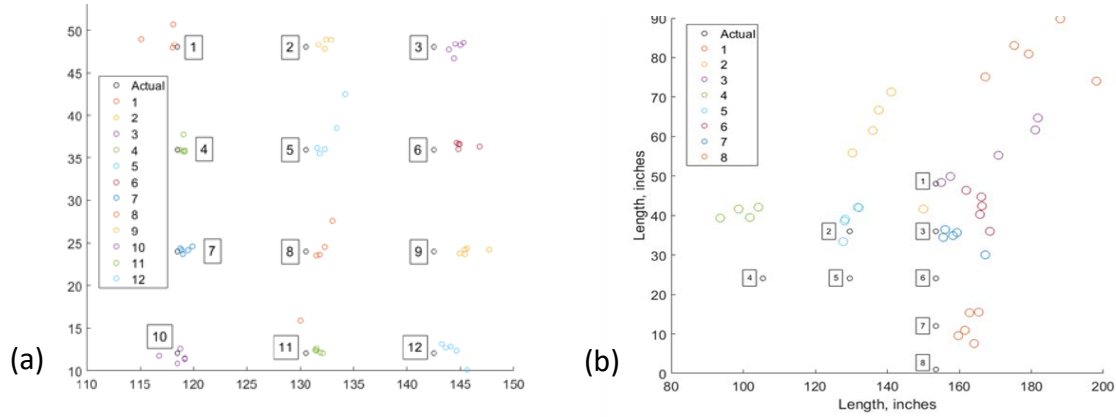


Figure 38 Localization on TN-32 using AE method. (a) local detection (small area on canister body), (b) global detection (entire canister)

## 6 Summary, Conclusions, and future work

In this 3-year project, we have finished the theoretical understanding of the waves as proposed. We have been working on the development of simulation tools to acquire simulated ultrasonic waves in steel plates. The simulation will help the understanding of wave propagation characteristics in order to develop effective damage detection algorithm in the future periods. We have completed two simulation developments including (1) multi-physics multi-domain predictive models for basic wave propagation simulation, and (2) nonlinear analysis models. Moreover we finished the development of a hybrid global-local model where we consider the elastic waves emission from a crack growth as a local solution. The energy release can be correlated by concentrated excitation force. According to Helmholtz decomposition, the exciting force can be decomposed further in to excitation potentials. A global solution was developed for wave propagation with the local excitation potentials. Theoretical formulation showed that due to excitation potentials the elastic waves in a plate followed the Raleigh-Lamb wave equation. Numerical simulation is presented to understand the coupled global-local behavior on different wave modes due to excitation potentials.

For active ultrasonic inspection, we have developed a fully non-contact guided waves based system in which air coupled transducer (ACT) is used to actuated waves and scanning laser Doppler vibrometer is used for sensing. The superior advantage of this full non-contact system compared to other contact type ones is that it is completely in a remote operating mode, and no sensing element will be placed onto the subject structure being inspected, leaving it intact. It therefore significantly reduces the labor hours consumed on installation and maintenance, minimizes sensor effect on sensing, while keeps the structures being maximally unaffected. We have also developed appropriate data analysis algorithms to allow for detection and evaluation of structural degradation.

Combining the advantages, an effort has been made to integrate the passive and active ultrasonic inspection. To accomplish this goal, a fatigue loading test has been designed and conducted to generate actual crack growth events for the proposed methods to be implemented. The growth of the crack during the fatigue test (real time monitoring) in the subject specimen is inspected by the passive acoustic emission and source localization method. Our results proved that AE signals were generated due to the crack growth during the fatigue loading. The AE

signals were subsequently captured by PWAS network installed on the specimen and the location of the crack tips (i.e. crack growth) was detected by AE source localization algorithm in Mistras AE system. The location was found very closely matching with the actual crack tip, where the crack growth happens during fatigue cycle. After the crack growth is indicated by the AE, the fatigue test was paused and the specimen was inspected by the active air-coupled transducer method (off-line NDE). Using the ACT evaluation method, we are able to confirm that the crack is present, as well as to provide quantitative evaluation of the length of the crack, so to estimate the growth of the crack. The passive-active method shows they are well integrated to provide an effective real time monitoring and offline quantitative inspection means for defect development or degradation in the stainless steel structure.

For the purpose to test the AE sensing and localization capability on the subject TN-32 cask structures as proposed we have performed various scale tests on realistic structures including visits to the Columbiana Hi Tech, LLC. to test on TN-32 cask. We performed multiple impacts on various locations in TN32 dry cask storage uni, inside the basket or on the outer wall. Localization techniques using acoustic emission sensors and simulated excitation were explored on the test facility. During experimentation, signal acquisition using acoustic emission sensors and software were preform to detect an impact hammer simulated acoustic emission, followed by localization techniques. Once proper localization settings were discovered, localization plots were produced for the two cases experimented. The first one consisted of a smaller area on the cylindrical surface produced excellent solutions for the impacting hammer excitation as most of the hits fell within a few inches of the actual event. The second experiment produced results while sensing on the entire TN32 cask structure. It is worth mentioning that even with the sensors not being placed directly on the internal cylindrical structure but rather on the trunnions, the acoustic emission approach was able to produce good results with the localization results being within a few feet of the actual locations. The three field tests on a TN-32 are successful.

In conclusion, we have explored the use of a combined passive-active acousto-ultrasonic inspection method for nuclear dry cask structures through analytical modeling, laboratory studies, as well as well-organized field tests on TN-32. In addition to what being included in the final report, extensive fundamental work on which these are built on have also been conducted such as the finite element modeling modules, simulation on cylindrical structures, field test on TN-32 mockup, damage detection algorithms based on array theory, detection on complicated structures, environmental effects on the piezoelectric sensors that are being used for the acousto-ultrasonic sensing, potential of using other types of sensors such as optical fibers which are great for embedding, etc. Potential future work can be done in regards on additional field testing of the developed active methods, as well as more theoretical and laboratory exploration to develop more advanced methods.

## 7 References

- [1] R. K. J. Lysmer, "Finite dynamic model for infinite media," J. Eng. Mech. Div. Proc. Am. Soc. Civ. Eng. EM4, p. 859–877, 1969.
- [2] V. Giurgiutiu. Y. Shen, "Effective non-reflective boundary for Lamb waves: Theory,," Wave Motion, vol. 58, p. 22–41, 2015.
- [3] V. Giurgiutiu, Structural Health Monitoring with Piezoelectric Wafer Active Sensors, second ed, 2014: Elsevier Academic Press.
- [4] Physical Acoustic Corporation, "AEwin for PCI2 user manual."



## 8 List of Publications and Presentations

1. Howden, S., Lin, B., Yu, L., Giurgiutiu, V. (2018) Acoustic emission and active sensing capabilities on full-scale nuclear dry cask storage structures, Proc. SPIE 10601, Smart Materials and Nondestructive Evaluation for Energy Systems IV, 1060109
2. Haider, M. F. and Giurgiutiu, V. (2018). Analysis of axis symmetric circular crested elastic wave generated during crack propagation in a plate: A Helmholtz potential technique. International Journal of Solids and Structures, 134, pp. 130-150.
3. Haider, M. F. and Giurgiutiu, V. (2018) A Helmholtz Potential Approach to the Analysis of Guided Wave Generation during Acoustic Emission Events. Journal of Nondestructive Evaluation, Diagnostics and Prognostics of Engineering Systems. 1(2), 021002.
4. Haider, M. F. and Giurgiutiu, V. (2018) Theoretical and Numerical Analysis of Acoustic Emission Guided Waves Released during Crack Propagation, Journal of Intelligent Material Systems and Structures, 1045389X18798948.
5. Haider, M. F., Giurgiutiu, V., Lin, B., Yu, L., Lam, P.S. and Verst, C. (2018) “Effects of Gamma Radiation on Resonant and Anti-resonant Characteristics of Piezoelectric Wafer Active Sensors” Journal of Nondestructive Evaluation, Diagnostics and Prognostics of Engineering Systems, 2(1), 011001.
6. Haider, M. F., Mei, H., Lin, B., Yu, L., Giurgiutiu, V., Lam, P. S., & Verst, C. (2018, March). Piezoelectric wafer active sensors under gamma radiation exposure toward applications for structural health monitoring of nuclear dry cask storage systems. In Nondestructive Characterization and Monitoring of Advanced Materials, Aerospace, Civil Infrastructure, and Transportation XII (Vol. 10599, p. 105992F). International Society for Optics and Photonics.
7. R. Joseph et al., (2017) “Active health monitoring of TN32 dry cask using a scaled down model,” Proc. SPIE (Health Monit. Struct. Biol. Syst, no. March, 2018.
8. 10. R. Joseph, M. Y. Bhuiyan, and V. Giurgiutiu, “Acoustic emission source modeling in a plate using buried moment tensors,” Proc. SPIE (Health Monit. Struct. Biol. Syst., vol. 10170, no. May, pp. 1017028-1–8, 2017.
9. Haider, M. F., Lin, B., Yu, L., & Giurgiutiu, V. (2017). Sensing capabilities of piezoelectric wafer active sensors in extreme nuclear environment. In Nondestructive Characterization and Monitoring of Advanced Materials, Aerospace, and Civil Infrastructure 2017 (Vol. 10169, p. 101691Z). International Society for Optics and Photonics.
10. Haider, M. F., Giurgiutiu, V., Lin, B. and Yu, L. (2017). Irreversibility effects in piezoelectric wafer active sensors after exposure to high temperature. Smart Material and Structures, 26(095019), 095019.
11. Haider, M. F., Giurgiutiu, V., Lin, B., & Yu, L. (2017). Simulation of Lamb Wave Propagation Using Excitation Potentials. In ASME 2017 Pressure Vessels and Piping Conference (pp. V06AT06A024-V06AT06A024). American Society of Mechanical Engineers.
12. Sun, X., Tian, Z., Lin, B., Yu, L. (2016) Guided Wave Damage Detection with PZT-FBG sensing, Proceedings Volume 9804, Nondestructive Characterization and Monitoring of Advanced Materials, Aerospace, and Civil Infrastructure 2016; 98042B (2016)

13. Ma, L., Lin, B., Sun, X., Howden, S., Yu, L. (2016) Developing an Piezoelectric Sensing Based on SHM System for Nuclear Dry Storage System, Proceedings of the SPIE, Volume 9806, id. 98060U 11 pp.
14. Tian, Z., Howden, S., Ma, L., Lin, B., Yu, L. (2016) Damage detection in thick steel plates using guided ultrasonic waves and non-contact laser vibrometry, Proceedings of ASME 2016 Pressure Vessels and Piping Conference Volume 6A: Materials and Fabrication
15. Sun, X., Tian, Z., Lin, B., Yu, L. (2016) Damage detection with guided waves and fiber Bragg grating sensor arrays, Proceedings of ASME 2016 Conference on Smart Materials, Adaptive Structures and Intelligent Systems Volume 1: Multifunctional Materials; Mechanics and Behavior of Active Materials; Integrated System Design and Implementation; Structural Health Monitoring
16. Ma, L., Sun, X., Lin, B., Yu, L. (2015) Temperature effects on piezoelectric wafer active sensors, Proceedings of ASME 2015 Pressure Vessels and Piping Conference Volume 6A: Materials and Fabrication

Abstract submitted:

1. Xiao, W., Yu, L. (2019) Nondestructive evaluation with fully non-contact ACT-SLDV guided wave system, Proceedings of SPIE 2019 Smart Structures/NDE, Nondestructive Characterization and Monitoring of Advanced Materials, Aerospace, Civil Infrastructure, and Transportation XIII

# Oregon State University

## Muon Imaging

Dr. Haori Yang - PI

### 1. Background

The goal of OSU's research is to investigate an imaging system for monitoring used nuclear fuel (UNF) dry storage casks (DSCs) using cosmic-ray muons. Such a system shall have the capability of verifying and measuring the content inside a DSC without opening it. Because of the growth of the nuclear power industry in the U.S. and the policy decision to ban reprocessing of commercial UNF, the used fuel inventory at commercial reactor sites has been increasing. Currently, UNF needs to be moved to independent spent fuel storage installations (ISFSIs), as its inventory approaches the limit on capacity of on-site wet storage. Thereafter, the fuel will be placed in shipping containers to be transferred to final disposal sites. The ISFSIs were initially licensed as temporary facilities for ~20-yr periods. Given the cancellation of the Yucca Mountain project and no clear path forward, extended dry-cask storage (~100 yr.) at ISFSIs is very likely. It is important to ensure the integrity of the fuel assemblies during long-term dry storage.

### 2. Simulation study on 2D muon radiography

Muon radiography has been utilized previously to image large-scale objects. It has also been used to measure the depth of the overburden of a tunnel, to search for hidden chambers in a pyramid and to predict volcano eruption. The image formed is an attenuation map of muon flux revealing the radiation length traveled by muons before entering the detectors, which indicates the thickness of the object.

A 1:1 model of a generic DSC was created in Geant4. The top view and 3D view of this model generated by Geant4 visualization tool are shown in Figure 2.1. One out of twenty-four used fuel assemblies was removed intentionally to test the detection capability of this imaging method. The muon source was modeled as a uniform plane source located above the cask, emitting 4 GeV monoenergetic muons with an angular distribution that is peaked at the zenith and falls off as  $\cos^2\theta$ . All the most significant particle types were declared in the simulations, but the less significant interactions like muon capture and muon decay in-flight were neglected. Specifically for muons, multiple scattering, ionization, bremsstrahlung and pair production were included in the simulation physics. For the purpose of this work, the detector geometry is generic and was simplified as an ideal position-sensitive detection plane placed underneath the cask, recording the positions of transmitted muons as they cross the detection plane. Also, the trackers were made insensitive to other particles.

The image was reconstructed from a 2D histogram of muon counts measured on the detection plane underneath the cask, forming a "projection" of the cask. The reconstructed image is shown in Figure 2.2 (a). From the image, one can observe the large attenuation caused by high-Z material residing inside the fuel assemblies, so the basic shape of the fuel assemblies as well as

the lead shielding ring can be recognized. One can also locate the missing assembly by examining a slice of the 2D histogram at the near position of it, as shown in Figure 2.2 (b). However, the image quality was so poor and no inside information is obtained. Moreover, if the fuel assemblies are not placed orderly, this method would be much less applicable. Also, to make a detector as an even bigger size than the diameter of a DSC is extremely expensive and difficult.

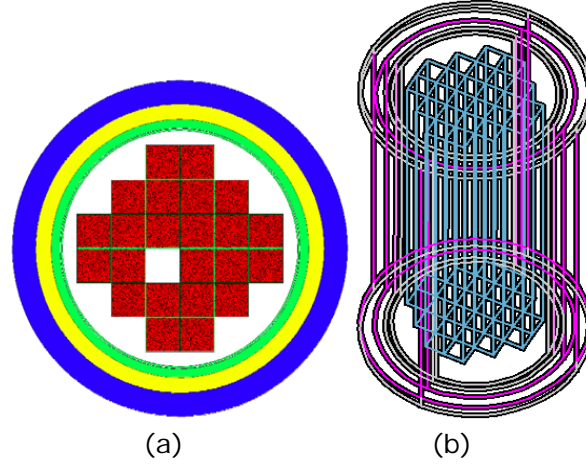


**Figure 2.1** The top view of a typical DSC (a) and its Geant4 and 3-D model (b)

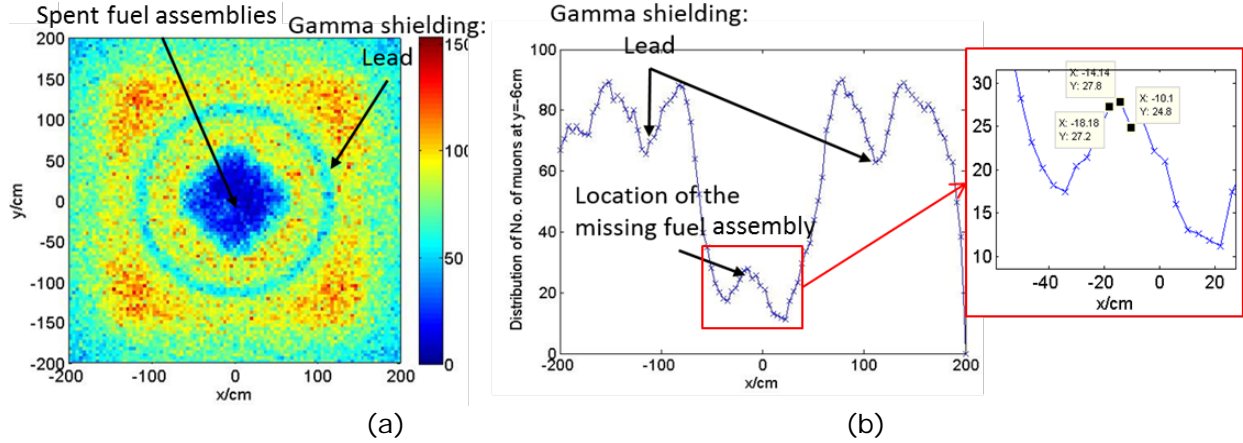


**Figure 2.2** (a) The reconstructed image based on muon “projection” (b) The cross-sectional curve showing the missing assembly

### 3. Simulation study on 3D muon tomography

Muon tomography was developed as an extension of the concept of muon attenuation radiography. In muon tomography, the incoming and outgoing directions are tracked for each muon. The spread of the deflection angle of scattered muons provides a way to distinguish high-Z materials in the volume of interest. In this section, we discuss the modeling and reconstruction of 3D images using two well-known algorithms.

#### 3.1 Modeling of a simplified DSC

To start with, a simulation study for imaging dry cask was also performed. The same layout of a dry cask shown in Figure 2.1 was used in this simulation. However, considering the dimension of our muon tomography system, the size of the dry cask was scaled down to 20 cm by 20 cm, and the fuel was simplified to a 10 cm by 10 cm by 10 cm cube. The sizes of other components (shielding) were reduced accordingly.

First, the point of closest approach (POCA) algorithm was implemented for the reconstruction of simulated data. The POCA algorithm ignores multiple coulomb scattering, instead assuming that a muon scattered at a single point. Based on the direction and position information on both the incident side and outgoing side, the scattering point is estimated as the midpoint of the line segment between the closest points on the two straight lines (see Figure 3.1). The scattering angle is evaluated by taking the scalar product of the direction vectors of the incident and outgoing muon.

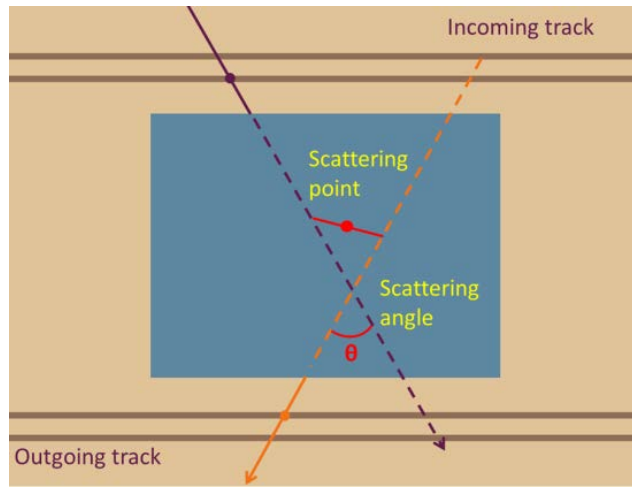


**Figure 3.1** The concept of POCA algorithm.

Another algorithm called Maximum Likelihood/Expectation-Maximization (ML/EM) is also applied. Maximum likelihood is widely used in medical image reconstructions, in particular, for PET and SPECT reconstructions. In the ML/EM algorithm, an instance of the iterative expectation maximization (EM) algorithm is used to find maximum likelihood estimates of the scattering densities of materials given by  $\lambda = (15/p_0)^2/L_0$ , where  $L_0$  is the radiation length and  $p_0$  is the nominal muon momentum. The scattering density of a material thus represents the mean square scattering angle of muons with nominal momentum passing through a unit depth of that material. Figure 3.2 illustrates the definitions of the parameters used in ML/EM algorithm.

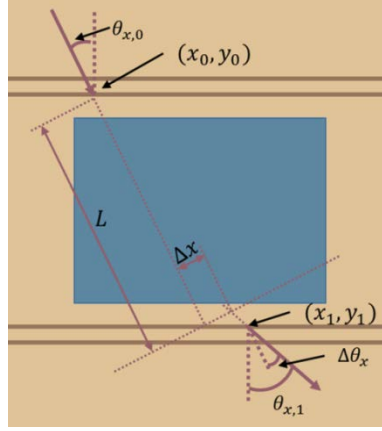


**Figure 3.2** The concept of ML/EM algorithm.

Both POCA and ML/EM algorithms were used for image reconstruction. The reconstructed images are shown in Figure 3.3. The high-Z fuel block and the lead shielding are clearly observed using both algorithms. The reconstructed image using ML/EM presents less blurry edges than those reconstructed using POCA; thus, ML/EM reconstruction results in better spatial resolution.

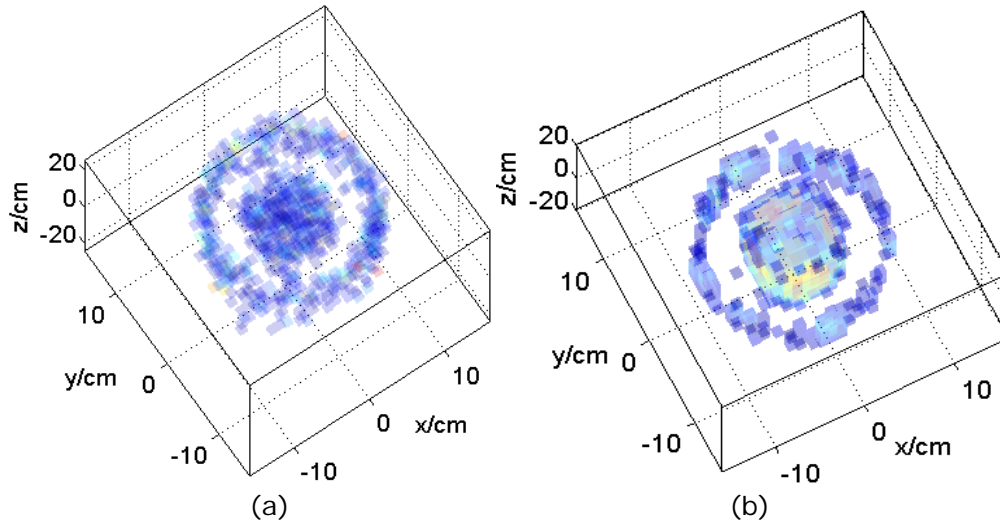


**Figure 3.3** (a) The reconstructed image of a scaled down DSC using POCA or (b) ML/EM.

### 3.2 Modeling of a more realistic DSC with different detector configurations

In the previous section, simulations of imaging a simplified DSC model via muon tomography were studied. It suggested the method is promising in locating a missing assembly in a DSC. However, in our case it is hard to place any detectors underneath a DSC. Therefore, some alternative designs are considered and studied. Twenty-four instead of five fuel assemblies were built in a DSC. The size of the assembly is identical to that stored in a typical DSC. The dimension and pitch of the fuel rods is taken as a typical PWR fuel assembly. Figure 3.4 shows the visualization of the DSC model. Four different fuel assemblies were removed, one at a time,

to study the expected ability of our scaled muon tomography design to locate a missing assembly.

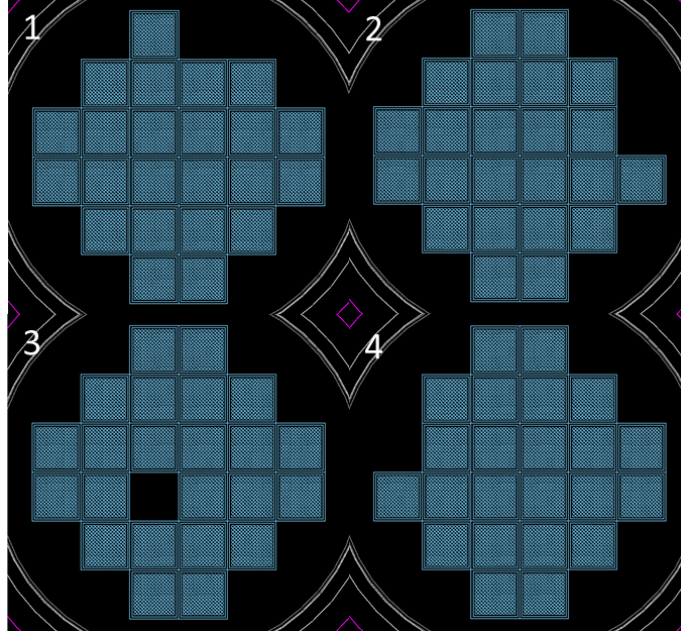


**Figure 3.4** The visualized top views of realistic DSCs with different missing assemblies

The point of closest approach (POCA) algorithm was implemented for the reconstruction of simulated data. Based on the direction and position information on both the incident side and outgoing side, the scattering point is estimated as the midpoint of the line segment between the closest points on the two straight lines. After calculating the POCA, a 2-D histogram of the coordinates of all the scattering points was taken as the reconstructed cross-sectional image of the DSC. A 2D plot of the reconstructed image is shown in Figure 3.5.

The difference matrixes are also plotted in Figure 3.6. From these difference matrixes, a trained human operator or algorithm (not yet developed) should be able to detect an anomaly and discern the approximate locations of a missing assembly. Though the results are not as good as the results for a simplified DSC, as expected, this method still appears to be promising, considering the planned detector array and proposed detector orientation. Additional study in this area will be carried out in the near future.

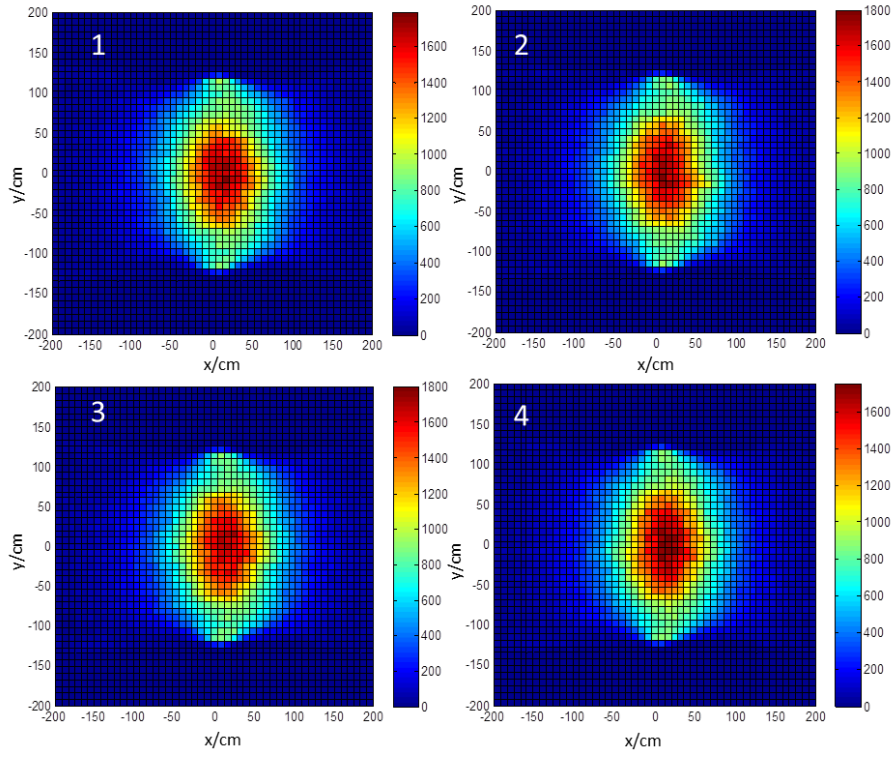


**Figure 3.5** The x-y views of reconstructed images of realistic DSCs with different missing assembly configurations

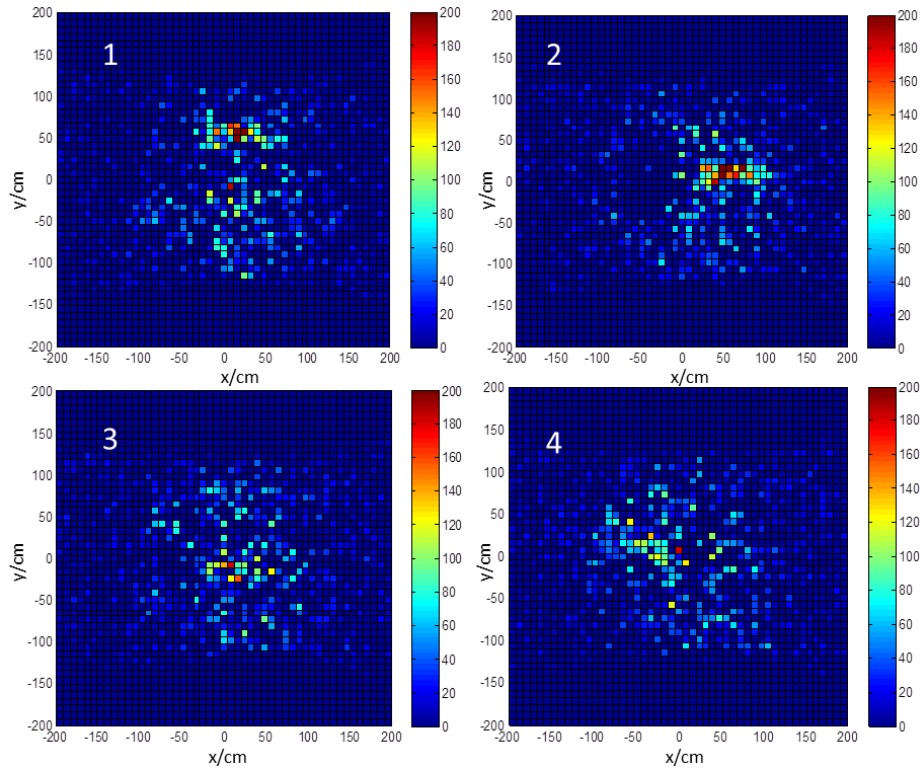


**Figure 3.6** The x-y plots of the difference matrixes of realistic DSCs with different missing assembly configurations corresponding to the drawings shown in Figure 3.5.



### 3.3 Modeling of a DSC with different detector configuration

During this quarter, we studied the simulation of a more realistic DSC. Specifically, we modeled the Westinghouse MC-10 DSC, which is shown in Figure 3.7. The exact dimensions and material properties were modeled. Also, in this section, we modeled the muon trackers with the same size as the LANL MMT (Mini Muon Tracker). Figure 1 also shows the orientation of detectors. The muon source was modeled as a uniform plane source located above the cask, emitting 4 GeV monoenergetic muons with an angular distribution that is peaked at the zenith and falls off as  $\cos^2\theta$ . All the most significant particle types were declared in the simulations, but the less significant interactions like muon capture and muon decay in-flight were neglected. Specifically, for muons, multiple scattering, ionization, bremsstrahlung and pair production were included in the simulation physics. During the simulation,  $10^9$  muons were generated, and only the muons that passed both detector planes were recorded.

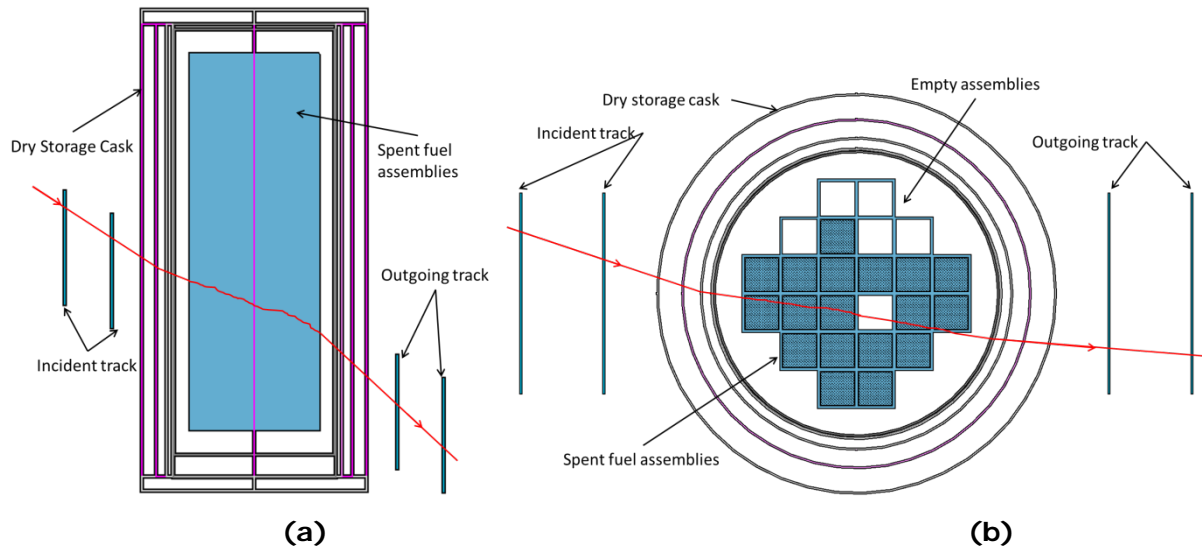


**Figure 3.7** The side view (a) and top view (b) of the detector and DSC showing the detector orientation and the DSC content.

The point of closest approach (POCA) algorithm was implemented for the reconstruction of simulated data. Based on the direction and position information on both the incident track and outgoing track, the scattering point is estimated as the midpoint of the line segment between the closest points on the two straight lines. After calculating the POCA, a 2-D histogram of the y and z positions of all the scattering points was taken as the reconstructed cross-sectional image of the DSC. The y-z plot of the reconstructed images is shown in Figure 3.8 (b). The outline shape of the fuel assemblies can be told as a whole piece. However, the scattering events at the inner part have higher probabilities to be registered. This is due to the bias brought by the geometry. To eliminate the influence of the bias and understand the image better, we modeled the same DSC with no missing assemblies. The image is shown in Figure 3.8 (a). Figure 3.8 (c) shows a subtraction of Figure 3.8 (b) from Figure 3.8 (a). From the subtraction image, it becomes possible to locate the missing assemblies. Moreover, since the difference mainly lies on y-axis, we added the values along z-axis. Figure 3.9 shows the total number of scattering points vs y

position. Before generating this plot, we rejected the events with small scattering angle. The threshold value of the cosine of the scattering angle was chosen as 0.9900 for best performance. From this figure, it is easy to find the position of the missing assemblies.

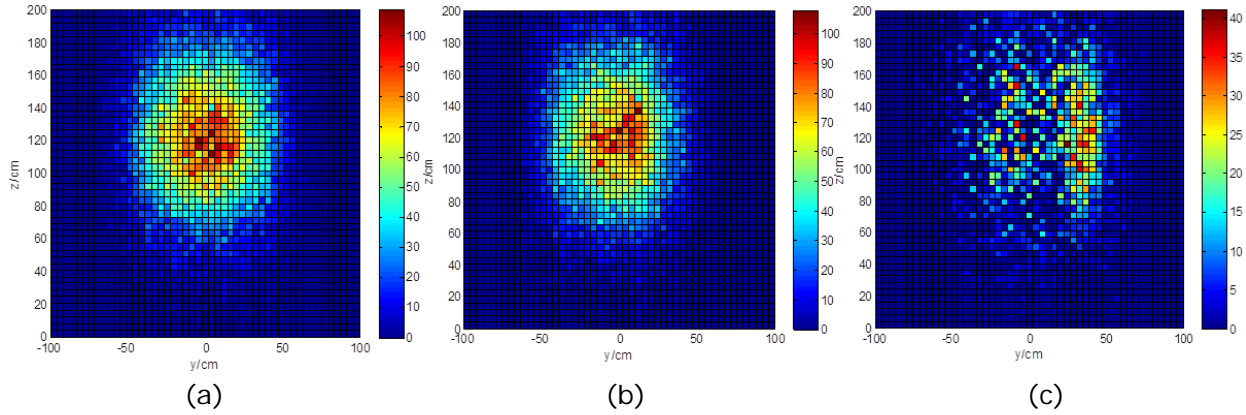


**Figure 3.8** (a) y-z 2D histogram of the POCA scattering points from the DSC with full assemblies (b) y-z 2D histogram of the POCA scattering points from the DSC with missing assemblies (c) image subtraction

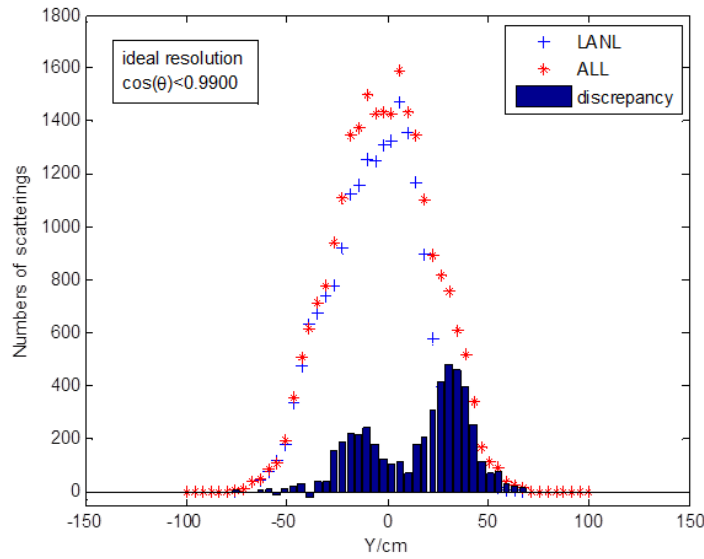


**Figure 3.9** Total number of scattering points vs y position

In the above part, we assumed perfect position resolution of the muon detectors. However, our detectors are not able to offer a position resolution better than 1 cm. Thus, we re-evaluated the images when we assume the position resolution of the detector to be 1 cm. The same processes are done. Figure 3.10 and Figure 3.11 show the result. Here we used a larger threshold of  $\cos(\theta)$ , because the distribution of the scattering angle is broadened due to the induced position error when the position resolution is degraded. Although it is harder to locate the missing assemblies from the subtraction image, it is still possible to identify and locate them in the integrated image.

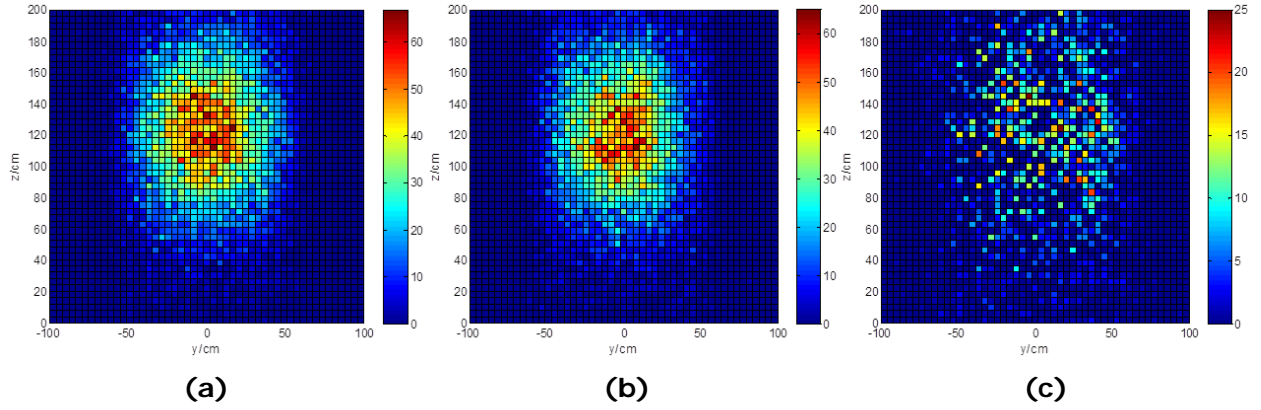


**Figure 3.10** Images reconstructed in the case of 1cm position (a) y-z 2D histogram of the POCA scattering points from the DSC with full assemblies (b) y-z 2D histogram of the POCA scattering points from the DSC with missing assemblies (c) image subtraction.

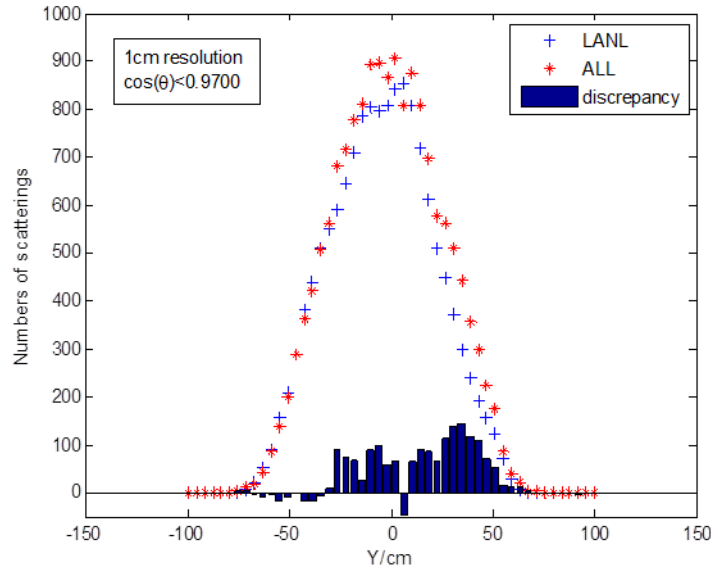


**Figure 3.11** Total number of scattering points vs y position in the case of 1cm position

#### 4. Design of the proof-of-concept muon tomography system

A scaled-down muon Tomography system was designed as a prototype for imaging DSC based on the theory of muon tomography. It comprises four position sensitive muon detectors. Two of them, separated by 50 cm, are located on top of the imaging cavity forming incident muon tracker, and the other two are positioned below the active volume forming the outgoing muon tracker. With the identification of a space point in each detector, the initial and scattered muon trajectories could be reconstructed enabling the determination of the scattering position and scattering angle needed for image reconstruction. The system configuration is shown in Figure 4.1.

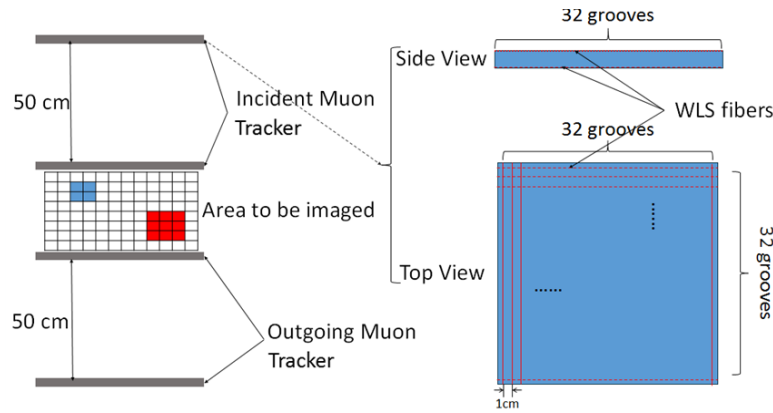


**Figure 4.1** The layout of the scaled-down muon tomography system

Each position-sensitive detector is a single layer of a plastic scintillator plane with size of 32 cm by 32 cm by 2.5 cm. 32 parallel grooves with 2 mm width, 4 mm depth pitch are curved on each side of the scintillator plane. The directions of the grooves on the top and bottom sides are perpendicular to each other and the pitch between two adjacent grooves is 1 cm. By doing this, the position resolution is theoretically achievable. EJ-200 by Eljen was chosen as the scintillator material. Bunches of wavelength shifting (WLS) optical fibers (BCF-92 by Saint-Gobain) are embedded in each groove for light readout. The optical fibers from each channel are coupled to Hamamatsu H8500C MAPMTs.

To derive the position information, the relative amplitudes of 32 channels are measured and an interpolation is done to obtain a distribution. However, this requires reading all channels, which means a 64-channel data acquisition system is required for a single detector in either analog or digital domain. Based on the idea of the Anger logic used to position events using the resulting four corner anode signals, a simple 1-D resistive ‘network’ is introduced. 33 resistors with the same resistance are connected in series to form the 32-channel 1-D network for one dimension in one scintillator plane. And the signals from the MAPMT corresponding to the 32 channels for one dimension in one scintillator plane are connected to the 32-channel network. By reading the two ports at the both ends of the network, the position in this dimension can be located based on ratio of the signals at the two ports. Figure 4.2 shows the schematic of the circuit. The scintillators are carefully wrapped with aluminum foil. The other ends of the WLS fibers are connect to the windows of H8500c MAPMTs in order. Then each scintillator assembly is put into a dark-box made of Acrylic plastic sheets. Figure 4.3 is a picture of the detector set in the dark box.

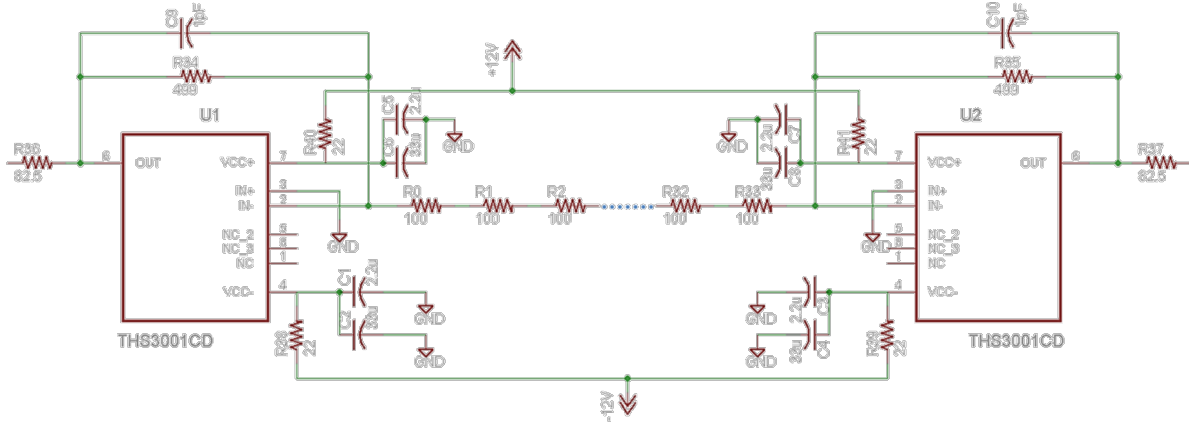


**Figure 4.2** The schematic of the resistive network for 32-channel readout

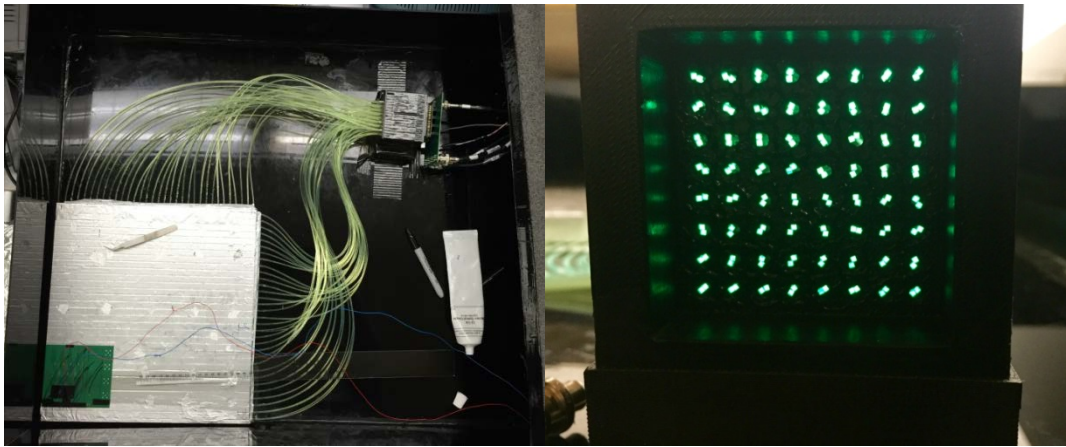


**Figure 4.3** The picture of the detector set in the dark box

## 5. Position calibration of position-sensitive scintillator

After all of the four muon detector sets are assembled, the relationship between position and the ratio has to be determined individually for each detector. This step is called the position calibration. The reason the position calibration has to be done individually for each detector is that a small difference among the detectors, such as the bending of the fibers and wrapping of the scintillators, could result in a big difference of the position-ratio relation.

Considering the unpredictability of the energy deposition location of a gamma-ray or a neutron particle and the light output of an alpha particle, we gave up using a radiation source to do the position calibration. Instead, a blue LED was used to simulate the scintillation light since the emission spectrum of EJ-200 scintillator mainly covers the blue range. The reason to use a LED instead of using a source is that it is easier to control the location of “scintillation” to use a LED. Holes on the foil were made at different locations to let the LED light in. The LED picture is shown in Figure 5.1. The LED was powered by a function generator to simulate a short “scintillation” pulse. Figure 5.2 shows the parameters of the pulse. Using the blue LED powered by the function generator, we can simulate the scintillation process of the scintillator. Then the light was wavelength-shifted and then transferred to the MAPMT. The readout board was

introduced in the previous report Y2Q1. Then the data were acquired using the DSO-X3104A oscilloscope and processed with MATLAB offline.

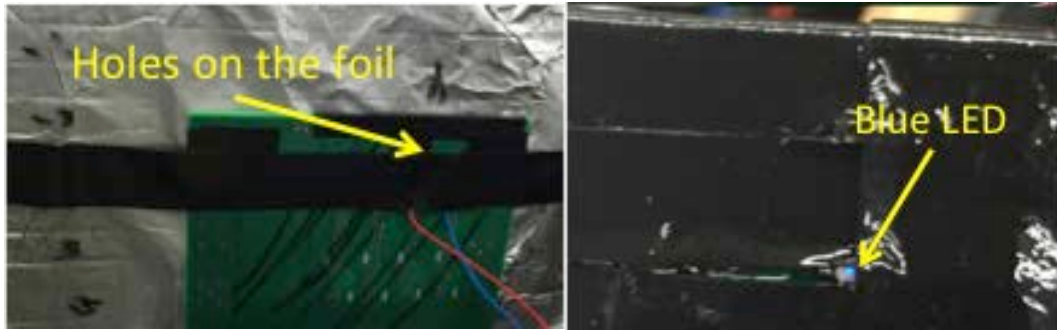


**Figure 5.1** The LED light used to simulate the scintillation light

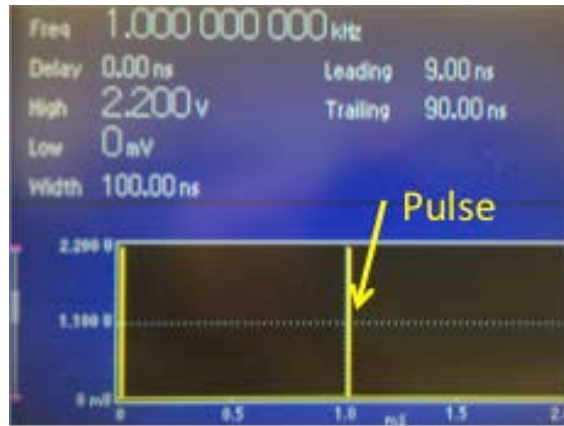


**Figure 5.2** The signal from the function generation used to power the blue LED

The test was done at 63 different locations. Figure 5.3 shows the position of the 63 points. The center of the scintillator was set to be [0, 0]. The [15, -15] point was missing because the space was not enough to place the LED board. At each position, 5000 sets of data were acquired. We measured the amplitudes at the four outputs from the readout board which was introduced in previous reports. The amplitudes of A and B are measured to determine x position, while the amplitudes of C and D are measured to determine y position. Then the  $A/(A+B)$  ratio, named the ratio\_x, and the  $C/(C+D)$  ratio, named the ratio\_y were then calculated. Then the plot of the mean ratio\_x vs. the mean ratio\_y is shown in Figure 5.4.

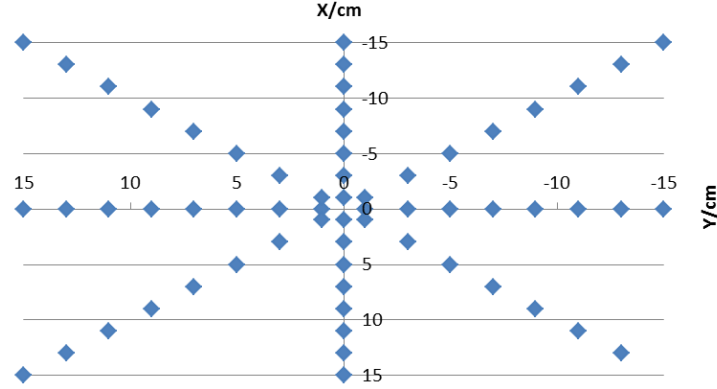


**Figure 5.3** The positions of the 63 tested points

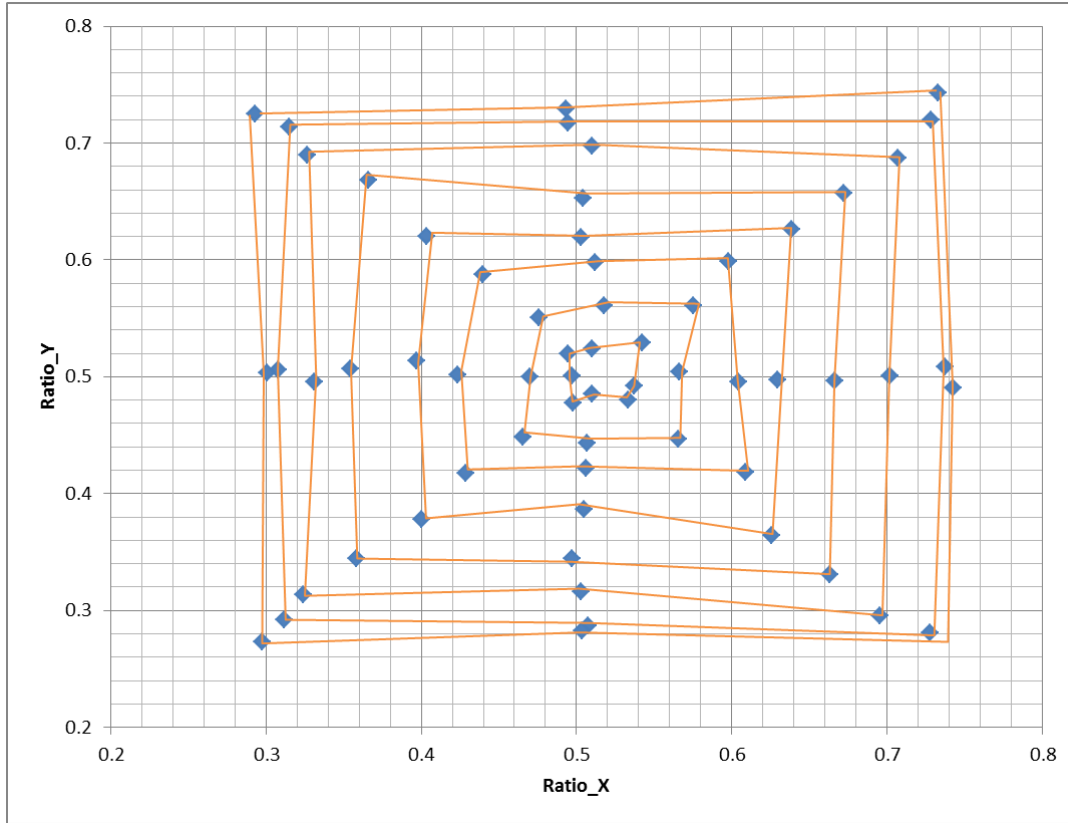


**Figure 5.4** The plot of the mean ratio at x dimension vs. the mean ratio at y dimension

From Figure 5.4, the average value for the points was calculated. The relation between the ratio and position was analyzed respectively for x and y dimensions. Figure 5.5 shows the plot of ratio\_x vs x. Figure 5.6 shows the plot of ratio\_y vs y. We used the 6th polynomial fitting to fit the relation between the ratio and position. The fitting results are also shown on the figures. The reason we don't use linear fitting is that the relation is not linear near the edges of the scintillators due to the reflection properties. This will be demonstrated using simulation tools.



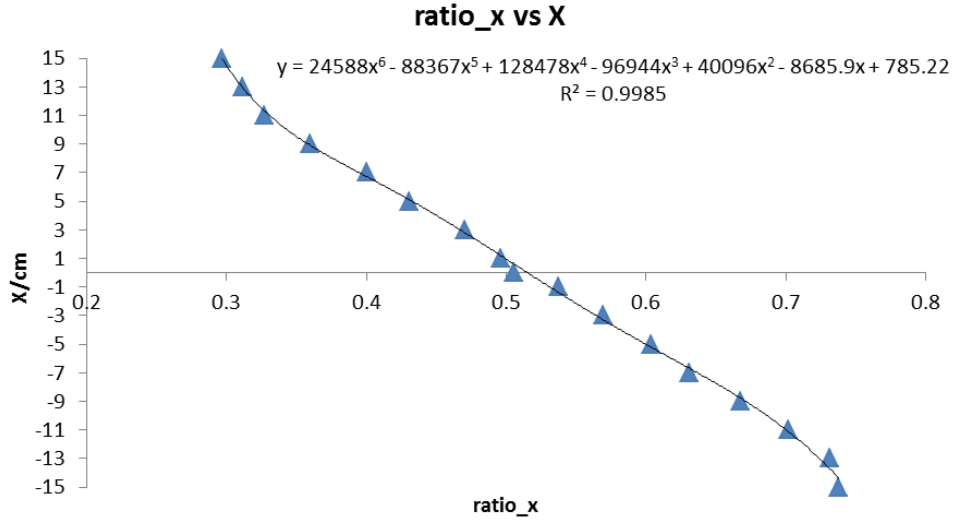


**Figure 5.5** The fitted curve of the mean ratios at x dimension vs. x positions

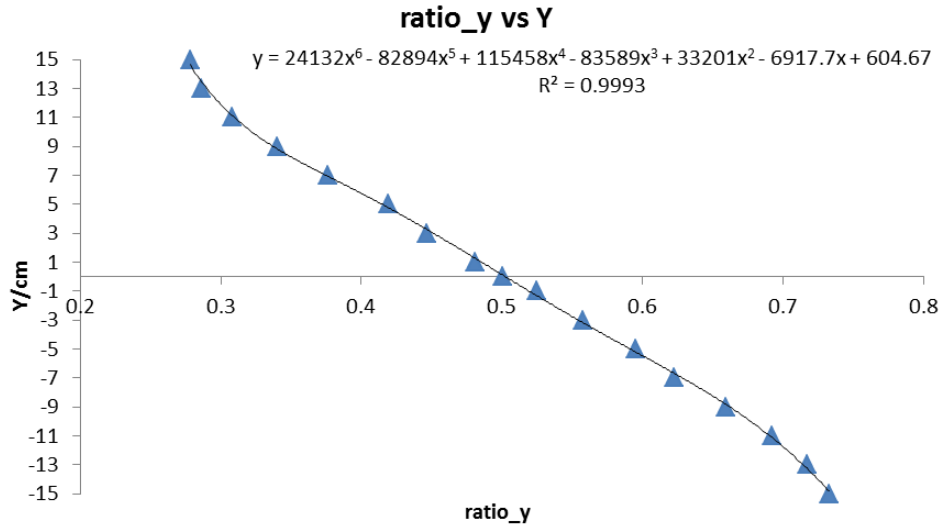


**Figure 5.6** The fitted curve of the mean ratios at y dimension vs. y positions

The same method was used to do the position calibration of the other three detectors. The results show the feasibility of the detector design to locate scintillation events is different positions. It also provides quantified relationship between the measured parameters and the event positions.

## 6. Building the Muon Tomography System

As introduced in previous reports, the prototype muon tomography system consists of four muon detectors, which forms the incoming tracker and the outgoing tracker. After assembling the missing muon detectors, #3 and #4, the whole muon tomography system was set up as shown in Figure 6.1.



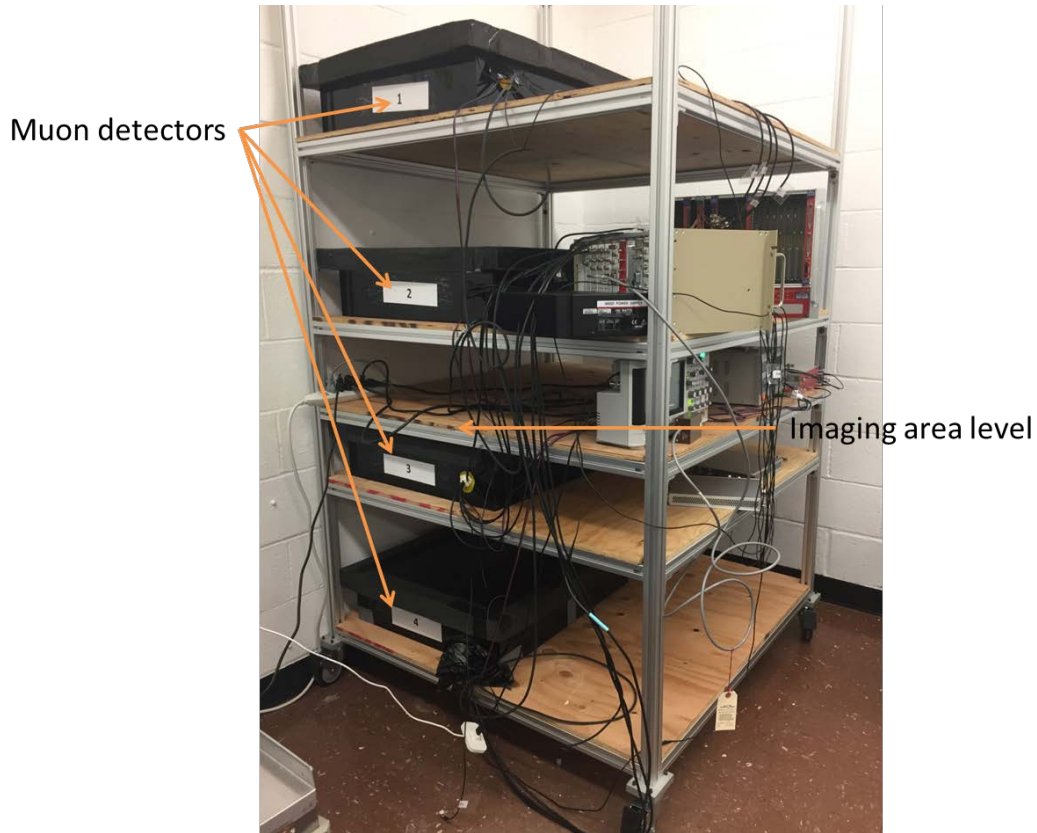


**Figure 6.1** A picture of the muon tomography system with all components.

According to the design of the signal processing and data acquisition system in previous sections, the signal chain is illustrated in Figure 6.2. The signal chain mainly consists of two paths: the triggering and digitizing paths. After the signal pre-processing board, each detector has four output signals that contain the muon information and one dynode signal used to generate trigger for data acquisition. The total 16 output signals are directly connected to the input of the CAEN VX1742 32-channel Digitizer. Only the first 16 channels are used. The four dynode signals are connected to the CAEN N605 4-channel constant-fraction Discriminator. When a signal gets beyond the threshold, a trigger output is given by the discriminator. Two N108 dual delay units are used to compensate the time difference brought by muon travelling. Then four outputs from the discriminator are fed into the V967B coincidence module. When a “real” muon hits all four detectors, a coincidence trigger is generated. The coincidence trigger is used as the trigger of the digitizer.

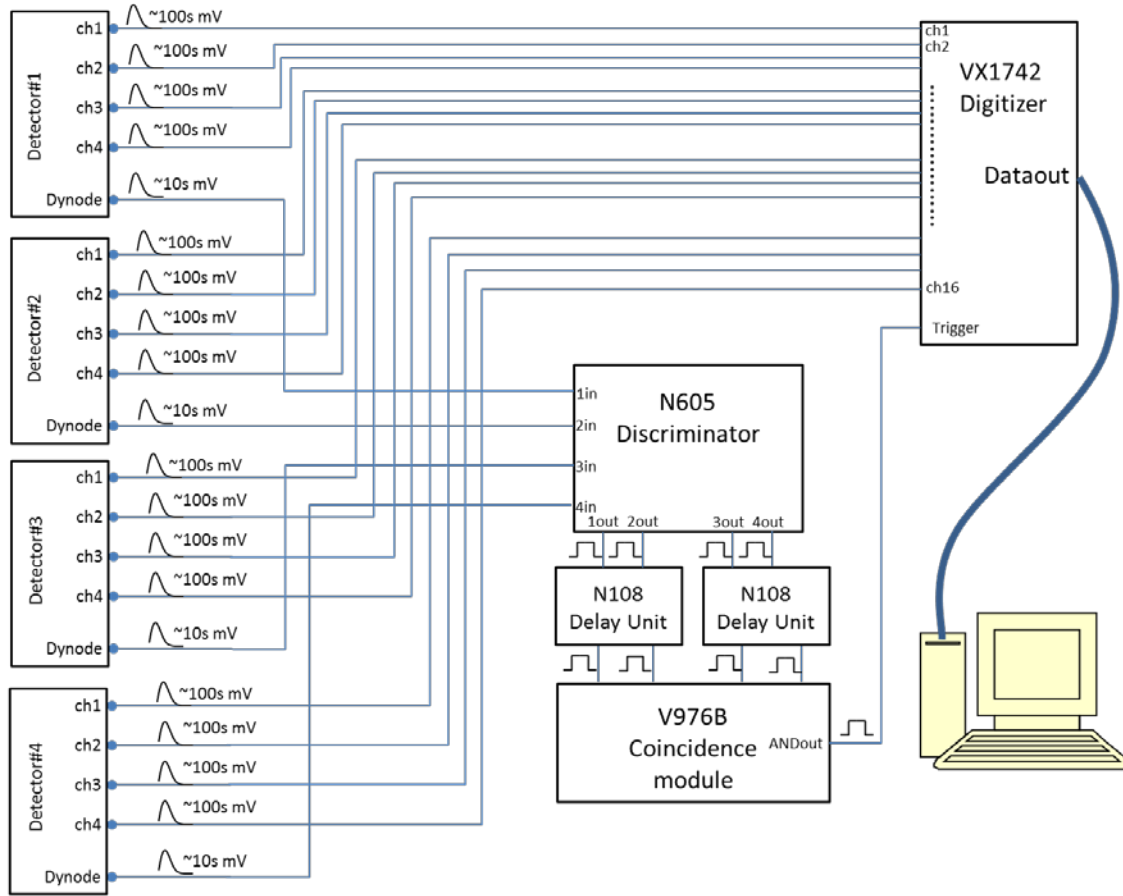


**Figure 6.2** The signal chain of the data acquisition system.

From previous initial tests, a typical dynode pulse from each muon detector is shown in Figure 6.3. The amplitude of the signal is small because it does not pass through any pre-amplification circuit. Moreover, the N605 Discriminator only take in negative signals. Thus, in the initial test, we use four individual Canberra 2031 single channel analyzers instead of the discriminator to generate trigger signals four each channel.

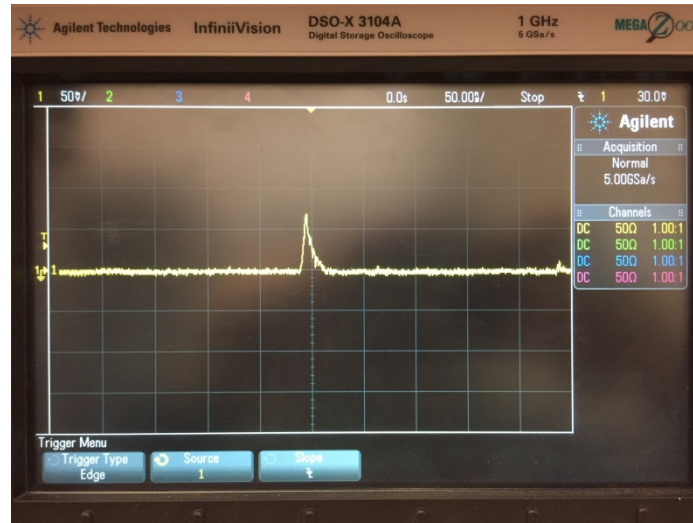


**Figure 6.3** A typical dynode pulse from the muon detector used for triggering.

A typical dynode signal has an amplitude of  $\sim 10$ s mV. Thus, we set the threshold of the discriminator to be 50mV. By doing this, the trigger rate of one channel is around 30 per minute, which is close to the cosmic muon source rate at earth surface. Then, the output signals from the discriminator are connected to the inputs of the coincidence module. Then the four-fold AND output can be used as the trigger signal to the digitizer. The coincidence rate was 3 to 4 per minute, which is also close to the simulation result. Ideally, the delay between two trigger signals is several nanoseconds. Figure 6.4 shows the trigger signals used to generate the coincidence trigger in one coincidence event. However, in the case of this example, the delay is not as expected. This is due to the pulse is not triggered at the same relative point. The difference between the four channels may also contribute to it. The problem is expected to be resolved when we use the N605 discriminator.



**Figure 6.4** The trigger signals used to generate the coincidence trigger in one coincidence event.

The initial test of the whole system is done with the above system setup. The first test was run with no imaging objects. Ideally, the four measured muon positions on the four detectors should form a straight line when a muon event is detected by all detectors, because no significant scattering happened along the trajectories.

For each registered muon events, total of 16 channels of signals are acquired. Using the digitized output signals and the position calibration results from last quarterly report, the positions can be calculated, individually for four detectors. Figure 6.5 shows an example of the detected muon trajectory. The four positions form a straight line as expected. The corresponding detector output signals used to extract the position information are also shown in this figure.

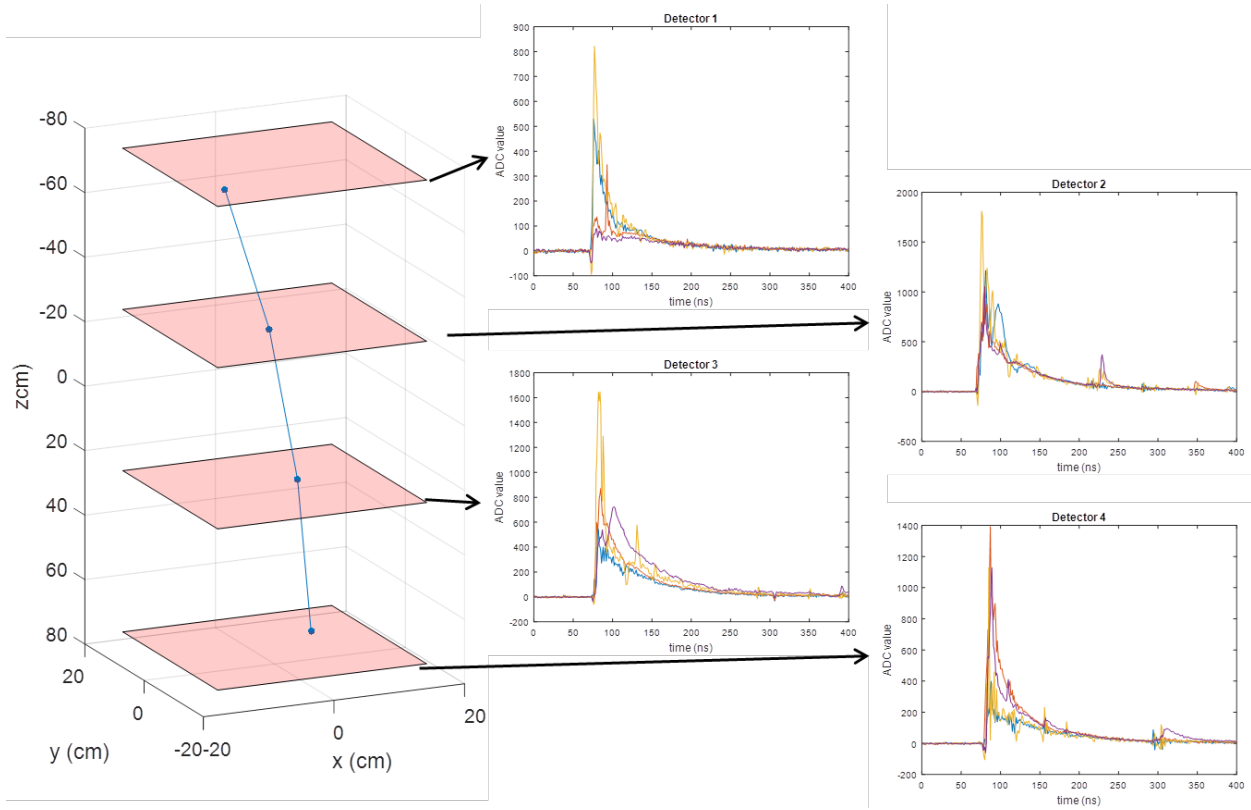


**Figure 6.5** An example of the detected muon trajectory.

However, some bad examples are also observed. A bad example is shown in Figure 6.6. The four points are not in a straight line. Some points are even out of the boundaries of the detector. Looking at the output signals, we observed some large distortions, which are possibly brought in by the signal processing PCB board. These distortions can lead to the loss of the amplitude information and therefore the loss of the position information. It might be one of the reasons. Moreover, the position calibration is not perfect. The factor will be examined after the signal distortion problem is resolved.

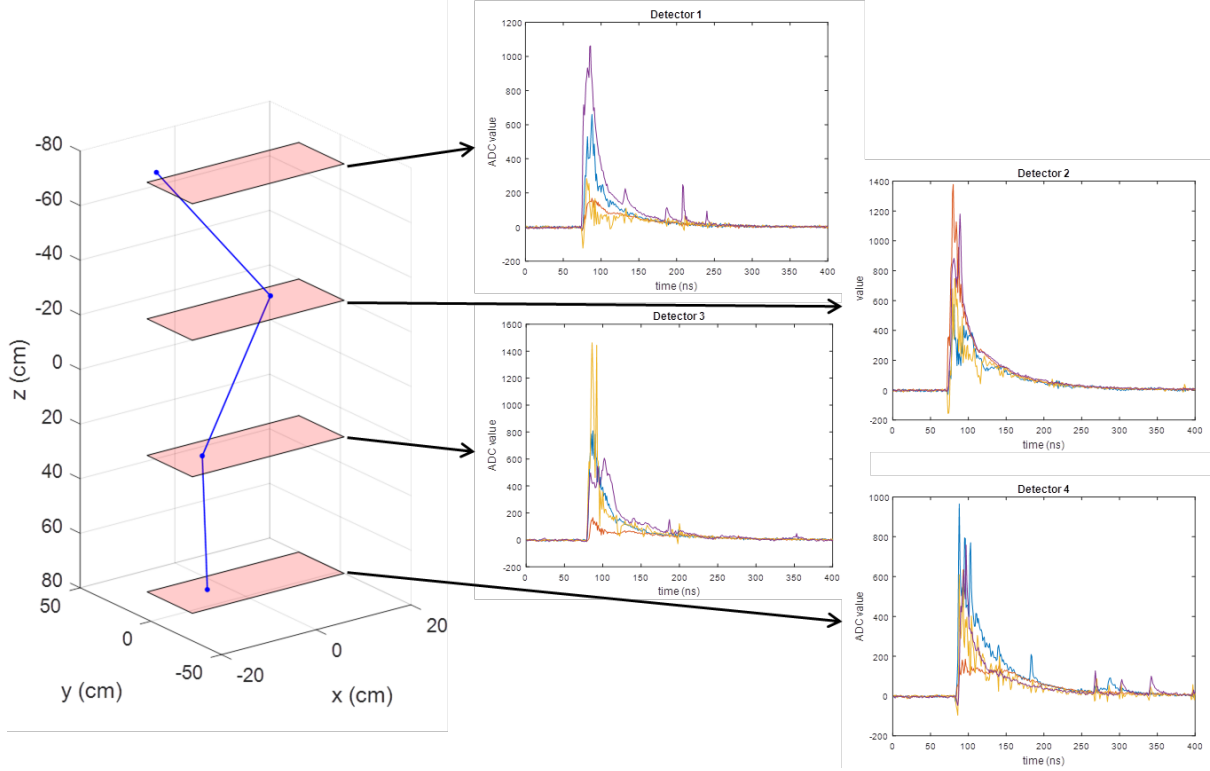


**Figure 6.6** A bad example of the detected muon trajectory.

## 7. Design of the preamplifier board for the dynode signals

As discussed, the N605 discriminator cannot be applied to our system because it only takes in negative pulses. And considering the amplitude of dynode signals, we design an amplification circuit to amplify and invert the dynode signals. The PCB design is shown in Figure 7.1.

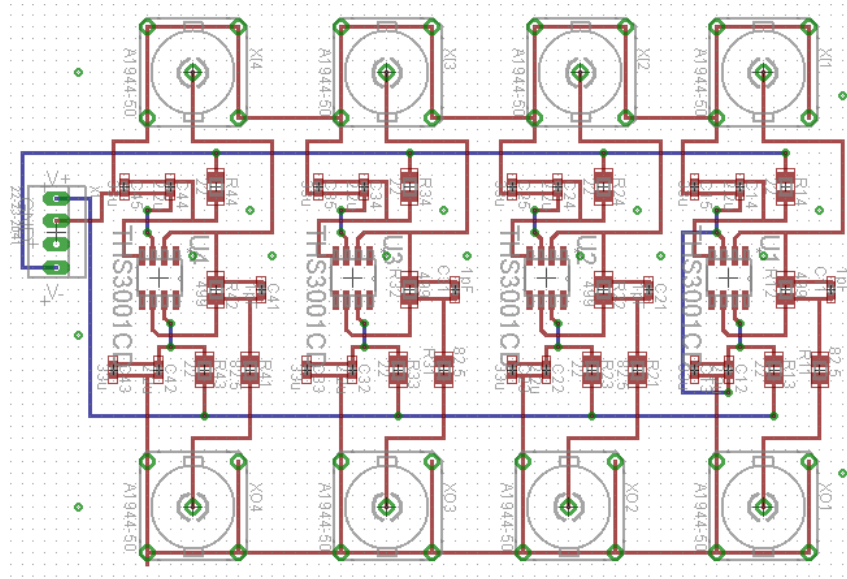


**Figure 7.1** The PCB board used to amplify and invert the dynode signals.

## 8. Debugging the Muon Tomography System

As mentioned in previous reports, the initial test of the whole system was done with the system setup. The first test was run with no imaging objects. Ideally, the four measured muon positions on the four detectors should form a straight line when a muon event is detected by all detectors, because no significant scattering is expected to happen along the trajectories. However, lots of unexpected events were observed, where the four points did not form a straight line. Some points are even out of the boundaries of the detector. Looking at the output signals, we observed some large distortions, which are possibly brought in by the signal processing PCB board. These distortions can lead to the loss of the amplitude information and therefore the loss of the position information. Thus, we optimized the circuit design by adding more space in between the components and avoiding routing traces with sharp bends. Some other minor changes are also done. Figure 8.1 shows the screenshot of the new design of the readout board.

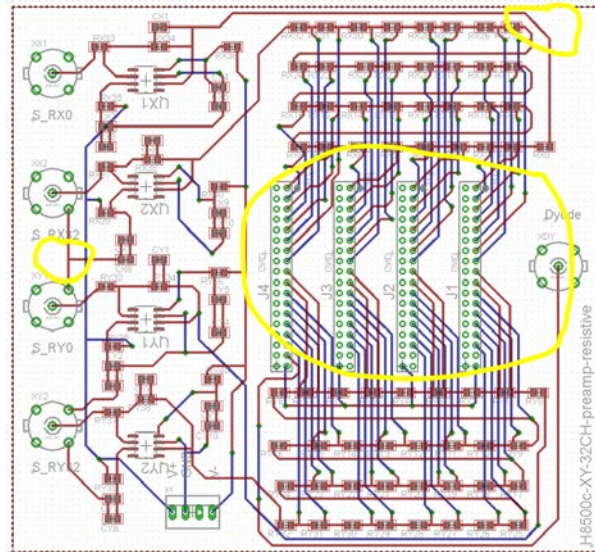


**Figure 8.1** The screenshot of the new design of the readout PCB.

After four new boards were made, we tested each board with each detector. Figure 8.2 gives a Comparison of the output signals from the old readout board and the revised board using Detector 3. Clearly, we see that the signals from the new board are much cleaner than those from the old board. No distorted signals are observed. All output signals follow a form of exponential decay.



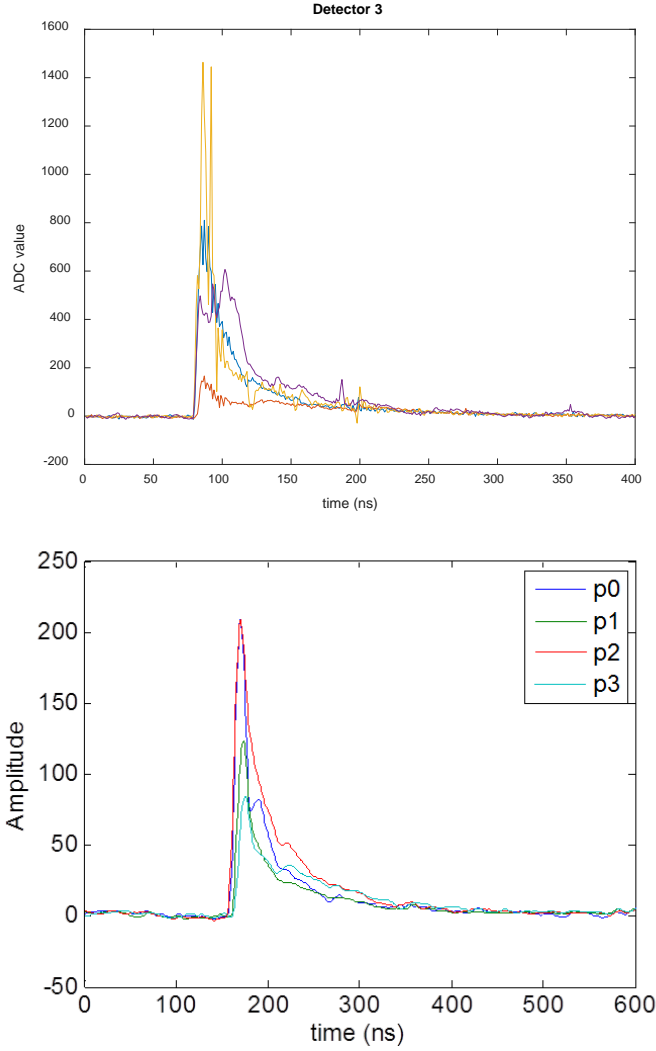


**Figure 8.2** Comparison of the output signals from the old readout board and the revised board.

We then did a new calibration to validate the board design. The new position calibration results showed great agreement with the old version. Thus, it was believed that the established relationship between position and signal ratio using the old board design is still valid. A new coincidence test for the whole system was then carried out. Three detectors were stacked up and aligned in z direction. Ideally, the three measured muon positions on the three detectors should form a straight line when a muon event is detected by all detectors, because no significant scattering is expected to happen along the trajectories. For each registered muon events, a total of 12 channels of signals are acquired. Using the digitized output signals and the position calibration results from last quarterly report, the positions can be calculated, individually for four detectors. Figure 8.3 shows an example of a detected muon trajectory. The three positions form a straight line as expected.

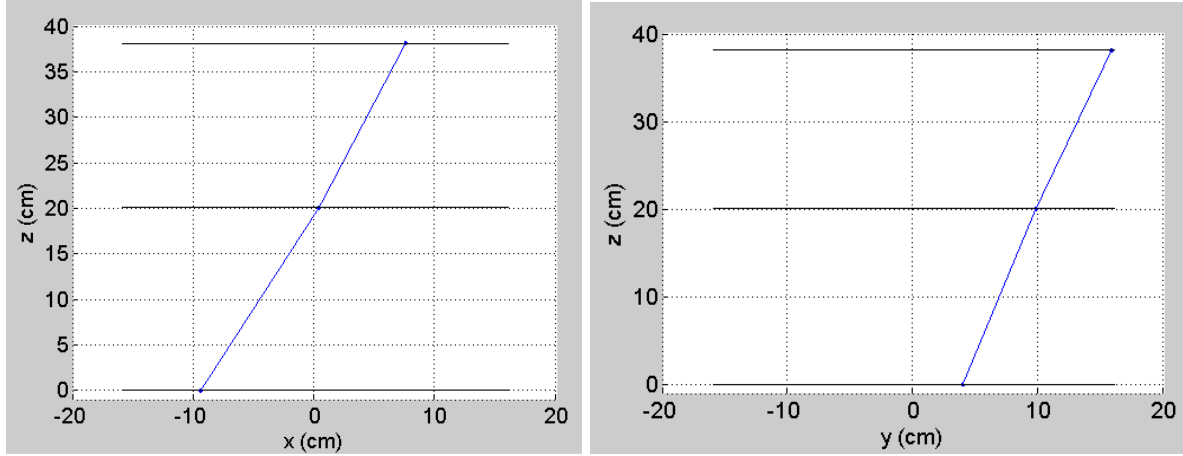


**Figure 8.3** An example of the detected muon trajectory from three stacked detectors.

Then we moved the detectors back to the frame. We ran a test with all four detectors. The first run was done with no imaging objects, the same as we did in the last quarterly report. Figure 8.4 shows an example of a detected muon trajectory. The four positions form a straight line as expected. The corresponding detector output signals used to extract the position information are also shown in this figure.

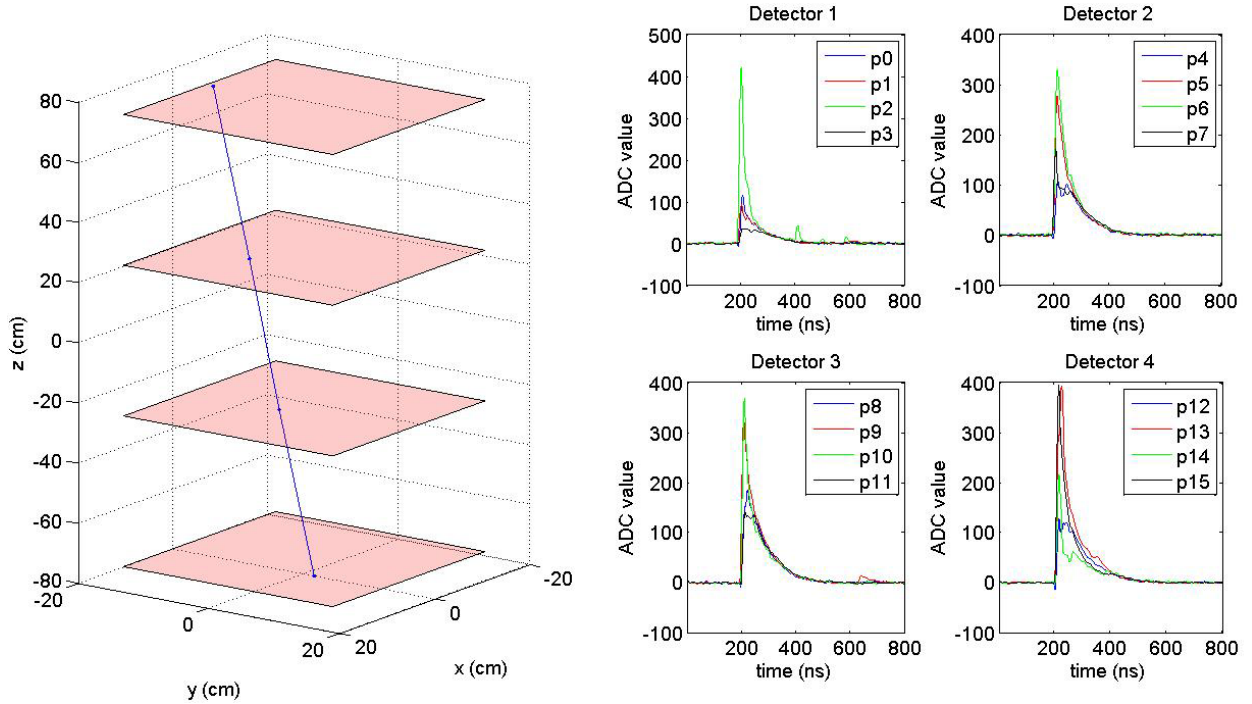


**Figure 8.4** An example of the detected muon trajectory from the whole system and the corresponding signals.

Two more tests were performed. One test was run with one lead brick place in the imaging volume; the other one was carried out with three lead bricks. We expect to see a difference in coincidence rate, the muon scattering angle distributions and scattering points. All the tests were run with the same setup, such as the high voltage, power supply and the thresholds of the discriminators. Table 8.1 shows the results of the measured coincidence counts and the running time of the three tests. The coincidence rate decreases as the number of lead bricks increases.



This relationship agrees with our expectation that more lead bricks will increase the probability of large angle scattering events thus decrease the coincidence rate.

*Table 8.1 Count rate measurement with different imaging objects.*

Imaging area	Time	Total counts of coincidence	Coincidence rate
Empty	16 hr	1462	$91.4 \pm 2.4/\text{hr}$
One lead bricks	19.32 hr	1418	$73.4 \pm 1.9/\text{hr}$
Three lead bricks	25.66 hr	1340	$52.2 \pm 1.4/\text{hr}$

## 9. An alternative detector design

After investigating and testing the previous design of the detector, we decided to abandon the previous detector design. We went back to one of our early-stage designs. In this version of design, the position sensitive detector is composed of two orthogonal detection planes with an active area of 32 cm by 32 cm, each of which contains 32 pieces of 1 cm by 1 cm by 32 cm scintillator bars. Each scintillator bar is read out with bunches of wavelength shifting (WLS) optical fibers. One can simply get the position information by reading just one channel that has a significant signal. Figure 9.1 shows the schematic drawing of the second detector design.

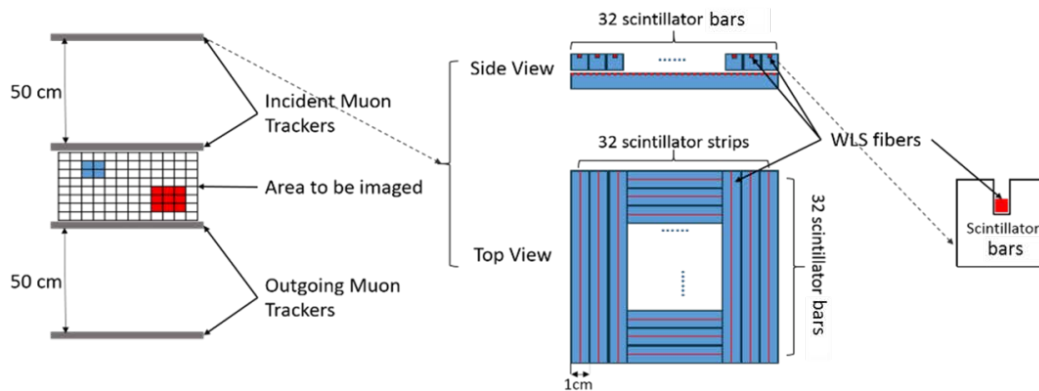


**Figure 9.1** The schematic drawing of the second detector design using plastic scintillator bars.

EJ-204 by Eljen was chosen as the scintillator material. Saint-Gobain BCF-92 WLS optical fibers were chosen for light readout. EJ-204 is another option. Their scintillation spectrum both overlaps a large portion of the absorption spectrum of the WLS fibers. The H8500C 64-pixel MAPMT by Hamamatsu has been identified as the light sensor because of its compact design and multichannel readout capability. And its response is good for reading lights from BCF-92 since it is sensitive to light whose wavelength is from 300 nm to 500 nm.

Since the scintillator bars are independent from each other, we don't have to consider the interference. If all output channels are read at the same time, the interaction can be located by only considering the channel that has the most significant signals. However, this requires reading all 256 output channels at the same time. This is extremely expensive. Therefore, we went back

to the traditional anger logic circuit. We use an 8 by 4 anger logic resistor network to decrease the readout channel for one dimension of one detector from 32 to 4. Figure 9.2 shows the idea of this 8 by 4 resistor network. Equation 9.1 is used to calculate the position.

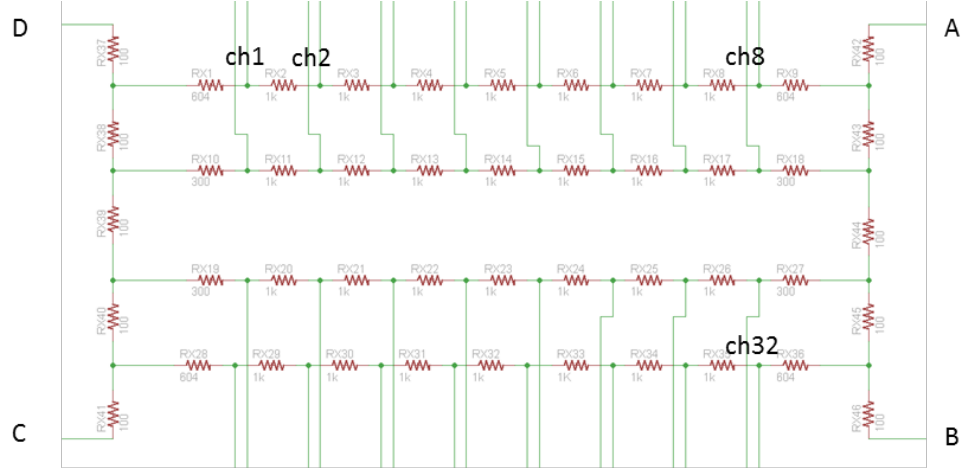


**Figure 9.2** The idea of this 8 by 4 resistor network

$$X = \frac{A + B}{A + B + C + D} \quad Y = \frac{A + D}{A + B + C + D}$$

- Equation 9.1

## 10. Testing of the second detector design

To validate the new detector design with the resistor network, some test was done with single scintillator bars (embedded with fibers). The test was done also with blue LEDs that was powered by a function generator. The equation 1 was used to calculate the parameter that represents the position. Table 10.1 shows the test results. Figure 10.1 shows the plot of ratio\_x vs ratio\_y. The standard deviations of the ratios are much smaller than the gap between the ratios at different position. Thus, this design improved the ability to distinguish different reaction locations.

**Table 10.1** Test result of the new design

Channel	Column (x)	Row (y)	Ratio x	std_x	Ratio y	std_y
1	1	1	0.01524	0.02918	0.77979	0.01815
2	2	1	0.15033	0.01639	0.78207	0.01434
3	3	1	0.29035	0.01144	0.78375	0.01519
4	4	1	0.43511	0.00830	0.78241	0.01333
13	5	2	0.57581	0.00599	0.59478	0.00600
14	6	2	0.71748	0.00917	0.59391	0.00584
15	7	2	0.86075	0.01373	0.59341	0.00602
16	8	2	0.99533	0.01709	0.59104	0.00665
17	1	3	0.01063	0.02263	0.40844	0.00881
18	2	3	0.13743	0.01420	0.40616	0.00691
19	3	3	0.28705	0.00767	0.40500	0.00597
20	4	3	0.43127	0.00450	0.40397	0.00573
29	5	4	0.56959	0.00476	0.22769	0.00836
30	6	4	0.70400	0.00668	0.23105	0.00760
31	7	4	0.83257	0.00892	0.23517	0.00705
32	8	4	0.99958	0.02596	0.21350	0.01565

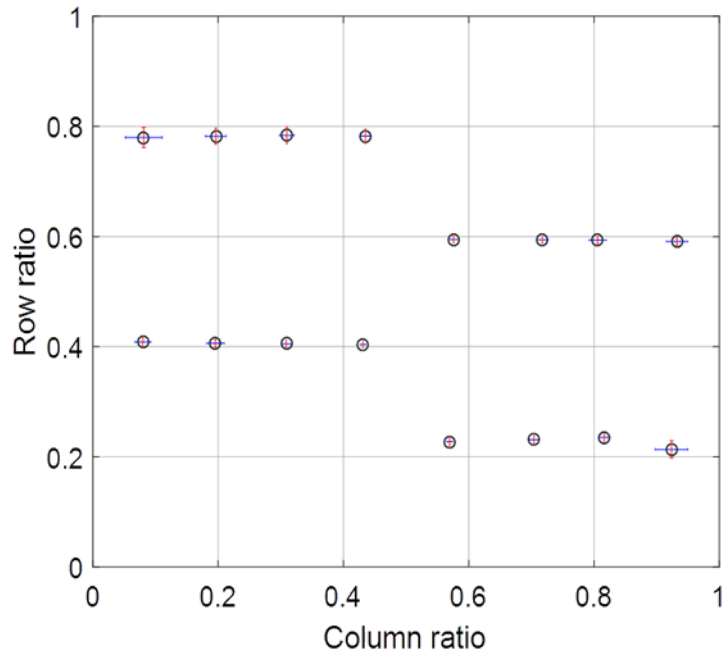


**Figure 10.1** The plot pf ratio x vs ration y

## 11. Study of the impact of elevated radiation background

In the previous test, the coincidence rate stays at 31~32 per minute with the short coincidence window setting, even though the natural background rate is not low. However, the system is aimed to image a DSC that emits much higher level of radiation than background. Thus, the impact of the radiation from a cask is necessary to be investigated. Due to the fact that we don't

have the access to a DSC site, we studied the impact with some radiation sources that are accessible in our lab. Based on a report from Idaho National Lab, the average gamma dose rate from an MC-10 cask for one detector is about 1.3 mrem/hr. The neutron dose rate is about the same level. Figure 11.1 also shows a gamma spectrum of the cask radiation.

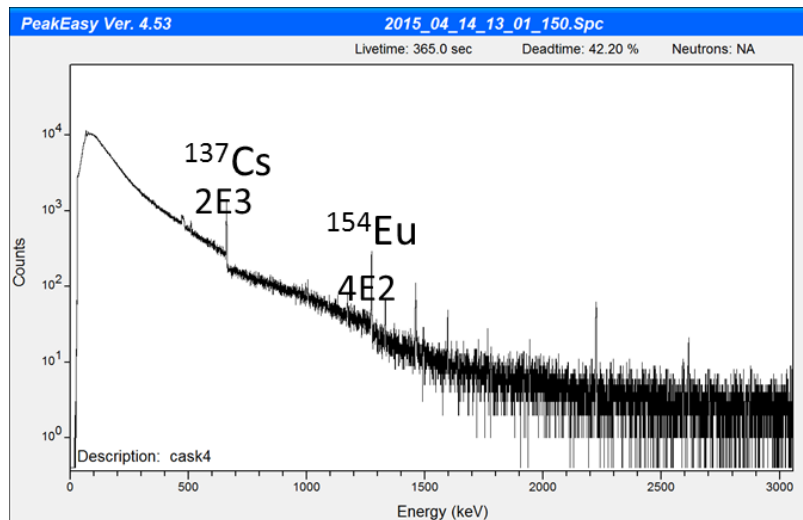


**Figure 11.1** The gamma spectrum of the MC-10 DSC radiation.

Thus, the test was mainly done with a Cs-137 source and a Co-60 source to represent the major gamma-rays. Strong sources were positioned at a contain point so that the average dose rate at each detector is equivalent to 1.3 mrem/hr. In this part, the discriminator thresholds were set to 30mV, 70mV, 65mV and 30mV, respectively for detector #1, #2, #3 and #4. First, the count rate of each detector was measured when the radiation sources were present. Table 11.1 listed the count rate of each detector from natural background, a Cs-137 source and a Co-60 source.

**Table 11.1** The count rates of each detector from natural background, a Cs-137 source and a Co-60 source.

		Natural	Cs-137 ~0.7mrem	Co-60 ~1.3mrem
	Th (mV)	count/s	count/s	count/s
<b>Det1</b>	30	102.38	600.38	4107.08
<b>Det2</b>	70	97.67	349.67	2789.07
<b>Det3</b>	65	159.05	281.32	2034.68
<b>Det4</b>	30	77.75	231.97	3993.22

From the count rate results, it is observed that lots of gamma events from Cs-137 are rejected with the threshold settings. Since it is hard to estimate the real count rate of each detector from a real cask, here we exaggerate the count rate by assuming all gamma counts are from Co-60. And we assume the neutron rate is equivalent to the gamma count rate. By making a large exaggeration, the total count rate of each detector from a real cask is estimated to be 10,000 per

second. The simple equation of accidental coincidence rate (ACR) is given by the following equation:

$$\text{ACR} = R_1 R_2 R_3 R_4 W^3 \quad \text{- Equation 11.1}$$

Using Equation 11.1, the ACR is estimated to be 0.00156 per second. This is negligible compared to the muon rate in our system. Therefore, with largely exaggerated count rate, the ACR is negligible. However, this conclusion is not completely convincing because a point source is so different from a volume source like a cask. The result is not quantitatively valid when the actual ACR is not estimated. Without an actual cask, the quantification is barely possible.

Instead, the impact of increased ACR on image is studied. The Co-60 source was moved much closer to the detectors in this test in order to observe significantly increased coincidence rate. By doing this, the coincidence rate is increased from 31.2 per minute to 51.8 per minute. In the situation with and without Co-60 source, the same imaging objects were imaged. Figure 11.2 is a picture of the imaging objects formed with smaller lead models.



**Figure 11.2** A picture of the imaging objects formed with smaller lead models

The same numbers of coincidence events were acquired for both scenarios; thus, the test without the additional source took longer. The images were reconstructed using the PoCA algorithm. Figure 11.3 shows the reconstructed images in both scenarios. From this comparison, the increase of the accidental coincidence rate did not affect the image capability and did not significantly degrade the image quality. The reason that fewer effective pixels were seen in the image with Co-60 was that most ACR events are rejected in the data processing stage. The majority of ACR events came from the coincidence with gamma events. The probability of gamma-ray events deposit energy in both layers of a detector was low. During the data processing, the inner coincidence of both layer of one detector was adopted. Therefore, most ACR were rejected. Even though the increased ACR does not significantly affect the image quality, it increases the data stream volume because the data is processed offline.

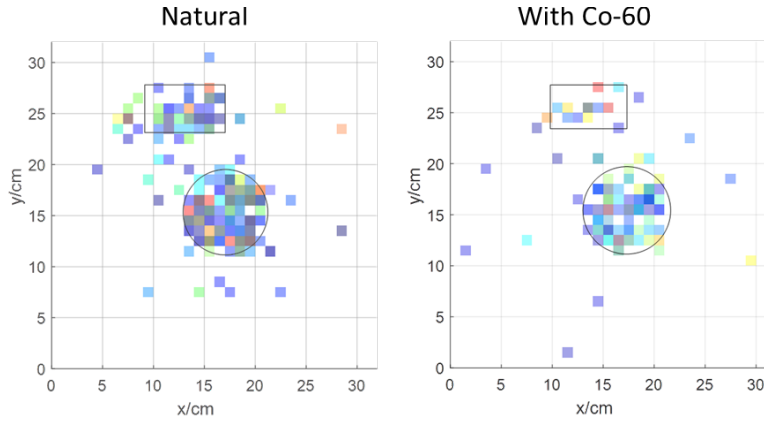


**Figure 11.3** The reconstructed images in both scenarios.

## 12. Image Spatial Resolution Study

After the prototype system was proven to have the capability to image simple objects, the spatial resolution was studied. Due to the fact that this muon detector has a granularity of 1 cm and the error introduced by the resistor network, the position resolution of the detector is actually worse than 1 cm. Moreover, the size of the pixel used in image reconstruction is also 1 cm. Thus, even with ideal imaging conditions, the spatial resolution cannot be better than 1 cm.

The test was done with 20 cm by 10 cm by 5 cm lead bricks. Two identical lead bricks were placed inside the imaging area with a 5 cm separation from each other. Figure 12.1 shows a picture of the lead bricks. Then the lead bricks were imaged with the prototype system for 24 hours. The POCA algorithm was used for the image reconstruction. Figure 12.2 shows the reconstructed image. The image was projected to x axis to show the gap more clearly.

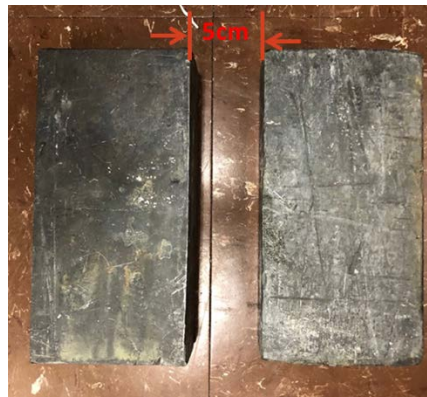


**Figure 12.1** The picture of the tested objects (5 cm separation) for spatial resolution study.

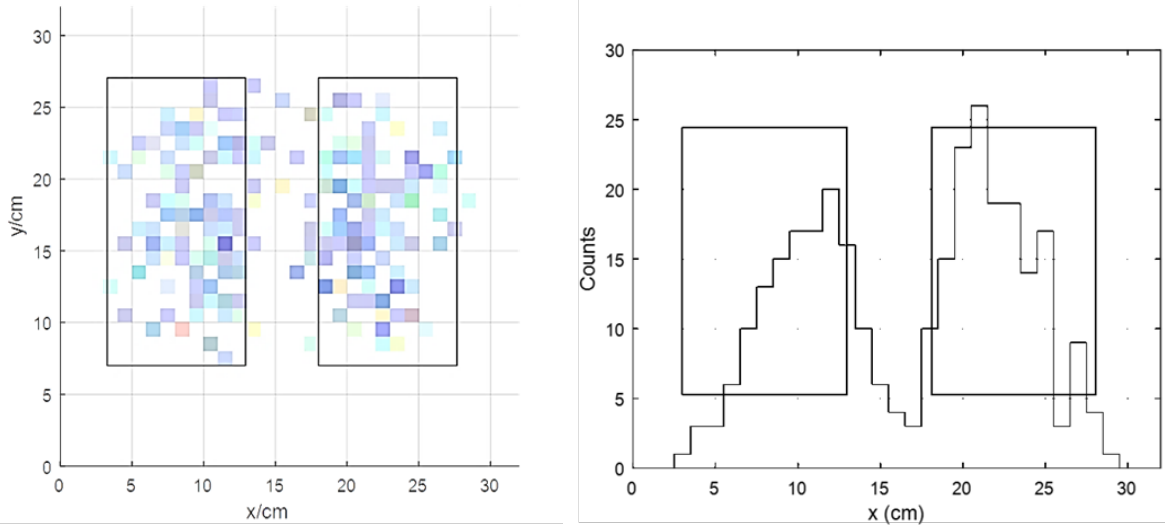


**Figure 12.2** Left: The reconstructed image of the lead bricks (5cm separation); right: the projected count of pixels vs x position

Then two lead bricks with 2 cm separation were imaged with the system. Figure 12.3 is the image of the lead bricks and the plot of the projected counts of pixels vs x position.

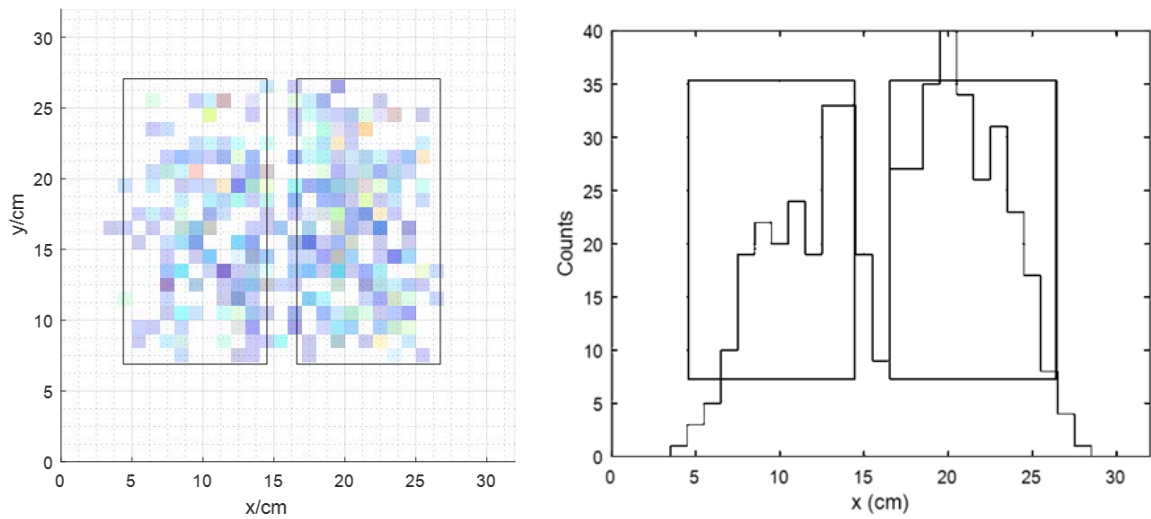


**Figure 12.3** Left: The reconstructed image of the lead bricks (2cm separation); right: the projected counts of pixels vs x position.

In Figure 12.3, the black boxes indicate the actual location of the two lead bricks. A gap of 2 cm wide is expected to be between the two lead bricks. However, the image does not exhibit a clear gap of 2 cm wide. Instead, a gap of 1 cm wide is observed, even though a few non-empty pixels exist. Considering that both the position resolution of the muon detector and the pixel size are 1 cm when the edge of some object lies inside certain pixels, it is impossible to decide the location the edge of the object relative to this pixel. In this case, one can conclude that the two lead bricks can be separated in the reconstructed image. Thus, the spatial resolution is roughly estimated to be 2 cm given the condition of 5 cm thick lead bricks and 24 hours of imaging.

### 13. Conclusions

A prototype muon tomography system based on scintillation detectors were designed, built, assembled and tested for the purpose of monitoring used nuclear fuel content inside dry storage casks. Two versions of detector designs (i.e. single scintillator panel and independent scintillator bars) were explored. The final version was the design with independent scintillator bars.

First, simulation study of muon radiography was performed. The results illustrated the idea of muon radiography and the possibility of using it for imaging DSC. Muon radiography was not further studied due to its poor performance and the infeasibility.

The next work was the simulation study of muon tomography. The simulation of simple object demonstrated the capability of imaging high-Z materials. The simulation study on a detailed cask model benchmarked the idea of utilizing muon image for cask inspection. Especially, the idea of comparing the image of a partially loaded cask and that of a fully loaded cask successfully demonstrated the feasibility to detect missing spent fuel assemblies, even with 1 cm detector position resolution.

Then, the first version of detector design based on scintillator panels was constructed. The position sensitivity of detector version I relies on arrays of WLS fibers and the resistor network. The position calibration of the detector, performed with a blue LED, proved its position sensitivity. The position solution was around 1-2 cm in the LED scenario. The integration test of the system showed that it could detect and locate muons. However, the position resolution for muon is not good enough for the system to do tomography.

The second version of the detector design based on independent scintillator bars was then built and assembled. The position sensitivity relies on the 2D resistor network. The position calibration was done with the natural background. The calibration showed that it was able to achieve ~1 cm position resolution. Then the integration test demonstrated the functionality of the system design version II.

With the new system design, the prototype system demonstrated imaging capability that is sufficient for the design purpose. The impact of elevated radiation background was also studied using the combination of field measurements and laboratory testing. The result indicated that the radiation emitted from a typical cask does not significantly impact the imaging capability and image quality. Finally, the image spatial resolution of lead bricks was quantified to be around 2 cm. Overall the prototype system showed encouraging results and the technical approach warrants further study.



## **List of Publications and Presentations**

C. Liao, H. Yang Z. Liu and J. P. Hayward, “A Scintillator-Fiber based Cosmic-ray Muon Tomography System for Imaging Dry Storage Cask,” 2016 ANS Winter Meeting, IEEE 2017

Nuclear Science Symposium Poster:

A Prototype Cosmic-ray Muon Tomography System for Dry Storage Cask Monitoring

C. Liao, H. Yang, Z. Liu, J. P. Hayward, “A Prototype Cosmic-ray Muon Tomography System for Dry Storage Cask Monitoring,” 2017 IEEE NSS/MIC Conference, Atlanta, Georgia, USA, 21 – 28 October, 2017

# AREVA

## Consultant for Cask Design and Full-Scale Cask Access

Arthur Niemoller - TPOC

Over the past three years, Orano / AREVA has supported this DOE-sponsored NEUP project in a variety of manners, including access to technical information, experimentation of physical resources, and assistance with logistic and planning activities. The first major contribution was to provide a detailed SolidWorks computer model of a TN-32 cask to two of projects' teammates, as well as meetings with AREVA experts who responded to questions and provided design details, particularly regarding dimensions and materials. In conjunction with providing details associated with the TN-32 cask design, AREVA experts also provided guidance with regards to cask operations and licensing requirements as well as standard practices used at a utility site.

Through-out the duration of the project, AREVA facilitated almost a dozen visits to our Columbiana HiTech (CHT) facility in Greensboro, NC. At this site, university partners were able to see, touch, and experiment on an actual dry storage cask. As this was the same cask being modified for the High Burn-up Fuel Cask Research and Development Project, a considerable amount of planning and scheduling was required, especially during the last visits when the cask was undergoing final testing and inspections.

Both an AREVA technical expert and an AREVA project manager were assigned to lead support efforts for the project, including participating in project meetings and reviewing final deliverables.

AREVA is currently discussing and negotiating with utilities for access to a fully loaded cask located at a commercial plant site, to further the investigations started during this project. This is particularly important to AREVA, as well as other used fuel cask providers and servicers, as older casks approach their lifetime licensing limit. In the near future loaded casks will have to commence inspection programs to allow for licensing extensions, and a program will need to be created that allows for cask content safeguards, as radiation levels decay to where the fuel can no longer be considered self-protecting. Both of these issues will soon become very important for the nuclear industry, and both warrant further investigation.

# **EPRI**

## **Thermographic Evaluation of a Dry Storage Canister Mockup to Evaluate Internal Conditions**

Jeremy Renshaw - TPOC

### **Task Overview/Abstract**

The EPRI team was tasked with the responsibility to evaluate whether or not thermal inspection methods could successfully interrogate the internals of a dry storage system for degradation, such as entrapped water, severely failed fuel (rubblized fuel), etc. from the exterior of a canister. The EPRI team used both thermal cameras as well as resistance temperature detectors (RTDs) to measure and record temperatures. The results demonstrated that while it was possible to detect large volumes of entrapped liquid water at the base of a canister (~100 liters/26 gallons), it was not possible to detect more realistic volumes of water on the order of <1 liter (<0.26 gallons) using the thermal camera measurements, even when the water was concentrated in a single location. Similarly, if a large volume of rubblized fuel were to be present near the bottom of the canister, it is anticipated that such thermal methods would be capable of detecting this condition, however, would almost certainly fail to detect more realistic fuel failure scenarios (cracks, debris frets) with minimal capability to lose significant volumes of fuel debris.

### **Introduction**

Nuclear power plants operate by utilizing the fission of atoms to generate heat, create steam, and drive turbines to make electricity. This process results in significant energy production with comparatively small waste volumes. Nuclear plants store their wastes (in the form of used fuel rods) in spent fuel pools for a period of time after discharge from the reactor to allow for cooling and for short-lived radionuclides to decay away. This decay process produces significant heat, which is removed via the cooling provided by the spent fuel pool water. After a period of time, on the order of 3-5 years, used fuel rods have cooled sufficiently to be placed into dry storage systems.

Dry storage systems consist of a stainless steel canister with a concrete overpack for shielding or a bolted cask system with integrated shielding. Both systems are in use around the world today. While the external appearance of casks and canisters may vary significantly, many of the key internal features are similar. Dry storage systems employ internal neutron absorbers to ensure fuel subcriticality as well as use helium as an inert cooling gas. The helium provides two key features:

1. The helium is an inert gas that helps to significantly reduce or eliminate corrosion inside of the dry storage system.
2. Helium gas has one of the highest thermal conductivities of any gas, which aids in heat removal from the fuel rods

While there is no anticipated fuel degradation from normal conditions of storage during periods of dry storage, it could be possible that dry storage systems could degrade over long periods of

time and inspection of the internal condition of the fuel would be desirable without the necessity of opening a canister for inspection. Therefore, this project evaluated various methods for assessing the condition of the fuel from outside of a dry storage system.

This work builds on previous work on thermographic nondestructive evaluation methods. Methods such as flash thermography, vibrothermography, and induction thermography have been successfully used for detecting defects in materials as well as in multi-layered structures [1,2]. Even simple, passive thermographic techniques have been successful at locating defects in large structures, such as hydroelectric dams [3,4], or in multi-layered structures as in the case of containment liner mockups [5]. These techniques can be robotically deployed for inspection into tight or confined spaces, though the radiation resistance of thermal cameras is largely unknown, however, many thermal cameras rely on CCD technology that is susceptible to degradation from exposure to radiation.

Previous work on thermal methods pertinent to dry storage canisters is shown below in Figure 1 wherein external surface cracking was detected using thermography. Thermal methods were used to detect matrix cracking in a sample using thermal inspection methods. The original aim of this work was to adapt techniques from previous thermal testing to the unique situation presented by dry storage canister inspections to detect conditions affecting the fuel on the inside of the canister from the external surface.

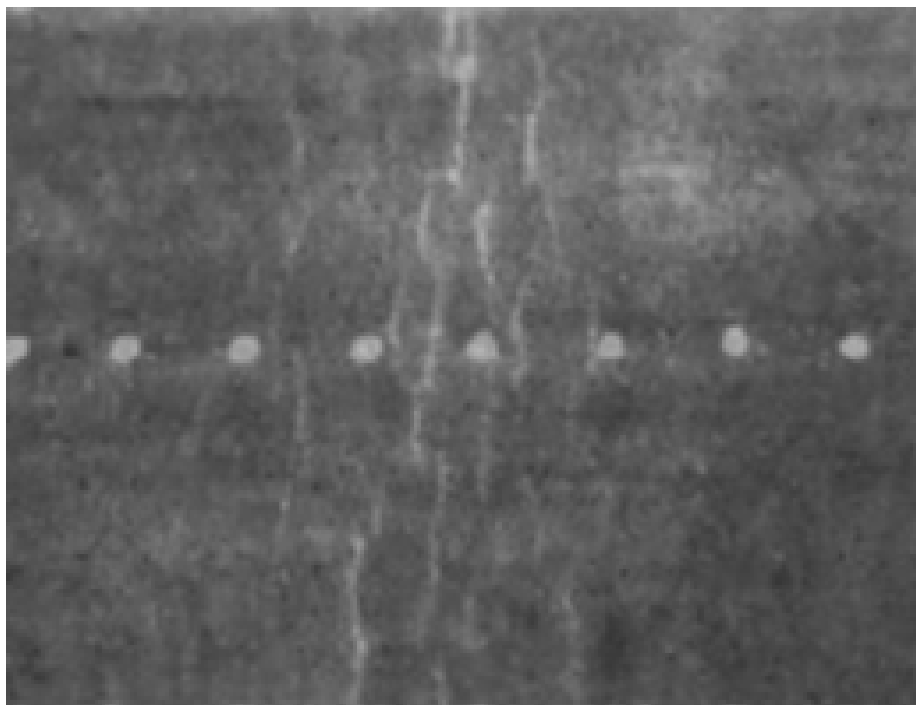


Figure 1 – Thermographic inspection of a stainless steel sample using thermography. Several cracks are observed in the sample in the vertical direction.

For this reason, thermography was proposed as a potential method for detection of conditions of interest within a dry storage canister, such as entrapped water and/or severely degraded (rubblized) fuel. While neither of these two conditions is considered credible for normal conditions of storage or transportation, this work would support the evaluation of a severe accident where water could potentially enter a canister or fuel failures may occur.

### **Experimental Setup**

The mockup used for testing was supplied by Sandia National Laboratories and is shown below in Figure 2. The mockup was constructed from 304L stainless steel with a thickness and diameter representative of actual canisters in service and manufactured by a company who has specialized in canister manufacturing in the past. The canister mockup also contains welds characteristic of those that may be encountered in the field. The mockup was painted for the first set of tests (test conditions 1-4 in Table 1) to provide a smooth, even surface finish and the paint was removed for subsequent, more realistic, testing. The as-received canister surface finish can be seen in Figure 2.



Figure 2 – Test setup for dry canister inspection using thermography

Four sets of test conditions of increasing difficulty were developed as shown in Table 1. Each test condition became increasingly more challenging than the previous test condition as the cases modeled actual conditions more closely. Prior to these tests, very little knowledge was available on the amount of remaining water that could be contained inside of a dry storage system after drying. As such, extreme cases (1-4) were tested to evaluate whether or not large volumes of water could be detected. Subsequent to these tests, more accurate numbers on the amount of remaining water inside of a dry storage system have become available. The 1L and 100L amounts appear to both be well beyond expected values of water that would be left behind in a dry storage system in the form of liquid water. It is anticipated that little, if any liquid water would remain after drying and water would only be in vapor form inside of a dry storage system. Since this information became available only well after these tests were completed and would be more challenging than test cases 5-12 – which largely failed to detect 1L of water – no additional testing was deemed appropriate or necessary.

Table 1 – Planned test conditions for dry canister inspection using thermography

Test Condition	Surface Condition	Camera Used	Amount of water	Dry/Wet
1	Painted	FLIR T650sc	100 Liters	Dry
2	Painted	FLIR T650sc	100 Liters	Wet
3	Painted	Seek Thermal	100 Liters	Dry
4	Painted	Seek Thermal	100 Liters	Wet
5	Unpainted	FLIR T650sc	1 Liter – bottom	Dry
6	Unpainted	FLIR T650sc	1 Liter – bottom	Wet
7	Unpainted	Seek Thermal	1 Liter – bottom	Dry

<b>8</b>	Unpainted	Seek Thermal	1 Liter – bottom	Wet
<b>9</b>	Unpainted	FLIR T650sc	1 Liter – trapped	Dry
<b>10</b>	Unpainted	FLIR T650sc	1 Liter – trapped	Wet
<b>11</b>	Unpainted	Seek Thermal	1 Liter – trapped	Dry
<b>12</b>	Unpainted	Seek Thermal	1 Liter – trapped	Wet

Thermal testing was performed on the Sandia dry cask storage system (DCSS) mockup. This is a mockup housed at the EPRI facilities that was provided to EPRI courtesy of Sandia National Laboratories. Figure 3 shows the test setup of this canister with three infrared heating lamps used to simulate an internal heat source. The testing apparatus was designed to hold the lamps in a vertical position to simulate the orientation of internal fuel assemblies that heat the canister. The canister was tested in both wet and dry environments to determine if thermography could identify the presence or absence of water in the bottom of a canister due to temperature differences observed from the external surface.



*Figure 3 – Test setup for dry canister inspection using thermography*

Based on the test setup used in Figure 3, external surface heating of the canister was achieved up to a value of approximately 77 °C (170 °F) for both the dry and wet cases. The surface of the canister was painted grey to slightly improve and maintain a consistent surface emissivity of the canister for the thermal image testing. In the field, most canisters will have a shinier finish, with a lower thermal emissivity (resulting in less efficient radiative heat transfer) and a wider

variation in surface emissivity. Some dry storage canisters may have a pickled finish, which would result in a surface with a higher emissivity than that tested herein, but could still be variable in emissivity. Field applications of a technique similar to the one evaluated in this phase of the project may require the use of contact thermocouples or RTDs instead of a thermal camera if surface conditions are not favorable to imaging using a thermal camera.

Figure 4 shows a closeup view of the inside of the DCSS mockup after adding water, but before inserting the thermography test equipment. The addition of approximately 100L of water results in a water level of approximately 38 mm (1.5”) in the canister. For reference, the ruler shown in the figure does not start exactly at zero, hence the small difference in the reported values and what appears to be the depth of water in the figure. Due to the additional submerged volume of the materials used in the test setup, this increased the water level to approximately 46 mm (1.8”) deep.



*Figure 4 – Water level after adding ~100 liters of water into the canister. The water level further increased after adding the thermal inspection test equipment.*

After performing testing with 100 liters of water, the canister was completely drained and allowed to dry. Subsequent testing involved pouring 1 liter of water into the base of the canister near the exterior wall for testing (test conditions 5-8) and finally adding 1 liter of “trapped” water in contact with the canister at a particular elevation (test conditions 9-12), as shown in Figure 5.





Figure 5 – View of the inner surface of the canister with a 1 liter volume of trapped water

## Results and Discussion

Figure 6 shows the surface heating profile of the DCSS mockup due to the three internal heating lamps. As can be observed in the image, heating of the canister was highest near the center lamp. The mockup's surface temperature slowly decreases axially (vertically) from the hot central point and circumferentially around the canister with slight increases at the locations of the peripheral heating lamps. In an actual canister, axial temperature changes would be expected, but the circumferential direction should be relatively uniform since the heat source (used fuel) is distributed throughout the canister instead of individual, confined locations as in this testing. The axial heating profile is more important to replicate for this testing to evaluate the feasibility of thermal inspection methods for detecting temperature changes in the axial direction (vertically oriented in the following figures). As shown in Figure 6, the heating profile slowly reduces axially until there is a step change at the bottom interface with the support structure.

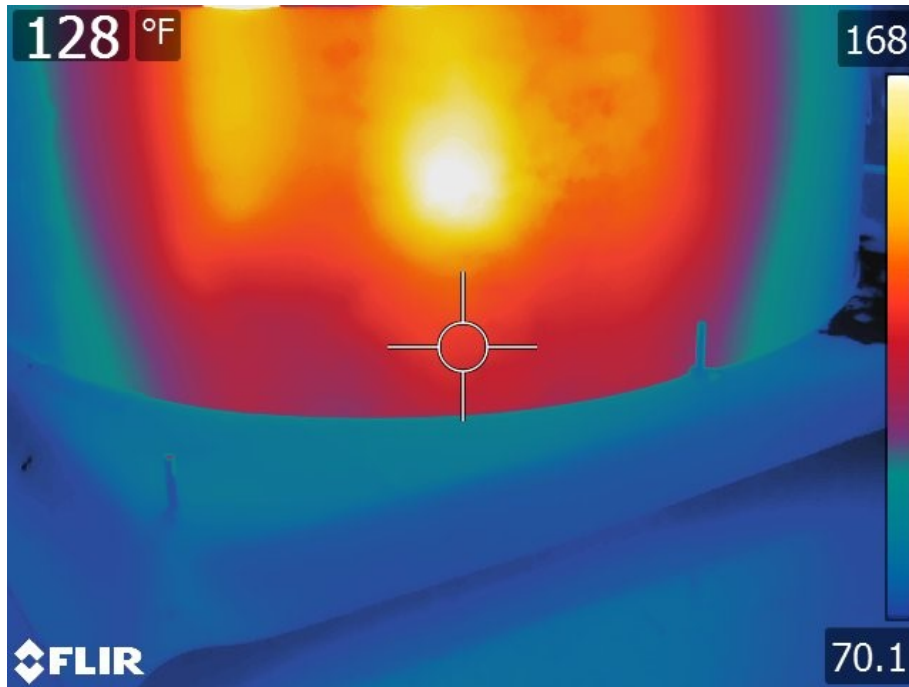


Figure 6 – DCSS Mockup tested in a dry condition. Notice temperatures steadily decreases down to the bottom of the canister

Figure 7 shows the same view of a canister after adding approximately 100 liters (~26 gallons) of water to the DCSS mockup and allowing about 2 hours for the system to reach a steady state temperature. Instead of the previously-observed smooth temperature profile along the vertical/axial direction in the canister, the temperature change is much more drastic in the case of the canister with water added. Instead of the step change in temperature at the base of the canister, there are instead two step changes. The first – and most pronounced – is near the water line of the canister, as shown in Figure 7. The second is again at the base of the canister mockup, but is far less pronounced than in the previous dry test condition.

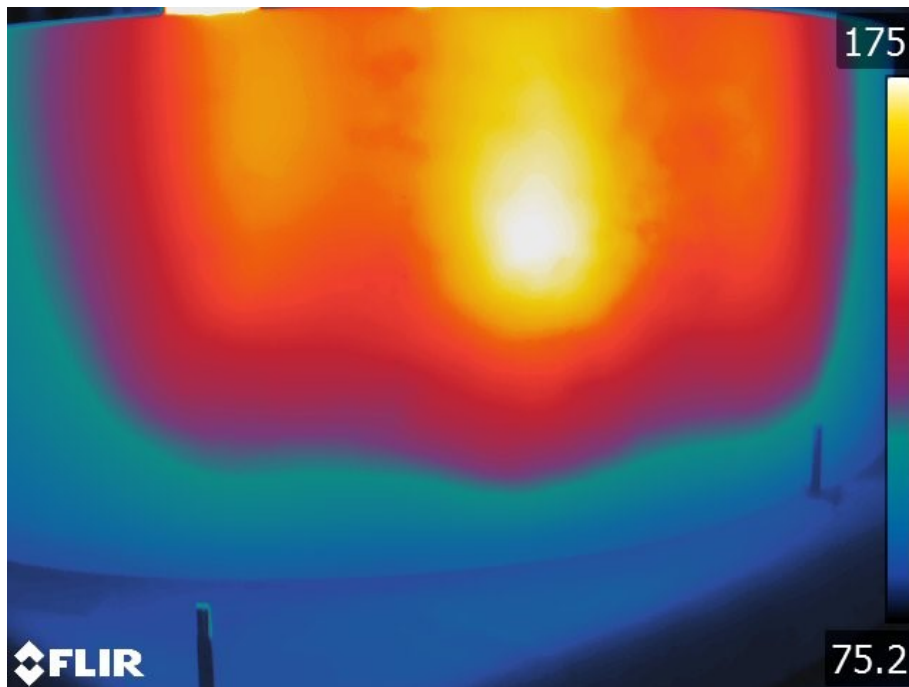


Figure 7 – DCSS mockup with ~100 liters (~26 gallons) of internal water. The water line is just over 46 mm (1.8”) from the bottom of the canister. The canister surface temperature abruptly changes near the bottom of the mockup, close to the water line.

Figure 8 shows a closeup view of the dry storage system mockup used in this testing. The addition of approximately 100L (26 gallons) of water resulted in a water level of approximately 38 mm (1.5”) in the canister. Due to the additional submerged volume of the materials used in the test setup, this increased the level to approximately 46 mm (1.8”), which is the level indicated by the pen tip on the tape measure in the figure. As shown in Figure 8, the thermographic inspection can accurately determine the water level inside of the canister due to the analysis. Due to the internal structure of an actual canister, it is likely that the water level inside of an actual canister would increase to a similar degree observed in this testing for a similar amount of internal free water. It is important to note, however, that this amount of free water was used simply for ease of testing and not in an attempt to be representative of an actual condition inside of a canister.

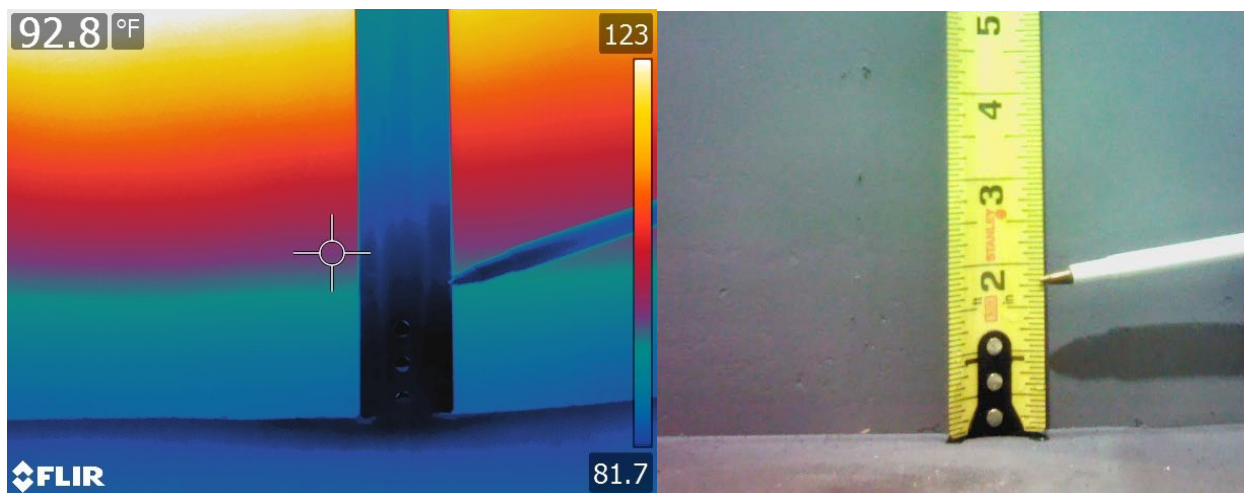


Figure 8 – Image showing a temperature difference on the order of  $\sim 22^{\circ}\text{C}$  ( $\sim 40^{\circ}\text{F}$ ) over a vertical length of approximately 100 mm ( $\sim 4$  inches)

Figure 9 below presents comparison images of the heating in the canister mockup for dry and wet setups. Note that the two left images compare the dry and wet maximum temperature – in this case the measured maximum temperatures were within  $0.6^{\circ}\text{C}$  ( $1^{\circ}\text{F}$ ), indicating that the test conditions were similar in both cases with nearly identical maximum steady state temperatures. Compare this to the areas near the water line in the right images which were  $23^{\circ}\text{C}$  ( $42^{\circ}\text{F}$ ) different, indicating a clear and easily observable difference between the dry and wet test setups for a dry canister system.

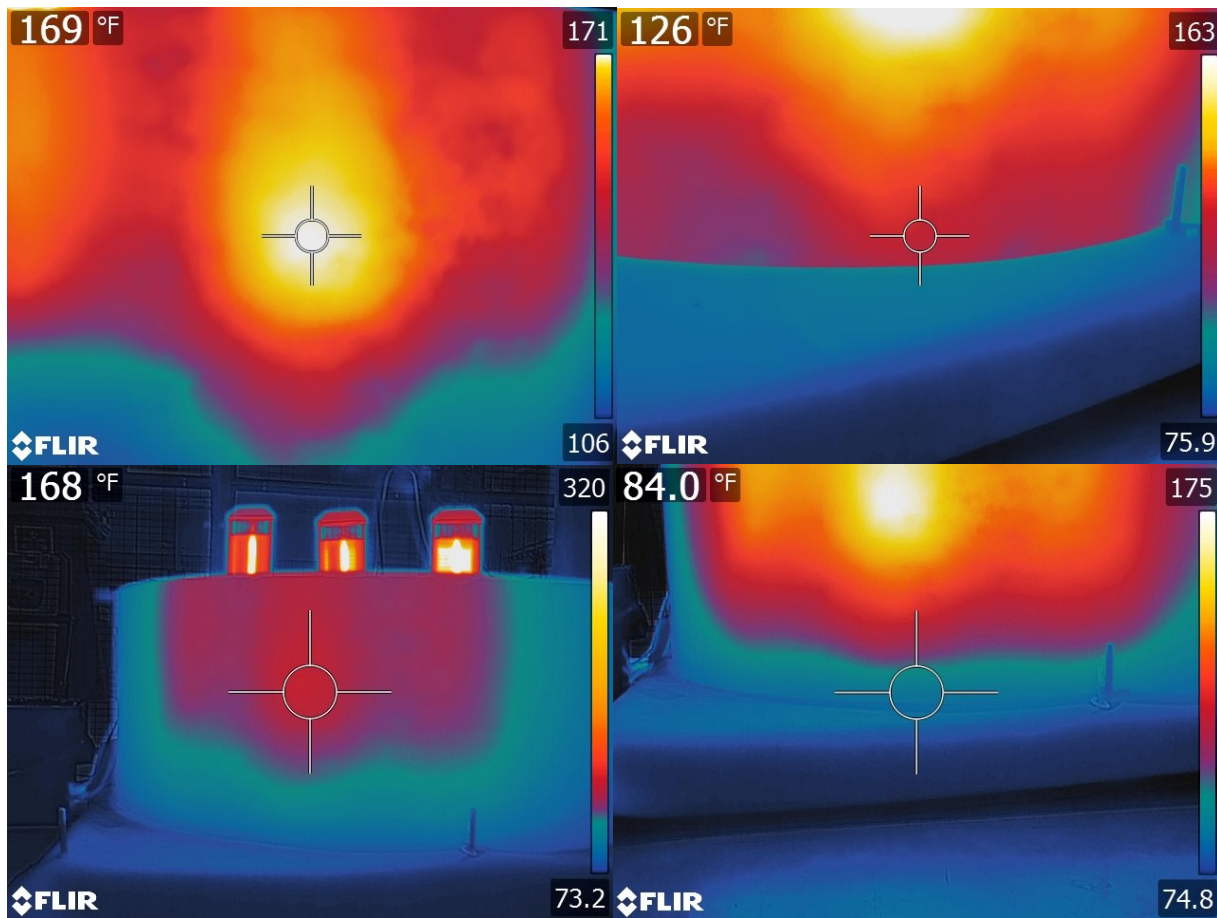


Figure 9 – Images of the heating in the canister mockup for dry (two upper images, test conditions 1 and 3) and wet (lower two images, test conditions 2 and 4) setups. Note that the two left images compare the dry and wet maximum temperature – in this case the measured maximum temperatures were within 0.6°C (1°F) while the areas near the water line were 23°C (42°F) different. Note that temperatures reported in the upper left corner of each image correlate to the temperature within the crosshair in each image.

It should be noted that the 100 liters (26 gallons) of water used in this test is an extreme upper bound, arbitrarily chosen for this test. It is not representative of actual amounts of water that could remain in a cask after either vacuum drying or forced helium dehydration processes. Small amounts of water may remain after drying, either due to residual water trapped in damaged (cracked or otherwise imperfect) fuel rods or occluded areas, such as dashpots. However, after 20-60+ years in storage (canisters are anticipated to be inspected after about 20 years of storage) trapped water may have ample time to evaporate and exit out of cracks in damaged fuel rods, meaning the water would no longer be trapped in the rods themselves. However, such water would likely undergo radiolysis, producing gaseous hydrogen and oxygen. Oxygen would likely be quickly consumed in corrosion reactions inside of the canister, though it should be noted with the small volumes of remaining water, there would be insufficient remaining water to cause sufficient corrosion to cause concern.

After showing that large amounts of water could be detected (test conditions 1-4), additional tests were performed with 1 liter of water added to the base of the canister to detect if more realistic (though still quite high) moisture levels could be detected. While 1 liter is still likely



much more water than would be expected after drying, this information was not known at the time of the tests.

Figure 10 shows the visual image (top) of the canister on the opposite side of the water and the resulting thermal image (bottom) showing a measurable difference in temperature for test condition 5 and 6 (high sensitivity thermal camera on an unpainted surface in dry or wet conditions), though it is somewhat inconclusive and not nearly as clear as test conditions 1-4. Notice that the water line in the images below – identified by the yellow arrows – can be somewhat resolved but it is not clear. This imaging was performed with a higher sensitivity, higher resolution, non-disposable thermal camera. This camera was used to detect if the method could work, however, using this camera could pose challenges in a radiation environment since similar high-sensitivity thermal cameras typically cost too much to be disposable (i.e. sacrificed if the camera sustains too high of a radiation dose and fails or becomes contaminated).



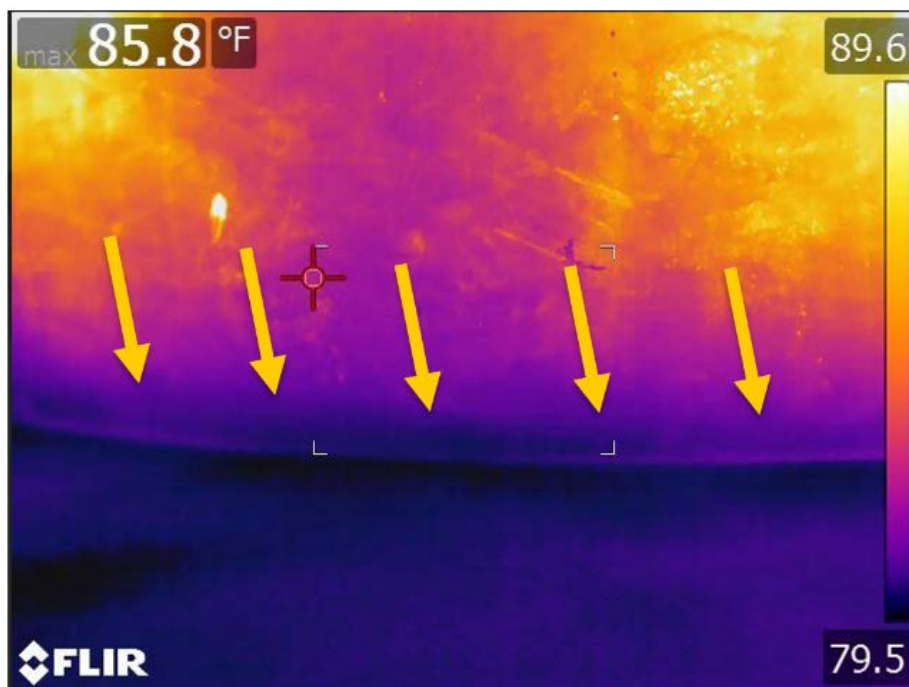


Figure 10 – Thermal images of test condition 6 using a high sensitivity camera to detect 1 liter of water in a canister. The water level is indicated by the yellow arrows, but is difficult to resolve.

Test conditions 5-6 appeared to yield a marginally-detectable difference between the dry and wet condition, however, this result was largely unclear and could result from some operator bias. Additionally, this test configuration would not be a field-deployable configuration with the current state of thermographic imaging technology and equipment, primarily due to cost and space limitations inside of a dry storage overpack. Test conditions 7-8 used a thermal camera that would be small enough to fit into a dry storage overpack and perform the same test. While test conditions 5-6 were marginally successful, the more realistic test conditions 7-8 failed to yield any perceptible difference between the dry and wet conditions.

The final round of testing (test conditions 9-12) involved creating a pocket of “trapped” water on the inner surface of the canister to evaluate the drop in temperature due to the presence of the water.

Due to the previous test condition, the pocket of water was located in a colder location between heating elements, which would also simulate where liquid water would be more likely to reside, if present. Due to the inconclusive results from test conditions 5-8, the pocket of water was elevated to avoid potential conduction effects at the base of the canister mockup. This would create a “best-case” scenario for testing in that a pocket of material would be cooler than the surrounding metal. If this test case were to be successful, additional tests under more realistic (less ideal) conditions would need to be run.

In this case, there was no detectable change observed between the case of a canister with 1 liter of trapped water and without the trapped water in an adjacent location of the canister mockup, as shown in Figure 11 below. There is some degree of uncertainty in the testing since the canister surfaces are highly variable in terms of certain areas having a duller finish (typically higher

emissivity) and other areas having a relatively shiny finish (resulting in a relatively low surface emissivity). Painting the surface would result in much better results, but as noted previously, painting is not a viable option for field deployment situations and was only evaluated for test conditions 1-4.

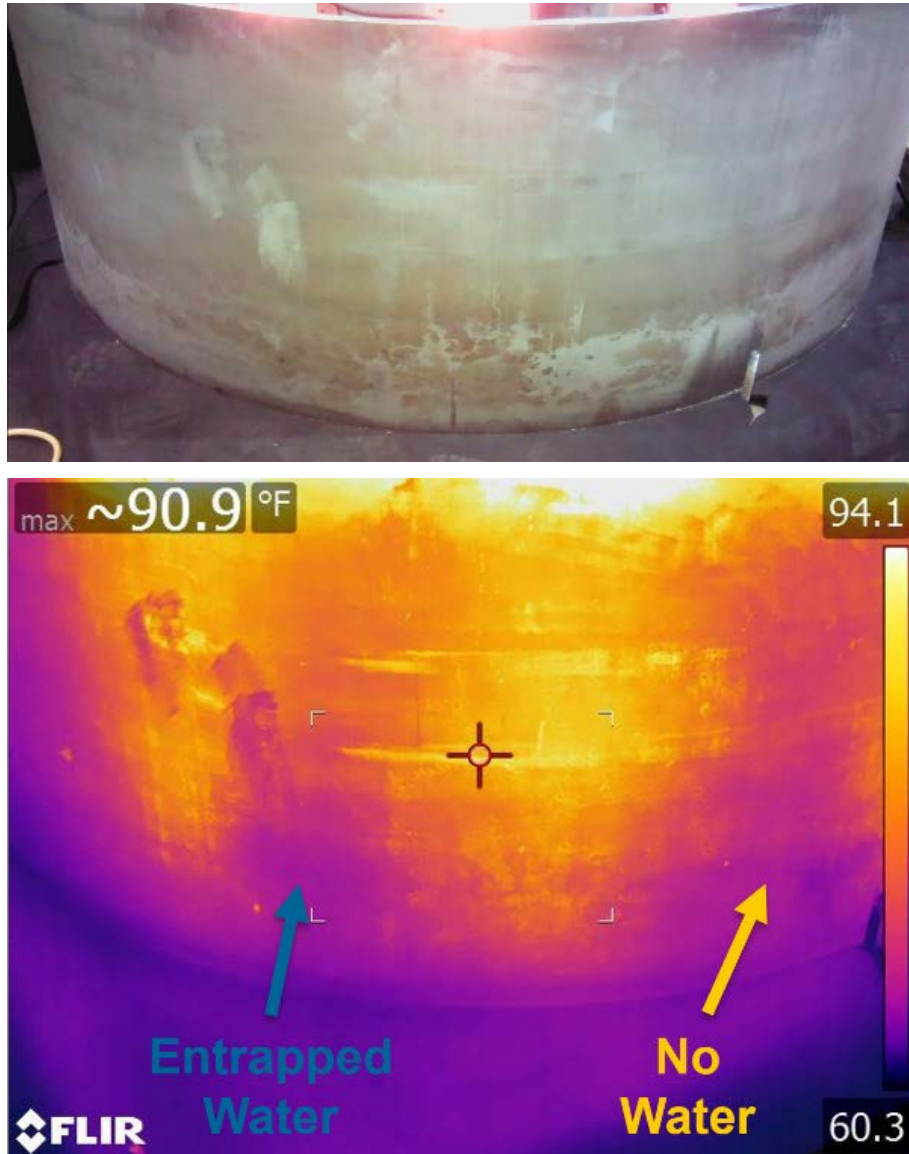


Figure 11 – Thermal images of test condition 10 – a pocket with 1 liter of trapped water

While the detection of internal pockets of water is secondary to the overall project goal, success of such an endeavor could support the nuclear industry during canister inspection campaigns. For safety reasons, the heat lamps used for testing could not be adjusted to fully simulate significant quantities of fuel located at the bottom of the canister to replicate a severe accident condition where fuel has rubblized to the bottom of a canister. However, it is anticipated that both temperature and dose measurements could be employed to provide sufficient data to determine whether or not fuel has experienced significant failures. Robotically-deployed systems have been demonstrated to work inside of the dry storage system environment to



perform various nondestructive evaluations possible, including visual inspection, eddy current inspection, temperature measurement, radiation dose measurement, etc. [6-8]. Such tools could be employed as needed for evaluation of a severe accident.

The final series of tests involved re-orienting the heat lamp to evaluate temperature fluctuations similar to those that would be expected from a hypothetical accident scenario involving rubblized fuel at the base of a dry storage canister. In such a case, it is anticipated that the temperature would increase near the base of the canister since radioactive decay from the fuel is the source of heating in real-world scenarios and if all or nearly all of the fuel were located near the base of the canister, it stands to reason that the base would have abnormally high heating. The test setup used for this evaluation is shown in Figure 12.

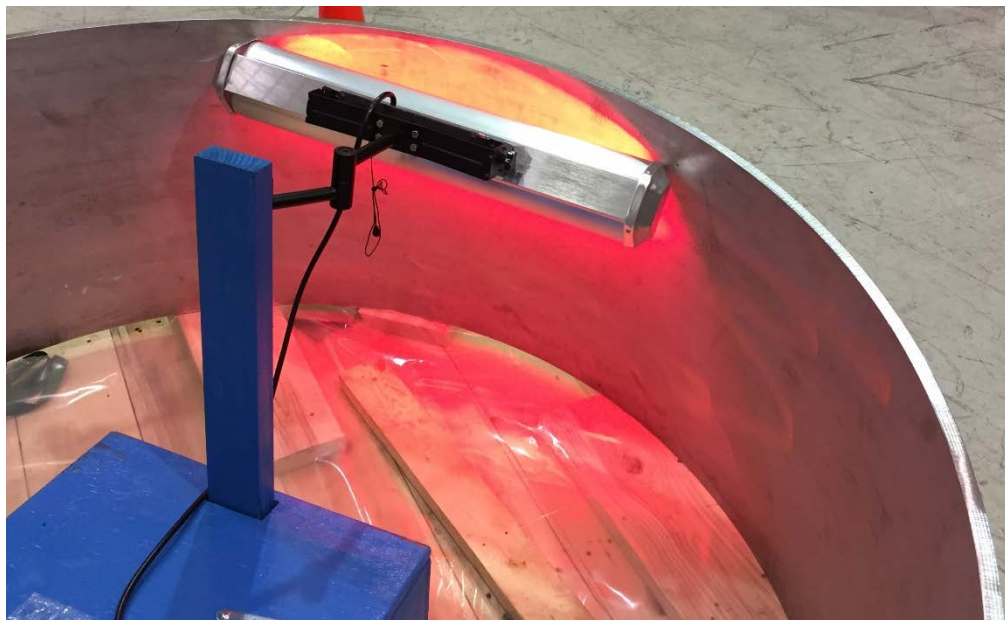


Figure 12 – UF heat lamp used to simulate an internal heat source near the base of a dry storage canister mockup

Figure 13 shows the resulting heat profile obtained from the test setup shown in Figure 12. In this case, only the low-cost, low-profile thermal camera was used for the evaluation. Even in this test setup with the lower sensitivity (disposable) thermal camera, there is a clear difference in the heat profile obtained. Based on these results, it appears plausible that a simple thermal evaluation – either with a thermal camera, RTD, or other temperature measurement device – would be capable of distinguishing between the scenario of an intact versus rubblized fuel canister; however, additional testing and/or baseline surveys would be required to make more definitive conclusions related to small fractions of fuel failure inside of a canister. It is anticipated that such surveys would be complemented by radiation measurements along and around a canister.

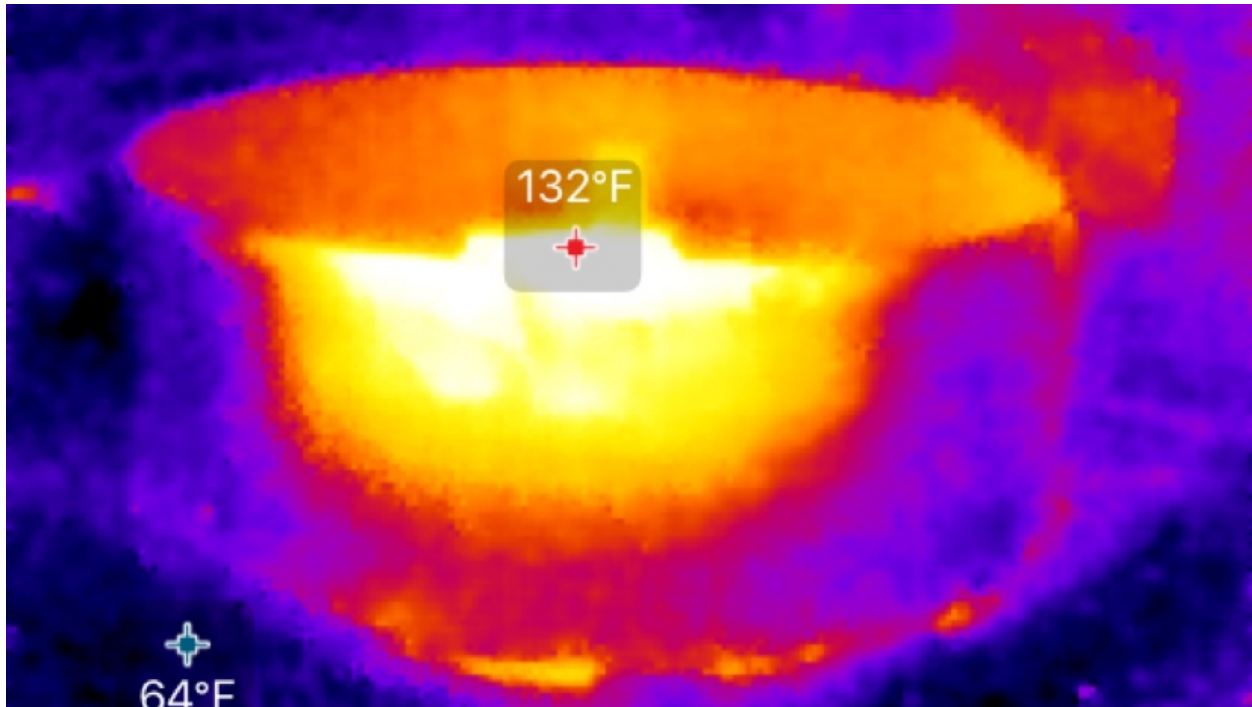


Figure 13 – UF heat lamp used to simulate an internal heat source near the base of a dry storage canister mockup

Similarly, for a hypothetical accident condition where canister temperatures far exceed normal operating conditions (i.e. peak cladding temperature reaches above 400 °C), such a condition could be detected by the use of thermal cameras as well as from a change in the dry storage system's temperature monitoring system.

### Field Trials

A test was performed in combination with McGuire Nuclear Station (Duke Energy) that showed that magnetic fields from surrounding equipment can impede the capability of the thermal camera to operate when deployed remotely from a robotic inspection delivery system in proximity to rare earth magnets. Due to this lesson learned during a field trial, the EPRI team identified a need to shield the camera from magnetic interference.

Figure 14 below shows the thermal camera mounted on a robotic delivery system that is used for inspection of dry storage systems. The thermal camera is indicated with the golden-colored arrow within the robot. Incidentally, this magnetic shielding could also serve to shield the camera from a portion of incident radiation from a dry storage system. The thermal camera is mounted in the top side of the robot, facing upward in the image, which corresponds to the camera oriented facing a dry storage canister when deployed onto the inner surface of the concrete overpack surrounding the dry storage canister during periods of storage at a nuclear plant site.



Figure 14 – Robotic deployment vehicle with an integrated, shielded thermal camera (golden arrow)

This robotic system with thermal camera was deployed to the Maine Yankee nuclear site in collaboration with an ongoing EPRI project to inspect canisters. The thermal camera operated in radiation fields up to 100 R/hr, however, the team noticed that the near-pristine canister surface was too reflective (shiny) for effective operation of the thermal camera since the surface emissivity was too low (shiny surfaces have a high reflectance and low emissivity, meaning that the camera essentially was looking at a mirror and saw itself rather than the surface to be inspected).

Due to these limitations, the EPRI team switched its focus from thermal camera-based temperature measurements to RTDs, which are a contact method for measuring temperatures that are not dependent on surface emissivities and reflectivities. Two related EPRI reports [6,8] provide significantly more detail on the testing performed as well as other related activities performed at these sites.

## Conclusions

In summary, thermographic methods were capable of detecting large volumes of remaining liquid water inside of a canister (~100 liters) but were not capable of definitively identifying smaller volumes of water closer to realistic remaining water volumes of less than 1 liter.

Test Condition	Surface Condition	Camera Used	Amount of water	Difference Detected?
1	Painted	FLIR T650sc	100 Liters	Pass
2	Painted	FLIR T650sc	100 Liters	
3	Painted	Seek Thermal	100 Liters	
4	Painted	Seek Thermal	100 Liters	
5	Unpainted	FLIR T650sc	1 Liter – bottom	Marginal
6	Unpainted	FLIR T650sc	1 Liter – bottom	
7	Unpainted	Seek Thermal	1 Liter – bottom	Fail
8	Unpainted	Seek Thermal	1 Liter – bottom	
9	Unpainted	FLIR T650sc	1 Liter – trapped	Fail
10	Unpainted	FLIR T650sc	1 Liter – trapped	
11	Unpainted	Seek Thermal	1 Liter – trapped	Fail
12	Unpainted	Seek Thermal	1 Liter – trapped	

While water trapped inside of a canister represents a minimal safety concern, this work shows that it may be possible to detect a large volume of free water inside of a canister-based system. It should be understood that the likelihood of having such a large volume of remaining water after the drying according to industry procedures is extremely small.

Additional testing evaluated the possibility of detecting severely failed (rubblized) fuel inside of a canister. As in the case for detection of water, it appears possible to detect a significant fraction of rubblized fuel that has fallen to the bottom of a canister, though the likelihood of such an occurrence is very small.

Based on these results, it is understood that the low-cost thermal cameras can potentially measure conditions adverse to safety occurring inside of the canister from the exterior (i.e. off-normal or accident conditions that would result in significantly higher canister surface temperatures). Such conditions could include extremely high levels of water remaining inside of a canister, severely damaged (rubblized) fuel at the bottom of a canister, and accident conditions. More representative conditions with much less than 1 liter (0.26 gallons) of remaining water as well as either lightly damaged fuel would likely not be detectable from dry, pristine conditions.

## References

1. Measurement of in-plane diffusivity in non-homogeneous slabs by applying flash thermography, J. Krapez, L. Spagnolo, M. Frieb, H. Maier, and G. Neuer, International Journal of Thermal Sciences, Vol. 43:10, pgs. 967-977, 2004.

2. The sources of heat generation in vibrothermography, J. Renshaw, J.C. Chen, S.D. Holland, and R.B. Thompson, NDT&E International, Vol. 44:8, pgs. 736-739, 2011.
3. *Enhanced Inspection of Hydroelectric Concrete Structures*, EPRI, Palo Alto, CA: 2014. 3002004453.
4. *Technology Insights Brief: Thermography for Power Industry Applications*, EPRI, Palo Alto, CA: 2016. 3002007326.
5. *Nondestructive Evaluation: NDE for Tanks and Containment Liners*. EPRI, Palo Alto, CA: 2013. 3002000462.
6. *Dry Canister Storage System Inspection and Robotic Delivery System Development*. EPRI, Palo Alto, CA: 2016. 3002008234.
7. *Extended Storage Collaboration Program (ESCP): Nondestructive Evaluation Subcommittee – Industry Progress Report*. EPRI, Palo Alto, CA: 2017. 3002010617.
8. *Inspection and Delivery System Development and Field Trial for Dry Canister Storage System Evaluation*. EPRI, Palo Alto, CA: 2017. 3002010621.

## Scale-Up Proposal for a Field Deployable System

A key component of this project is the focus on a multi-modal approach to the assessment of the health of the interior structures and fuel assemblies of dry storage casks which leverages strengths and capabilities of a diverse set of NDE methodologies: active mechanical resonances, emissions tomography, muon tomography, and passive/active ultrasonics. A goal of this project was to assess the feasibility, strengths, and weaknesses of each of these methodologies which would inform concepts for a deployable system for assessment and monitoring of cask structural health.

The original proposed plan was to demonstrate the methodologies in a scaled up field test on a full scale TN-32 at the end of the experimental, simulation, and laboratory work performed in the earlier phases of this IRP. However, soon after the project start date, an opportunity emerged for this team to get access to a full scale (unloaded) TN-32 cask at Columbiana Hi Tech in Greensboro, NC. This cask was being prepared for testing with real spent fuel at North Anna Power Station and was transferred to North Anna in October of 2017. Before that date, the active acoustics team made 4 field measurement trips testing progressively refined concepts (see that section for details), and the passive/active ultrasonics group were able to make 1 field trip. The data and insight obtained during these early phases proved extremely valuable in guiding the subsequent lab measurements in the direction of practical deployment. Because these unplanned early field measurements pushed back the proposed timeline and because of the administrative difficulty in gaining access to loaded TN-32 casks at ISFSIs, the team was not able to put together a scale-up demonstration system in the time frame of the IRP.

The team would like to offer some thoughts and suggestions about how the methodologies investigated might be integrated in a future system. Several criteria are considered in these suggestions: testing time, testing cost (both in equipment and on a per-test basis), complexity of setup, and level of detail feasible. Recall from earlier in the report, the target defect modality of interest was a catastrophic failure of a fuel assembly. The rationale is that

- (a) smaller scale defects such as cracks in the basket or fuel assemblies are likely inconsequential if the primary containment structure is healthy
- (b) “rubblized” fuel rods may result in fuel distribution that could cause criticality issues
- (c) large scale defects would have a higher reliability of being detected.

The last point is important because subsequent corrective action based on a test result would likely be extremely costly and introduce risk. So, minimization of “false positives” would be of high importance.



The two methodologies we see with the highest promise for near-term field testing would be the active acoustics resonance and muon tomography. Strengths and weaknesses are described in the table below.

Methodology	Strengths	Weaknesses
Active Acoustics	<ul style="list-style-type: none"> <li>• Robust, proven technology</li> <li>• Inexpensive</li> <li>• Fast time to result (hours)</li> <li>• Simple to set up</li> </ul>	<ul style="list-style-type: none"> <li>• Low level of detail</li> <li>• Test administration and interpretation may require a high level of training</li> </ul>
Muon Tomography	<ul style="list-style-type: none"> <li>• High level of detail is possible</li> <li>• System could be designed for simple interpretation of results</li> <li>• High degree of reliability</li> </ul>	<ul style="list-style-type: none"> <li>• Novel technology</li> <li>• Long testing times (days to weeks)</li> <li>• Expensive</li> <li>• Complex to setup</li> </ul>

The concept we would propose would be a two tiered testing strategy. The acoustics based testing would be conducted first. It is anticipated that several casks could be tested on one work day. If no problems were detected, the cask would be assessed as structurally sound. If a problem was detected, the cask would be flagged for further testing. A second acoustics test could be conducted to verify the presence of a problem. If verified, a muon tomography based test could be administered over a longer period of time (days to a few weeks) depending on the level of detail required to resolve the defect of interest. These muon imaging results could finally inform a course of corrective action for that cask.

The other methodologies investigated would likely have applications in related problems. The active/passive ultrasonics approach would likely have value in monitoring during transportation of a storage cask. It is relatively inexpensive and robust and can be tuned to be sensitive to particular developing defects (such as growing cracks). The emissions tomography based system needs further exploration and field testing data on loaded storage casks of varying age. Given the sensitivity to shielding, this method may well have applications for storage systems of a different design.